On the FFT-based homogenization of cohesive zones

An application to the fiber-matrix composite core of metal sandwich plates

Dissertation

Zur Erlangung des akademischen Grades des Doktors der Ingenieurwissenschaften (Dr.-Ing.)

Dem Promotionszentrum für Ingenieurwissenschaften
am Forschungscampus Mittelhessen

vorgelegt von
Felix Christian Bödeker, M.Sc.
Aus Gießen

Gießen
30. Januar 2026

Begutachtung durch:
Prof. Dr.-Ing. Stephan Marzi, Prof. Dr. Sangam Chatterjee
und Prof. Dr. Matti Schneider

Affidavit

I declare that I have completed this dissertation single-handedly without the unauthorized help of a second party and only with the assistance acknowledged therein. I have appropriately acknowledged and cited all text passages that are derived verbatim from or are based on the content of published work of others, and all information relating to verbal communications. I consent to the use of an anti-plagiarism software to check my thesis. I have abided by the principles of good scientific conduct laid down in the regulations of the leading University which were delivered to me in carrying out the investigations described in the dissertation.

Abstract

Advanced, lightweight materials with good structural performance and advantageous fracture behavior, such as Hybrix^{TM} sandwich plates with a composite core (Lamera AB, Gothenburg, Sweden), are essential for various industries. They enable the reduction of energy consumption, which makes them crucial in the fight against climate change. However, these materials are often complex and highly adaptable to the desired industrial applications. Hence, a full experimental characterization of the fracture behavior can be time-consuming and costly. For example, the sandwich core, which largely defines the fracture behavior of the entire plate, consists of polymer fibers and binder as well as a large amount of porosity.

Computational homogenization techniques can significantly reduce this experimental effort for the development of advanced engineering materials. In this approach, a virtual model for the microstructure of the material of interest is generated. Then, with the known material models of the constituents, effective macroscopic properties are obtained using computational methods. Compared with the classical Finite Element Method (FEM), which is commonly used for this purpose, solvers based on the Fast Fourier Transform (FFT) can significantly reduce the (computational) effort needed.

Nevertheless, the classical approaches cannot be applied straightforwardly to fracture behavior. Material layers, such as the composite core, can be modeled as a cohesive zone with a finite thickness, which allows for accounting for the fracture behavior with specialized computational methods. Building on such an existing classical FEM-based method, this work introduces a novel FFT-based homogenization scheme for cohesive zones, which extends the application of the FFT methods to fracture behavior. The novel FFT solver uses a displacement-based Barzilai-Borwein scheme and a non-local ductile damage model for the fracture behavior.

In addition, an innovative micromechanical modeling approach for the fracture behavior of the sandwich core is presented. It combines a novel method for the virtual microstructure generation for the composite core with the FFT-based homogenization scheme for cohesive zones. Furthermore, the parameters of the elastic-plastic material model including a non-local, ductile damage model were identified using microindentation and mode I tests (Double Cantilever Beam). The novel modeling approach, along with the FFT-based homogenization scheme for cohesive zones, was furthermore experimentally validated using mode III tests (Split Cantilever Beam). Hence, this modeling approach lays the foundation for an extension to other material layers, e.g., adhesives.

Kurzzusammenfassung

Fortschrittliche Werkstoffe mit guten Struktur- und Brucheigenschaften, wie zum Beispiel Hybrix^{TM}-Sandwichplatten mit einem Composite-Kern (Lamera AB, Göteborg, Schweden), können den Energieverbrauch in vielen Industriebereichen erheblich reduzieren und sind daher im Kampf gegen den Klimawandel von großer Bedeutung. Diese Werkstoffe sind jedoch oft komplex und individuell anpassbar, was eine experimentelle Charakterisierung des Bruchverhaltens zeitaufwändig und kostenintensiv macht. Der genannte Composite-Kern, der maßgeblich das Bruchverhalten der gesamten Platte bestimmt, besteht beispielsweise aus Polymerfasern, Bindemittel und einem hohen Porenanteil.

Um diesen experimentellen Aufwand erheblich zu reduzieren, können rechnergestützte Homogenisierungsverfahren eingesetzt werden. Dabei wird ein virtuelles Modell der Mikrostruktur generiert, aus dem anhand der bekannten Materialmodelle der jeweiligen Bestandteile und entsprechender Simulationen die effektiven makroskopischen Eigenschaften berechnet werden. Im Vergleich zu den häufig verwendeten klassischen Finite-Elemente-Methoden (FEM) können Simulationen auf Basis der Schnellen Fourier-Transformation (FFT) den (Rechen-)Aufwand dabei signifikant verringern.

Diese klassischen Homogenisierungsverfahren lassen sich jedoch nicht direkt auf das Bruchverhalten anwenden. Materialschichten wie der Composite-Kern können allerdings als Kohäsivzonen mit finiter Dicke modelliert werden, wofür spezielle Methoden die Berücksichtigung des Bruchverhaltens ermöglichen. Aufbauend auf einer entsprechenden bestehenden Methode basierend auf der klassischen FEM wird in dieser Arbeit ein neuartiges, FFT-basiertes Homogenisierungsschema für Kohäsivzonen vorgestellt. Dieses ermöglicht die Anwendung der FFT-basierten Methoden auf das Bruchverhalten. Der FFT-Solver nutzt ein verschiebungsbasiertes Barzilai-Borwein-Schema mit einem nicht-lokalen duktilen Schädigungsmodell.

Zusätzlich wird eine mikromechanische Modellierungsmethode für das Bruchverhalten des Composite-Kerns vorgestellt. Diese kombiniert eine neue Methode zur Generierung virtueller Modelle für die Mikrostruktur des Composite-Kerns mit dem FFT-basierten Homogenisierungsschema für Kohäsivzonen. Die Parameter des verwendeten elastisch-plastischen Materialmodells mit nicht-lokaler Schädigung wurden anhand von Mikroindentierungen und Mode-I-Versuchen (Double Cantilever Beam) ermittelt. Die vorgestellte Methode wurde experimentell durch Mode-III-Versuche (Split Cantilever Beam) und entsprechende FE-Simulationen validiert. Diese Arbeit bildet dabei die Grundlage für eine Erweiterung der Modellierungsmethode auf andere Materialschichten, wie z.B. Klebstoffe.

Acknowledgements

This dissertation is based on my research at the Doctoral Center for Engineering Science of the Research Campus of Central Hessen, carried out under the supervision of Justus Liebig University Giessen, in partnership with the Technische Hochschule Mittelhessen (THM). Its completion would not have been possible without the invaluable supervision, as well as the professional and personal support of many individuals who have accompanied me throughout this chapter of my life.

First, I would like to express my sincere gratitude to Prof. Dr.-Ing. Stephan Marzi for accepting me into his research group and for providing me with the opportunity to conduct the research presented in this thesis. His guidance has helped me grow both personally and professionally, and despite various challenges, he always managed to ensure the necessary support for my research at THM, for which I am truly grateful. In addition, I would like to thank Prof. Dr. Sangam Chatterjee for his supervision and support of my doctoral project as part of the collaboration between THM and Justus Liebig University. I am grateful to Prof. Dr. Matti Schneider for his time and effort in reviewing my dissertation, as well as for the insightful lectures and discussions at the "FFT-workshop" in Paris, which were highly valuable for my work. My sincere thanks also go to Prof. Dr.-Ing. Beate Lauterbach and Senior Lecturer Dr. Anders Biel for serving on my examination committee.

During my doctoral project, I had the opportunity to undertake a research stay at Karlstad University in Sweden. This experience would not have been possible without the support of Senior Lecturer Dr. Anders Biel, who warmly welcomed me and supervised my work. He and his wife Karin Lidgren were always available to listen and offer support, both personally and professionally. I am also grateful to Prof. Dr. Ulf Stigh for our discussions and for his valuable advice on approaching theoretical research topics during my stay at Karlstad University. Additionally, I would like to sincerely thank the members of the Department of Engineering and Physics for making my experience a great one, despite the challenges of being there at the beginning of the COVID-19 pandemic.

My sincere thanks also go to Dr. Ramin Moshfegh, formerly of Lamera AB (Gothenburg, Sweden), and currently at the Research Institutes of Sweden (Gothenburg), for the valuable and fruitful collaboration during my doctoral project.

I would like to express my heartfelt gratitude to my colleagues at the Institute of Mechanics and Materials at THM for their support, collaboration, and the inspiring working environment throughout my entire time there. A special thanks goes to Lea,

Kardelen, Ihssane, Peer, Dennis, Niklas, Pauline, Lena, Christopher, Lukas Loh, and Lukas Geisel. I truly enjoyed my time with you, and your support made my work a pleasure. Beyond being great colleagues, we also became friends, sharing many engaging discussions during work and coffee breaks. Special highlights were the conferences, where we shared valuable experiences and memorable moments together. In particular, the week at the "FFT-workshop" in Paris was an experience that I will always cherish.

I would like to extend my sincere thanks to Prof. Dr. Joachim Heil for our inspiring discussions on fundamental mathematical and physical problems.

Furthermore, I would like to acknowledge Prof. Dr. Georgios Stamoulis of Université de Bretagne Occidentale, who supervised me in my research internship at ENSTA Bretagne during my bachelor's studies. Along with Prof. Dr.-Ing. Stephan Marzi, he sparked my interest and curiosity in research in the field of mechanics.

Besides the research itself, administrative matters are also vital to the success of a doctoral project, and I am very thankful for the support that I received in this regard from the team at the Doctoral Center for Engineering Science of the Research Campus of Central Hessen, especially Ivana Büttner.

Last but not least, I could not have undertaken this journey without my family and friends. I am extremely grateful for their unconditional love, encouragement, and understanding. In particular, I am deeply grateful to my parents, Claudia and Thomas, whose love and advice have always guided and supported me. Their strength and resilience will always inspire me. It was also their childhood friend, Dr. Ralf Guckert, who first introduced me to the fascination of physics and science when I was a child, for which I am very grateful.

My special thanks also go to my grandfather, Karl-Heinz. His ability to unite an impressive work ethic, which enables the achievement of desired goals, with his unwavering support for his family will always serve as a role model to me. (Und wenn jemand weiß, wie man vieles "unter einen Hut" bekommt, dann er.) I find it remarkable that my grandfather has been attending nearly all of my handball games for almost 25 years.

I would also like to express my gratitude to my handball team HSG Butzbach. A training session in the evening after a tough day at work has always helped me free my mind and rethink ideas from a fresh perspective. Lastly, a very special thanks goes to my loyal companion, Rudi, for always being by my side and bringing joy to my days.

List of publications

This dissertation is not a cumulative thesis but is based on several publications that were produced as part of my doctoral project. Results from **Papers A**, **B**, and **C** are presented in Secs. 2 and 3, while results from **Paper D** are used in Secs. 4, 5, and 6. Excerpts from the papers are also incorporated into Secs. 1, 7, and 8. For transparency, the contributions of all co-authors are detailed alongside the respective scientific papers in the following using the CRediT format:

Paper A:

F. Bödeker, P. Herr, R. Moshfegh, A. Biel, and S. Marzi, "A novel FFT-based homogenization scheme for cohesive zones," *Procedia Structural Integrity*, vol. 42, pp. 490–497, 2022, 23rd European Conference on Fracture, doi:10.1016/j.prostr.2022.12.062.

Felix Bödeker: Conceptualization, Methodology, Formal Analysis, Software, Investigation, Writing - Original Draft, Visualization
Pauline Herr: Software, Investigation
Anders Biel: Investigation, Writing - Review & Editing, Supervision, Funding acquisition
Ramin Moshfegh: Resources, Writing - Review & Editing, Funding acquisition
Stephan Marzi: Resources, Writing - Review & Editing, Supervision, Funding acquisition

Paper B:

P. Herr, F. Bödeker, and S. Marzi, "Numerical investigation on the effect of fillers on the fracture behavior of adhesives," *Procedia Structural Integrity*, vol. 42, pp. 498–505, 2022, 23rd European Conference on Fracture, doi:10.1016/j.prostr.2022.12.063.

Pauline Herr: Software, Investigation, Visualization, Writing - Original Draft, Writing - Review & Editing
Felix Bödeker: Conceptualization, Methodology, Formal Analysis, Software, Investigation, Writing - Original Draft, Visualization, Supervision
Stephan Marzi: Resources, Writing - Review & Editing, Supervision, Funding acquisition

Paper C:

F. Bödeker, P. Herr, A. Biel, R. Moshfegh, and S. Marzi, "An FFT-based homogenization scheme for cohesive zones with an application to adhesives and the core material of thin metal sandwich plates," *Theoretical and Applied Fracture Mechanics*, vol. 129, p. 104186, 2024, doi:10.1016/j.tafmec.2023.104186.

Felix Bödeker: Conceptualization, Methodology, Formal Analysis, Software, Investigation, Writing - Original Draft, Visualization
Pauline Herr: Software, Investigation
Anders Biel: Investigation, Writing - Review & Editing, Supervision, Funding acquisition
Ramin Moshfegh: Resources, Writing - Review & Editing, Funding acquisition
Stephan Marzi: Resources, Writing - Review & Editing, Supervision, Funding acquisition

Paper D:

F. Bödeker, A. Biel, R. Moshfegh, and S. Marzi, "A novel FFT-based micromechanical modeling approach for the fracture behavior of a composite core in metal sandwich plates using a cohesive zone model," *Composites Structures*, vol. 368, p. 119231, 2025, 10.1016/j.compstruct.2025.119231.

Felix Bödeker: Conceptualization, Methodology, Formal Analysis, Software, Investigation, Writing - Original Draft, Writing - Review & Editing, Visualization
Anders Biel: Investigation, Writing - Review & Editing, Supervision, Funding acquisition
Ramin Moshfegh: Resources, Writing - Review & Editing, Funding acquisition
Stephan Marzi: Resources, Writing - Review & Editing, Supervision, Funding acquisition

Contents

Abstract i

Kurzzusammenfassung ii

Acknowledgements iii

List of publications v

Nomenclature xxvi

1 Introduction 1

1.1 Motivation 1

1.2 Objectives and solution strategy 4

1.3 State of the art 5

1.3.1 Part I: FFT-based homogenization of bulk materials including damage and fracture 5

1.3.2 Part II: Computational homogenization of cohesive zones 9

1.3.3 Part III: Generation of virtual models for microstructures 10

1.3.4 Part IV: Determination of material parameters at the microscale 13

1.3.5 Part V: Experimental determination of cohesive zone models . . 14

2 FFT-based homogenization of bulk materials 16

2.1 Governing equations 16

2.2 Scale transition relations between macro- and microscale 19

2.3 Reformulation into Lippmann-Schwinger framework 21

2.3.1 Homogenization problem 21

2.3.2 Damage regularization problem 25

2.4 Discretization 28

2.4.1 Homogenization problem 28

2.4.2 Damage regularization problem 37

2.5 FFT-based solution methods 38

2.5.1 Homogenization problem 38

2.5.2 Damage regularization and coupled problem 57

2.6 Implementation details 59

3 Extension of the FFT-based homogenization to Cohesive Zone Modeling 60
3.1 Governing equations and scale transition relations 60
3.2 Representativeness of the mechanical behavior compared with bulk homogenization 65
3.3 Estimation of the required marginal layer properties using numerical experiments 72
3.3.1 Peel mode I 72
3.3.2 Shear modes II/III 77
3.3.3 Discussion and recommendations for the parameter estimation . 80

4 Virtual model of the microstructure of the sandwich core 81
4.1 Experimental characterization of the microstructure of the sandwich core 81
4.2 Generation of the virtual model of the microstructure 88
4.2.1 Generation of the fiber structure 88
4.2.2 Addition of binder 99
4.2.3 Marginal layers and final algorithm 102
4.2.4 Implementation details 103
4.3 Evaluation of the representativeness of the generated model for the geometry and mechanical behavior of the sandwich core 104
4.3.1 Orientation angle β 104
4.3.2 Fiber nearest neighbor distance 105
4.3.3 Radial pair distribution function 107
4.3.4 Ripley's K function 108
4.3.5 Two-point correlation and volume fractions 109
4.3.6 Mechanical behavior and discussion 114

5 Experimental parameter identification for the material models at the microscale 115
5.1 Elastic properties 115
5.2 Plastic properties 120
5.3 Damage properties 125

6 Model validation using mode III Split Cantilever Beam tests 130
6.1 Experimental procedure 130
6.2 Numerical modeling 132

6.3 Results 135
6.4 Comparison of experimental fracture surfaces with simulated crack patterns 139
6.5 Discussion 142

7 Conclusions **142**

8 Outlook **146**

Appendices **150**

A Distance between the central line segments of two fiber segments **150**

B Operator norm of the tangent stiffness **151**

References **154**

Nomenclature

Scalars

α	constant used in variational calculus
α_+, α_-	Lipschitz constant of the gradient and strong convexity constant of the objective function in optimization theory
$\bar{\eta}$	parameter to define the slope of the linear Drucker-Prager type plastic flow potential
β, γ	orientation angles between the fiber (segment) and the z-axis and fiber (segment) and the x-axis
$\beta_i^{\mathrm{b}}, \gamma_i^{\mathrm{b}}$	global orientation angle of the bottom segment of fiber i around the global y- and z-axis
$\beta_{ij}^{\mathrm{r}}, \gamma_{ij}^{\mathrm{r}}$	relative orientation angles of segment j of fiber i around the local y- and z-axis
$\beta_{\max}, \beta_{\mathrm{str}}$	maximum orientation angle β, and β for a straight fiber between the face sheets
$\beta_i^{\mathrm{ts}}, \beta_i^{\mathrm{bs}}$	orientation angle with respect to the z-axis of the segment with highest and lowest z positions
$\left[\vec{x}_i^{\mathrm{ts}}\right]_3$, $\left[\vec{x}_i^{\mathrm{bs}}\right]_3$	z component of the segment end point of fiber i with the largest and the smallest values of z
δ_{ij}^{c}	overlap between two fiber segments caused by fiber curvature
$\delta_i^{\mathrm{ts}}, \delta_i^{\mathrm{bs}}$	overlap between a fiber i with the top and bottom face sheet
$\Delta_{ijkl}^{\mathrm{fib\_fib}}, \delta_{ijkl}^{\mathrm{fib\_fib}}$	distance and overlap between segment j of fiber i and segment l of fiber k
δ_{ij}	Kronecker delta; one if $i = j$ and zero otherwise
$\dot{\lambda}$	plastic multiplier
η, ξ	parameters to define the shape of the linear Drucker-Prager yield surface

κ	Lagrange multiplier
λ^0, μ^0	Lamé parameters of the isotropic elastic homogeneous reference material
λ_i^{eig}, $\tilde{\lambda}^{\text{eig}}$	(sorted) eigenvalues of the tangent stiffness tensor for $i \in \{1, 2, ..., 6\}$, where λ_1^{eig} and λ_6^{eig} denote the largest and smallest eigenvalue, respectively; eigenvalue in the computation of the operator norm of the tangent stiffness tensor
$\mathcal{L}$	Lagrange function
ν, ν_{ind}	Poisson's ratio and Poisson's ratio of the indenter material
Φ, Ψ	yield surface and plastic flow potential
$\overline{\Delta\varepsilon}_i^{*1,2}$, $\widetilde{\Delta\varepsilon}_i^{*1,2}$	coefficients for the representation of $\underline{\Delta\varepsilon}^{*1,2}$ in the eigentensor basis $\underline{M}_i$ and the corresponding coefficients that solve the optimization problem for the operator norm
ρ_{fib}	area density of fibers on the surface of a micrograph
σ,τ_{II}, τ_{III}	mode I peel stress, mode II in-plane shear stress and, mode III out-of-plane shear stress component of the macroscopic traction vector $\vec{t}_{\text{M}}$
σ_{p}	undamaged hydrostatic pressure
θ	beam rotation
θ_{a}	half-apex angle of a canonical indenter tip
A_{coh}	transverse area of the virtual model of the microstructure for the cohesive zone
a_i	$i \in \{1, 2, 3, 4, 5\}$ constants for the computation of the distance between two fiber segments
c_1, c_2, ω	cognitive, social, and inertia parameters in the Particle Swarm Optimization
$CDF_{\text{emp}}, PDF_{\text{emp}}$	empirical cumulative distribution and probability density functions of the fiber orientation

$CDF_{\mathrm{m}}, PDF_{\mathrm{m}}$	model cumulative distribution and probability density functions of the fiber orientation
D	scalar damage parameter
d^0	initial yield stress
$d_{\mathrm{B}}, d_{\mathrm{S}}$	diameter of a projected contact circle of Berkovich and spherical indenter tip
d_{ij}^{f}	distance between the center points of two fibers i and j on a micrograph
E	Young's modulus
$E_{\mathrm{ind}}, E_{\mathrm{red}}$	Young's modulus of the indenter material and reduced modulus
F	force
$f, f_{\mathrm{c}}, f_{\mathrm{f}}, f_{\mathrm{s}}$	(general) objective function and contributions from fiber curvature, overlap, and overlap with face sheets in the optimization problem for the generation of virtual models of the microstructure for the sandwich core material
$F_{\mathrm{b}}^{\mathrm{exp}}, F_{\mathrm{b}}^{\mathrm{sim}}$	experimental and simulated force in Berkovich indentation
$F_{\mathrm{load}}, F_{\mathrm{unload}}$	force during loading and unloading in microindentation experiments
$F_{\mathrm{s}}^{\mathrm{exp}}, F_{\mathrm{s}}^{\mathrm{sim}}$	experimental and simulated force in spherical indentation
f_j	discrete spatial points for the computation of the discrete spatial frequencies in the direction of the j-th axis
G_{r}	Radial Pair Distribution
H	hardening modulus
h, h_{max}	indentation depth and its maximum in microindentation experiments
h_{v}	edge length of a voxel (or pixel)
J	J-integral
J_2	second invariant of the undamaged stress deviator

K_r	Ripley's K function
l	non-uniform characteristic length parameter for the damage regularization problem
l_0, l_d, l_nd	homogeneous reference length and characteristic length parameters in the damaging and non-damaging phases
l_ch	characteristic length scale for the constituents of a microstructure
$l_\mathrm{fib}, r_\mathrm{fib}, l_\mathrm{seg}$	fiber length and radius, and fiber segment length
$l_\mathrm{mi}, l_\mathrm{ma}$	length of the minor and major axis of an ellipse
L_j	the edge length of the virtual model of the microstructure in the direction of the j-th axis
MSE, MSE_a	(relative) Mean Squared Errors for microindentation
MSE_β	Mean Squared Error for orientation angle β
$n_\mathrm{fib}, n_\mathrm{seg}$	number of fibers and segments of each fiber
$n_\mathrm{b}, n_\mathrm{s}$	number of microindentation experiments with a Berkovich and a spherical tip
N_j	number of points (voxels) in the direction of the j-th axis
$p^0_\mathrm{nl}, p^\mathrm{f}_\mathrm{nl}$	non-local equivalent plastic strain at damage initiation and at failure
$p_\mathrm{l}, p_\mathrm{nl}$	local and non-local equivalent plastic strain
R	radius of spherical indenter tip
$r, \Delta r$	radius and width of an annulus
r_1^n, r_2^n	random variables for each particle in each step of the Particle Swarm Optimization
r_se	radius of structuring element for morphological operations
s	parameter in the geometrical description of the central line segment of a fiber segment

S, S^+, S^-	general boundary and two opposite surfaces of the cuboid virtual model of the microstructure
s^+_{coh}, s^-_{coh}	macroscale interfaces between cohesive zone and bulk material in the current configuration
S^+_{coh}, S^-_{coh}	macroscale interfaces between cohesive zone and bulk material in the reference configuration
S_{TP}, S_{f}	Two-point correlation function and correction factor for its computation
s^i_{gd}	step size of the gradient descent in iteration i
S_1, S_2	outer surface of the damaging and non-damaging phases in the control volume V_{C}
S_{D}	interface between damaging and non-damaging phase
s_i, s^{c}_i	$i \in \{1, 2\}$, parameters s, and s of the critical point for the shortest distance of two fiber segments
t	time
t_ε	coefficient for the interpolation of the strain fluctuation fields $\underline{\varepsilon}^{*1}$ and $\underline{\varepsilon}^{*2}$
t_{coh}	thickness of the cohesive zone
tol	tolerance of solution accuracy in numerical algorithms
tol^{D}, tol^{M}	tolerance of solution accuracy of the solvers for the damage regularization and homogenization problems
u, v, w	mode I, II, and III components of the separation vector
u_{f}	mode I separation at failure
V	volume of the virtual model of the microstructure
$v_{\mathrm{ft}}, v_{\mathrm{bt}}$	fiber and binder target volume fraction
$v_{\mathrm{f}}, v_{\mathrm{b}}$	fiber and binder volume fraction

$V_{\mathrm{C}}^{\mathrm{D}}$, $V_{\mathrm{C}}^{\mathrm{ND}}$	volume of damaging and non-damaging phase in control volume V_{C}
w_{β}, w_{ij}	weight factors
$W_{\mathrm{el}}, W_{\mathrm{t}}, W_{\mathrm{diss}}$	elastic, total, and dissipated indentation work
w_{pot}, W_{pot}	condensed, incremental strain energy density at the microscale and its volumetric average
x, y, z	(Cartesian) coordinates
X_{M}, X_{M}, Z_{M}	(Cartesian) coordinates in the reference configuration at the macroscale
x_{M}, y_{M}, z_{M}	(Cartesian) coordinates in the current configuration at the macroscale
$X_{\mathrm{M}}^{\mathrm{l}}$, $Y_{\mathrm{M}}^{\mathrm{l}}$, $Z_{\mathrm{M}}^{\mathrm{l}}$	local (Cartesian) coordinate system in the reference configuration at the macroscale
$x_{\mathrm{M}}^{\mathrm{l}}$, $y_{\mathrm{M}}^{\mathrm{l}}$, $z_{\mathrm{M}}^{\mathrm{l}}$	local, co-rotational (Cartesian) coordinate system in the current configuration at the macroscale

Vectors

$\left[\vec{u}^{\,*}\right]^i$	i-th iteration of the displacement fluctuation field in the FFT-based solution algorithm
$\left[\dot{\vec{u}}^{\,*}\right]^+$, $\left[\dot{\vec{u}}^{\,*}\right]^-$	displacement fluctuation rates on opposite surfaces of the cuboid virtual model of the microstructure S^+ and S^-
$\left[\overrightarrow{du}^{\,*}\right]^i$	i-th iteration of a displacement fluctuation type field to store the application of the discrete solution operator for the homogenization problem in the FFT-based solution algorithm
$\vec{\delta}_{\mathrm{M}}^{\mathrm{gl}}$, $\vec{\delta}_{\mathrm{M}}$	macroscale separation vector of the cohesive zone in the global coordinate system in the current configuration and in the co-rotational local coordinate system
$\vec{\xi}$	continuous (angular) spatial frequency vector in Fourier space
$\vec{\xi}^{\,\mathrm{D}}$	discrete (angular) spatial frequency vector in Fourier space
$\vec{\xi}^{\,\widetilde{\mathrm{D}}}$	discrete auxiliary dimensionless (angular) spatial frequency vector
$\vec{a}$, $\vec{b}$	vectors in sets A and B
$\vec{d}_{ij}$	vector between the two segment end points $\vec{x}_{ij}^{\,\mathrm{se}}$ and $\vec{x}_{i(j-1)}^{\,\mathrm{se}}$ of a segment j of fiber i
$\vec{e}_n$	unit vector in the x-, y-, or z-direction, $n \in \{1, 2, 3\}$
$\vec{m}$	vector containing the index of the discrete position on the underlying integer lattice $\mathbb{Z}^3$ in the virtual model of the microstructure
$\vec{n}$	normal vector on a general outer surface of the virtual model of the microstructure
$\vec{n}_{\mathrm{coh}}$	orientation of the cohesive zone at the microscale
$\vec{n}_{\mathrm{d}}$, $\vec{n}_1$, $\vec{n}_2$	normal vector on the phase boundary of the damaging phase, and surfaces S_1 and S_2
$\vec{N}_{\mathrm{M}}$	normal to the middle surface of the macroscale cohesive zone with a finite thickness in the reference configuration

$\vec{n}_{\mathrm{M}}$	normal to the middle surface of the macroscale cohesive zone with a finite thickness in the current configuration
$\vec{q}$, $\vec{q}^{*}$	discrete (angular) spatial frequency vector for the staggered grid finite difference discretization and its complex conjugate
$\vec{r}$	line element
$\vec{t}$, $\vec{t}^{+}$, $\vec{t}^{-}$	(general) traction vector on a boundary S and traction vectors on opposite surfaces S^{+} and S^{-} at the microscale
$\vec{u}$	displacement vector
$\vec{u}^{*}$	displacement fluctuation vector
$\vec{u}^{*1}$, $\vec{u}^{*2}$	specified displacement fluctuation fields
$\vec{u}_{\mathrm{M}}^{+}$, $\vec{u}_{\mathrm{M}}^{-}$	macroscale displacement vector from the reference to the current configuration on the opposite interfaces S_{coh}^{+}, s_{coh}^{+} and S_{coh}^{-}, s_{coh}^{-} between cohesive zone and surrounding bulk material
$\vec{v}$	auxiliary vector
$\vec{w}_{ijkl}$	distance between the central line segments of segments j and l of fibers i and k
$\vec{x}$	position vector at the microscale
$\vec{x}^{\mathrm{D}}$	discrete spatial position at the microscale
$\vec{x}_{ij}^{\mathrm{se}}$	position vector of segement end point j of fiber i
$\vec{x}_{ij}^{\mathrm{cs}}$	position vector of a point on the central line segment of segment j of fiber i
$\vec{X}_{\mathrm{M}}^{+}$, $\vec{X}_{\mathrm{M}}^{-}$	macroscale position vector in the reference configuration on the opposite interfaces S_{coh}^{+} and S_{coh}^{-} between cohesive zone and surrounding bulk material
$\vec{x}_{\mathrm{M}}^{+}$, $\vec{x}_{\mathrm{M}}^{-}$	macroscale position vector in the current configuration on opposite interfaces s_{coh}^{+} and s_{coh}^{-} between cohesive zone and surrounding bulk material

$\vec{y}$, $\vec{y}_n$	vector in space Y and specified arbitrary points $n \in \{1, 2\}$
$\vec{y}^*$, $\vec{y}^i$	value of $\vec{y}$ at the minimum of f and the i-th iteration of $\vec{y}$ in the gradient descent

Second order tensors

$\underline{\bar{\sigma}}$	undamaged stress tensor at the microscale
$\underline{\bar{s}}$	undamaged stress deviator
$\underline{\Delta\varepsilon}^{*1,2}$	difference of two strain fluctuation fields $\underline{\varepsilon}^{*1}$ and $\underline{\varepsilon}^{*2}$
$\underline{\sigma}$	stress tensor at the microscale
$\underline{\sigma}^i$	i-th iteration of the stress field in the FFT-based solution algorithm
$\underline{\sigma}_{\mathrm{M}}$	stress tensor at the macroscale
$\underline{\tau}$	stress fluctuation tensor
$\underline{\varepsilon}$, $\underline{\varepsilon}^*$	strain tensor and strain fluctuation tensor at the microscale
$\underline{\varepsilon}^{*1}$, $\underline{\varepsilon}^{*2}$	specified strain fluctuation fields
$\underline{\varepsilon}^i$	i-th iteration of the strain field in the FFT-based solution algorithm
$\underline{d\varepsilon}^i$	i-th iteration of a strain fluctuation type field to store the application of the discrete Green operator in the FFT-based solution algorithm
$\underline{E}$	volumetric average strain in the virtual model of the microstructure
$\underline{G}^0$, $\underline{G}$	solution operator to the homogenization problem with arbitrary linear elastic reference material and with the fourth order identity tensor; explicit expression known in Fourier space
$\underline{G}^0_{\mathrm{SG}}$, $\underline{G}_{\mathrm{SG}}$	solution operator to the discrete homogenization problem with arbitrary linear elastic reference material and with the fourth order identity tensor for the staggered grid finite difference discretization; explicit expression known in Fourier space
$\underline{H}$	macroscopic (average) displacement gradient of the separation vector
$\underline{I}$	second order identity tensor
$\underline{M}_i$	eigentensor of the tangent stiffness tensor

$\underline{R}_{\mathrm{M}}^{\mathrm{l}}$ macroscale rotation matrix for the coordinate transformation from the global coordinates in the current configuration into the co-rotational local coordinate system of the cohesive zone

$\underline{R}_{\mathrm{M}}^{\mathrm{rig}}$ rotation matrix for rigid body rotations at the macroscale

$\underline{R}_{\gamma_i^{\mathrm{b}}}$, $\underline{R}_{\gamma_{ij}^{\mathrm{r}}}$ rotation matrix around the corresponding z-axis with angles γ_i^{b} and γ_{ij}^{r};

$$\underline{R}_{\gamma_i^{\mathrm{b}}} = \begin{pmatrix} \cos\left(\gamma_i^{\mathrm{b}}\right) & -\sin\left(\gamma_i^{\mathrm{b}}\right) & 0 \\ \sin\left(\gamma_i^{\mathrm{b}}\right) & \cos\left(\gamma_i^{\mathrm{b}}\right) & 0 \\ 0 & 0 & 1 \end{pmatrix},$$

$$\underline{R}_{\gamma_{ij}^{\mathrm{r}}} = \begin{pmatrix} \cos\left(\gamma_{ij}^{\mathrm{r}}\right) & -\sin\left(\gamma_{ij}^{\mathrm{r}}\right) & 0 \\ \sin\left(\gamma_{ij}^{\mathrm{r}}\right) & \cos\left(\gamma_{ij}^{\mathrm{r}}\right) & 0 \\ 0 & 0 & 1 \end{pmatrix}$$

$\underline{R}_{\beta_i^{\mathrm{b}}}$, $\underline{R}_{\beta_{ij}^{\mathrm{r}}}$ rotation matrix around the corresponding y-axis with angles β_i^{b} and β_{ij}^{r};

$$\underline{R}_{\beta_i^{\mathrm{b}}} = \begin{pmatrix} \cos\left(\beta_i^{\mathrm{b}}\right) & 0 & \sin\left(\beta_i^{\mathrm{b}}\right) \\ 0 & 1 & 0 \\ -\sin\left(\beta_i^{\mathrm{b}}\right) & 0 & \cos\left(\beta_i^{\mathrm{b}}\right) \end{pmatrix},$$

$$\underline{R}_{\beta_{ij}^{\mathrm{r}}} = \begin{pmatrix} \cos\left(\beta_{ij}^{\mathrm{r}}\right) & 0 & \sin\left(\beta_{ij}^{\mathrm{r}}\right) \\ 0 & 1 & 0 \\ -\sin\left(\beta_{ij}^{\mathrm{r}}\right) & 0 & \cos\left(\beta_{ij}^{\mathrm{r}}\right) \end{pmatrix}$$

Fourth order tensors

$\underline{\underline{\Gamma}}^0, \underline{\underline{\Gamma}}$	Green operator for the homogenization problem with arbitrary linear elastic reference material and with the fourth order identity tensor; explicit expression known in Fourier space
$\underline{\underline{\Gamma}}^0_{\mathrm{SG}}, \underline{\underline{\Gamma}}_{\mathrm{SG}}$	Green operator for the discrete homogenization problem with arbitrary linear elastic reference material and with the fourth order identity tensor for the staggered grid finite difference discretization; explicit expression known in Fourier space
$\underline{\underline{C}}^0$	stiffness of isotropic, linear elastic reference material
$\underline{\underline{C}}^{\mathrm{t}}$	tangent stiffness tensor
$\underline{\underline{I}}$	symmetric fourth order identity tensor: $\underline{\underline{I}} := \frac{1}{2}\sum_{i,j,k,l=1}^{3}\left(\delta_{ik}\delta_{jl}+\delta_{il}\delta_{jk}\right)\vec{e}_i\otimes\vec{e}_j\otimes\vec{e}_k\otimes\vec{e}_l$

Sets, n-tuples, and vector spaces

$\beta^{\mathrm{b}}, \gamma^{\mathrm{b}}, \vec{x}^{\mathrm{b}}$	n-tuples containing β_i^{b}, γ_i^{b}, and $\vec{x}_i^{\mathrm{b}}$ of all fibers i
$\beta^{\mathrm{r}}, \gamma^{\mathrm{r}}$	n-tuples containing β_{ij}^{r} and γ_{ij}^{r} of all fibers i and segments j
$\mathbb{Z}^3$	three-dimensional integer lattice; subset of the corresponding Euclidean vector space
A, B	image and structural element; subsets of the integer lattice with the corresponding dimension
A_n^i	set A after n iterations of the closing operation in the i-th global iteration of the algorithm
A_{f}	fiber structure
A_b, A_{-b}	set A translated by vector $\vec{b}$ and $-\vec{b}$
H^1_{per}	first-order Sobolev and Hilbert space for fluctuation displacement fields of the homogenization problem
v_n^{PSO}	"particle" velocity in step n of the particle swarm optimization, n-tuple
$x_{\mathrm{lm}}^{\mathrm{PSO}}, x_{\mathrm{gm}}^{\mathrm{PSO}}$	"particle" position of the local and global minimum in the Particle Swarm Optimization, n-tuple
x_n^{PSO}	"particle" position in step n of the Particle Swarm Optimization, n-tuple
Y	arbitrary admissible vector space

Mathematical symbols

$\bullet^{\mathrm{T}}$	standard transpose of vector or tensor $\bullet$
$\dot{\bullet}$	time derivative of variable $\bullet$
$((A \oplus B)^n \ominus B)^n$	n iterations of closing applied to set A using structural element B
$(\vec{\bullet}, \vec{\bullet})_{\mathrm{H}^1_{\mathrm{per}}}$	inner product of space H^1_{per}: $(\vec{\bullet}, \vec{\bullet})_{\mathrm{H}^1_{\mathrm{per}}} := \langle \operatorname{grad}^{\mathrm{S}} \vec{\bullet} : \operatorname{grad}^{\mathrm{S}} \vec{\bullet} \rangle_{\mathrm{V}}$
$\langle \bullet \rangle_{\mathrm{V}}$	volumetric average of variable $\bullet$ in the virtual model of the microstructure: $\langle \bullet \rangle_{\mathrm{V}} = \frac{1}{V} \int_V \bullet \, \mathrm{d}\, V$
$\lvert \vec{\bullet} \rvert$	magnitude of vector $\vec{\bullet}$
$\lvert\lvert \underline{\underline{\bullet}} \rvert\rvert_{\mathrm{op}}$	operator norm of fourth order tensor $\underline{\underline{\bullet}}$: $\lvert\lvert \underline{\underline{\bullet}} \rvert\rvert_{\mathrm{op}} := \sup \frac{\lvert\lvert \underline{\underline{\bullet}} : \underline{\bullet} \rvert\rvert_{\mathrm{F}}}{\lvert\lvert \underline{\bullet} \rvert\rvert_{\mathrm{F}}}$ with an arbitrary, admissible second order tensor $\underline{\bullet}$
$\lvert\lvert \vec{\bullet} \rvert\rvert_{\mathrm{H}^1_{\mathrm{per}}}$	norm of space H^1_{per}: $\lvert\lvert \vec{\bullet} \rvert\rvert_{\mathrm{H}^1_{\mathrm{per}}} := (\vec{\bullet}, \vec{\bullet})^{\frac{1}{2}}_{\mathrm{H}^1_{\mathrm{per}}} = \langle \operatorname{grad}^{\mathrm{S}} \vec{\bullet} : \operatorname{grad}^{\mathrm{S}} \vec{\bullet} \rangle^{\frac{1}{2}}_{\mathrm{V}}$
$\lvert\lvert \underline{\bullet} \rvert\rvert_{\mathrm{F}}$	Frobenius norm of the second order tensor $\underline{\bullet}$: $\lvert\lvert \underline{\bullet} \rvert\rvert_{\mathrm{F}} = \sqrt{\underline{\bullet} : \underline{\bullet}}$
$\mathcal{F}(\bullet)$	continuous Fourier Transform of $\bullet$
$\mathcal{F}^{-1}(\bullet)$	inverse continuous Fourier Transform of $\bullet$
$\nabla^2 \bullet$	Laplacian of $\bullet$
DFT	Discrete Fourier Transform
DFT^{-1}	Inverse Discrete Fourier Transform
$\operatorname{div}(\bullet)$	divergence of a vector or tensor field
$\operatorname{eig}(\underline{\underline{\bullet}})$	eigenvalue of fourth order tensor $\underline{\underline{\bullet}}$
FFT	Fast Fourier Transform
FFT^{-1}	inverse Fast Fourier Transform
$\operatorname{grad}(\bullet)$	gradient of a vector or scalar field
$\operatorname{grad}^{\mathrm{S}} \vec{\bullet}$	symmetric gradient of vector $\vec{\bullet}$: $\frac{1}{2}\left[\operatorname{grad} \vec{\bullet} + (\operatorname{grad} \vec{\bullet})^{\mathrm{T}}\right]$

$\max(\bullet)$, $\min(\bullet)$	maximum and minimum of the an arbitrary variable or set of variables $\bullet$
$\mathrm{tr}(\underline{\bullet})$	trace of a second order tensor $\underline{\bullet}$
$\sup_{\bullet}$, $\inf_{\bullet}$	supremum and infimum with respect to the arbitrary variable $\bullet$
$\underline{\bullet}$	second order tensor
$\underline{\bullet}^1 : \underline{\bullet}^2$	double dot product of two second order tensors $\underline{\bullet}^1$ and $\underline{\bullet}^2$: $\underline{\bullet}^1 : \underline{\bullet}^2 := \sum_{i,j=1}^{3} \bullet_{ij}^1 \bullet_{ij}^2$
$\underline{\bullet}^1 \cdot \vec{\bullet}^2$	(right) dot product of second order tensor $\underline{\bullet}^1$ and vector $\vec{\bullet}^2$: $\underline{\bullet}^1 \cdot \vec{\bullet}^2 := \sum_{i,j=1}^{3} \bullet_{ij}^1 \bullet_{j}^2 \vec{e}_i$
$\underline{\underline{\bullet}}$	fourth order tensor
$\underline{\underline{\bullet}} = \underline{\bullet}^1 \otimes \underline{\bullet}^2$	outer product between two second order tensors $\underline{\bullet}^1$ and $\underline{\bullet}^2$; returns a fourth order tensor, whose components compute as $\underline{\underline{\bullet}}_{ijkl} := \underline{\bullet}_{ij}^1 \underline{\bullet}_{kl}^2$
$\underline{\underline{\bullet}}^1 : \underline{\bullet}^2$	double dot product of a fourth and a second order tensor $\underline{\underline{\bullet}}^1$ and $\underline{\bullet}^2$: $\underline{\underline{\bullet}}^1 : \underline{\bullet}^2 := \sum_{i,j,k,l=1}^{3} \bullet_{ijkl}^1 \bullet_{kl}^2 \vec{e}_i \otimes \vec{e}_j$
$\underline{\underline{\Gamma}}^0 : \underline{\bullet}$	application of the respective Green operator to a second order tensor field, also holds for $\underline{\underline{\Gamma}}$, $\underline{\underline{\Gamma}}_{\mathrm{SG}}^0$, and $\underline{\underline{\Gamma}}_{\mathrm{SG}}$
$\underline{G}^0 : \vec{\bullet}$	application of the respective solution operator for the homogenization problem to a vector field, also holds for $\underline{G}$, $\underline{G}_{\mathrm{SG}}^0$, and $\underline{G}_{\mathrm{SG}}$
$\vec{\bullet} \otimes \vec{\bullet}$	standard dyadic product of two vectors $\vec{\bullet}$
$\vec{\bullet}$	vector
$\vec{\bullet} \cdot \vec{\bullet}$	standard dot product of two vectors
$\vec{\bullet}^1 \cdot \underline{\bullet}^2$	(left) dot product of vector $\vec{\bullet}^1$ and second order tensor $\underline{\bullet}^2$: $\vec{\bullet}^1 \cdot \underline{\bullet}^2 := \sum_{i,j=1}^{3} \bullet_{i}^1 \bullet_{ij}^2 \vec{e}_j$
$\widehat{\bullet}$	continuous Fourier Transform of $\bullet$
$A \ominus B$	erosion of set A with structural element B
$A \oplus B$	dilation of set A with structural element B

$D_i^{\pm}$	staggered grid finite difference operators in the direction of the i-th axis
$I(\bullet)$	Indicator function, one if $\bullet$ is true and zero otherwise
$m(\vec{x})$	one, if the position vector $\vec{x}$ in the function argument is within fibers or binder, and zero otherwise.

Abbreviations

µ-CT	Microtomography
CG	Conjugate Gradient
CRA	Collective Rearrangement Algorithm
CTOD	Crack Tip Opening Displacement
CZM	Cohesive Zone Model/Cohesive Zone Modeling
DCB	Double Cantilever Beam
DFT	Discrete Fourier Transform
ENF	End-Notched Flexure
ERR	Energy Release Rate
FE/FEM	Finite Element/Finite Element Method
FFT	Fast Fourier Transform
GB	Glass Beads
ML	Marginal Layers
MPC	Multi-Point Constraints
MSE	Mean Squared Error
OFS	Optical Fiber Strain
PSO	Particle Swarm Optimization
QQ	Quantile-Quantile
RSA	Random Sequential Adsorption
RVE	Representative Volume Element
SCB	Split Cantilever Beam
TSL	Traction Separation Law
UC	Unit Cell

1. Introduction

1.1. Motivation

The development of advanced lightweight materials with a high structural performance is crucial for reducing energy consumption in many industries, e.g., in automotive, naval, aerospace, and civil engineering. It can thus contribute significantly to combating climate change. Sandwich plates are such a type of lightweight material, which allow for a reduction of the weight and amount of required material significantly. They are designed to maintain similar structural performance, especially under bending loads.

Hybrix^{TM} sandwich plates (Lamera AB, Gothenburg, Sweden) consist of metal face sheets, aluminum in this work, and a composite core. Within the composite core, polymer fibers are bonded to one another and to the face sheets with a polymer binder. Apart from fibers and binder, the core also contains a large amount of porosity, which leads to a complex microstructure, but also reduces the weight of the plates. Such a plate is depicted in Fig. 1. The relatively more lightweight plates allow for the use of similar manufacturing technologies as classical metal plates, such as metal forming, owing to their metal face sheets. Accordingly, they have the potential to directly replace metal plates in many applications.

The mechanical behavior of the core is highly dependent on the complex heterogeneous microstructure that can be individually adapted to the requirements of different applications by modifying the production parameters. However, the core is also expected to be crucial for the failure of the entire plates and therefore its structural performance, which is why this work focuses on the core. During the processing of the plates, such as forming, damage may also be induced in the core. Hence, a fracture mechanics approach is well-suited to fully evaluate the remaining structural performance.

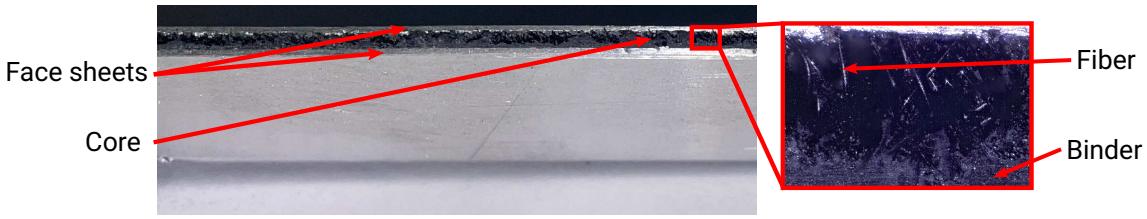

Figure 1: Hybrix^{TM} metal sandwich plate with 1.5 mm thick porous, polymeric fiber-binder core and 0.5 mm thick aluminum face sheets.

Cohesive Zone Modeling (CZM) can be applied to describe the fracture behavior of material layers with a given thickness at the macroscale, where the crack path is already

known to be within the material layer, such as the Hybrix^{TM} sandwich core. In CZM, the mechanical behavior of a full material layer can be completely described as a finite thickness cohesive zone, where the entire thickness is modeled by the CZM. In this approach, displacement jumps between the interfaces of the surrounding bulk material and the material layer, also referred to as the separation vector, and possible additional internal state variables, e.g., a damage variable, are mapped to the traction vector by a constitutive law. CZM is most prominently applied to adhesive layers in the literature, as in, e.g., [1, 2], but can also be used for other material layers, such as adhesive tapes and paperboard, see [3, 4].

The required Traction Separation Laws (TSLs) for the determination of a CZM, which relate the traction to the separation vector for specified load cases, are usually obtained from experiments, see Sec. 1.3.5 for an overview. Despite the possibility of fully characterizing material layers experimentally, the process can be time-consuming and costly. This is especially true when experiments are needed to characterize different configurations during the design process of a novel (composite) material layer.

A micromechanical modeling approach based on CZM could thus facilitate the design of new configurations of the plates. It can decrease the required development time by making predictions on the mechanical behavior for different production parameters, so that fewer complex experiments are needed. The main idea in these micromechanical modeling approaches for heterogeneous materials is to create a direct link between the production parameters that define the properties at the microscale and the final properties of the product at the macroscale that are relevant for the engineering applications.

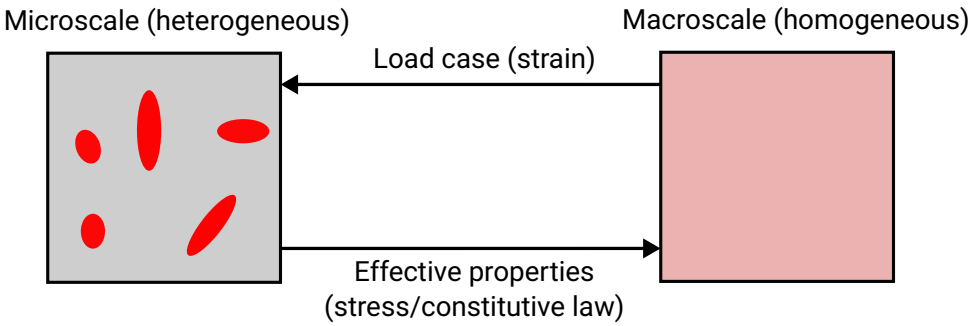

Figure 2: Scheme for the determination of effective mechanical properties via computational homogenization.

For this purpose, computational homogenization is well-suited as a micromechanical modeling approach [5]. In this approach, virtual models of the microstructure for the materials of interest are generated first. Then, a load case, usually the strain or a similar

measure for the deformation from the macroscale is prescribed at the microscale. For the respective load case, a computational method is used to determine the effective properties in the form of the effective stress response. If a sufficient number of load cases is investigated and an admissible theory is available, even a complete constitutive law can be obtained. A corresponding scheme for computational homogenization is depicted in Fig. 2. The heterogeneity of the microstructure on the left-hand side of the figure is represented as red ellipses in a grey matrix, whereas the homogenized material is displayed in light red.

Specialized homogenization methods for cohesive zones were developed based on the classical Finite Element Method (FEM), which is often used for computational homogenization in many engineering applications [6, p.15]. It should be noted for the sake of clarity that, in this work, the term "classical FEM" refers to the discretization of the weak form of the given problem with specified elements. This further includes the computation of a global stiffness matrix and an explicit or implicit numerical solution using Newton and similar methods, as is typical in standard commercial FEM solvers such as Abaqus [7]. The clarification is necessary, since the term "FEM" itself actually means the discretization method only, which also exists for FFT-based homogenization, but is commonly used for the entire numerical procedure described above.

As an alternative to classical FEM-based solvers for computational homogenization, FFT-based computational homogenization was developed in the pioneering work of Moulinec and Suquet [8, 9] using the Lippmann-Schwinger equation for the homogenization problem. FFT-based homogenization is well-suited for industrial applications, as no meshing of the virtual models of the microstructures is needed, which can be time-consuming and complex. In addition, high computational efficiency can be achieved for many materials, also owing to the fact that no stiffness matrix is explicitly formed, see Sec. 1.3.1 of this work. Furthermore, the memory footprint of FFT-based homogenization is significantly lower than that of classical FEM, which allows for computing larger and more complex models.

However, neither an FFT-based homogenization scheme for cohesive zones nor a micromechanical modeling approach for the Hybrix^{TM} core material itself is available in the literature yet. A combination of both may allow a virtual optimization and design process for novel configurations instead of extensive experiments. Therefore, it could provide improved lightweight sandwich plates for the industry. This FFT-based homogenization scheme could also lay the foundation for further applications, such as adhesives.

1.2. Objectives and solution strategy

Based on this motivation, the objective of this work is to develop a novel FFT-based homogenization scheme for cohesive zones and a micromechanical modeling approach for the Hybrix^{TM} sandwich core, which could allow for a virtual design process of various configurations in future work.

A scheme of the solution strategy to achieve this objective is depicted in Fig. 3, where the boxes correspond to respective topics and sections. The arrows denote the transfer of results from one topic/section to another one. The foundation of this doctoral thesis is

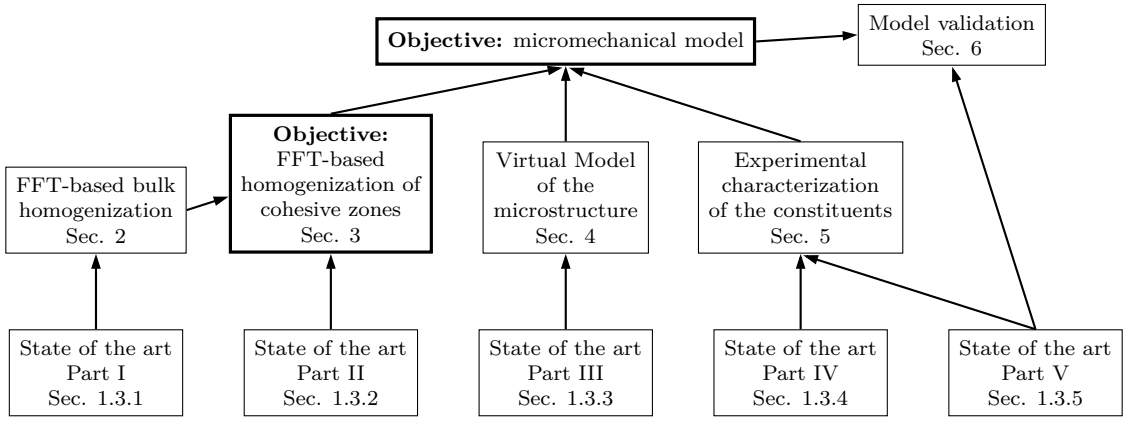

Figure 3: Scheme of the solution strategy for this work.

built by a literature study on the current state of the art in the following Sec. 1.3. It is divided into five different subsections with the corresponding subtopics that are needed for the micromechanical model and its validation, which are also the main sections of this thesis. These main sections contain the major novelty of this work, which extends the current state of the art.

In the first of these main sections, Sec. 2, FFT-based homogenization for bulk materials including a non-local ductile damage model and the selected material models for the microscale is discussed. Based on the literature from Sec. 1.3.1 and the presented theory, suitable discretization and solution methods are chosen and the implementation of the corresponding algorithms for the novel FFT solver in Fortran is presented.

The subsequent Sec. 3 represents the first "ingredient" for the micromechanical model, where the FFT-based homogenization scheme is extended to the homogenization of cohesive zones. Furthermore, the choice of required parameters is discussed as well as the validity from a physical standpoint is investigated. The current state of the art from the literature concerning the (FEM-based) computational homogenization of cohesive zones is presented in Sec. 1.3.2.

Besides the FFT-based homogenization scheme for cohesive zones, a virtual model of the microstructure for the core is required for the micromechanical model, which is presented in Sec. 4. The corresponding current state of the art is discussed in Sec. 1.3.3. The section consists of an experimental characterization of the microstructure, a novel algorithm for the generation of virtual models, and an evaluation of the generated model with respect to experimental data. In order to allow for a design/optimization process, the production parameters of the plates should be used as input parameters for the generation of virtual models only. Without detailed knowledge of the production process of the plates, those production parameters can be identified as the core thickness, the fiber volume fraction and fiber geometry, and the binder volume fraction.

Moreover, an experimental mechanical characterization of the fiber and binder materials is another necessary "ingredient" for the micromechanical model to obtain the parameters for the material models at the microscale. It is described in Sec. 5. Suitable experimental methods at the micro- and macroscale for this purpose are selected based on the literature from Secs. 1.3.4 and 1.3.5, respectively. Nevertheless, it should be noted that if such a virtual design process is applied in the industry, the material properties of the constituents are usually known. However, this was not the case in this work.

In the last step, in Sec. 6, an experimental validation of the developed modeling approach and thus the theoretical FFT-based homogenization scheme itself is carried out. The resulting (single-mode) TSLs from FFT-based homogenization can also be implemented into macroscale models in standard, commercial FEM solvers in a straightforward fashion, which is used for this purpose. A suitable experimental method for the determination of TSLs is selected based on the literature, which is presented in Sec. 1.3.5. The results are compared with the simulated TSL as well as to a simulation of the corresponding test setup at the macroscale.

1.3. State of the art

1.3.1. Part I: FFT-based homogenization of bulk materials including damage and fracture

As already mentioned in the introductory Sec. 1.1, FFT-based homogenization is a promising more recent method in comparison with the widely-used, classical FEM-based methods. It was introduced in the pioneer work of Moulinec and Suquet [8, 9], and is based on the solution of the Lippmann-Schwinger equation with a Green operator that is explicitly known in Fourier space, see Sec. 2.3.1 for details. FFT simulations

can be performed on uniform voxelized grids of virtual models for the microstructure of the materials of interest only. The voxels of these grids correspond to points of a three-dimensional image of the virtual model of the microstructure. Periodic boundary conditions are naturally imposed by the FFT and, hence, the virtual models of the microstructure used are often also periodic. In order to obtain a consistent mechanical behavior at the macroscale, the virtual models should satisfy specific properties. In the case of materials with a random microstructure, the models are referred to as Representative Volume Elements (RVE), if they are representative of both the mechanical behavior and the geometry of the microstructure. Furthermore, the concept of Unit Cells (UC) is adopted in this work, which is the smallest virtual model of a deterministic microstructure with representative (mechanical) properties, see [10] for a detailed discussion of both concepts.

The computational performance of the FFT-based homogenization is influenced by the stiffness contrast of the constituents in the microstructure. In Moulinec and Suquet's original form, its applicability was limited to microstructures with relatively low contrasts owing to the fact that the convergence rate becomes very low otherwise. Thus, it could not be applied to materials with porosity, such as the sandwich core in this work. Furthermore, the resulting solution fields show spurious oscillation artifacts that arise from the Discrete Fourier Transforms (DFT), see also Sec. 2.4.1 for an example and a detailed discussion of the properties.

In order to address these drawbacks, different discretization and solution methods have been developed. One of the most widely-used discretization methods is Willot's rotated centered finite differences [11]. It leads to significantly more accurate solution fields and an improved computational performance of the FFT-based homogenization, in particular for high stiffness contrasts. Using Willot's discretization, convergence can also be achieved for porous microstructures, but it is still relatively slow. Moreover, it can also be interpreted as an underintegrated tri-linear FE discretization, see [12]. The well-known hourglassing effects from these types of elements were found to be the reason for remaining artifacts in the solution fields and the slow convergence for porous microstructures [13]. In the latter work, an hourglass control as in classical FE solvers was developed to overcome these drawbacks. However, it could not achieve the computational efficiency of Willot's original discretization and it required the choice of an hourglass control parameter by numerical experiments. Similarly, a fully integrated tri-linear FE discretization also led to accurate solution fields and a very good convergence for porous microstructures, but a high memory footprint is required and it was relatively

slow [12, 13]. The staggered grid finite difference discretization, which was developed by Schneider et al. [14], combines all of these desired properties, the accurate solution fields, a good convergence for microstructures with porosity and the best computational performance. However, some issues arise owing to the placement of the stress, strain, and displacement variables on the uniform grid. First, the resulting solution fields may become asymmetrical despite a symmetric microstructure. Additionally, material properties and a consistent application of anisotropic material laws at the microscale are not straightforward, see [14] and also Sec. 2.4.1 for detailed discussions and examples.

Furthermore, there are also discretization methods that are of less practical relevance (at least for this work), but can provide important theoretical insights for an improved understanding of FFT-based homogenization. In the Fourier-Galerkin discretization [15, 16], trigonometric polynomials are used for a Galerkin approximation of the homogenization problem. It has similar properties as the original Moulinec-Suquet discretization, but allows for computing guaranteed upper and lower bounds for the properties at the macroscale. Brisard and Dormieux [17, 18] proposed a Galerkin approximation of the Hashin-Shtrikman variational principle with voxel-wise constant fields. Their approach led to mathematically advantageous properties of the system of equations and allowed to prove the convergence of Moulinec and Suquet's original discretization. Bounds on the homogenized properties at the macroscale can also be obtained. However, the result depends on the choice of an elastic reference material, which is not the case in the original method. In addition, the Green operator in the Lippmann-Schwinger equation needs to be precomputed and stored before the actual numerical computations, which makes it impractical for many applications. Furthermore, classical central finite difference discretizations were also explored in the context of FFT-based homogenization, see e.g. [19], but did not achieve the computational efficiency of the rotated grid and staggered grid finite differences.

Apart from the discretization methods, also solvers with improved computational performance compared with Moulinec and Suquet's original fixed-point iteration, the basic scheme, have been developed. The usually most efficient solver is the conjugate gradient (CG) method, but it is limited to linear elastic problems only, see e.g. [20]. Kabel et al. [21] proposed a Newton-CG solver, where the system is linearized in the Newton step and the linearized system is then solved using the CG solver. It is particularly efficient for problems with computationally expensive material laws, as in crystal plasticity. Nevertheless, other solution schemes can be faster for less expensive material laws owing to the relatively expensive Newton steps and the larger memory

footprint. One of these other fast solution schemes is a nonlinear CG solver, which was implemented in [22] and is also applicable for non-linear material laws. For this solution scheme, significantly less memory is required in comparison with the Newton-CG. The Barzilai-Borwein scheme was introduced in [23] in the context of FFT-based homogenization. It is fast, straightforward to implement, and requires even less memory than the nonlinear CG, but the convergence is usually not monotone. This is less problematic in scientific applications, but it may be unexpected for some application engineers in the industry. Quasi-Newton type solution schemes were also already applied in FFT-based homogenization [24, 25]. These methods were found to be fast and robust but require a significantly higher memory footprint compared with the Barzilai-Borwein scheme. Furthermore, fast gradient methods were discussed in [26], which also served as the basis for the development of the nonlinear CG method.

In all previously described methods, the iteration is typically performed on the strain fields. However, depending on the discretization, displacement-based variants can be implemented, see, e.g. [14]. In contrast, polarization methods, as presented in [27, 28], arise from a reformulation of the Lippmann-Schwinger equation, such that the iteration is performed on the stress polarization fields instead of the strain fields. As reported in [29], the polarization schemes are also very efficient. They can be even faster than the previous solution methods for finite stiffness contrasts at the microscale, but for porous materials, it was found that the fastest of the previous solution methods could also outperform the polarization schemes. For a detailed overview of FFT solvers and their applications, the reader is referred to Lucarini et al. [30] and Schneider [31]. The latter reference was also used as a guideline for the overview on discretization and solution methods above.

In comparison with their classical FEM-based counterparts, FFT-based homogenization is expected to have reduced computational costs for many applications. Lucarini et al. [32] found that computational times could be decreased by a factor of six to ten for polycrystals under cyclic loading. In addition, models with sizes that were not accessible with FEM could be computed owing to the low memory footprint. Furthermore, the computational times were up to a factor of eight lower than in classical FEM for lattice-based materials. Nevertheless, classical FEM was also faster for a few of the models studied in [33]. However, a comparison between classical FEM and FFT-based homogenization is out of the scope of this work. It also cannot be easily carried out in a straightforward fashion, since there are plenty of factors that influence the performance of both numerical methods, such as the material studied, the exact implementation, and

solution methods. Therefore, the cited works give a good indication that FFT-based homogenization can be expected to be computationally more efficient in many cases, but they do not explicitly represent a general proof.

In order to model fracture at the microscale, models for damage and fracture mechanics can also be included into the FFT-based homogenization. Magri et al. [34] implemented a non-local, ductile gradient damage model. Gradient regularization is preferred over integral regularization in computational homogenization since the non-local damage variable is obtained by a weighted average of the local variable in the surrounding volume. However, if the volume for the weighted average includes a constituent that does not damage and the weighted average is computed straightforwardly, it still distributes the non-local damage variable "through" this constituent. This unphysical behavior does not occur in the gradient regularization owing to intrinsically applied boundary conditions, which avoid flux of the damage field through other constituents. Furthermore, Ernesti et al. [35], Chen et al. [36], and Ma and Sun [37] studied phase field models for brittle fracture in the context of FFT-based homogenization. Stiffness reduction due to cyclic loading was investigated in [38–40] and the model was successfully integrated into full component simulations at the macroscale.

1.3.2. Part II: Computational homogenization of cohesive zones

Although it is possible to simulate material softening through damage and fracture at the microscale, the resulting fracture properties cannot be straightforwardly translated to the macroscale. Since the results significantly depend on the size of the virtual model of the microstructure, they never converge toward representative fracture properties and, hence, an RVE or UC by increasing the model size [41].

For material layers whose macroscopic fracture behavior can be described with CZMs, this issue can be overcome. This is because the fixed thickness of the cohesive zone determines the model size at the microscale perpendicular to the crack extension direction. Hence, specialized homogenization methods for cohesive zones were developed based on the classical FEM, see [42, 43]. They consider the differences in the boundary conditions in comparison with the standard homogenization for bulk materials and mainly deal with adhesive layers. Furthermore, the method was extended to three dimensions and large deformations in [44, 45]. In [46] the effect of particle decohesion within a heterogeneous adhesive layer was studied. Soghrati and Liang [47] used the method to investigate the influence of pores, the volume fraction of glass beads as filler, and the surface roughness of the adherends on the fracture behavior of an adhesive layer.

Despite the already successful application of computational homogenization to cohesive zones in the previous references, care has to be taken regarding some assumptions. These may lead to deviations in the predictions, and their influence is currently uncertain. First, the periodic boundary conditions within the cohesive zone cause the crack at the microscale to be periodic as well. However, at the macroscale, a periodic crack is unphysical, as a crack with a single global crack tip is expected. This periodic crack in the FFT-based homogenization can always propagate in all directions, whereas the single, real crack usually propagates in one direction only. Furthermore, this can cause the simulated crack to propagate faster through the model with less resistance than real cracks. Hence, it can result in an underestimation of fracture toughness and joint strength. A similar effect was observed in [48], where multiscale simulations using an FEM-based homogenization approach for cohesive zones were compared with direct numerical simulations of heterogeneous adhesive layers. In addition, the separation at the crack tip is usually significantly higher than the separation slightly behind it, which represents a gradient load in the vicinity of the crack tip. This effect is also not considered in the homogenization approach and may lead to deviations in the simulations. Nonetheless, a generally good agreement between the FEM-based homogenization and direct numerical simulation was found in [48].

However, to my knowledge, there is no validation of computational homogenization for cohesive zones through comparisons with experimental results yet. Such a validation is especially necessary, if the method should be applied in design processes of novel composite material layers in the future. It should also be emphasized that all of the cited literature used the classical FEM for the simulations and the FFT-based homogenization has not yet been applied to cohesive zones.

1.3.3. Part III: Generation of virtual models for microstructures

In computational homogenization, it is crucial to obtain an accurate virtual model of the microstructure, which is representative of its overall geometry. These models are often not deterministic and hence of a statistical nature in the case of random materials. For the purpose of determining such a model, an experimental characterization of the microstructure is usually carried out first in order to analyze it statistically. For composites with discrete inclusions, such as fiber or particulate composites, microscopy is typically used to obtain two-dimensional images of the microstructure [49, 50], also referred to as micrographs. Moreover, microtomography (µ-CT) scans return three-dimensional images of it, see [51, 52] for the analysis of fiber composites and also [53] for

a detailed overview of experimental µ-CT techniques and their applications in material science. Standard image processing methods, as presented in [54, pp.129-156] and [55, pp.79-148], are then usually applied to segment the images into the different constituents of the microstructure, so that particles, and/or fibers, and possible pores can be identified individually.

In the next step, the characteristic properties of the inclusions and pores are typically extracted, which are shape, size, orientation, and spatial distribution, see e.g. [56]. Depending on the material studied, it is assumed that these properties are either statistically distributed or have fixed deterministic values. An overview of frequently used types of statistical descriptors for the spatial distribution of the constituents in the microstructure is given in [57]. One relatively general widely-used class of these descriptors for random microstructures are the n-point probability functions. They represent the probability of simultaneously finding n different points in a given constituent of the microstructure. It is usually defined for microstructures with two constituents, but can also be extended to more general cases, see [58]. The two-point correlation or autocorrelation function is a special case of the n-point probability functions. For statistically homogeneous microstructures, it is defined as the probability of finding two points of the same constituent at the end of a line segment of given length and orientation. Moreover, the one-point probability corresponds to the volume fraction of a constituent and is implicitly included in the two-point correlation function as its value for a line segment of zero length.

The two-point correlation function belongs to the types of statistical descriptors that are defined for any arbitrary type of microstructure, provided that the corresponding statistical conditions are met. In contrast, there are also special descriptors for microstructures of composites with discrete inclusions. One of these functions is the distribution of nearest neighbor distance, which is the distance between each inclusion and its nearest neighbor inclusion. It has also been applied to investigate the microstructure of fiber composites in the literature, see e.g. [59, 60]. In these cited works, the radial pair distribution function, which is also called pair distribution function, and Ripley's K function were used for the statistical analysis of the spatial distribution of the fibers as well. The former represents the probability of finding an inclusion within an annulus of a given inner radius and width around another, randomly selected inclusion, see also [61–63]. Again following [59, 60], the latter can be interpreted as the ratio between the number of inclusions, which are expected to be located within a circle or sphere with a given radius around another, randomly selected inclusion, and the number of inclusions

per unit area.

Once the properties of the inclusions and the corresponding model distributions are known, the virtual model of the microstructure can be generated. A detailed overview of algorithms developed for this purpose for various types of materials is provided by Bargmann et al. [64]. For composites with discrete inclusions, their paper distinguishes between two main types of algorithms: Random Sequential Adsorption (RSA) and Collective Rearrangement Algorithms (CRA). The RSA was originally introduced in [65] and places each inclusion one after another randomly within the microstructure until the desired volume fraction is achieved. If no overlap between the inclusions is intended, but it still occurs, the positioning of a inclusion is rejected and another random position is tried. Owing to this not very systematic reduction of overlap, it is not very efficient for the generation of virtual models of the microstructure with high volume fractions of the inclusions. In particular, inclusions with high aspect ratios, such as fibers, are the most critical here. Moreover, desired spatial distributions cannot be prescribed straightforwardly. Nevertheless, the RSA is widely used because of its easy implementation and the natural integration of statistical model distributions for the inclusion size, shape, and orientation.

However, the other type of algorithm, the CRA, was developed to overcome the drawbacks of the RSA. According to Bargmann et al. [64], CRAs usually start with an initial positioning of the inclusions, mostly using the RSA with remaining overlap. In a second step, the overlap is removed by repositioning and/or shrinking. The CRAs are characterized by the fact that all inclusions are moved simultaneously in this process. Among other algorithms, those that are formulated as a minimization problem of an objective function have proven to be efficient. A rather general framework for the formulation and minimization of such an objective function is presented in [66]. Xu et al. [56] distributed ellipsoidal particles to follow an experimentally determined distribution of nearest neighbor distances using an optimization-based algorithm with simulated annealing. Nakka et al. [67] applied gradient-based methods to the corresponding optimization problems to particulate composites with various particle shapes. Schneider and coworkers introduced a similar type of algorithm for short fiber composites [68–70]. Unlike the CRA, their "Sequential Addition and Migration" method adds fibers sequentially rather than simultaneously.

1.3.4. Part IV: Determination of material parameters at the microscale

When studying industrial materials, as in this work, the constituents of the material and its properties are often a secret of the material manufacturer. Therefore, the experimental identification of material models and parameters at the microscale is required to apply computational homogenization approaches to these materials.

One option to test the mechanical properties of materials at the microscale is miniaturized versions of macroscale mechanical tests. Almost all types of macroscale tests can also be performed at the micro- or even the nanoscale, see [71] for an overview and detailed discussions. Examples for micro-tensile tests can be found in [72, 73] for metals and in [74] for polymers. A miniaturized three-point bending test for polymer specimens was presented in [75] and also fracture mechanics tests at the microscale were developed, as, e.g. in [76] a micro Double Cantilever Beam (DCB) test in peel mode I. However, as reported by Dehm et al. [71], limitations in the resolution of load and strain measurements, geometry imperfections in manufacturing of the corresponding specimens, and unintended deviations from the desired load cases may occur. Therefore, a careful evaluation of the results is required in order to avoid misinterpretations.

Apart from miniaturized macroscale test setups, atomic force microscopy can be applied to measure localized material properties of constituents in a microstructure at the nanoscale [77]. In this method, the surface of a sample is indented using a cantilever with a sharp tip, which is controlled by a piezo scanner. The displacement of the piezo scanner and the beam deflection of the cantilever are measured in order to obtain the experimental force-indentation depth curves. If the geometry of the tip is known, mechanical properties can be extracted from the measurements using the theory of contact mechanics. This tip radius usually needs to be calibrated using a reference sample with known properties [78].

A similar method is the nanoindentation, also called microindentation if performed at the microscale instead of the nanoscale. In this experimental technique, the sample surface is probed using an indenter tip with a given geometry and force-indentation depth curves are measured as well. Typical tip geometries are spherical or pyramidal, such as the Berkovich and Vickers tips, which are three-sided and four-sided pyramids made from industrial diamond, respectively. The reader is referred to [79, pp.21–24] for an overview of various types of indenter tips. It was shown by Griepentrog et al. [80] that both methods, atomic force microscopy and nanoindentation, can be successfully applied for the determination of the Young's modulus of a polymer. Plasticity models and their respective parameters can also be determined using indentation experiments.

This can be achieved either by directly measuring experimental stress–strain curves with a special test control strategy, as reported by Pathak and Kalidindi [81]. Alternatively, it can be done by comparing numerical simulations with experimental data and adjusting the model parameters until the simulated curves match the experimental ones, as done in [82] for a linear Drucker-Prager model. A measurement of the local fracture toughness is possible with indentation techniques as well, see [79, pp.166–169].

Furthermore, grid indentation techniques allow for determining the mechanical properties of multiple constituents of a sample in a single series of experiments, see [83, 84]. Multiple indentation experiments are performed along a (heterogeneous) surface of the composite sample. Measurement curves for each of the constituents are recorded with this single series of experiments. These curves are then used to determine the mechanical properties of interest, e.g., the Young's modulus or dissipated (plastic) work, for each measurement point. Statistical deconvolution methods are applied to assign the individual measurements to the respective constituent, as it has also been done in the references given.

1.3.5. Part V: Experimental determination of cohesive zone models

The required TSLs for the determination of a CZM, which map the separation to the traction vector for specified load cases, are usually obtained from fracture mechanics experiments for material layers. In these types of experiments, the material layer of interest is typically placed between two beams (or is already so placed owing to the nature of the material). The load is applied to either one end of the specimen or by using specialized fixtures for the introduction of bending loads. These principles also apply to all references given in the following paragraphs of this section. A recent overview of various fracture mechanics tests for material layers, adhesive layers in this case, is given in [85].

Many of these fracture mechanics experiments are based on the J-integral, which was independently introduced by Rice [86] and Cherepanov [87] in the 1960s. As already discussed in Rice's pioneering work, the peel stress for the traction vector can be computed using the derivative of the J-integral with respect to the separation at the crack tip, the Crack Tip Opening Displacement (CTOD), under pure peel mode I loads if sufficient theoretical requirements are satisfied. This finding is exploited in the determination of TSLs in mode I by DCB tests. De Moura et al. [88] estimated the J-integral by setting it equal to the energy release rate from the Irwin-Kies equation and computing the specimen compliance based on the Timoshenko beam theory. Another common method

is to measure the J-integral directly using the measured force and beam rotation at the load introduction points, which was done in, e.g., [89, 90].

Similar experimental approaches based on the J-integral for the determination of TSLs were also developed for out-of-plane shear mode III and in-plane shear mode II. Examples of the former are given in [3, 91, 92]. In [3, 92], specimens similar to those used in DCB experiments are rotated to apply a mode III load instead of a mode I load. Alternatively, one end of the specimen is loaded with a corresponding moment [91]. Biel and Stigh [93] discussed three different evaluation methods of the J-integral for End-Notched Flexure (ENF) specimens. This test setup is widely used for the measurement of fracture properties in mode II. The mode II load is induced using a three-point bending fixture. In Biel and Stigh's work, a computation of the J-integral based on Euler–Bernoulli beam theory, the direct measurement of force and rotation at the load introduction points, and a mixture of both variants was performed. There are also recent publications on the full identification of CZMs using mixed-mode experiments, where the load cases from single mode experiments are superimposed, see [94] for mixed-mode I+II and [95] for I+III. Both works also used the J-integral for the evaluation. However, care must be taken in mixed-mode, since it was found by Scheel et al. [96] that local coupled contributions to J from the superimposed modes can occur. These coupled contributions are usually neglected in the determination of the traction vector.

Apart from methods based on the J-integral, CZMs can also be identified by adapting the model parameters in FE simulations of a given test setup to the respective experimental results using numerical optimization, see, e.g. [97, 98]. Recently, Schrader et al. [99] introduced a novel method for the measurement of TSLs using an Optical Fiber Strain (OFS) measurement system, which records the bending strain along the adherends. This allows for computing the local bending moment in the adherend at each measurement point. Furthermore, the corresponding component of the traction vector of interest multiplied with the specimen width can be considered a line load in the classical Euler–Bernoulli beam theory. The line load is then proportional to the second derivative of the bending moment with respect to the position at the adherend, which was exploited by Schrader et al. to determine the respective TSLs.

2. FFT-based homogenization of bulk materials

2.1. Governing equations

This section first presents the relevant equations and the associated material models from which the FFT-based homogenization is derived. For details on the mathematical notation used in this work, please refer to the nomenclature. In order to use homogenization techniques to obtain the effective properties of materials at the macroscale from computations at the microscale, some key assumptions are typically made, see [5]. First, it is assumed that the material is "statistically homogeneous", which means that it has the same effective properties at each point at the macroscale. Second, the scales, in this case the micro- and macroscale, must be separable, so that local, microscopic effects do not influence the solutions at the macroscale significantly.

This basic concept of scale separation for the bulk homogenization is visualized in Fig. 4. At the macroscale, the material is considered to be homogeneous, whereas the heterogeneity is marked by the red ellipses in a grey matrix and appears in the RVE at the microscale only. It is usually assumed that the typical length scale of the macroscale is significantly larger than the one at the microscale. An RVE is assigned to each individual point at the macroscale.

In Ameen et al. [100], it was found that the classical homogenization, which is also used within this work, is accurate if the typical length scale at the microscale is at least one order of magnitude smaller than the one at the macroscale. In their work, an elastic two-dimensional particulate composite with a stiffness contrast of 20 under anti-plane shear loading was investigated. The macroscale often refers to full components, where the standard boundary value problem is usually solved by classical FEM. Since those governing equations and numerical solution methods at the macroscale are not used further in this work, they are not discussed in the following. Both can also be found in any (good) book on fundamental continuum mechanics and/or FEM, e.g., in [101].

Following [9], the homogenization problem, the system of equations at the microscale, is given by

$$\begin{cases} \underline{\sigma}\left(\vec{x}\right) \text{computed from constitutive law} \\ \operatorname{div} \underline{\sigma}\left(\vec{x}\right) = \vec{0} \\ \underline{\varepsilon}\left(\vec{u}^{*}\left(\vec{x}\right)\right) = \underline{E} + \operatorname{grad}^{\mathrm{S}} \vec{u}^{*}\left(\vec{x}\right) \\ \text{periodic boundary conditions,} \end{cases} \tag{2.1}$$

where the small deformation theory is used only, as it is often done in FFT-based homogenization, see [31]. The stress field $\underline{\sigma}\left(\vec{x}\right)$ in the first line is computed at each

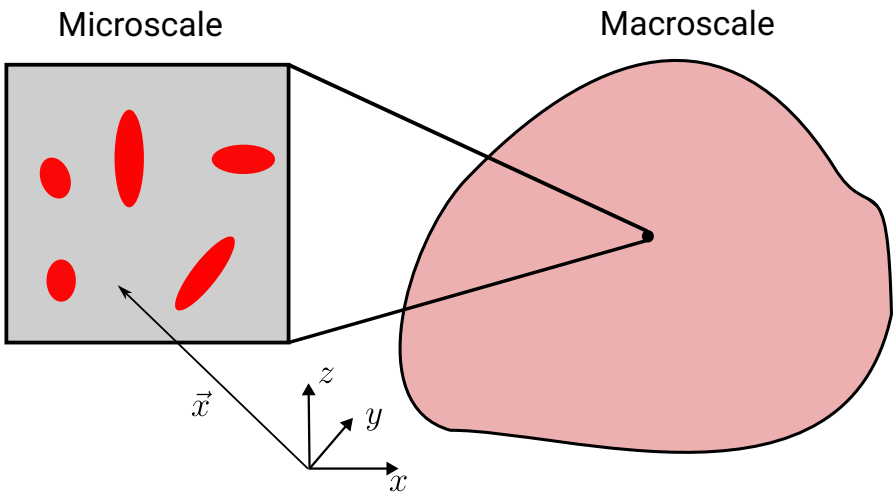

Figure 4: Principle of scale separation in standard bulk homogenization.

position $\vec{x}$ at the microscale using the respective constitutive law of the corresponding constituent of the microstructure. The subsequent lines are the balance of momentum (static and without body forces), the strain compatibility, and the periodic boundary conditions for the displacement fluctuation field $\vec{u}^*$ as well as the strain fluctuation field $\mathrm{grad}^{\mathrm{S}}\,\vec{u}^*\,(\vec{x})$. The strain field $\underline{\varepsilon}\,(\vec{u}^*\,(\vec{x}))$ is decomposed into a volumetric average part $\underline{E}$ and the fluctuation part $\underline{\varepsilon}^* = \mathrm{grad}^{\mathrm{S}}\,\vec{u}^*\,(\vec{x})$. In addition, $\mathrm{grad}^{\mathrm{S}}\,\vec{\bullet} = \frac{1}{2}\left[\mathrm{grad}\,\vec{\bullet} + (\mathrm{grad}\,\vec{\bullet})^{\mathrm{T}}\right]$ denotes the symmetric gradient of a vector $\vec{\bullet}$.

In this work, all materials are modeled as linear elastic and isotropic in the elastic regime. Furthermore, a linear Drucker-Prager plasticity model with non-associative plastic flow potential is used for all polymer materials considered, such as the binder and fibers in the Hybrix$^{\mathrm{TM}}$ sandwich core. This plasticity model can consider the dependence of the plastic behavior on the hydrostatic pressure, which is present in many polymers.

In addition, significant rate effects, such as viscoelasticity or viscoplasticity, also may occur for some polymers. However, a first simplification of the model is made at this point and possible rate effects are neglected. A consideration of these effects would substantially increase the experimental effort that is required for the parameter identification.

Following de Souza et al. [102, pp.324-343], the yield surface of the model is defined by

$$\Phi = \sqrt{J_2} - \eta\sigma_{\mathrm{p}} - \xi\left(d^0 + Hp_{\mathrm{l}}\right) = 0 \tag{2.2}$$

and the corresponding non-associative plastic flow potential is given by

$$\Psi = \sqrt{J_2} - \bar{\eta}\sigma_{\mathrm{p}}, \tag{2.3}$$

where η, $\bar{\eta}$ and ξ are the model parameters to define the shape of yield surface and flow potential. d^0 represents the initial yield stress and H corresponds to the hardening modulus. Furthermore, σ_p and J_2 are the hydrostatic pressure and the second invariant of the stress deviator $\underline{\bar{s}}$, which are computed according to

$$\sigma_\mathrm{p} = -\frac{1}{3}\,\mathrm{tr}\,(\underline{\bar{\sigma}}) \quad \text{and} \quad J_2 = \frac{1}{2}\,\underline{\bar{s}} : \underline{\bar{s}} \quad \text{with} \quad \underline{\bar{s}} = \underline{\bar{\sigma}} + \sigma_\mathrm{p}\,\underline{I}. \tag{2.4}$$

Accordingly, the flow rule in this model yields

$$\underline{\dot{\bar{\varepsilon}}}^{\mathrm{pl}} = \dot{\lambda}\frac{\partial \Psi}{\partial \underline{\bar{\sigma}}} = \dot{\lambda}\left(\frac{1}{2\sqrt{J_2}}\,\underline{\bar{s}} + \frac{\bar{\eta}}{3}\,\underline{I}\right) \tag{2.5}$$

for the local plastic strain rate at the smooth part of flow potential and

$$\dot{p_\mathrm{l}} = \xi\dot{\lambda} \tag{2.6}$$

for the rate of the equivalent local plastic strain, where $\dot{\lambda}$ is the plastic multiplier.

Moreover, it is assumed that damage occurs in the polymers only. Based on the discussion in Sec. 1.3.1 on the state of the art in FFT-based homogenization, the non-local, ductile, implicit gradient damage model from Magri et al. [34] is adopted to model this fracture behavior at the microscale. The model is described by

$$\begin{cases} p_\mathrm{nl} - l_\mathrm{d}^2\,\nabla^2 p_\mathrm{nl} = p_\mathrm{l} & \text{in the damaging phase} \\ \mathrm{grad}\,p_\mathrm{nl} \cdot \vec{n}_\mathrm{d} = \vec{0} & \text{on the boundary of the damaging phase} \\ p_\mathrm{nl} = 0 & \text{elsewhere,} \end{cases} \tag{2.7}$$

where the spatial dependences are neglected for notational clarity. The non-local equivalent plastic strain p_nl is regularized by a Helmholtz-type equation with the local equivalent plastic strain p_l as source term. ∇^2 denotes the Laplacian here. This regularization only holds within the constituents of the microstructure, where damage with the same damage mechanism can occur. They are referred to as the "damaging phase" here. The damage field is distributed within a certain localization region, whose size is related to the characteristic internal length l_d. Damage propagation into constituents of the microstructure without active damage mechanics in the model (non-damaging phases) has also to be prevented. This is ensured by enforcing the gradient of the non-local damage field in the normal direction $\vec{n}_\mathrm{d}$ to the boundaries of the damaging phase to zero. If multiple damaging phases with different damage mechanisms are present, a separate

regularization is used for each and other damaging phases are treated as non-damaging phases in Eq. (2.7). However, in this work only a single damaging phase is used in all simulations.

Furthermore, the evolution equation for the scalar damage variable D is given by

$$D = \begin{cases} 0, & \text{for } p_{\mathrm{nl}} < p_{\mathrm{nl}}^{0} \\ \frac{p_{\mathrm{nl}} - p_{\mathrm{nl}}^{0}}{p_{\mathrm{nl}}^{\mathrm{f}} - p_{\mathrm{nl}}^{0}}, & \text{for } p_{\mathrm{nl}}^{0} \leq p_{\mathrm{nl}} < p_{\mathrm{nl}}^{\mathrm{f}} \\ 1, & \text{for } p_{\mathrm{nl}} \geq p_{\mathrm{nl}}^{\mathrm{f}} \end{cases} \tag{2.8}$$

with initiation parameter p_{nl}^{0} and failure parameter $p_{\mathrm{nl}}^{\mathrm{f}}$. In addition, the stress is computed as

$$\underline{\sigma} = (1 - D)\, \underline{\bar{\sigma}}, \tag{2.9}$$

where $\underline{\bar{\sigma}}$ is the undamaged, effective stress from the plasticity model used.

2.2. Scale transition relations between macro- and microscale

For the computation of the effective properties or constitutive law in the homogenization, it is necessary to know how the quantities at the microscale are related to those at the macroscale and vice versa. The scale transition relations are introduced for this purpose. The (kinematic) macro-to-micro scale transition is usually established by setting the volumetric average strain at the microscale $\langle \underline{\varepsilon} \rangle_{\mathrm{V}} =: \underline{E}$ equal to the macroscopic strain

$$\underline{\varepsilon}_{\mathrm{M}} = \underline{E}. \tag{2.10}$$

The micro-to-macro coupling via the stress tensor follows from the Hill-Mandel condition, see [103, 104]. Here, the volumetric average of a variable $\bullet$ is denoted by

$$\langle \bullet \rangle_{\mathrm{V}} = \frac{1}{V} \int_{V} \bullet \, \mathrm{d}V \tag{2.11}$$

with V being the volume of the virtual model of the microstructure.

The Hill-Mandel condition requires that the energy rate balance at the macro- and microscale are equal for energetic consistency, such that

$$\underline{\sigma}_{\mathrm{M}} : \dot{\underline{E}} = \langle \underline{\sigma} : \dot{\underline{\varepsilon}} \rangle_{\mathrm{V}}. \tag{2.12}$$

The left-hand side corresponds to the rate of energy at the macroscale and the right-hand

side is the one at the microscale. The strain rate at the microscale can be divided into a volumetric average and a fluctuation part $\dot{\underline{\varepsilon}} = \langle \dot{\underline{\varepsilon}} \rangle_{\mathrm{V}} + \dot{\underline{\varepsilon}}^*$ and the Hill-Mandel condition becomes

$$\underline{\sigma}_{\mathrm{M}} : \dot{\underline{E}} = \langle \underline{\sigma} \rangle_{\mathrm{V}} : \langle \dot{\underline{\varepsilon}} \rangle_{\mathrm{V}} + \langle \underline{\sigma} : \dot{\underline{\varepsilon}}^* \rangle_{\mathrm{V}}. \tag{2.13}$$

Integration by parts can be used to replace the volume integral $\langle \underline{\sigma} : \dot{\underline{\varepsilon}}^* \rangle_{\mathrm{V}}$ with an equivalent surface integral. The integration by parts for the problem reads

$$\begin{aligned} \int_V \operatorname{div}\left(\underline{\sigma} \cdot \dot{\vec{u}}^*\right) \mathrm{d}V &= \int_S \vec{t} \cdot \dot{\vec{u}}^* \, \mathrm{d}S \\ &= \int_V \operatorname{div}\left(\underline{\sigma}\right) \cdot \dot{\vec{u}}^* \, \mathrm{d}V + \int_V \underline{\sigma} : \operatorname{grad}^{\mathrm{S}} \dot{\vec{u}}^* \, \mathrm{d}V, \end{aligned} \tag{2.14}$$

where the divergence theorem is used to rewrite the volume integral as an equivalent surface integral over the boundary of the virtual model of the microstructure S in the first line. $\dot{\vec{u}}^*$ denotes the displacement fluctuation rate vector. Note that in the classical integration by parts the gradient of $\dot{\vec{u}}^*$ instead of the symmetric gradient occurs. However, it can be shown that it also applies to the symmetric gradient, since the relation $\underline{\sigma} : \operatorname{grad} \dot{\vec{u}}^* = \underline{\sigma} : \left(\operatorname{grad} \dot{\vec{u}}^*\right)^{\mathrm{T}}$ holds owing to the symmetry of the stress tensor.

Furthermore, the divergence of the stress field vanishes at each point at the microscale, $\operatorname{div}\left(\underline{\sigma}\right) = \vec{0}$, according to the balance of momentum from Eq. (2.1). Therefore, the integration by parts yields

$$\int_S \vec{t} \cdot \dot{\vec{u}}^* \, \mathrm{d}S = \int_V \underline{\sigma} : \operatorname{grad}^{\mathrm{S}} \dot{\vec{u}}^* \, \mathrm{d}V \tag{2.15}$$

and one arrives at

$$\underline{\sigma}_{\mathrm{M}} : \dot{\underline{E}} = \langle \underline{\sigma} \rangle_{\mathrm{V}} : \dot{\underline{E}} + \int_S \vec{t} \cdot \dot{\vec{u}}^* \, \mathrm{d}S \tag{2.16}$$

for the Hill-Mandel condition.

In the next step, the surface integral $\int_S \vec{t} \cdot \dot{\vec{u}}^* \, \mathrm{d}S$ for the periodic boundary conditions of $\dot{\vec{u}}^*$ from Eq. (2.1) is computed. Consider that the boundary of the cuboid virtual model of the microstructure is composed by a set of opposing surfaces S^+ and S^- with the corresponding tractions $\vec{t}^{\,+}$, $\vec{t}^{\,-}$ and the displacement fluctuation rates $\left[\dot{\vec{u}}^*\right]^+$, $\left[\dot{\vec{u}}^*\right]^-$. Then the surface integral over the boundary yields

$$\int_S \vec{t} \cdot \dot{\vec{u}}^* \, \mathrm{d}S = \int_{S^+} \vec{t}^{\,+} \cdot \left[\dot{\vec{u}}^*\right]^+ \mathrm{d}S + \int_{S^-} \vec{t}^{\,-} \cdot \left[\dot{\vec{u}}^*\right]^- \mathrm{d}S. \tag{2.17}$$

In the case of the periodic boundary conditions, the traction vector $\vec{t} = \underline{\sigma} \cdot \vec{n}$ is antiperiodic. This arises from the periodic nature of the stress field at the microscale,

which is a consequence of the periodic strain field and the fact that the normal vectors $\vec{n}$ are orthogonal to opposing surfaces and thus oriented in opposite directions. Accordingly, the antiperiodicity and periodicity properties read $\vec{t}^{\,-} = -\vec{t}^{\,+}$ and $\left[\dot{\vec{u}}^*\right]^+ = \left[\dot{\vec{u}}^*\right]^-$. Using these properties and the fact that the area of the opposing surfaces is equal, one can replace the integral over S^- by an equal integral over S^+. Hence, one obtains

$$\int_S \vec{t} \cdot \dot{\vec{u}}^* \,\mathrm{d}S = \int_{S^+} \vec{t}^{\,+} \cdot \left[\dot{\vec{u}}^*\right]^+ \mathrm{d}S - \int_{S^+} \vec{t}^{\,+} \cdot \left[\dot{\vec{u}}^*\right]^+ \mathrm{d}S = 0 \tag{2.18}$$

for the surface integral.

Consequently, the Hill-Mandel condition for the periodic boundary conditions reads

$$\underline{\sigma}_{\mathrm{M}} : \underline{\dot{E}} = \langle \underline{\sigma} \rangle_{\mathrm{V}} : \underline{\dot{E}} \tag{2.19}$$

and, from a comparison of the coefficients, one obtains the micro-to-macro coupling via the stress tensor

$$\underline{\sigma}_{\mathrm{M}} = \langle \underline{\sigma} \rangle_{\mathrm{V}}. \tag{2.20}$$

The same result is also obtained for other boundary conditions, for which the integral $\int_S \vec{t} \cdot \dot{\vec{u}}^* \,\mathrm{d}S$ vanishes. Examples are Dirichlet (displacement) and Neumann (traction) boundary conditions, see [105] for details.

2.3. Reformulation into Lippmann-Schwinger framework

2.3.1. Homogenization problem

The system of equations in Eq. (2.1) can be reformulated into the Lippmann-Schwinger equation, which serves as the foundation for FFT-based homogenization methods, see [9, 31]. The following derivation of the Lippmann-Schwinger equation in this section is also based on the cited works.

In the first step of the derivation, the linear elastic reference material with stiffness $\underline{\underline{C}}^0$ is introduced and the balance of momentum in Eq. (2.1) is rewritten as

$$\operatorname{div}\left(\underline{\sigma} + \underline{\underline{C}}^0 : \operatorname{grad}^{\mathrm{S}} \vec{u}^* - \underline{\underline{C}}^0 : \operatorname{grad}^{\mathrm{S}} \vec{u}^*\right) = \vec{0}. \tag{2.21}$$

It should be noted that the spatial dependence is neglected for notational clarity here. Then, $\underline{\sigma} - \underline{\underline{C}}^0 : \operatorname{grad}^{\mathrm{S}} \vec{u}^*$ is moved to the right-hand side of the equation and $\underline{\underline{C}}^0 : \underline{E}$ that

has a divergence of zero is added. This results in

$$\operatorname{div}\left(\underline{\underline{C}}^0 : \operatorname{grad}^{\mathrm{S}} \vec{u}^*\right) = -\operatorname{div}\left(\underline{\sigma} - \underline{\underline{C}}^0 : \underline{\varepsilon}\right), \tag{2.22}$$

where the strain compatibility $\underline{\varepsilon} = \underline{E} + \operatorname{grad}^{\mathrm{S}} \vec{u}^*$ was also exploited.

Eq. (2.22) can be solved for $\vec{u}^*$ using the property of the Fourier Transform that derivatives become products with the corresponding frequencies and the imaginary unit in the Fourier space. Accordingly, the continuous Fourier Transform $\mathcal{F}$ is applied to both sides of the equation and it reads

$$i\vec{\xi} \cdot \mathcal{F}\left(\underline{\underline{C}}^0 : \operatorname{grad}^{\mathrm{S}} \vec{u}^*\right) = -\mathcal{F}\left[\operatorname{div}\left(\underline{\tau}\right)\right]. \tag{2.23}$$

i corresponds to the imaginary unit $i^2 = -1$, $\vec{\xi}$ is the continuous angular frequency vector in Fourier space, and the right-hand side is summarized as the stress fluctuation $\underline{\tau} := \underline{\sigma} - \underline{\underline{C}}^0 : \underline{\varepsilon}$.

The double dot product of the stiffness tensor $\underline{\underline{C}}^0$ and the strain fluctuation $\operatorname{grad}^{\mathrm{S}} \vec{u}^*$ is computed as

$$\underline{\underline{C}}^0 : \operatorname{grad}^{\mathrm{S}} \vec{u}^* = \lambda^0 \operatorname{tr}\left(\operatorname{grad}^{\mathrm{S}} \vec{u}^*\right) \underline{I} + 2\mu^0 \operatorname{grad}^{\mathrm{S}} \vec{u}^*. \tag{2.24}$$

The operator $\operatorname{tr}(\underline{\bullet})$ denotes the trace of the respective second order tensor $\underline{\bullet}$, and λ^0 and μ^0 are the Lamé parameters of the isotropic elastic homogeneous reference material. The Fourier Transform of Eq. (2.24) is correspondingly given by

$$\mathcal{F}\left(\underline{\underline{C}}^0 : \operatorname{grad}^{\mathrm{S}} \vec{u}^*\right) = \lambda^0 \left(\widehat{\vec{u}^*} \cdot i\vec{\xi}\right) \underline{I} + \mu^0 \left(i\vec{\xi} \otimes \widehat{\vec{u}^*} + \widehat{\vec{u}^*} \otimes i\vec{\xi}\right), \tag{2.25}$$

where the identity

$$\operatorname{tr}\left(\frac{1}{2}\left(\widehat{\vec{u}^*} \otimes i\vec{\xi} + i\vec{\xi} \otimes \widehat{\vec{u}^*}\right)\right) = \widehat{\vec{u}^*} \cdot i\vec{\xi} \tag{2.26}$$

was used and $\widehat{\bullet} = \mathcal{F}(\bullet)$ abbreviates the Fourier Transform of an arbitrary variable $\bullet$.

Inserting Eq. (2.25) into Eq. (2.23) yields

$$\lambda^0 \left(\widehat{\vec{u}^*} \cdot i\vec{\xi}\right) i\vec{\xi} \cdot \underline{I} + \mu^0 i\vec{\xi} \cdot \left(i\vec{\xi} \otimes \widehat{\vec{u}^*} + \widehat{\vec{u}^*} \otimes i\vec{\xi}\right) = -\mathcal{F}\left[\operatorname{div}\left(\underline{\tau}\right)\right]. \tag{2.27}$$

$\vec{\xi} \cdot \underline{\bullet}$ denotes the left dot product between vector $\vec{\xi}$ and second order tensor $\underline{\bullet}$, as defined

in the nomenclature. Eq. (2.27) can be summarized to

$$-\lambda^0 \left(\widehat{\vec{u}^*} \cdot \vec{\xi}\right) \vec{\xi} - \mu^0 \left(\vec{\xi} \cdot \vec{\xi}\right) \widehat{\vec{u}^*} - \mu^0 \left(\vec{\xi} \cdot \widehat{\vec{u}^*}\right) \vec{\xi} = -\mathcal{F}\left[\operatorname{div}\left(\underline{\tau}\right)\right] \tag{2.28}$$

using the relation $\vec{\bullet}^1 \cdot \left(\vec{\bullet}^2 \otimes \vec{\bullet}^3\right) = \left(\vec{\bullet}^1 \cdot \vec{\bullet}^2\right) \vec{\bullet}^3$ for arbitrary three-dimensional vectors $\vec{\bullet}^1$, $\vec{\bullet}^2$, and $\vec{\bullet}^3$. Moreover, the first and the last terms on the left-hand side can be combined, such that one obtains

$$\left(\lambda^0 + \mu^0\right) \left(\widehat{\vec{u}^*} \cdot \vec{\xi}\right) \vec{\xi} + \mu^0 \left(\vec{\xi} \cdot \vec{\xi}\right) \widehat{\vec{u}^*} = \mathcal{F}\left[\operatorname{div}\left(\underline{\tau}\right)\right]. \tag{2.29}$$

Multiplying $i\vec{\xi}$ to both sides with the dot product reads

$$i\left(\lambda^0 + 2\mu^0\right) \left(\widehat{\vec{u}^*} \cdot \vec{\xi}\right) \left(\vec{\xi} \cdot \vec{\xi}\right) = i\vec{\xi} \cdot \mathcal{F}\left[\operatorname{div}\left(\underline{\tau}\right)\right], \tag{2.30}$$

which can be solved for $\widehat{\vec{u}^*} \cdot \vec{\xi}$, such that one arrives at

$$\widehat{\vec{u}^*} \cdot \vec{\xi} = \frac{\vec{\xi} \cdot \mathcal{F}\left[\operatorname{div}\left(\underline{\tau}\right)\right]}{\left(\lambda^0 + 2\mu^0\right) |\vec{\xi}|^2} \tag{2.31}$$

for $\vec{\xi} \neq \vec{0}$. $|\vec{\bullet}| = \sqrt{\vec{\bullet} \cdot \vec{\bullet}}$ denotes the magnitude of a vector $\vec{\bullet}$ and was used to summarize $\vec{\xi} \cdot \vec{\xi}$ in the denominator.

This result can then be plugged into Eq. (2.29), which yields

$$\left(\lambda^0 + \mu^0\right) \frac{\vec{\xi} \cdot \mathcal{F}\left[\operatorname{div}\left(\underline{\tau}\right)\right]}{\left(\lambda^0 + 2\mu^0\right) |\vec{\xi}|^2} \vec{\xi} + \mu^0 |\vec{\xi}|^2 \widehat{\vec{u}^*} = \mathcal{F}\left[\operatorname{div}\left(\underline{\tau}\right)\right]. \tag{2.32}$$

Solving for $\widehat{\vec{u}^*}$ returns

$$\widehat{\vec{u}^*} = \frac{1}{\mu^0 |\vec{\xi}|^2} \left(\mathcal{F}\left[\operatorname{div}\left(\underline{\tau}\right)\right] - \frac{\left(\lambda^0 + \mu^0\right) \vec{\xi} \cdot \mathcal{F}\left[\operatorname{div}\left(\underline{\tau}\right)\right]}{\left(\lambda^0 + 2\mu^0\right) |\vec{\xi}|^2} \vec{\xi}\right) \tag{2.33}$$

and using the relation $\vec{\bullet}^1 \cdot \left(\vec{\bullet}^2 \otimes \vec{\bullet}^3\right) = \left(\vec{\bullet}^1 \cdot \vec{\bullet}^2\right) \vec{\bullet}^3$ again gives

$$\widehat{\vec{u}^*} = -\left(-\frac{1}{\mu^0 |\vec{\xi}|^2} \underline{I} + \frac{\left(\lambda^0 + \mu^0\right)}{\mu^0 \left(\lambda^0 + 2\mu^0\right) |\vec{\xi}|^4} \vec{\xi} \otimes \vec{\xi}\right) \cdot \mathcal{F}\left[\operatorname{div}\left(\underline{\tau}\right)\right]. \tag{2.34}$$

Now, the solution operator (or Green's function) $\underline{G}^0$ of the original problem in Eq.

(2.22) and its Fourier Transform $\underline{\widehat{G}}^0$ is introduced. The solution of the problem reads

$$\widehat{\vec{u}^*} = -\underline{\widehat{G}}^0 \cdot \mathcal{F}\left[\operatorname{div}\left(\underline{\tau}\right)\right], \tag{2.35}$$

where the explicit expression of the solution operator in Fourier space is given by

$$\underline{\widehat{G}}^0 := -\frac{1}{\mu^0 |\vec{\xi}|^2}\,\underline{I} + \frac{(\lambda^0 + \mu^0)}{\mu^0\,(\lambda^0 + 2\mu^0)\,|\vec{\xi}|^4}\,\vec{\xi} \otimes \vec{\xi}. \tag{2.36}$$

This explicit expression is only known in Fourier space and cannot be computed straightforwardly in the physical space. Eq. (2.35) still only holds for $\vec{\xi} \neq \vec{0}$ and vanishes for $\vec{\xi} = \vec{0}$, since the latter point corresponds to the (volumetric) average of the displacement fluctuation field, which must be zero according to its definition.

However, for more notational clarity, the operator

$$\underline{G}^0 \cdot \operatorname{div}\left(\underline{\tau}\right) := \mathcal{F}^{-1}\left(\underline{\widehat{G}}^0 \cdot \mathcal{F}\left[\operatorname{div}\left(\underline{\tau}\right)\right]\right) \tag{2.37}$$

is also introduced, which corresponds to the application of the Fourier Transform to $\operatorname{div}\left(\underline{\tau}\right)$, the multiplication with $\underline{\widehat{G}}^0$ and the inverse Fourier Transform $\mathcal{F}^{-1}$.

The resulting equation then reads

$$\vec{u}^* = -\underline{G}^0 \cdot \operatorname{div}\left(\underline{\sigma} - \underline{\underline{C}}^0 : \underline{\varepsilon}\right) \tag{2.38}$$

and represents the displacement-based variant of the Lippmann-Schwinger equation in the physical space.

It can be used to obtain the strain fluctuation field by computing the symmetric gradient in Fourier space, which yields

$$\widehat{\operatorname{grad}^{\mathrm{S}}\,\vec{u}^*} = \frac{1}{2}\Big(\vec{\xi} \otimes \Big[\,\underline{\widehat{G}}^0 \cdot \Big(\vec{\xi} \cdot \underline{\widehat{\tau}}\,\Big)\Big] + \Big[\,\underline{\widehat{G}}^0 \cdot \Big(\vec{\xi} \cdot \underline{\widehat{\tau}}\,\Big)\Big] \otimes \vec{\xi}\,\Big). \tag{2.39}$$

An equivalent formulation in the physical space then reads

$$\operatorname{grad}^{\mathrm{S}}\,\vec{u}^* = -\underline{\underline{\Gamma}}^0 : \underline{\tau}, \tag{2.40}$$

where the application of the solution operator for the strain fluctuations, also referred to as "Green operator", is defined according to

$$\underline{\underline{\Gamma}}^0 : \underline{\tau} := -\mathcal{F}^{-1}\left[\frac{1}{2}\Big(\vec{\xi} \otimes \Big[\,\underline{\widehat{G}}^0 \cdot \Big(\vec{\xi} \cdot \underline{\widehat{\tau}}\,\Big)\Big] + \Big[\,\underline{\widehat{G}}^0 \cdot \Big(\vec{\xi} \cdot \underline{\widehat{\tau}}\,\Big)\Big] \otimes \vec{\xi}\,\Big)\right]. \tag{2.41}$$

The total strain field can be computed using the strain compatibility equation from Eq. (2.1) by adding the volumetric average and one arrives at the Lippmann-Schwinger equation for the homogenization problem

$$\underline{\varepsilon} = \underline{E} - \underline{\underline{\Gamma}}^0 : \left(\underline{\sigma} - \underline{\underline{C}}^0 : \underline{\varepsilon} \right). \tag{2.42}$$

2.3.2. Damage regularization problem

In the case of the non-local damage model, the Helmholtz-type regularization in Eq. (2.7) is valid in the damaging phase only. However, for the reformulation into a Lippmann-Schwinger-type equation, an equivalent system of equations is needed that is valid in the entire virtual model of the microstructure owing to the application of the Fourier Transform. Following [34], the original regularization problem Eq. (2.7) can be modified to

$$p_{\mathrm{nl}} - \operatorname{div}\left[l^2\left(\vec{x}\right) \operatorname{grad} p_{\mathrm{nl}} \right] = p_{\mathrm{l}} \tag{2.43}$$

with a non-uniform characteristic length parameter

$$l\left(\vec{x}\right) = \begin{cases} l_{\mathrm{d}}, & \text{in the damaging phase} \\ 0, & \text{elsewhere} \end{cases} \tag{2.44}$$

for this purpose.

The equivalence with the original regularization problem is demonstrated below, following the proof in [34, Section 2.2.1]. First, it is easily seen that Eq. (2.43) reduces to the Helmholtz-type regularization in Eq. (2.7) in the damaging phase, since l_{d}^2 is uniform and can be factored out of the divergence operator.

In the next step, it is shown that the non-local equivalent plastic strain field p_{nl} vanishes in the non-damaging phase as in the original regularization problem. The divergence term in Eq. (2.43) becomes zero there owing to the fact that the characteristic length is zero. Hence, it follows

$$p_{\mathrm{nl}} = p_{\mathrm{l}} = 0 \tag{2.45}$$

within the non-damaging phase.

In the final step, it must be demonstrated that the no-flux boundary condition between the damaging and non-damaging phases in the original regularization problem Eq. (2.7) is satisfied by the proposed modified system of equations. For this purpose, consider Fig. 5, which shows an arbitrary control volume V_{C} in the zoom on the left-hand side

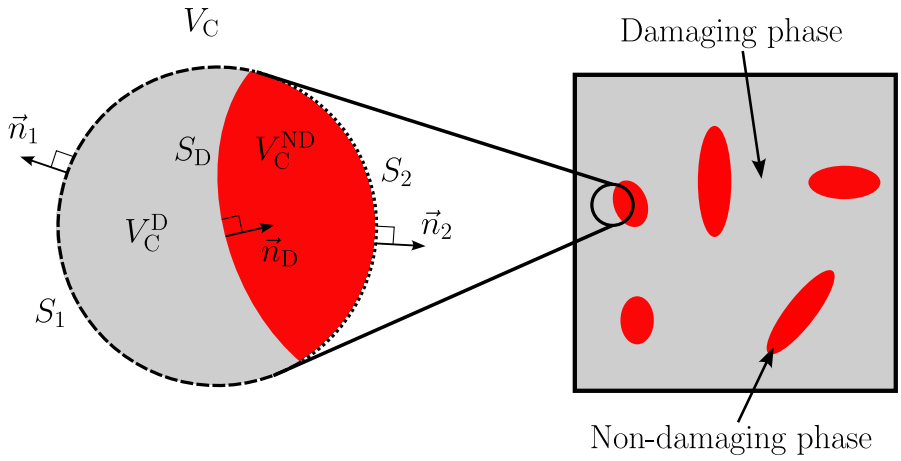

Figure 5: Arbitrary control volume within the virtual model of a microstructure including a damaging and non-damaging phase and the corresponding boundaries.

that is located within the virtual model of a microstructure on the right-hand side. The control volume contains both the gray damaging phase with the volume V_C^D and the red non-damaging phase with the volume V_C^ND. Now, integrating the modified regularization equation Eq. (2.43) over this control volume yields

$$\int_{V_\mathrm{C}^\mathrm{D}} p_\mathrm{nl} - \operatorname{div}\left[l_\mathrm{d}^2 \operatorname{grad} p_\mathrm{nl}\right] - p_\mathrm{l}\,\mathrm{d}V + \int_{V_\mathrm{C}^\mathrm{ND}} p_\mathrm{nl} - \operatorname{div}\left[l_\mathrm{nd}^2 \operatorname{grad} p_\mathrm{nl}\right] - p_\mathrm{l}\,\mathrm{d}V = 0, \tag{2.46}$$

where the integral is already divided into the contributions from V_C^D and V_C^ND. The characteristic length parameter in the non-damaging phase $l_\mathrm{nd}^2 = 0$ is introduced for further calculations and the respective contribution from V_C^ND is kept first.

Applying the divergence theorem then gives

$$\begin{aligned}&\int_{V_\mathrm{C}^\mathrm{D}} p_\mathrm{nl} - p_\mathrm{l}\,\mathrm{d}V - \int_{S_1} l_\mathrm{d}^2 \operatorname{grad} p_\mathrm{nl} \cdot \vec{n}_1\,\mathrm{d}S - \int_{S_\mathrm{D}} l_\mathrm{d}^2 \operatorname{grad} p_\mathrm{nl} \cdot \vec{n}_\mathrm{D}\,\mathrm{d}S + \\ &\int_{V_\mathrm{C}^\mathrm{ND}} p_\mathrm{nl} - p_\mathrm{l}\,\mathrm{d}V - \int_{S_2} l_\mathrm{nd}^2 \operatorname{grad} p_\mathrm{nl} \cdot \vec{n}_2\,\mathrm{d}S + \int_{S_\mathrm{D}} l_\mathrm{nd}^2 \operatorname{grad} p_\mathrm{nl} \cdot \vec{n}_\mathrm{D}\,\mathrm{d}S = 0,\end{aligned} \tag{2.47}$$

where S_1, S_2, and S_D are the surface of the control volume of the damaging phase, the non-damaging phase, and the interface between the phases, respectively. S_1 is depicted as the dashed line in Fig. 5, whereas the dotted line corresponds to S_2. $\vec{n}_1$, $\vec{n}_2$, and $\vec{n}_\mathrm{D}$ are the normal vectors on the corresponding surface. Note that the last summand is positive because $\vec{n}_\mathrm{D}$ is pointing inwards into the non-damaging phase.

In order to ensure that the expression is always zero, each independent summand has to be zero as well. Both integrals over S_D are independent from the other ones and thus

it follows

$$\int_{S_\mathrm{D}} \left(l_\mathrm{d}^2 \operatorname{grad} p_\mathrm{nl} \cdot \vec{n}_\mathrm{D} + l_\mathrm{nd}^2 \operatorname{grad} p_\mathrm{nl} \cdot \vec{n}_\mathrm{D} \right) \mathrm{d}S = 0. \tag{2.48}$$

Since the integrand must vanish at every point to ensure that the integral itself always vanishes, one obtains

$$l_\mathrm{d}^2 \operatorname{grad} p_\mathrm{nl} \cdot \vec{n}_\mathrm{D} = l_\mathrm{nd}^2 \operatorname{grad} p_\mathrm{nl} \cdot \vec{n}_\mathrm{D} \tag{2.49}$$

for the flux of p_nl through every point on S_D. This result holds in the entire virtual model of the microstructure owing to the fact that the control volume can be chosen arbitrarily. Moreover, l_nd^2 is always zero and l_d^2 is always non-zero, such that one arrives at the no-flux condition

$$\operatorname{grad} p_\mathrm{nl} \cdot \vec{n}_\mathrm{D} = 0 \tag{2.50}$$

from the original regularization Eq. (2.7). Therefore, it could be demonstrated successfully that this original regularization problem is satisfied by the modified one.

For the sake of completeness, it can also be seen that Eq. (2.47) reduces to

$$\int_{V_\mathrm{C}^\mathrm{D}} p_\mathrm{nl} - p_\mathrm{l} \, \mathrm{d}V - \int_{S_1} l_\mathrm{d}^2 \operatorname{grad} p_\mathrm{nl} \cdot \vec{n}_1 \, \mathrm{d}S = 0 \tag{2.51}$$

using Eqs. (2.45) and (2.50). Applying the divergence theorem gives

$$\int_{V_\mathrm{C}^\mathrm{D}} p_\mathrm{nl} - p_\mathrm{l} - l_\mathrm{d}^2 \nabla^2 p_\mathrm{nl} \, \mathrm{d}V = 0, \tag{2.52}$$

which again yields the original Helmholtz-type regularization from Eq. (2.7) and shows that all integrals in Eq. (2.47) indeed vanish separately.

In summary, the equivalence of the original damage regularization problem and the modified regularization problem that holds in the entire virtual model of the microstructure could be demonstrated. Thus, a Lippmann-Schwinger-type equation can be derived in the following based on the latter problem.

Following [106], a reference characteristic length l_0^2 is introduced similar to the linear elastic reference material for the homogenization problem in the previous Sec. 2.3.1 and the regularization Eq. (2.43) becomes

$$p_\mathrm{nl} + l_0^2 \nabla^2 p_\mathrm{nl} - \operatorname{div} \left(\left[l^2 - l_0^2 \right] \operatorname{grad} p_\mathrm{nl} \right) = p_\mathrm{l} \tag{2.53}$$

Then, applying the continuous Fourier Transform $\mathcal{F}(\bullet)$ and solving for $\hat{p}_\mathrm{nl}$ yields the

Lippmann-Schwinger-type regularization equation in Fourier space

$$\hat{p}_{\mathrm{nl}} = \frac{\widehat{p}_{\mathrm{l}} + i\vec{\xi} \cdot \mathcal{F}\Big([\, l^2 - l_0^2 \,]\, \mathcal{F}^{-1}\Big(i\vec{\xi}\,\hat{p}_{\mathrm{nl}}\Big)\Big)}{1 + l_0^2 |\vec{\xi}\,|^2}. \tag{2.54}$$

2.4. Discretization

2.4.1. Homogenization problem

In this section, the discretization method for the FFT-based homogenization, which is used in this work, is presented. As it was already discussed in Sec. 1.3.1, the staggered grid finite difference discretization has proven to be the most efficient for porous microstructures like the sandwich core, see [31, 107] and is thus best-suited for this work. Since the staggered grid discretization builds on Moulinec and Suquet's original discretization, it is started with a brief derivation of the latter one.

The idea behind the original discretization is replacing the continuous Fourier Transform by the Discrete Fourier Transform (DFT) from classical signal processing. For this purpose, the virtual model of the microstructure is divided into a regular grid of points, whose discrete positions are given by

$$x_j^{\mathrm{D}} = \frac{m_j L_j}{N_j}. \tag{2.55}$$

The index j of x_j^{D} denotes the component of the discrete position vector, L_j the edge length of the virtual model, N_j the number of points in the corresponding direction, and

$$m_j = 1, 2, ..., N_j - 1, N_j \tag{2.56}$$

is the index in the underlying integer lattice $\mathbb{Z}^3$.

This structure allows for storing the model and all fields as a three-dimensional array in practice such that the position of each entry in the virtual model is known from the index itself. The concept is very similar to image processing, where each point is referred to as a "pixel" in two dimensions and a "voxel" in three dimensions. These terms are also used in FFT-based homogenization in order to refer to the discrete points. In addition, tools from classical image processing can be applied for the visual representation and the processing of model and fields.

The components of the discrete (angular) frequency vector from the classical DFT are

then given by

$$\xi_j^{\mathrm{D}} = \frac{2\pi f_j}{L_j} \tag{2.57}$$

with

$$f_j = \begin{cases} -\frac{N_j}{2}+1, -\frac{N_j}{2}+2, ..., 0, ..., \frac{N_j}{2}-1, \frac{N_j}{2}, & \text{for even } N_j \\ -\frac{N_j-1}{2}, -\frac{N_j-1}{2}+1, .., 0, ..., \frac{N_j-1}{2}-1, \frac{N_j-1}{2} & \text{for odd } N_j. \end{cases} \tag{2.58}$$

The forward and inverse DFTs read

$$\widehat{\bullet}\left(\vec{\xi}^{\,\mathrm{D}}\right) := \frac{1}{N_1 N_2 N_3} \sum_{\vec{x}^{\,\mathrm{D}}} \bullet\left(\vec{x}^{\,\mathrm{D}}\right) \exp\left(-i\vec{x}^{\,\mathrm{D}} \cdot \vec{\xi}^{\,\mathrm{D}}\right) \tag{2.59}$$

and

$$\bullet\left(\vec{x}^{\,\mathrm{D}}\right) := \sum_{\vec{\xi}^{\,\mathrm{D}}} \widehat{\bullet}\left(\vec{\xi}^{\,\mathrm{D}}\right) \exp\left(i\vec{x}^{\,\mathrm{D}} \cdot \vec{\xi}^{\,\mathrm{D}}\right), \tag{2.60}$$

where $\bullet\left(\vec{x}^{\,\mathrm{D}}\right)$ is an arbitrary, discrete field in the physical space and $\widehat{\bullet}\,(\vec{\xi}^{\,\mathrm{D}})$ corresponds to its counterpart in Fourier space.

In Moulinec and Suquet's discretization method [9], the continuous frequencies $\vec{\xi}$ are substituted with the discrete frequencies $\vec{\xi}^{\,\mathrm{D}}$ in the application of the Green operator in Eq. (2.39). In addition, the continuous Fourier Transforms $\mathcal{F}(\bullet)$ are replaced by the corresponding DFTs. In practice, the latter are computed by efficient implementations of the FFT in order to exploit the full potential for optimal computational efficiency.

In the next step, the staggered grid finite difference discretization [14] is derived. The placement of the variables in the staggered grid discretization is shown in Fig. 6 for the components of the displacement and strain fluctuations. The representation is limited to the two-dimensional case for the sake of clarity. Similar to Moulinec and Suquet's discretization, the virtual model of the microstructure is divided into a regular grid. This regular grid consists of square cells and the displacement fluctuations are placed on the faces of each cell. The different gray tones in the background of the grid exemplarily demonstrate the heterogeneity at the microscale.

The indices i and j represent the components of the two-dimensional vector $\vec{m}$ and correspond to the array indices used to store the discretized microstructure model and associated fields. To distinguish between direct dependences on these indices and dependences on position vectors, such as $\vec{x}^{\,\mathrm{D}}$ and also $\vec{m}$ further below, brackets $[\bullet]$ are used instead of parentheses $(\bullet)$.

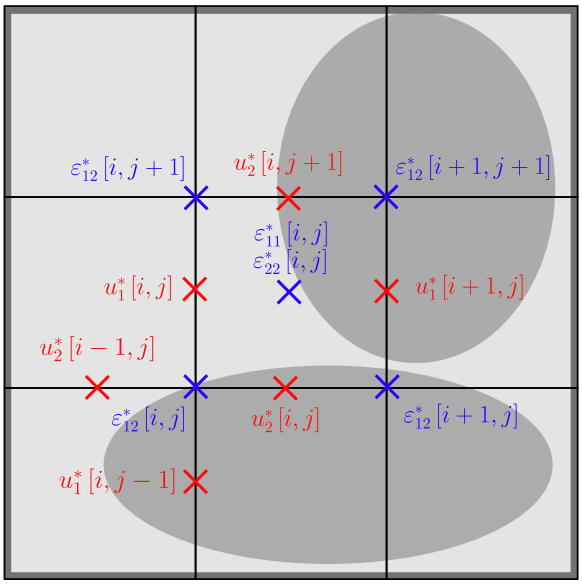

Figure 6: Placement of the displacement and strain fluctuations on the regular grid for the staggered grid discretization. The gray tones in the background visualize the heterogeneity of the microstructure.

The diagonal strain fluctuation components are computed with the forward difference

$$\varepsilon^*_{11}[i,j] \approx \frac{u^*_1[i+1,j] - u^*_1[i,j]}{h_\mathrm{v}} \tag{2.61}$$

and

$$\varepsilon^*_{22}[i,j] \approx \frac{u^*_2[i,j+1] - u^*_2[i,j]}{h_\mathrm{v}}, \tag{2.62}$$

whereas the off-diagonal strain fluctuation components are computed according to

$$\varepsilon^*_{12}[i,j] = \varepsilon^*_{21}[i,j] \approx \frac{1}{2}\left(\frac{u^*_1[i,j] - u^*_1[i,j-1] + u^*_2[i,j] - u^*_2[i-1,j]}{h_\mathrm{v}}\right) \tag{2.63}$$

using the backward difference. h_v denotes the edge length of a pixel (or voxel). Accordingly, the diagonal components of the strain fluctuation are placed at the center of the square cell and the off-diagonal ones at the corners.

Introducing the forward finite difference operator

$$D^\pm_1 \bullet[i,j] = \pm\frac{\bullet[i\pm1,j] - \bullet[i,j]}{h_\mathrm{v}} \tag{2.64}$$

and the backward finite difference operator

$$D_2^{\pm} \bullet [i,j] = \pm \frac{\bullet [i,j \pm 1] - \bullet [i,j]}{h_\mathrm{v}} \tag{2.65}$$

applied to an arbitrary field $\bullet [i,j]$, one arrives at

$$\operatorname{grad}^{\mathrm{S}} \vec{u}^{\,*} [i,j] = \underline{\varepsilon}^* [i,j] = \begin{pmatrix} D_1^+ u_1^* [i,j] & \frac{1}{2}\left(D_2^- u_1^* [i,j] + D_1^- u_2^* [i,j] \right) \\ \text{Sym.} & D_2^+ u_2^* [i,j] \end{pmatrix}. \tag{2.66}$$

for the symmetric strain fluctuation tensor.

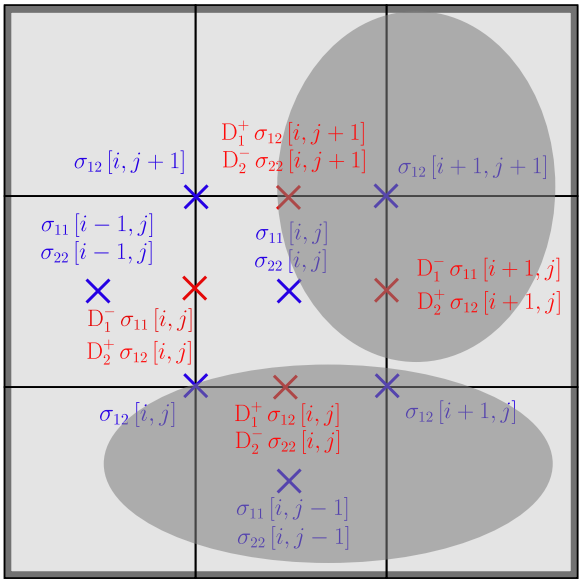

Figure 7: Placement of the stress and its divergence on the regular grid for the staggered grid discretization. The gray tones in the background visualize the heterogeneity of the microstructure.

In order to obtain an explicit expression for the discrete solution operator $\widehat{\underline{G}}^{\,0}$ and Green operator $\widehat{\underline{\underline{\Gamma}}}^{\,0}$, the divergence of a stress field in the staggered grid discretization needs to be derived first. Fig. 7 shows the placement of the corresponding stress components, which is equivalent to the placement of the strain fluctuations. The spatial derivatives of the stress tensor read

$$\frac{\partial \sigma_{11}}{\partial x_1} [i,j] \approx \frac{\sigma_{11}[i,j] - \sigma_{11}[i-1,j]}{h_\mathrm{v}} = D_1^- \sigma_{11}[i,j], \tag{2.67}$$

$$\frac{\partial \sigma_{22}}{\partial x_2}[i,j] \approx \frac{\sigma_{22}[i,j] - \sigma_{22}[i,j-1]}{h_\mathrm{v}} = D_2^- \sigma_{22}[i,j], \tag{2.68}$$

$$\frac{\partial \sigma_{21}}{\partial x_1}[i,j] \approx \frac{\sigma_{21}[i+1,j] - \sigma_{21}[i,j]}{h_\mathrm{v}} = D_1^+ \sigma_{21}[i,j], \tag{2.69}$$

and

$$\frac{\partial \sigma_{12}}{\partial x_2}[i,j] \approx \frac{\sigma_{12}[i,j+1] - \sigma_{12}[i,j]}{h_\mathrm{v}} = D_2^+ \sigma_{12}[i,j], \tag{2.70}$$

where the derivatives of the diagonal components are approximated by backward finite differences and the derivatives of the off-diagonal components by forward finite differences. Therefore, the resulting components of the divergence in Fig. 7 are located at the same positions as the corresponding components of the displacement fluctuation vector. The divergence is then given by

$$\operatorname{div}(\underline{\sigma})[i,j] = \begin{pmatrix} D_1^- \sigma_{11}[i,j] + D_2^+ \sigma_{12}[i,j] \\ D_1^+ \sigma_{21}[i,j] + D_2^- \sigma_{22}[i,j] \end{pmatrix}. \tag{2.71}$$

Similar to the two-dimensional case, the finite difference operators can also be calculated in three-dimensions, where the additional operator in the z-direction is computed as

$$D_3^\pm \bullet[i,j,k] = \pm \frac{\bullet[i,j,k\pm 1] - \bullet[i,j,k]}{h_\mathrm{v}}. \tag{2.72}$$

The other operators from Eqs. (2.64) and (2.65) remain the same except for the addition of spatial index k for the z-direction. Then, the strain fluctuation tensor becomes

$$\begin{aligned} \operatorname{grad}^\mathrm{S} \vec{u}^{\,*}[i,j,k] &= \underline{\varepsilon}^*[i,j,k] \\ &= \begin{pmatrix} D_1^+ u_1^* & \frac{1}{2}\left(D_2^- u_1^* + D_1^- u_2^*\right) & \frac{1}{2}\left(D_3^- u_1^* + D_1^- u_3^*\right) \\ & D_2^+ u_2^* & \frac{1}{2}\left(D_2^- u_3^* + D_3^- u_2^*\right) \\ \text{Sym.} & & D_3^+ u_3^* \end{pmatrix} \end{aligned} \tag{2.73}$$

and the divergence of a stress field reads

$$\operatorname{div}(\underline{\sigma})[i,j,k] = \begin{pmatrix} D_1^- \sigma_{11} + D_2^+ \sigma_{12} + D_3^+ \sigma_{13} \\ D_1^+ \sigma_{21} + D_2^- \sigma_{22} + D_3^+ \sigma_{23} \\ D_1^+ \sigma_{31} + D_2^+ \sigma_{32} + D_3^- \sigma_{33} \end{pmatrix}. \tag{2.74}$$

The spatial indices $[i,j,k]$ of $\vec{u}^*$ and $\underline{\sigma}$ on the right-hand side of the equations are omitted for the sake of notational clarity.

In the next step, the finite difference operators in the Fourier space are derived in order to compute the discretized versions of $\underline{\widehat{G}}^0$ and $\underline{\underline{\widehat{\Gamma}}}^0$. The DFT of these finite difference operators from Eqs. (2.64), (2.65), and (2.72) can be expressed as

$$\begin{aligned}\mathrm{DFT}\left[D_n^{\pm} \bullet \left(\vec{m}\right)\right] &= \mathrm{DFT}\left[\pm\frac{\bullet\left(\vec{m} \pm \vec{e}_n\right) - \bullet\left(\vec{m}\right)}{h_\mathrm{v}}\right] \\ &= \pm\frac{1}{h_\mathrm{v}}\left(\mathrm{DFT}\left[\bullet\left(\vec{m} \pm \vec{e}_n\right)\right] - \mathrm{DFT}\left[\bullet\left(\vec{m}\right)\right]\right).\end{aligned} \tag{2.75}$$

The dependence on the spatial indices $[i, j, k]$ is summarized in the discrete position vector $\vec{m}$ and $\vec{e}_n$ is the unit vector in the x-, y-, or z-direction, which is denoted by index $n \in \{1, 2, 3\}$. Moreover, the linearity of the DFT is used to obtain the second line of the equation.

A discrete field can also be expressed in terms of the inverse DFT. For this purpose, the dot product in the exponential function of the inverse DFT from Eq. (2.60) is rewritten as

$$\vec{x}^{\,\mathrm{D}} \cdot \vec{\xi}^{\,\mathrm{D}} = \sum_{n=1}^{3} \frac{m_n L_n}{N_n} \frac{2\pi f_n}{L_n} = \sum_{n=1}^{3} \frac{2\pi f_n m_n}{N_n} = \vec{m} \cdot \vec{\xi}^{\,\widetilde{\mathrm{D}}}, \tag{2.76}$$

where

$$\xi_n^{\widetilde{\mathrm{D}}} := \frac{2\pi f_n}{N_n}. \tag{2.77}$$

Hence, the inverse DFT can be reformulated to

$$\bullet\left(\vec{m}\right) = \sum_{\vec{\xi}^{\widetilde{\mathrm{D}}}} \widehat{\bullet}\left(\vec{\xi}^{\,\widetilde{\mathrm{D}}}\right) \exp\left(i\vec{\xi}^{\,\widetilde{\mathrm{D}}} \cdot \vec{m}\right) \tag{2.78}$$

and depends on $\vec{m}$ instead of $\vec{x}^{\,\mathrm{D}}$.

Now, $\bullet\left(\vec{m} \pm \vec{e}_n\right)$ can also be expressed using the inverse DFT

$$\begin{aligned}\bullet\left(\vec{m} \pm \vec{e}_n\right) &= \sum_{\vec{\xi}^{\widetilde{\mathrm{D}}}} \widehat{\bullet}\left(\vec{\xi}^{\,\widetilde{\mathrm{D}}}\right) \exp\left(i\vec{\xi}^{\,\widetilde{\mathrm{D}}} \cdot \left(\vec{m} \pm \vec{e}_n\right)\right) \\ &= \sum_{\vec{\xi}^{\widetilde{\mathrm{D}}}} \widehat{\bullet}\left(\vec{\xi}^{\,\widetilde{\mathrm{D}}}\right) \exp\left(i\vec{\xi}^{\,\widetilde{\mathrm{D}}} \cdot \vec{m}\right) \exp\left(\pm i\vec{\xi}^{\,\widetilde{\mathrm{D}}} \cdot \vec{e}_n\right)\end{aligned} \tag{2.79}$$

and applying the DFT yields

$$\begin{aligned}\mathrm{DFT}\left[\bullet\left(\vec{m}\pm\vec{e}_n\right)\right] &= \mathrm{DFT}\left[\sum_{\vec{\xi}^{\widetilde{\mathrm{D}}}} \widehat{\bullet}\left(\vec{\xi}^{\widetilde{\mathrm{D}}}\right)\exp\left(i\vec{\xi}^{\widetilde{\mathrm{D}}}\cdot\vec{m}\right)\exp\left(\pm i\vec{\xi}^{\widetilde{\mathrm{D}}}\cdot\vec{e}_n\right)\right] \\ &= \widehat{\bullet}\left(\vec{\xi}^{\widetilde{\mathrm{D}}}\right)\exp\left(\pm i\vec{\xi}^{\widetilde{\mathrm{D}}}\cdot\vec{e}_n\right) = \widehat{\bullet}\left(\vec{\xi}^{\widetilde{\mathrm{D}}}\right)\exp\left(\pm i\xi_n^{\widetilde{\mathrm{D}}}\right).\end{aligned} \tag{2.80}$$

The term in the second line was obtained by a comparison of coefficients with the inverse DFT in Eq. (2.78).

Plugging this result into Eq. (2.75) and using $\widehat{\bullet}\left(\vec{\xi}^{\widetilde{\mathrm{D}}}\right) = \mathrm{DFT}\left[\bullet\left(\vec{m}\right)\right]$, one arrives at

$$\begin{aligned}\mathrm{DFT}\left[\mathrm{D}_n^{\pm}\bullet\left(\vec{m}\right)\right] &= \pm\frac{\widehat{\bullet}\left(\vec{\xi}^{\widetilde{\mathrm{D}}}\right)\exp\left(\pm i\xi_n^{\widetilde{\mathrm{D}}}\right) - \widehat{\bullet}\left(\vec{\xi}^{\widetilde{\mathrm{D}}}\right)}{h_{\mathrm{v}}} \\ &= \pm\frac{\exp\left(\pm i\xi_n^{\widetilde{\mathrm{D}}}\right)-1}{h_{\mathrm{v}}}\,\widehat{\bullet}\left(\vec{\xi}^{\widetilde{\mathrm{D}}}\right)\end{aligned} \tag{2.81}$$

for the DFT of the finite difference operators with index $n\in\{1,2,3\}$. By introducing the components

$$q_n = \frac{\exp\left(i\xi_n^{\widetilde{\mathrm{D}}}\right)-1}{h_{\mathrm{v}}} \tag{2.82}$$

of vector $\vec{q}$ and the corresponding complex conjugate components

$$q_n^* = \frac{\exp\left(-i\xi_n^{\widetilde{\mathrm{D}}}\right)-1}{h_{\mathrm{v}}} \tag{2.83}$$

of vector $\vec{q}^{\,*}$, the DFT of the forward and backward finite difference operators can be summarized to

$$\mathrm{DFT}\left[\mathrm{D}_n^{+}\bullet\left(\vec{m}\right)\right] = q_n\,\widehat{\bullet}\left(\vec{\xi}^{\widetilde{\mathrm{D}}}\right) \qquad \text{and} \qquad \mathrm{DFT}\left[\mathrm{D}_n^{-}\bullet\left(\vec{m}\right)\right] = -q_n^*\,\widehat{\bullet}\left(\vec{\xi}^{\widetilde{\mathrm{D}}}\right). \tag{2.84}$$

Then, one arrives at

$$\mathrm{DFT}\left[\mathrm{grad}^{\mathrm{S}}\,\vec{u}^{\,*}\right] = \widehat{\underline{\varepsilon}}^{\,*} = \begin{pmatrix} q_1\,\widehat{u_1^*} & -\frac{1}{2}\left(q_2^*\,\widehat{u_1^*}+q_1^*\,\widehat{u_2^*}\right) & -\frac{1}{2}\left(q_3^*\,\widehat{u_1^*}+q_1^*\,\widehat{u_3^*}\right) \\ & q_2\,\widehat{u_2^*} & -\frac{1}{2}\left(q_3^*\,\widehat{u_2^*}+q_2^*\,\widehat{u_3^*}\right) \\ \mathrm{Sym.} & & q_3\,\widehat{u_3^*} \end{pmatrix} \tag{2.85}$$

and

$$\mathrm{DFT}\Big[\operatorname{div}\underline{\sigma}\Big] = \begin{pmatrix} -q_1^*\,\widehat{\sigma}_{11} + q_2\,\widehat{\sigma}_{12} + q_3\,\widehat{\sigma}_{13} \\ q_1\,\widehat{\sigma}_{21} - q_2^*\,\widehat{\sigma}_{22} + q_3\,\widehat{\sigma}_{23} \\ q_1\,\widehat{\sigma}_{31} + q_2\,\widehat{\sigma}_{32} - q_3^*\,\widehat{\sigma}_{33} \end{pmatrix} \tag{2.86}$$

for the strain fluctuation tensor and the divergence of the stress field in Fourier space, respectively. The spatial dependences have been omitted here to enhance notational clarity.

Now, the procedure for the computation of the continuous operators from Sec. 2.3 is adopted to compute the discrete solution and Green operators. Applying the DFT to the discretized form of the reformulated balance of momentum in Eq. (2.22) yields

$$\mathrm{DFT}\left[\operatorname{div}\left(\underline{\underline{C}}^0 : \underline{\varepsilon}^*\right)\right] = -\,\mathrm{DFT}\left[\operatorname{div}\left(\underline{\tau}\right)\right]. \tag{2.87}$$

Then, plugging in the explicit expression of $\underline{\underline{C}}^0$ from Eq. (2.24) returns

$$\mathrm{DFT}\left[\operatorname{div}\left(\lambda^0 \operatorname{tr}\left(\underline{\varepsilon}^*\right)\underline{I} + 2\mu^0\underline{\varepsilon}^*\right)\right] = -\,\mathrm{DFT}\left[\operatorname{div}\left(\underline{\tau}\right)\right]. \tag{2.88}$$

By using the formulas for the DFT of the $\operatorname{grad}^{\mathrm{S}}(\vec{\bullet})$ and $\operatorname{div}(\underline{\bullet})$ operators from Eq. (2.85) and Eq. (2.86), one obtains

$$-\lambda^0\Big(\widehat{\vec{u}^*}\cdot\vec{q}\Big)\vec{q}^* - \mu^0\Big(\vec{q}^*\cdot\vec{q}\Big)\widehat{\vec{u}^*} - \mu^0\Big(\vec{q}\cdot\widehat{\vec{u}^*}\Big)\vec{q}^* = -\,\mathrm{DFT}\left[\operatorname{div}\left(\underline{\tau}\right)\right]. \tag{2.89}$$

Similar to the previous Sec. 2.3, summarizing and multiplying $\vec{q}$ to both sides with the dot product yields

$$\Big(\lambda^0 + 2\mu^0\Big)\Big(\widehat{\vec{u}^*}\cdot\vec{q}\Big)\Big(\vec{q}^*\cdot\vec{q}\Big) = \vec{q}\cdot\mathrm{DFT}\left[\operatorname{div}\left(\underline{\tau}\right)\right], \tag{2.90}$$

which can be solved for

$$\widehat{\vec{u}^*}\cdot\vec{q} = \frac{\vec{q}\cdot\mathrm{DFT}\left[\operatorname{div}\left(\underline{\tau}\right)\right]}{\Big(\lambda^0 + 2\mu^0\Big)\left|\vec{q}\,\right|^2}. \tag{2.91}$$

Substituting the result into Eq. (2.89) and solving for $\widehat{\vec{u}^*}$ returns

$$\widehat{\vec{u}^*} = \left(\frac{1}{\mu^0\left|\vec{q}\,\right|^2}\,\underline{I} - \frac{\Big(\lambda^0 + \mu^0\Big)}{\mu^0\Big(\lambda^0 + \mu^0\Big)\left|\vec{q}\,\right|^4}\,\vec{q}^*\otimes\vec{q}\right)\cdot\mathrm{DFT}\left[\operatorname{div}\left(\underline{\tau}\right)\right]. \tag{2.92}$$

Then, the corresponding discrete solution operator for the staggered grid can be defined

according to

$$\underline{\widehat{G}}^0_{\mathrm{SG}} := -\left(\frac{1}{\mu^0 \left| \vec{q} \right|^2} \underline{I} - \frac{\left(\lambda^0 + \mu^0 \right)}{\mu^0 \left(\lambda^0 + \mu^0 \right) \left| \vec{q} \right|^4} \vec{q}^{\,*} \otimes \vec{q} \right) \tag{2.93}$$

and one arrives at the discrete, displacement-based Lippmann-Schwinger equation in Fourier space

$$\widehat{\vec{u}^*} = -\underline{\widehat{G}}^0_{\mathrm{SG}} \cdot \mathrm{DFT}\Big[\mathrm{div}\left(\underline{\tau} \right) \Big]. \tag{2.94}$$

As in the derivation of the continuous Lippmann-Schwinger equation in Eq. (2.38), one can also define the application of the discrete solution operator from Eq. (2.93) in the physical space as

$$\underline{G}^0_{\mathrm{SG}} \cdot \mathrm{div}\left(\underline{\tau} \right) := \mathrm{DFT}^{-1}\Big(\underline{\widehat{G}}^0_{\mathrm{SG}} \cdot \mathrm{DFT}\Big[\mathrm{div}\left(\underline{\tau} \right) \Big] \Big) \tag{2.95}$$

for the sake of notational clarity. With this definition at hand, the discrete displacement-based Lippmann-Schwinger equation becomes

$$\vec{u}^* = -\underline{G}^0_{\mathrm{SG}} \cdot \mathrm{div}\left(\underline{\sigma} - \underline{\underline{C}}^0 : \underline{\varepsilon} \right). \tag{2.96}$$

Moreover, the application of the discrete Green operator $\underline{\underline{\Gamma}}^0_{\mathrm{SG}}$ can be defined as

$$\underline{\underline{\Gamma}}^0_{\mathrm{SG}} : \underline{\tau} := \mathrm{DFT}^{-1}\Big[\mathrm{DFT}\Big(\mathrm{grad}^{\mathrm{S}}\Big[\underline{G}^0_{\mathrm{SG}} \cdot \mathrm{div}\Big(\underline{\tau} \Big) \Big] \Big) \Big], \tag{2.97}$$

where the DFT of the divergence and the symmetric gradient can be explicitly computed according to Eqs. (2.85) and (2.86), respectively. Using this discrete Green operator, the Lippmann-Schwinger equation for the staggered grid discretization

$$\underline{\varepsilon} = \underline{E} - \underline{\underline{\Gamma}}^0_{\mathrm{SG}} : \left(\underline{\sigma} - \underline{\underline{C}}^0 : \underline{\varepsilon} \right) \tag{2.98}$$

can be introduced.

To illustrate the properties of the staggered grid discretization compared with Moulinec and Suquet's original method [9], a simple two-dimensional numerical experiment is presented. It consists of a disk embedded in a matrix, which can also be used as a simple unit cell for fiber-reinforced plastics owing to the intrinsic periodic boundary conditions. The disk has a diameter of 37 pixels and the model size is of 101 × 101 pixels. The Young's moduli of the disk and the matrix are at 10,000 MPa and 1,000 MPa, respectively, whereas a Poisson's ratio of 0.3 was used for both materials. The model was loaded in y-direction with a volumetric average strain of $E_{22} = 2\%$ and all

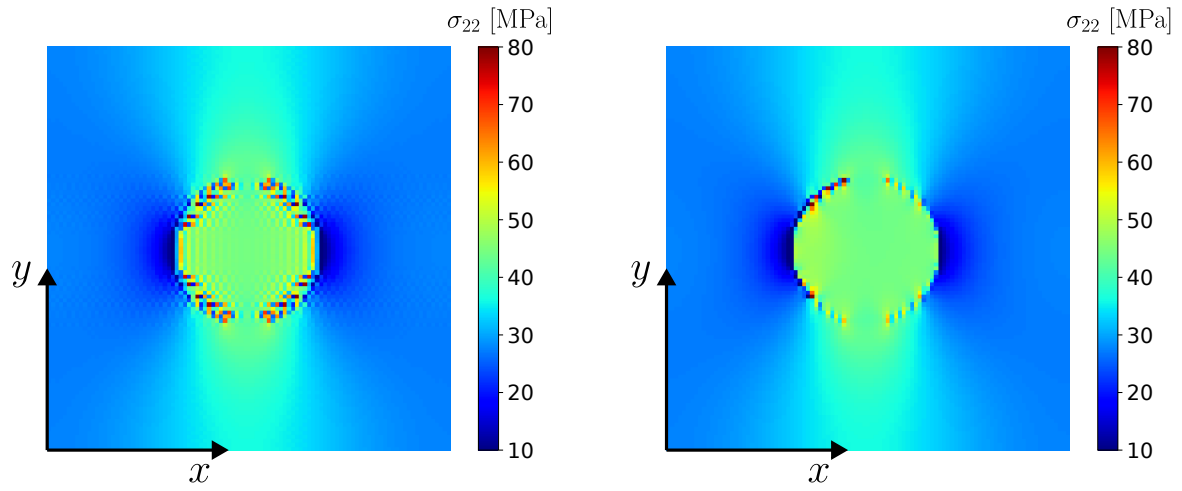

(a) (b)

Figure 8: Stress fields for a disk in a matrix loaded with $E_{22} = 2\%$: Original discretization method from Moulinec and Suquet [9] (a) and staggered grid finite difference discretization [14] (b).

other strain components were zero. Figs. 8a and 8b show the resulting stress field σ_{22} of the original and the staggered grid discretization.

Spurious oscillations in the stress field occur in the Moulinec-Suquet discretization, whereas the staggered grid discretization provides a smoother and more accurate stress field. Nonetheless, the stress peaks at the interface of disk and matrix cannot be completely avoided owing to the fact that the regular grid in the FFT-based homogenization is inherently non-conforming to circular interfaces. Furthermore, it can be observed that the stress field is, in contrast to the Moulinec-Suquet discretization, not completely symmetric. This is also a well-known issue that arises from the placement of the stress and strain fluctuation components outside of the pixel or voxel center, but is accepted in practical application.

2.4.2. Damage regularization problem

The damage problem Eq. (2.54) is discretized using Moulinec and Suquet's original method. Thus, the frequencies in Fourier space and the Fourier Transforms are replaced by their discrete counterparts. Consequently, the discrete form of the Lippmann-Schwinger-

type equation for the damage regularization Eq. (2.54) becomes

$$p_{\mathrm{nl}}\left(\vec{x}^{\,\mathrm{D}}\right) = \mathrm{DFT}^{-1}\left[\frac{\widehat{p}_{\mathrm{l}} + i\vec{\xi}^{\,\mathrm{D}} \cdot \mathrm{DFT}\left(\left[l^2 - l_0^2\right]\mathrm{DFT}^{-1}\left[i\vec{\xi}^{\,\mathrm{D}}\widehat{p}_{\mathrm{nl}}\right]\right)}{1 + l_0^2\left|\vec{\xi}^{\,\mathrm{D}}\right|^2}\right]. \tag{2.99}$$

While it is also possible to use one of the other, advanced discretization methods, numerical experiments revealed that the computational time spent on the damage regularization problem as well as the influence on the solution field are negligible compared with the homogenization problem. Hence, the original discretization is sufficient for this work, which was also found by other authors who studied similar problems, see, e.g., [35].

2.5. FFT-based solution methods

2.5.1. Homogenization problem

In this section, the FFT-based solution methods for the Lippmann-Schwinger equation of the homogenization problem are discussed. They are derived using continuous functional analysis rather than directly from the discretized form of the equation in order to be more general. A discretization scheme of choice can then be included in the description of the implemented algorithm. This is special for FFT-based solution methods compared with classical (implicit) FEM, where the stiffness matrix from the discretization is required to apply a solution method.

Based on the literature study in Sec. 1.3.1, the Barzilai-Borwein method was selected as a solution scheme for this work. It is straightforward to implement, requires little memory and is very competitive regarding the computational times and convergence. The method was introduced in [108] and in [23] in the context of FFT-based homogenization and builds on the Moulinec and Suquet's original basic scheme [9]. The method corresponds to a gradient descent with a variable step size that is updated in every iteration. Moreover, it is implemented as a novel displacement-based variant instead of a standard strain-based one, which allows for reducing the memory footprint and computational times even more.

The procedure for the derivation of the solution scheme includes four major steps and is based on [23, 31]: First, the standard basic scheme and a simplified version of it are presented. Then, the gradient descent is derived and it is shown that it is equivalent to the (simplified) basic scheme, if the step size is constant. In the next step, the theory for the gradient descent is used to compute the optimal constant step size, which is shown to correspond to the parameters of the elastic reference material in the following. This step

size also serves as the initial one for the Barzilai-Borwein method. In the last step, an explicit expression for the adaptive step size update is computed and the implemented displacement-based algorithm is presented in comparison with the strain-based one, where the staggered grid discretization is also incorporated. The section is concluded with a discussion on the selected convergence criterion and the practical significance of the assumptions from the mathematical theory.

In their pioneer work, Moulinec and Suquet [9] proposed to solve the Lippmann-Schwinger equation Eq. (2.42) with the basic scheme, where the iterations are given by

$$\underline{\varepsilon}^{i+1} = \underline{E} - \underline{\underline{\Gamma}}^0 : \left(\underline{\sigma}^i - \underline{\underline{C}}^0 : \underline{\varepsilon}^i \right). \tag{2.100}$$

Here, i is the iteration counter, and the method corresponds to a classical fixed-point iteration, see [31]. In addition, the relation

$$\underline{E} + \underline{\underline{\Gamma}}^0 : \left(\underline{\underline{C}}^0 : \underline{\varepsilon}^i \right) = \underline{\varepsilon}^i \tag{2.101}$$

can be used to simplify the basic scheme to

$$\underline{\varepsilon}^{i+1} = \underline{\varepsilon}^i - \underline{\underline{\Gamma}}^0 : \underline{\sigma}^i. \tag{2.102}$$

In order to show that this simplification in Eq. (2.101) holds, consider Eq. (2.22) first, where $\underline{G}^0$ is the solution operator for

$$\operatorname{div}\left(\underline{\underline{C}}^0 : \operatorname{grad}^{\mathrm{S}} \vec{u}^* \right) \tag{2.103}$$

such that the application of the operator yields

$$\vec{u}^* = \underline{G}^0 \cdot \operatorname{div}\left(\underline{\underline{C}}^0 : \operatorname{grad}^{\mathrm{S}} \vec{u}^* \right). \tag{2.104}$$

Then, the average strain $\underline{E}$ is added to the strain fluctuation $\operatorname{grad}^{\mathrm{S}} \vec{u}^*$, which is feasible because $\underline{\underline{C}}^0 : \underline{E}$ is a constant field and thus its divergence is zero. Using the decomposition of the strain at the microscale into the volumetric average and the fluctuation parts $\underline{\varepsilon} = \underline{E} + \operatorname{grad}^{\mathrm{S}} \vec{u}^*$, one arrives at

$$\vec{u}^* = \underline{G}^0 \cdot \operatorname{div}\left(\underline{\underline{C}}^0 : \left[\underline{E} + \operatorname{grad}^{\mathrm{S}} \vec{u}^* \right] \right) = \underline{G}^0 \cdot \operatorname{div}\left(\underline{\underline{C}}^0 : \underline{\varepsilon} \right). \tag{2.105}$$

Applying the symmetric gradient and adding the volumetric average strain yields

$$\underline{\varepsilon} = \underline{E} + \operatorname{grad}^{\mathrm{S}} \underline{G}^0 \cdot \operatorname{div} \left(\underline{\underline{C}}^0 : \underline{\varepsilon} \right) = \underline{E} + \underline{\underline{\Gamma}}^0 : \left(\underline{\underline{C}}^0 : \underline{\varepsilon} \right), \tag{2.106}$$

where the definition of $\underline{\underline{\Gamma}}^0 = \operatorname{grad}^{\mathrm{S}} \underline{G}^0 \cdot \operatorname{div}$ is used, cf. Eqs. (2.39) and (2.41). Plugging in $\underline{\varepsilon}^i$ for $\underline{\varepsilon}$ demonstrates that the initial simplification, Eq. (2.101), holds.

The simplified basic scheme will be needed in the following to demonstrate that it can be interpreted as a gradient descent. This interpretation then enables to derive the Barzilai-Borwein solution method and the optimal choice of the reference material for the FFT-based homogenization, see Schneider [31, Section 3.1]. Similarly, Kabel et al. [21] provided a related proof showing that it can also be understood as a projected gradient descent. The following derivation is also inspired by the work of Schneider.

A gradient descent is usually applied to solve minimization problems of the type

$$\underset{\vec{y} \in Y}{\text{minimize}} \quad f\left(\vec{y}\right) \tag{2.107}$$

[109, p.68]. f and $\vec{y}$ denote an arbitrary objective function and a corresponding variable. The vector $\vec{y}$ is defined in the space Y, which is also a placeholder for any arbitrary admissible mathematical vector space. The gradient descent then reads

$$x^{i+1} = x^i - s^i_{\mathrm{gd}} \operatorname{grad} f\left(\vec{y}^{\,i}\right), \tag{2.108}$$

where the superscript denotes the corresponding iteration and s^i_{gd} is the step size that can be updated in every iteration [109, p.68].

In the case of the original homogenization problem from Eq. (2.1), the continuous minimization problem, also called variational problem, reads

$$\underset{\vec{u}^* \in H^1_{\mathrm{per}}}{\text{minimize}} \quad W_{\mathrm{pot}} = \left\langle w_{\mathrm{pot}}\Big(\vec{x}, \underline{\varepsilon}\Big) \right\rangle_{\mathrm{V}}. \tag{2.109}$$

W_{pot} is the volumetric average of a condensed, incremental strain energy density at the microscale $w_{\mathrm{pot}}\Big(\vec{x}, \underline{\varepsilon}\Big)$. The spatial dependence of the strain field is omitted for notational clarity. $w_{\mathrm{pot}}\Big(\vec{x}, \underline{\varepsilon}\Big)$ is also required to be a potential for the stress

$$\underline{\sigma} = \frac{\partial w_{\mathrm{pot}}\Big(\vec{x}, \underline{\varepsilon}\Big)}{\partial \underline{\varepsilon}}, \tag{2.110}$$

whose practical significance is discussed in the final part of this section.

Moreover, W_{pot} is minimized with respect to the displacement fluctuation vector $\vec{u}^*$, which is defined in the first order Sobolev and Hilbert space

$$H^1_{\mathrm{per}} := \left\{ \vec{u}^* : V \to \mathbb{R}^3 \,\middle|\, \langle \vec{u}^* \rangle_V = \vec{0}\,;\, \vec{u}^* \text{ and } \operatorname{grad}^{\mathrm{S}} \vec{u}^* \text{ are periodic} \right\}, \tag{2.111}$$

see [23, 31]. The space H^1_{per} is furthermore equipped with the inner product

$$\left(\vec{\bullet}, \vec{\bullet} \right)_{\mathrm{H}^1_{\mathrm{per}}} := \left\langle \operatorname{grad}^{\mathrm{S}} \vec{\bullet} : \operatorname{grad}^{\mathrm{S}} \vec{\bullet} \right\rangle_{\mathrm{V}} \tag{2.112}$$

and the corresponding norm

$$\left\| \vec{\bullet} \right\|_{\mathrm{H}^1_{\mathrm{per}}} := \left(\vec{\bullet}, \vec{\bullet} \right)^{\frac{1}{2}}_{\mathrm{H}^1_{\mathrm{per}}} = \left\langle \operatorname{grad}^{\mathrm{S}} \vec{\bullet} : \operatorname{grad}^{\mathrm{S}} \vec{\bullet} \right\rangle^{\frac{1}{2}}_{\mathrm{V}} \tag{2.113}$$

to measure distances in the space, e.g., the distance of the numerical, approximated solution from the correct one. The first part of the definition just describes that $\vec{u}^*$ is a function that is defined within the model of the microstructure V and returns a three-dimensional real (Euclidean) vector in $\mathbb{R}^3$. The other properties are required in order to satisfy the compatibility and periodic boundary conditions in the third and fourth lines of the homogenization problem Eq. (2.1). Similar definitions are typical in the analysis of partial differential equations and are also used in the theoretical description of the classical FEM, as they enable the definition of weak derivatives, see e.g. [110]. This is essential for allowing discontinuities in material properties, which typically occur in heterogeneous microstructures, as well as in classical FEM models of components at the macroscale.

First, it needs to be shown that the variational problem Eq. (2.109) is indeed equivalent to the original homogenization problem from Eq. (2.1) before the FFT-based solution schemes can be derived based on it. The problem can be addressed using standard variational calculus by varying $\vec{u}^*$ with $\alpha \vec{v}$, where $\vec{v} \in H^1_{\mathrm{per}}$. This yields

$$\left[\frac{\mathrm{d}}{\mathrm{d}\alpha} \left\langle w_{\mathrm{pot}}\left(\vec{x}, \underline{E} + \operatorname{grad}^{\mathrm{S}} \vec{u}^* + \alpha \operatorname{grad}^{\mathrm{S}} \vec{v} \right) \right\rangle_{\mathrm{V}} \right]_{\alpha=0} = 0 \tag{2.114}$$

and the computation of the respective derivatives then returns

$$\left[\left\langle \frac{\partial w_{\mathrm{pot}}\left(\vec{x}, \underline{\varepsilon} + \alpha \operatorname{grad}^{\mathrm{S}} \vec{v} \right)}{\partial \left(\underline{\varepsilon} + \alpha \operatorname{grad}^{\mathrm{S}} \vec{v} \right)} \;:\; \frac{\partial \left(\underline{\varepsilon} + \alpha \operatorname{grad}^{\mathrm{S}} \vec{v} \right)}{\partial \alpha} \right\rangle_{\mathrm{V}} \right]_{\alpha=0} = 0, \tag{2.115}$$

where $\underline{\varepsilon} = \underline{E} + \operatorname{grad}^{\mathrm{S}} \vec{u}^{*}$ is summarized. The solution of the variational problem reads

$$\left\langle \frac{\partial w_{\mathrm{pot}}\left(\vec{x}, \underline{\varepsilon}\right)}{\partial \underline{\varepsilon}} : \operatorname{grad}^{\mathrm{S}} \vec{v} \right\rangle_{\mathrm{V}} = \left\langle \underline{\sigma} : \operatorname{grad}^{\mathrm{S}} \vec{v} \right\rangle_{\mathrm{V}} = 0, \tag{2.116}$$

where the fact that w_{pot} is required to be a potential from Eq. (2.110) is used.

Similar as in the derivation of the Hill-Mandel condition in Eq.(2.14), integration by parts alongside the divergence theorem

$$\begin{aligned} \int_V \operatorname{div}\left(\underline{\sigma} \cdot \vec{v}\right) \mathrm{d}V &= \int_S \vec{t} \cdot \vec{v} \, \mathrm{d}S \\ &= \int_V \operatorname{div}\left(\underline{\sigma}\right) \cdot \vec{v} \, \mathrm{d}V + \int_V \underline{\sigma} : \operatorname{grad}^{\mathrm{S}} \vec{v} \, \mathrm{d}V \end{aligned} \tag{2.117}$$

is applied. As discussed previously in the corresponding Sec. 2.2, the surface integral $\int_S \vec{t} \cdot \vec{v} \, \mathrm{d}S$ vanishes, since $\vec{v}$ is periodic and the traction vector $\vec{t} = \underline{\sigma} \cdot \vec{n}$ is antiperiodic. Consequently,

$$\int_V \underline{\sigma} : \operatorname{grad}^{\mathrm{S}} \vec{v} \, \mathrm{d}V = -\int_V \operatorname{div}\left(\underline{\sigma}\right) \cdot \vec{v} \, \mathrm{d}V \tag{2.118}$$

is obtained. Multiplying $\frac{1}{V}$ to both sides and abbreviating the volume integral with $\langle \bullet \rangle_{\mathrm{V}} = \frac{1}{V} \int_V \bullet \, \mathrm{d}V$, the term $\left\langle \underline{\sigma} : \operatorname{grad}^{\mathrm{S}} \vec{v} \right\rangle_{\mathrm{V}}$ in the solution of the variational problem from Eq. (2.116) can be replaced by

$$\left\langle \underline{\sigma} : \operatorname{grad}^{\mathrm{S}} \vec{v} \right\rangle_{\mathrm{V}} = -\left\langle \operatorname{div}\left(\underline{\sigma}\right) \cdot \vec{v} \right\rangle_{\mathrm{V}} = 0. \tag{2.119}$$

Since the integrand must vanish at every point for the integral to always be zero, this ultimately gives

$$\operatorname{div}\left(\underline{\sigma}\right) = \vec{0} \tag{2.120}$$

for the solution of the variational problem. This expression corresponds to the balance of momentum in the second line of the original homogenization problem in Eq. (2.1). The first line of the homogenization, the constitutive law, is also trivially included in the variational problem.

Furthermore, the periodic boundary conditions in the fourth line of the homogenization problem are also satisfied in the variational problem by the definition of H^1_{per}, where the periodicity of $\vec{u}^{*}$ also implies that $\operatorname{grad}^{\mathrm{S}} \vec{u}^{*}$ is periodic. For the strain compatibility in the third line of the homogenization problem, the volume average of the strain fluctuation field $\left\langle \operatorname{grad}^{\mathrm{S}} \vec{u}^{*} \right\rangle_{\mathrm{V}}$ must vanish, such that the strain field can be decomposed into the fluctuation part and the volumetric average. However, in the definition of the

mathematical space for the displacement fluctuation field H^1_{per}, it is only assumed that the volume average of the displacement fluctuation field itself vanishes.

Nonetheless, the latter can be shown by considering the average theorem for the strain

$$\left\langle \operatorname{grad}^{\mathrm{S}} \vec{u}^{*} \right\rangle_{\mathrm{V}} = \int_{S} \frac{1}{2} \left(\vec{u}^{*} \otimes \vec{n} + \vec{n} \otimes \vec{u}^{*} \right) \mathrm{d}S, \tag{2.121}$$

see e.g. [103, Eq. (12)]. By employing the same reasoning as for the traction vector in the derivation of the Hill-Mandel condition from Sec. 2.2, $\vec{u}^{*} \otimes \vec{n}$ and $\vec{n} \otimes \vec{u}^{*}$ are antiperiodic. This follows from the fact that the fluctuation displacement field is periodic and the orientation vector $\vec{n}$ points in opposite directions for opposing surfaces. Hence, the integral over the entire boundary of the virtual model of the microstructure vanishes and it is demonstrated that $\left\langle \operatorname{grad}^{\mathrm{S}} \vec{u}^{*} \right\rangle_{\mathrm{V}} = 0$ holds. In summary, it can be concluded that the variational problem Eq. (2.107) is indeed equivalent to the original homogenization problem Eq. (2.1).

In the next step, the gradient of the variational problem needs to be calculated in order to demonstrate that the basic scheme can be interpreted as a gradient descent. This can be achieved using the concept of directional derivatives, where the gradient is given by

$$\left(\operatorname{grad} f, \vec{v} \right)_{\mathrm{Y}} = \left[\frac{\mathrm{d}}{\mathrm{d}\alpha} f\left(\vec{y} + \alpha \vec{v} \right) \right]_{\alpha=0} \tag{2.122}$$

for any function $f\left(\vec{y}\right)$ with $\vec{y} \in \mathrm{Y}$ and orientation vector $\vec{v} \in Y$. Space Y again denotes any admissible vector space. Applied to the homogenization problem, one obtains

$$\left(\operatorname{grad} W_{\text{pot}}, \vec{v} \right)_{\mathrm{H}^1_{\text{per}}} = \left[\frac{\mathrm{d}}{\mathrm{d}\alpha} \left\langle w_{\text{pot}}\left(\vec{x}, \underline{E} + \operatorname{grad}^{\mathrm{S}} \vec{u}^{*} + \alpha \operatorname{grad}^{\mathrm{S}} \vec{v} \right) \right\rangle_{\mathrm{V}} \right]_{\alpha=0}. \tag{2.123}$$

Using the inner product for H^1_{per} from Eq. (2.112) for the left-hand side of the equation and the solution of the variational problem from Eq. (2.116) for its right-hand side yields

$$\left\langle \operatorname{grad}^{\mathrm{S}} \left(\operatorname{grad} W_{\text{pot}} \right) : \operatorname{grad}^{\mathrm{S}} \vec{v} \right\rangle_{\mathrm{V}} = \left\langle \frac{\partial w_{\text{pot}}}{\partial \underline{\varepsilon}} : \operatorname{grad}^{\mathrm{S}} \vec{v} \right\rangle_{\mathrm{V}}. \tag{2.124}$$

Then, the integration by parts is applied to both sides similar to Eq. (2.117) and the potential property $\underline{\sigma} = \frac{\partial w_{\text{pot}}}{\partial \underline{\varepsilon}}$ is exploited, which gives

$$\left\langle \operatorname{div}\left[\operatorname{grad}^{\mathrm{S}} \left(\operatorname{grad} W_{\text{pot}} \right) \right] \cdot \vec{v} \right\rangle_{\mathrm{V}} = \left\langle \operatorname{div}\left(\underline{\sigma} \right) \cdot \vec{v} \right\rangle_{\mathrm{V}}. \tag{2.125}$$

For the integral to be always equal, the integrands have to be equal and by comparison of the coefficients, one gets

$$\operatorname{div}\left[\operatorname{grad}^{\mathrm{S}}\left(\operatorname{grad} W_{\mathrm{pot}}\right)\right] = \operatorname{div}\left(\underline{\sigma}\right), \tag{2.126}$$

which can be solved for the sought gradient using the solution operator $\underline{G}^0$.

Recall that it is the solution operator for $\operatorname{div}\left(\underline{\underline{C}}^0 : \operatorname{grad}^{\mathrm{S}} \vec{u}^*\right)$ with respect to $\vec{u}^*$, see Eq. (2.104). This relation can be written in a more abstract way, which reads

$$\underline{G}^0 \cdot \operatorname{div}\left(\underline{\underline{C}}^0 : \operatorname{grad}^{\mathrm{S}} \vec{\bullet}\right) = \vec{\bullet}. \tag{2.127}$$

The displacement fluctuation vector $\vec{u}^*$ is only replaced by an arbitrary placeholder $\vec{\bullet}$ with the same mathematical properties. This allows for introducing a very similar solution operator $\underline{G}$ with the property

$$\underline{G} \cdot \operatorname{div}\left(\underline{\underline{I}} : \operatorname{grad}^{S} \vec{\bullet}\right) =: \vec{\bullet}. \tag{2.128}$$

$\underline{\underline{I}}$ denotes the fourth order identity tensor computed as defined in the nomenclature.

Similarly, the application of $\underline{\underline{C}}^0$ from Eq. (2.24) to an arbitrary strain-type second order tensor $\underline{\bullet}$ can also be written in a more abstract way as

$$\underline{\underline{C}}^0 : \underline{\bullet} = \lambda^0 \operatorname{tr}\left(\underline{\bullet}\right) \underline{I} + 2\mu^0 \underline{\bullet}. \tag{2.129}$$

Setting the Lamé parameter $\lambda^0 = 0$ and multiplying the identity tensor to the right-hand side of the equation gives

$$\underline{\underline{C}}^0 : \underline{\bullet} = 2\mu^0 \underline{\underline{I}} : \underline{\bullet}. \tag{2.130}$$

A comparison of the coefficients then returns

$$\underline{\underline{C}}^0 = 2\mu^0 \underline{\underline{I}} \tag{2.131}$$

and plugging this result into the abstracted application of the solution operator $\underline{G}^0$ in Eq. (2.127) yields

$$2\mu^0 \underline{G}^0 \cdot \operatorname{div}\left(\underline{\underline{I}} : \operatorname{grad}^{\mathrm{S}} \vec{\bullet}\right) = \vec{\bullet}. \tag{2.132}$$

It is exploited that $2\mu^0$ is a constant and can be placed in front of the differential operators. By comparing the coefficients in the abstracted application of both solution

operators Eqs. (2.128) and (2.132), one obtains the explicit relation

$$\underline{G} = 2\mu^0 \, \underline{G}^0. \tag{2.133}$$

Therefore, $\underline{G}$ can be computed using the explicit expression for $\underline{G}^0$ in Fourier space from Eqs. (2.36) – (2.37).

With this result at hand, Eq. (2.126) can be solved for the gradient $\operatorname{grad} W_{\text{pot}}$ by applying $\underline{G}$ to both sides, which returns

$$\begin{aligned} \underline{G} \cdot \operatorname{div}\left(\underline{\underline{I}} : \operatorname{grad}^{\text{S}}\left[\operatorname{grad} W_{\text{pot}}\right]\right) &= \underline{G} \cdot \operatorname{div}\left(\underline{\sigma}\right) \\ \implies \operatorname{grad} W_{\text{pot}} &= \underline{G} \cdot \operatorname{div}\left(\underline{\sigma}\right). \end{aligned} \tag{2.134}$$

A multiplication with $\underline{\underline{I}}$ is added without affecting the result to emphasize the similarity of the left-hand side with the definition of the solution operator $\underline{G}$ from Eq. (2.128).

Following the definition of the scheme in Eq. (2.108), the gradient descent for the homogenization problem is given by

$$\left[\vec{u}^*\right]^{i+1} = \left[\vec{u}^*\right]^i - s^i_{\text{gd}} \, \underline{G} \cdot \operatorname{div}\left(\underline{\sigma}^i\right) \tag{2.135}$$

with iteration counter i. Applying the symmetric gradient and adding the average strain $\underline{E}$ on both sides, which is not influenced by the iterations on the fluctuation fields, the strain-based variant of the gradient descent reads

$$\underline{\varepsilon}^{i+1} = \underline{\varepsilon}^i - s^i_{\text{gd}} \, \underline{\underline{\Gamma}} : \underline{\sigma}^i, \tag{2.136}$$

where the new Green operator $\underline{\underline{\Gamma}} = \operatorname{grad}^{\text{S}} \underline{G} \cdot \operatorname{div}$ is introduced. Owing to its linearity with respect to $\underline{G}$, it can be computed according to

$$\underline{\underline{\Gamma}} = 2\mu^0 \, \underline{\underline{\Gamma}}^0, \tag{2.137}$$

see also the definition of $\underline{\underline{\Gamma}}^0$ in Eq. (2.41) and the relation between $\underline{G}$ and $\underline{G}^0$ from Eq. (2.133).

Now it can be observed that the gradient descent is equivalent to the simplified basic scheme in Eq. (2.102) by setting $\underline{\underline{\Gamma}}^0 = s^i_{\text{gd}} \, \underline{\underline{\Gamma}}$ and thus $\underline{G}^0 = s^i_{\text{gd}} \, \underline{G}$. A comparison of

coefficients with Eqs. (2.133) and (2.137) returns

$$\mu^0 = \frac{1}{2\, s^i_{\mathrm{gd}}}. \tag{2.138}$$

This result also gives rise to an interpretation of the linear elastic reference material as a measure for the step size of the gradient descent.

Since it could be shown that the gradient descent is equal to the basic scheme, the rich theory for gradient descent methods can be exploited to find the optimal parameters for the step size and derive faster solution methods. In this theory, the best case for the fastest convergence rate requires the gradient of the function f to be Lipschitz continuous, such that

$$|| \operatorname{grad} f(\vec{y}_1) - \operatorname{grad} f(\vec{y}_2) ||_{\mathrm{Y}} \leq \alpha_+ || \vec{y}_1 - \vec{y}_2 ||_{\mathrm{Y}} \tag{2.139}$$

holds, and f itself to be strongly convex, which is ensured by the condition

$$\left(\operatorname{grad} f(\vec{y}_1) - \operatorname{grad} f(\vec{y}_2), \vec{y}_1 - \vec{y}_2 \right)_{\mathrm{Y}} \geq \alpha_- || \vec{y}_1 - \vec{y}_2 ||^2_{\mathrm{Y}}, \tag{2.140}$$

see [109, p.65]. $||\bullet||_{\mathrm{Y}}$ and $\left(\bullet, \bullet\right)_{\mathrm{Y}}$ denote the norm and inner product of space Y, respectively. $\vec{y}_1$ and $\vec{y}_2$ correspond to specified arbitrary points $\vec{y}$. α_+ and α_- are positive constants and the optimal, constant step size is

$$s_{\mathrm{gd}} = const. = \frac{2}{\alpha_+ + \alpha_-}, \tag{2.141}$$

for which a linear convergence rate of

$$|| \vec{y}^{\,i} - \vec{y}^{\,*} ||_{\mathrm{Y}} \leq \left(\frac{\alpha_+ - \alpha_-}{\alpha_+ + \alpha_-} \right)^i || \vec{y}^{\,0} - \vec{y}^{\,*} ||_{\mathrm{Y}} \tag{2.142}$$

is obtained, see [109, p.70]. Furthermore, $\vec{y}^{\,*}$ denotes the value of $\vec{y}$ at the minimum of f and $\vec{y}^{\,i}$ is the i-th iteration of the gradient descent. For details regarding the origin of the conditions in Eqs. (2.139) and (2.140), the determination of the optimal step size, and the proof of the linear convergence rate, it is again referred to Nesterov's book [109].

In the case of the homogenization of mechanical properties, the Lipschitz continuity is discussed first in order to compute α_+. With the gradient from Eq. (2.134) and the corresponding norm of space H^1_{per} from Eq. (2.113), it reads

$$\left|\left| \operatorname{grad} W_{\mathrm{pot}}\left(\vec{u}^{*1}\right) - \operatorname{grad} W_{\mathrm{pot}}\left(\vec{u}^{*2}\right) \right|\right|_{\mathrm{H}^1_{\mathrm{per}}} \leq \alpha_+ \left|\left| \vec{u}^{*1} - \vec{u}^{*2} \right|\right|_{\mathrm{H}^1_{\mathrm{per}}}, \tag{2.143}$$

where $\vec{u}^{*1}\left(\vec{x}\right)$ and $\vec{u}^{*2}\left(\vec{x}\right)$ are displacement fluctuation fields and the spatial dependence of $\operatorname{grad} W_{\mathrm{pot}}$ is omitted for notational clarity. Furthermore, the relation $\operatorname{grad}^{\mathrm{S}}\left(\operatorname{grad} W_{\mathrm{pot}}\right) = \underline{\sigma}$ from Eq. (2.124) and the definition of the norm from Eq. (2.113) can be used to rewrite Eq. (2.143) to

$$\begin{aligned}\left\langle \left[\underline{\sigma}\left(\vec{x}, \underline{\varepsilon}^{*1}\right) - \underline{\sigma}\left(\vec{x}, \underline{\varepsilon}^{*2}\right)\right] : \left[\underline{\sigma}\left(\vec{x}, \underline{\varepsilon}^{*1}\right) - \underline{\sigma}\left(\vec{x}, \underline{\varepsilon}^{*2}\right)\right] \right\rangle_{\mathrm{V}}^{\frac{1}{2}} \\ \leq \alpha_{+} \left\langle \left(\underline{\varepsilon}^{*1} - \underline{\varepsilon}^{*2}\right) : \left(\underline{\varepsilon}^{*1} - \underline{\varepsilon}^{*2}\right) \right\rangle_{\mathrm{V}}^{\frac{1}{2}}.\end{aligned} \tag{2.144}$$

This expression can be summarized to

$$\left\langle \left|\left| \underline{\sigma}\left(\vec{x}, \underline{\varepsilon}^{*1}\right) - \underline{\sigma}\left(\vec{x}, \underline{\varepsilon}^{*2}\right) \right|\right|_{\mathrm{F}}^{2} \right\rangle_{\mathrm{V}}^{\frac{1}{2}} \leq \alpha_{+} \left\langle \left|\left| \underline{\Delta\varepsilon}^{*1,2}\left(\vec{x}\right) \right|\right|_{\mathrm{F}}^{2} \right\rangle_{\mathrm{V}}^{\frac{1}{2}} \tag{2.145}$$

using the Frobenius norm $||\bullet||_{\mathrm{F}} = \sqrt{\bullet : \bullet}$ and $\underline{\Delta\varepsilon}^{*1,2} = \underline{\varepsilon}^{*1} - \underline{\varepsilon}^{*2}$. The variables $\underline{\varepsilon}^{*1}$ and $\underline{\varepsilon}^{*2}$ are the strain fluctuation fields that follow from the symmetric gradient of $\vec{u}^{*1}$ and $\vec{u}^{*2}$, respectively.

In order to compute α_{+} such that the Lipschitz continuity of the gradient is satisfied, the following procedure is carried out. First, the relation between stress and strain fields is established using the tangent stiffness. Then, the operator norm of the tangent stiffness is introduced and its result is determined through a spectral decomposition of the corresponding tensor. In the subsequent step, the definition of the operator norm is reformulated into an inequality of the same type as the condition for Lipschitz continuity. α_{+} can then be obtained by comparing the coefficients with the original condition.

For this purpose, it is started with an interpolation between the fields $\underline{\varepsilon}^{*1}\left(\vec{x}\right)$ and $\underline{\varepsilon}^{*2}\left(\vec{x}\right)$ which reads

$$\underline{\varepsilon}\left(\vec{x},\, t_{\varepsilon},\, \underline{\Delta\varepsilon}^{*1,2}\right) = \underline{\varepsilon}^{*1}\left(\vec{x}\right) - t_{\varepsilon}\, \underline{\Delta\varepsilon}^{*1,2}\left(\vec{x}\right) \tag{2.146}$$

with $t_{\varepsilon} \in [0, 1]$. Computing the derivative of the stress field with respect to t_{ε} returns

$$\begin{aligned}\frac{\mathrm{d}}{\mathrm{d}t_{\varepsilon}} \underline{\sigma}\left(\vec{x}, \underline{\varepsilon}\left(t_{\varepsilon}, \underline{\Delta\varepsilon}^{*1,2}\right)\right) &= \frac{\partial \underline{\sigma}\left(\vec{x}, \underline{\varepsilon}\left(t_{\varepsilon}, \underline{\Delta\varepsilon}^{*1,2}\right)\right)}{\partial \underline{\varepsilon}} : \frac{\partial\left(\underline{\varepsilon}^{*1} - t_{\varepsilon}\, \underline{\Delta\varepsilon}^{*1,2}\right)}{\partial t_{\varepsilon}} \\ &= \underline{\underline{C}}^{\mathrm{t}}\left(\vec{x}, \underline{\varepsilon}\left(t_{\varepsilon}, \underline{\Delta\varepsilon}^{*1,2}\right)\right) : \underline{\Delta\varepsilon}^{*1,2},\end{aligned} \tag{2.147}$$

where

$$\underline{\underline{C}}^{\mathrm{t}}\left(\vec{x}, \underline{\varepsilon}\left(t_\varepsilon, \underline{\Delta\varepsilon}^{*1,2}\right)\right) := \frac{\partial \underline{\sigma}\left(\vec{x}, \underline{\varepsilon}\left(t_\varepsilon, \underline{\Delta\varepsilon}^{*1,2}\right)\right)}{\partial \underline{\varepsilon}} \tag{2.148}$$

represents the tangent stiffness tensor of the constitutive law. By applying the fundamental theorem of calculus, one arrives at

$$\int_0^1 \frac{\mathrm{d}}{\mathrm{d}t_\varepsilon} \underline{\sigma}\left(\vec{x}, \underline{\varepsilon}\right) \mathrm{d}t_\varepsilon = \underline{\sigma}\left(\vec{x}, \underline{\varepsilon}^{*1}\right) - \underline{\sigma}\left(\vec{x}, \underline{\varepsilon}^{*2}\right) = \int_0^1 \underline{\underline{C}}^{\mathrm{t}} : \underline{\Delta\varepsilon}^{*1,2} \, \mathrm{d}t_\varepsilon, \tag{2.149}$$

which also occurs on the left-hand side of the Lipschitz condition in Eq. (2.145). The dependences of the tangent stiffness, interpolated strain field, and the difference of the strain fluctuation fields are omitted for better readability.

For the next step, consider a fixed spatial point with given t_ε, $\underline{\Delta\varepsilon}^{*1,2}$, and $\vec{x}$. The pointwise operator norm for the tangent stiffness can then be defined according to

$$||\underline{\underline{C}}^{\mathrm{t}}||_{\mathrm{op}} := \sup \frac{||\underline{\underline{C}}^{\mathrm{t}}\left(\underline{\Delta\varepsilon}^{*1,2} = const.\right) : \underline{\Delta\varepsilon}^{*1,2}||_{\mathrm{F}}}{||\underline{\Delta\varepsilon}^{*1,2}||_{\mathrm{F}}}, \tag{2.150}$$

see e.g. [111, Definition 6.2.2 and Lemma 6.2.4]. The operator "sup" denotes the supremum, which is the least upper bound to a set and corresponds to the maximum if the bound is a part of the set. $\underline{\Delta\varepsilon}^{*1,2} = const.$ is emphasized in the function argument of $\underline{\underline{C}}^{\mathrm{t}}$, since $\underline{\Delta\varepsilon}^{*1,2}$ is varied to find the orientation, for which the supremum is obtained. However, the tangent stiffness is also dependent on this strain fluctuation difference and can therefore change by the change of the orientation, but the operator norm is defined for a given, constant tangent stiffness tensor. Any admissible tensor could also be used instead of $\underline{\Delta\varepsilon}^{*1,2}$ in the calculation, nevertheless it is retained for better clarity in the following steps.

To obtain an explicit result for the operator norm, the tangent stiffness can also be expressed in its spectral representation

$$\underline{\underline{C}}^{\mathrm{t}} = \sum_{i=1}^{6} \lambda_i^{\mathrm{eig}} \, \underline{M}_i \otimes \underline{M}_i, \tag{2.151}$$

where λ_i^{eig} are the eigenvalues and $\underline{M}_i$ are the symmetric, orthogonal eigentensors that form a basis, cf. [112]. $\otimes$ denotes the outer product between the two second order tensors, as explicitly defined in the nomenclature. The resulting eigenvalues and -tensors for different symmetries of the (elastic) stiffness tensor are presented in [113].

Owing to the orthogonality, a linear combination of $\underline{M}_i$ with coefficients $\overline{\Delta\varepsilon}_i^{*1,2}$ can

also be used to represent the difference of the strain fluctuations, such that one can write

$$\underline{\Delta\varepsilon}^{*1,2} = \sum_{i=1}^{6} \overline{\Delta\varepsilon}_i^{*1,2}\, \underline{M}_i, \tag{2.152}$$

see also [112, Eq. 6.16] and [114]. Using the identities

$$\underline{M}_i : \underline{M}_j = \delta_{ij} \tag{2.153}$$

and

$$\left(\underline{M}_i \otimes \underline{M}_j\right) : \underline{M}_j = \left(\underline{M}_i : \underline{M}_j\right) \underline{M}_j, \tag{2.154}$$

the double dot product between the tangent stiffness tensor and the difference of the strain fluctuations yields

$$\underline{\underline{C}}^{\mathrm{t}} : \underline{\Delta\varepsilon}^{*1,2} = \sum_{i=1}^{6} \lambda_i^{\mathrm{eig}}\ \overline{\Delta\varepsilon}_i^{*1,2}\, \underline{M}_i, \tag{2.155}$$

where δ_{ij} denotes the Kronecker delta, cf. also [112, Eq. 6.17] and [114]. Furthermore, the numerator of the operator norm in Eq. (2.150) can then be expressed similarly according to

$$||\underline{\underline{C}}^{\mathrm{t}} : \underline{\Delta\varepsilon}^{*1,2}||_{\mathrm{F}} = \sqrt{\left[\underline{\underline{C}}^{\mathrm{t}} : \underline{\Delta\varepsilon}^{*1,2}\right] : \left[\underline{\underline{C}}^{\mathrm{t}} : \underline{\Delta\varepsilon}^{*1,2}\right]} = \sqrt{\sum_{i=1}^{6}\left(\lambda_i^{\mathrm{eig}}\ \overline{\Delta\varepsilon}_i^{*1,2}\right)^2}, \tag{2.156}$$

whereas the denominator becomes

$$||\underline{\Delta\varepsilon}^{*1,2}||_{\mathrm{F}} = \sqrt{\underline{\Delta\varepsilon}^{*1,2} : \underline{\Delta\varepsilon}^{*1,2}} = \sqrt{\sum_{i=1}^{6}\left(\overline{\Delta\varepsilon}_i^{*1,2}\right)^2}. \tag{2.157}$$

The operator norm is ultimately given by

$$||\underline{\underline{C}}^{\mathrm{t}}||_{\mathrm{op}} = \sup \frac{\sqrt{\sum_{i=1}^{6}\left(\lambda_i^{\mathrm{eig}}\ \overline{\Delta\varepsilon}_i^{*1,2}\right)^2}}{\sqrt{\sum_{i=1}^{6}\left(\overline{\Delta\varepsilon}_i^{*1,2}\right)^2}}. \tag{2.158}$$

The supremum can be computed by optimizing this spectral form of the operator norm with respect to $\overline{\Delta\varepsilon}_i^{*1,2}$. The solution procedure for the optimization problem is presented in Appendix B and returns

$$||\underline{\underline{C}}^{\mathrm{t}}||_{\mathrm{op}} = \lambda_1^{\mathrm{eig}}, \tag{2.159}$$

which is also a well-known result from mathematical analysis. λ_1^{eig} represents the largest eigenvalue of the (positive semi-definite) $\underline{\underline{C}}^{\mathrm{t}}$.

Now, the definition of the operator norm can serve a basis for the derivation of an inequality of the same type as the condition for Lipschitz continuity. Using this definition from Eq. (2.150) and the fact that the supremum of an expression is always greater than or equal to the expression itself, one can write

$$\begin{aligned} \frac{||\,\underline{\underline{C}}^{\mathrm{t}} : \underline{\Delta\varepsilon}^{*1,2}\,||_{\mathrm{F}}}{||\,\underline{\Delta\varepsilon}^{*1,2}\,||_{\mathrm{F}}} &\leq \sup \frac{||\,\underline{\underline{C}}^{\mathrm{t}}\left(\underline{\Delta\varepsilon}^{*1,2} = const.\right) : \underline{\Delta\varepsilon}^{*1,2}\,||_{\mathrm{F}}}{||\,\underline{\Delta\varepsilon}^{*1,2}\,||_{\mathrm{F}}} \\ &= ||\,\underline{\underline{C}}^{\mathrm{t}}\,||_{\mathrm{op}} = \lambda_1^{\mathrm{eig}}, \end{aligned} \tag{2.160}$$

which holds pointwise for given $\underline{\Delta\varepsilon}^{*1,2}$, t_ε, and $\vec{x}$. Now, considering the supremum with respect to all admissible strain fluctuation differences and spatial locations, the inequality still remains valid for all such combinations. This results in

$$\frac{||\,\underline{\underline{C}}^{\mathrm{t}} : \underline{\Delta\varepsilon}^{*1,2}\,||_{\mathrm{F}}}{||\,\underline{\Delta\varepsilon}^{*1,2}\,||_{\mathrm{F}}} \leq \sup_{\vec{x},\,\underline{\Delta\varepsilon}^{*1,2}} \lambda_1^{\mathrm{eig}}\left(\vec{x}, \underline{\varepsilon}\left(t_\varepsilon, \underline{\Delta\varepsilon}^{*1,2}\right)\right), \tag{2.161}$$

which holds pointwise for a given t_ε and for all $\underline{\Delta\varepsilon}^{*1,2}$ and $\vec{x}$. By moving the denominator to the right-hand side and squaring both sides, one obtains

$$||\,\underline{\underline{C}}^{\mathrm{t}} : \underline{\Delta\varepsilon}^{*1,2}\,||_{\mathrm{F}}^2 \leq \sup_{\vec{x},\,\underline{\Delta\varepsilon}^{*1,2}} \left[\left(\lambda_1^{\mathrm{eig}}\right)^2\right] ||\underline{\Delta\varepsilon}^{*1,2}||_{\mathrm{F}}^2. \tag{2.162}$$

The brackets on the right-hand side clarify that the supremum applies only to the squared eigenvalue. The dependences of λ_1^{eig} are omitted for better readability. Integrating both sides over t_ε returns

$$\begin{aligned} \int_0^1 ||\,\underline{\underline{C}}^{\mathrm{t}} : \underline{\Delta\varepsilon}^{*1,2}\,||_{\mathrm{F}}^2 \;\mathrm{d}t_\varepsilon &= ||\,\underline{\sigma}\left(\vec{x}, \underline{\varepsilon}^{*1}\right) - \underline{\sigma}\left(\vec{x}, \underline{\varepsilon}^{*2}\right)||_{\mathrm{F}}^2 \\ &\leq \int_0^1 \sup_{\vec{x},\,\underline{\Delta\varepsilon}^{*1,2}} \left[\left(\lambda_1^{\mathrm{eig}}\right)^2\right] \mathrm{d}t_\varepsilon \;||\underline{\Delta\varepsilon}^{*1,2}||_{\mathrm{F}}^2, \end{aligned} \tag{2.163}$$

where Eq. (2.149) is used in the first line to replace the integral of the tangent stiffness and the strain fluctuation difference by the stress difference. Owing to the occurrence of the integral over t_ε, the equation also holds for all admissible t_ε.

Taking the supremum with respect to t_ε is always greater than or equal to all other λ_1^{eig}, such that the second line of Eq. (2.163) becomes also always greater or equal. Moreover, the supremum with respect to t_ε is constant and hence the integral just returns

the supremum itself, which gives

$$||\,\underline{\sigma}\left(\vec{x},\underline{\varepsilon}^{*1}\right)-\underline{\sigma}\left(\vec{x},\underline{\varepsilon}^{*2}\right)||_{\mathrm{F}}^{2}\leq\sup_{\vec{x},\,\underline{\Delta\varepsilon}^{*1,2},\,t_{\varepsilon}}\left[\left(\lambda_{1}^{\mathrm{eig}}\right)^{2}\right]\,||\underline{\Delta\varepsilon}^{*1,2}||_{\mathrm{F}}^{2}. \tag{2.164}$$

Then, applying the volume average to both sides yields

$$\left\langle||\,\underline{\sigma}\left(\vec{x},\underline{\varepsilon}^{*1}\right)-\underline{\sigma}\left(\vec{x},\underline{\varepsilon}^{*2}\right)||_{\mathrm{F}}^{2}\right\rangle_{\mathrm{V}}\leq\left\langle\sup_{\vec{x},\,\underline{\Delta\varepsilon}^{*1,2},\,t_{\varepsilon}}\left[\left(\lambda_{1}^{\mathrm{eig}}\right)^{2}\right]\,||\underline{\Delta\varepsilon}^{*1,2}||_{\mathrm{F}}^{2}\right\rangle_{\mathrm{V}}. \tag{2.165}$$

Exploiting the fact that the supremum is a constant to move it in front of the volume integral and taking the square root on both sides leads to

$$\left\langle||\,\underline{\sigma}\left(\vec{x},\underline{\varepsilon}^{*1}\right)-\underline{\sigma}\left(\vec{x},\underline{\varepsilon}^{*2}\right)||_{\mathrm{F}}^{2}\right\rangle_{\mathrm{V}}^{\frac{1}{2}}\leq\sup_{\vec{x},\,\underline{\Delta\varepsilon}^{*1,2},\,t_{\varepsilon}}\left[\lambda_{1}^{\mathrm{eig}}\right]\,\left\langle||\underline{\Delta\varepsilon}^{*1,2}||_{\mathrm{F}}^{2}\right\rangle_{\mathrm{V}}^{\frac{1}{2}}. \tag{2.166}$$

By comparing coefficients with the condition for Lipschitz continuity of the gradient in Eq. (2.145), one obtains

$$\begin{aligned}\alpha_{+}&=\sup_{\vec{x},\,\underline{\Delta\varepsilon}^{*1,2},\,t_{\varepsilon}}\left[\lambda_{1}^{\mathrm{eig}}\left(\vec{x},\underline{\varepsilon}\left(\underline{\Delta\varepsilon}^{*1,2},t_{\varepsilon}\right)\right)\right]\\&=\sup_{\vec{x},\underline{\varepsilon}}\left[\lambda_{1}^{\mathrm{eig}}\left(\vec{x},\underline{\varepsilon}\right)\right]=\max\left[\mathrm{eig}\left(\underline{\underline{C}}^{\mathrm{t}}\left(\vec{x},\ \underline{\varepsilon}\right)\right)\right]\end{aligned} \tag{2.167}$$

for the Lipschitz constant, where the supremum over $\underline{\Delta\varepsilon}^{*1,2}$ and t_{ε} is summarized to the supremum over $\underline{\varepsilon}$. The supremum can be replaced by the maximum, as in practice, only tangent stiffnesses that actually occur in the corresponding simulations rather than theoretical bounds are considered.

In the next step, the determination of constant α_{-} is discussed using the condition that the objective function is strongly convex, Eq. (2.140). It reads

$$\left(\mathrm{grad}\,W_{\mathrm{pot}}\left(\vec{u}^{*1}\right)-\mathrm{grad}\,W_{\mathrm{pot}}\left(\vec{u}^{*2}\right),\vec{u}^{*1}-\vec{u}^{*2}\right)_{\mathrm{H}_{\mathrm{per}}^{1}}\geq\alpha_{-}\,||\,\vec{u}^{*1}-\vec{u}^{*2}||_{\mathrm{H}_{\mathrm{per}}^{1}}^{2} \tag{2.168}$$

for the mechanical homogenization problem, where again all other dependences except for the dependence on $\vec{u}^{*1}$ and $\vec{u}^{*2}$ are omitted for better notational clarity. Using the definition of the inner product Eq. (2.112) of the space H_{per}^{1} and the relation $\mathrm{grad}^{\mathrm{S}}\left(\mathrm{grad}\,W_{\mathrm{pot}}\right)=\underline{\sigma}:\mathrm{grad}^{\mathrm{S}}$ from Eq. (2.124), one arrives at

$$\left\langle\left[\,\underline{\sigma}\left(\vec{x},\underline{\varepsilon}^{*1}\right)-\underline{\sigma}\left(\vec{x},\underline{\varepsilon}^{*2}\right)\right]:\underline{\Delta\varepsilon}^{*1,2}\,\right\rangle_{\mathrm{V}}\geq\alpha_{-}\left\langle||\underline{\Delta\varepsilon}^{*1,2}||_{\mathrm{F}}^{2}\,\right\rangle_{\mathrm{V}} \tag{2.169}$$

for the convexity condition.

As in the computation of α_+, it is started with the interpolated stresses and strains from Eqs. (2.146)–(2.149) and by investigating a fixed spatial point with given t_ε, $\underline{\Delta\varepsilon}^{*1,2}$, and $\vec{x}$. Based on the double dot product between the tangent stiffness and the difference of the strain fluctuations in the spectral representation from Eq. (2.155), the inequality

$$\begin{aligned}\left(\underline{\underline{C}}^{\mathrm{t}} : \underline{\Delta\varepsilon}^{*1,2}\right) : \underline{\Delta\varepsilon}^{*1,2} &= \sum_{i=1}^{6} \lambda_i^{\mathrm{eig}} \left(\overline{\Delta\varepsilon}_i^{*1,2}\right)^2 \\ &\geq \lambda_6^{\mathrm{eig}} \sum_{i=1}^{6} \left(\overline{\Delta\varepsilon}_i^{*1,2}\right)^2 = \lambda_6^{\mathrm{eig}} \, ||\underline{\Delta\varepsilon}^{*1,2}||_{\mathrm{F}}^2\end{aligned} \tag{2.170}$$

can be obtained. λ_6^{eig} denotes the smallest eigenvalue of the tangent stiffness and Eq. (2.157) is used to summarize the second line. The sum of the eigenvalues multiplied with the corresponding components of the strain fluctuation difference has always to be greater than or equal to this smallest eigenvalue multiplied with the respective components. Furthermore, it is required to assume that $\underline{\underline{C}}^{\mathrm{t}}$ is positive definite and not only positive semi-definite as for α_+. This ensures that the determined α_- is always positive, as required by the strong convexity.

In the subsequent steps, the same arguments are used as in the computation of α_+. First, the integral over t_ε is applied to both sides, which gives

$$\begin{aligned}\int_0^1 \left(\underline{\underline{C}}^{\mathrm{t}} : \underline{\Delta\varepsilon}^{*1,2}\right) \mathrm{d}t_\varepsilon : \underline{\Delta\varepsilon}^{*1,2} &= \left[\underline{\sigma}\left(\vec{x}, \underline{\varepsilon}^{*1}\right) - \underline{\sigma}\left(\vec{x}, \underline{\varepsilon}^{*2}\right)\right] : \underline{\Delta\varepsilon}^{*1,2} \\ &\geq \inf_{\vec{x},\, \underline{\Delta\varepsilon}^{*1,2},\, t_\varepsilon} \left[\lambda_6^{\mathrm{eig}}\left(\vec{x}, \underline{\varepsilon}\left(t_\varepsilon, \underline{\Delta\varepsilon}^{*1,2}\right)\right)\right] ||\underline{\Delta\varepsilon}^{*1,2}||_{\mathrm{F}}^2.\end{aligned} \tag{2.171}$$

It is again exploited that the integral in the first line just returns the difference of the stress fields, see Eq. (2.149). Similar to the supremum previously, the operator "inf" represents the infimum, which is the greatest lower bound to a set and corresponds to the minimum if it is a part of the set. The infimum with respect to all $\vec{x}$, $\underline{\Delta\varepsilon}^{*1,2}$, and t_ε is also a constant and the integral over t_ε again just returns the infimum itself. Moreover, applying the volume average to both sides yields

$$\left\langle \left[\underline{\sigma}\left(\vec{x}, \underline{\varepsilon}^{*1}\right) - \underline{\sigma}\left(\vec{x}, \underline{\varepsilon}^{*2}\right)\right] : \underline{\Delta\varepsilon}^{*1,2} \right\rangle_{\mathrm{V}} \geq \inf_{\vec{x},\, \underline{\Delta\varepsilon}^{*1,2},\, t_\varepsilon} \left[\lambda_6^{\mathrm{eig}}\right] \left\langle ||\underline{\Delta\varepsilon}^{*1,2}||_{\mathrm{F}}^2 \right\rangle_{\mathrm{V}}. \tag{2.172}$$

By a comparison of coefficients, this expression corresponds to the condition that W_{pot} is

strongly convex from Eq. (2.169), if

$$\alpha_- = \inf_{\vec{x},\, \underline{\Delta\varepsilon}^{*1,2},\, t_\varepsilon} \left[\lambda_6^{\mathrm{eig}}\Big(\vec{x}, \underline{\varepsilon}\left(\underline{\Delta\varepsilon}^{*1,2}, t_\varepsilon \right) \Big) \right] = \min\Big[\mathrm{eig}\Big(\underline{\underline{C}}^{\mathrm{t}}\left(\vec{x}, \underline{\varepsilon} \right) \Big) \Big]. \tag{2.173}$$

Making the same argument as for α_+, the infimum can be replaced by the minimum, as only tangent stiffnesses that actually occur in the corresponding simulations rather than theoretical bounds are considered.

Therefore, the theoretically optimal constant step size for the gradient descent from Eq. (2.141) becomes

$$s_{\mathrm{gd}} = \frac{2}{\min\Big[\mathrm{eig}\Big(\underline{\underline{C}}^{\mathrm{t}}\left(\vec{x}, \underline{\varepsilon} \right) \Big) \Big] + \max\Big[\mathrm{eig}\Big(\underline{\underline{C}}^{\mathrm{t}}\left(\vec{x}, \underline{\varepsilon} \right) \Big) \Big]}. \tag{2.174}$$

Recall that the Barzilai-Borwein method corresponds to a gradient descent with an adaptive step size, cf. Eq. (2.108). In the next step, this step size update is derived. In general, it can be computed according to

$$s_{\mathrm{gd}}^i = \left(1 - \frac{\Big(\mathrm{grad}\, f\left(\vec{y}^{\,i} \right), \mathrm{grad}\, f\left(\vec{y}^{\,i-1} \right) \Big)_{\mathrm{Y}}}{|| \mathrm{grad}\, f\left(\vec{y}^{\,i-1} \right) ||_{\mathrm{Y}}^2} \right)^{-1} s_{\mathrm{gd}}^{i-1}, \tag{2.175}$$

see [23, Eq. 6], and in the case of the homogenization problem, it becomes

$$s_{\mathrm{gd}}^i = \left(1 - \frac{\Big(\mathrm{grad}\, W_{\mathrm{pot}}\Big([\,\vec{u}^{\,*}\,]^i \Big), \mathrm{grad}\, W_{\mathrm{pot}}\Big([\,\vec{u}^{\,*}\,]^{i-1} \Big) \Big)_{\mathrm{H}^1_{\mathrm{per}}}}{\Big|\Big| \mathrm{grad}\, W_{\mathrm{pot}}\Big([\,\vec{u}^{\,*}\,]^{i-1} \Big) \Big|\Big|_{\mathrm{H}^1_{\mathrm{per}}}^2} \right)^{-1} s_{\mathrm{gd}}^{i-1}. \tag{2.176}$$

The previous results for the gradient from Eq. (2.134) can then be inserted, along with the definitions of the inner product and norm for space H^1_{per} from Eqs. (2.112) and (2.113). In order to avoid storing additional solution fields, the identity $\mathrm{grad}^{\mathrm{S}}\left(\mathrm{grad}\, W_{\mathrm{pot}} \right) = \underline{\sigma}$ from Eq. (2.124) is exploited. Accordingly, the adaptive step size is computed as

$$s_{\mathrm{gd}}^i = \left(1 - \frac{\Big\langle \underline{\sigma}^{\,i} : \Big(\underline{\underline{\Gamma}} : \underline{\sigma}^{\,i-1} \Big) \Big\rangle_{\mathrm{V}}}{\Big\langle \Big(\underline{\underline{\Gamma}} : \underline{\sigma}^{\,i-1} \Big) : \Big(\underline{\underline{\Gamma}} : \underline{\sigma}^{\,i-1} \Big) \Big\rangle_{\mathrm{V}}} \right)^{-1} s_{\mathrm{gd}}^{i-1} \tag{2.177}$$

with iteration counter i.

From the point of view of functional analysis, everything is now in place to formulate the discretized Barzilai-Borwein scheme and to discuss the algorithm for a practical

implementation. This discretized Barzilai-Borwein scheme given by

$$\underline{\varepsilon}^{i+1} = \underline{\varepsilon}^{i} - s^{i}_{\mathrm{gd}}\, \underline{\underline{\Gamma}}_{\mathrm{SG}} : \underline{\sigma}^{i} \tag{2.178}$$

with the step size update

$$s^{i}_{\mathrm{gd}} = \left(1 - \frac{\left\langle \underline{\sigma}^{i} : \left(\underline{\underline{\Gamma}}_{\mathrm{SG}} : \underline{\sigma}^{i-1}\right)\right\rangle_{\mathrm{V}}}{\left\langle \left(\underline{\underline{\Gamma}}_{\mathrm{SG}} : \underline{\sigma}^{i-1}\right) : \left(\underline{\underline{\Gamma}}_{\mathrm{SG}} : \underline{\sigma}^{i-1}\right)\right\rangle_{\mathrm{V}}}\right)^{-1} s^{i-1}_{\mathrm{gd}}, \tag{2.179}$$

cf. Eq. (2.136) for the continuous gradient descent. The continuous Green operator $\underline{\underline{\Gamma}}$ is replaced by its discrete counterpart for the staggered grid discretization, $\underline{\underline{\Gamma}}_{\mathrm{SG}}$. Owing to the mathematical similarity, the same relation as for the continuous Green operator in Eq. (2.137) also holds for the discrete operator, such that $\underline{\underline{\Gamma}}_{\mathrm{SG}} = 2\mu^0\, \underline{\underline{\Gamma}}^0_{\mathrm{SG}}$. Therefore, it can be computed from the known $\underline{\underline{\Gamma}}^0_{\mathrm{SG}}$ in Eq. (2.97).

The resulting algorithm is summarized in Alg. 1. All DFTs from the previous derivation of the discretization scheme are computed by using efficient implementations of the FFT in practice. As it is usual in FFT-based homogenization, the volumetric average strain $\underline{E}$ is prescribed depending on the load case, see [31]. It is also possible to prescribe the average stress or mixed loads, however, it is not used in this work and for details the reader is referred to [115].

Algorithm 1 (Strain-based) Barzilai-Borwein scheme

1: **Initialize:** $\underline{\varepsilon}^1 = \underline{E}$, $i = 0$ and $s^1_{\mathrm{gd}} = \dfrac{2}{\alpha_+ + \alpha_-}$

2: **Iterate:** $i = i + 1$ **until convergence:**

3: compute $\underline{\sigma}^i$ from $\underline{\varepsilon}^i$ and state variables ▷ constitutive law

4: **if** $i > 1$ **then** $s^i_{\mathrm{gd}} = \left(1 - \dfrac{\langle \underline{\sigma}^i : \underline{d\varepsilon}^{i-1}\rangle_{\mathrm{V}}}{\langle \underline{d\varepsilon}^{i-1} : \underline{d\varepsilon}^{i-1}\rangle_{\mathrm{V}}}\right)^{-1} s^{i-1}_{\mathrm{gd}}$ ▷ update step size

5: $\widehat{\underline{d\varepsilon}}^{\,i} = \begin{cases} \underline{0}, & \text{for } \vec{\xi}^{\,\mathrm{D}} = \vec{0} \\ \widehat{\underline{\underline{\Gamma}}}_{\mathrm{SG}} : \mathrm{FFT}\left(\underline{\sigma}^i\right), & \text{else} \end{cases}$ ▷ apply Green operator

6: $\underline{\varepsilon}^{i+1} = \underline{\varepsilon}^{i} - s^{i}_{\mathrm{gd}}\, \mathrm{FFT}^{-1}\left(\widehat{\underline{d\varepsilon}}^{\,i}\right)$ ▷ update strain field

Moreover, the application of the discrete differential operators $\mathrm{grad}^{\mathrm{S}}\, \vec{u}^*$ and $\mathrm{div}\, \underline{\sigma}$ can be computed directly in the physical space for the staggered grid discretization method without the need of a Fourier Transform, see Eqs. (2.73) and (2.74). Hence, the algorithm can be adapted to iterate on the displacement fluctuation fields instead of the strain

fields using the discrete version of the gradient descent from Eq. (2.135)

$$[\,\vec{u}^{*}\,]^{i+1} = [\,\vec{u}^{*}\,]^{i} - s^{i}_{\mathrm{gd}}\,\underline{G}_{\mathrm{SG}} \cdot \mathrm{div}\left(\underline{\sigma}^{i}\right). \tag{2.180}$$

Again the continuous solution operator is replaced by $\underline{G}_{\mathrm{SG}}$. As for the Green operator, the relation $\underline{G}_{\mathrm{SG}} = 2\mu^{0}\underline{G}^{0}_{\mathrm{SG}}$, which was originally derived for the continuous solution operator in Eq. (2.133), holds owing to the mathematical similarity between both cases. $\underline{G}_{\mathrm{SG}}$ can then be obtained from $\underline{G}^{0}_{\mathrm{SG}}$ in Eq. (2.95). The number of Fourier Transforms, which often represent a computational bottleneck, can be reduced from six to three in the displacement-based variant. The required memory footprint is also reduced accordingly. This displacement-based Barzilai-Borwein scheme, which was used for all simulations in this work, is presented in Alg. 2. A similar scheme is also presented in [13].

Algorithm 2 Displacement-based Barzilai-Borwein scheme

1: **Initialize:** $[\vec{u}^{*}]^{1} = \vec{0}$, $i = 0$ and $s^{1}_{\mathrm{gd}} = \dfrac{2}{\alpha_{+} + \alpha_{-}}$

2: **Iterate:** $i = i + 1$ **until convergence:**

3: Compute $\underline{\sigma}^{i}$ from $\underline{E} + \mathrm{grad}^{\mathrm{S}}[\vec{u}^{*}]^{i}$ and state variables ▷ constitutive law

4: **if** $i > 1$ **then**

$$s^{i}_{\mathrm{gd}} = \left(1 - \frac{\left\langle \underline{\sigma}^{\,i} : \left(\mathrm{grad}^{\mathrm{S}}\left[\overrightarrow{du}^{\,*}\right]^{i-1}\right)\right\rangle_{\mathrm{V}}}{\left\langle \left(\mathrm{grad}^{\mathrm{S}}\left[\overrightarrow{du}^{\,*}\right]^{i-1}\right) : \left(\mathrm{grad}^{\mathrm{S}}\left[\overrightarrow{du}^{\,*}\right]^{i-1}\right)\right\rangle_{\mathrm{V}}}\right)^{-1} s^{i-1}_{\mathrm{gd}} \qquad \triangleright \text{ update step size}$$

5: $$\left[\widehat{\overrightarrow{du}^{\,*}}\right]^{i} = \begin{cases} \vec{0}, & \text{for } \vec{\xi}^{\,\mathrm{D}} = \vec{0}, \\ \widehat{\underline{G}}_{\mathrm{SG}} \cdot \mathrm{FFT}\left[\mathrm{div}\left(\underline{\sigma}^{i}\right)\right], & \text{else} \end{cases} \qquad \triangleright \text{ apply Green operator}$$

6: $$[\,\vec{u}^{*}\,]^{i+1} = [\,\vec{u}^{*}\,]^{i} - s^{i}_{\mathrm{gd}}\,\mathrm{FFT}^{-1}\left(\left[\widehat{\overrightarrow{du}^{\,*}}\right]^{i}\right) \qquad \triangleright \text{ update displacement fluctuation field}$$

In order to assess whether the algorithm has found a sufficiently accurate solution, a consistent convergence criterion is required. For this purpose, recall that the gradient of W_{pot} is zero at the critical point. Thus, a natural convergence criterion for the gradient descent is to check if the norm of the gradient becomes smaller than a given tolerance *tol*

$$\left|\left|\,\mathrm{grad}\, W_{\mathrm{pot}}\left([\,\vec{u}^{*}\,]^{i}\right)\right|\right|_{\mathrm{H}^{1}_{\mathrm{per}}} < tol. \tag{2.181}$$

Inserting the gradient from Eq. (2.134) and the norm from Eq. (2.112) returns

$$\frac{\left\langle \left(\underline{\underline{\Gamma}}_{\mathrm{SG}} : \underline{\sigma}^i \right) : \left(\underline{\underline{\Gamma}}_{\mathrm{SG}} : \underline{\sigma}^i \right) \right\rangle_{\mathrm{V}}^{\frac{1}{2}}}{|| \left\langle \underline{\sigma}^i \right\rangle_{\mathrm{V}} ||_{\mathrm{F}}} < tol^{\mathrm{M}}. \tag{2.182}$$

The norm of the gradient is divided by the Frobenius norm of the average stress tensor in order to ensure that the condition is dimensionless. Furthermore, the discretized Green operator is used and tol^{M} represents the tolerance for the solver.

Now, since the theory and the algorithms of the solution method used were derived, the practical significance of the assumptions made is discussed in this final part of the section. First, the existence of the condensed incremental potential W_{pot} is assumed, where the stress can be computed as the derivative with respect to the strain. This existence is trivial for purely hyperelastic materials, but critical for all other types of material models.

For the class of Generalized Standard Materials the existence of such a condensed incremental potential based on a particular variational principle can be proven, see [116, 117]. Generalized Standard Materials are formulated using a (convex) Helmholtz free energy density and a (convex) dissipation potential [118, 119], as e.g. in von Mises plasticity. However, many phenomenological material models do not represent Generalized Standard Materials and some effects cannot be straightforwardly captured by the framework, such as non-associative plasticity, which is also used in this work.

Classical (softening) damage models and porosity are also critical, as the condition for strong convexity Eq. 2.168 is not always satisfied in the damaging phases and pores. To compute α_-, the tangent stiffness must be positive definite. This condition is violated in softening materials with negative eigenvalues and in pores where all eigenvalues of the tangent stiffness are zero.

Nevertheless, it was recently shown in [120] that damage models can be formulated as Generalized Standard Materials by using the evolving compliance instead of the damage as a state variable. The model avoids the localization phenomenon associated with the classical softening damage models. This behavior is mathematically beneficial, but the localization is required to model the formation of a single, global crack. Therefore, it is not (yet) applicable to fracture mechanics problems, see also [121]. Moreover, Köhler and Balzani [122] recently proposed a numerical reconvexification method for condensed incremental potentials of a continuum damage model. Their method can also consider softening and hence may be interesting for future work.

It should be noted that the derived solution schemes can still be applied to these materials, for which the existence of a condensed incremental potential could not be proven (yet). However, the insights from the mathematical theory need to be interpreted with caution, see also [123, Section 4.2.2]. This conclusion also applies to the present work, since a softening damage model is used.

The mathematical theory presented above can also be extended to pores, which makes them less critical in the homogenization of the sandwich core. The convergence and numerical efficiency of the derived solution methods can be proven under some basic assumptions on the geometry of the pore space, see [107] for details.

2.5.2. Damage regularization and coupled problem

The Lippmann-Schwinger equation for the damage regularization problem from Eq. (2.54) can be solved for p_{nl} using a fixed-point iteration similar to Moulinec and Suquet's basic scheme, which reads

$$p_{\mathrm{nl}}^{j+1} = \mathcal{F}^{-1}\left(\frac{\widehat{p}_{\mathrm{l}} + i\vec{\xi}\cdot\mathcal{F}\left(\left[l^2 - l_0^2\right]\mathcal{F}^{-1}\left[i\vec{\xi}\,\hat{p}_{\mathrm{nl}}^{j}\right]\right)}{1 + l_0^2\left|\vec{\xi}\right|^2}\right). \tag{2.183}$$

Here, more sophisticated algorithms based on rigorous functional analysis could be developed as well. However, it was observed that the time needed for the solution of the damage regularization problem is negligible compared with the time spent for the homogenization problem. Similar findings were also reported in [35] for a phase field model for brittle damage. The corresponding discretized form of the fixed-point iteration is outlined in lines 3–5 of Alg. 3, as part of the solution scheme for the coupled damage regularization and homogenization problem. This solution for the coupled problem is further discussed in detail below in this section. In the discretized form of the fixed-point iteration, the continuous frequencies $\vec{\xi}$ are replaced by their discrete counterparts $\vec{\xi}^{\,\mathrm{D}}$ and the FFT is performed instead of the continuous Fourier Transform, see Sec. 2.4.2.

The solution scheme for the damage regularization is stopped once the convergence criterion is reached. This criterion reads

$$\frac{\left\langle\left(p_{\mathrm{nl}}^{j} - \operatorname{div}\left[l^2\left(\vec{x}\right)\operatorname{grad}p_{\mathrm{nl}}^{j}\right] - p_{\mathrm{l}}\right)^2\right\rangle_{\mathrm{V}}^{\frac{1}{2}}}{\langle p_{\mathrm{l}}\rangle_{\mathrm{V}}} < tol^{\mathrm{D}}, \tag{2.184}$$

where tol^{D} corresponds to the tolerance for the damage solver. In practice, the criterion

Algorithm 3 Staggered solution of the coupled homogenization and damage problem

1: **Until convergence:**
2: Solve Eq. (2.1) using Alg. 2 and obtain p_{l} ▷ keep p_{nl} constant
3: **Initialize:** $j = 0$ and use p_{nl} from previous load step for p_{nl}^{1}
4: **Iterate** $j = j + 1$ **until convergence:** ▷ keep p_{l} constant
5: $$p_{\mathrm{nl}}^{j+1} = \mathrm{FFT}^{-1}\left(\frac{\widehat{p}_{\mathrm{l}} + i\vec{\xi}^{\,\mathrm{D}} \cdot \mathrm{FFT}\left(\left[l^2 - l_0^2\right]\mathrm{FFT}^{-1}\left[i\vec{\xi}^{\,\mathrm{D}}\,\hat{p}_{\mathrm{nl}}^{j}\right]\right)}{1 + l_0^2\left|\vec{\xi}^{\,\mathrm{D}}\right|^2}\right)$$

can be computed as

$$\frac{\left\langle \left(p_{\mathrm{nl}}^{j+1} - p_{\mathrm{nl}}^{j}\right)^2 \right\rangle_{\mathrm{V}}^{\frac{1}{2}}}{\langle p_{\mathrm{l}} \rangle_{\mathrm{V}}} < tol^{\mathrm{D}} \tag{2.185}$$

using consecutive iterations of the non-local damage field, which is briefly discussed in the following. First, it can be shown that

$$\mathrm{div}\left[l^2\left(\vec{x}\right)\mathrm{grad}\, p_{\mathrm{nl}}\right] + p_{\mathrm{l}} \tag{2.186}$$

is equivalent to the inverse Fourier Transform of the right-hand side of Eq. (2.54)

$$\mathcal{F}^{-1}\left(\frac{\widehat{p}_{\mathrm{l}} + i\vec{\xi} \cdot \mathcal{F}\left(\left[l^2 - l_0^2\right]\mathcal{F}^{-1}\left[i\vec{\xi}\,\hat{p}_{\mathrm{nl}}\right]\right)}{1 + l_0^2\left|\vec{\xi}\right|^2}\right), \tag{2.187}$$

since it is only rearranged by means of the Fourier Transform. If p_{nl}^{j} is then substituted for p_{nl}, the resulting expression

$$\mathcal{F}^{-1}\left(\frac{\widehat{p}_{\mathrm{l}} + i\vec{\xi} \cdot \mathcal{F}\left(\left[l^2 - l_0^2\right]\mathcal{F}^{-1}\left[i\vec{\xi}\,\hat{p}_{\mathrm{nl}}^{j}\right]\right)}{1 + l_0^2\left|\vec{\xi}\right|^2}\right) \tag{2.188}$$

then corresponds to p_{nl}^{j+1} according to the fixed-point iteration in Eq. (2.183). Therefore,

$$p_{\mathrm{nl}}^{j+1} = \mathrm{div}\left[l^2\left(\vec{x}\right)\mathrm{grad}\, p_{\mathrm{nl}}^{j}\right] + p_{\mathrm{l}} \tag{2.189}$$

holds in the convergence criterion. Furthermore, the criterion is activated when the denominator becomes larger than zero. Otherwise, there is no (local) equivalent plastic strain and, hence, no damage is present. Numerical experiments revealed that the

criterion is independent on the mesh and model size.

The coupled homogenization and damage regularization problem is then solved in a staggered fashion, as also shown in Alg. 3 and as it was also done in [34]. The same convergence criterion is used for consecutive global (staggered) iterations of the non-local damage field. Except for the first iteration of the staggered solution algorithm, the final displacement fluctuation field from the previous iteration is used as initialization for $[\vec{u}^*]^1$ in the first line of Alg. 2. A linear extrapolation from previous (converged) load steps is used in the first iteration of each load step.

2.6. Implementation details

Alg. 3 was implemented as Fortran code and the parallelization was realized using the OpenMP library [124]. The FFTs were carried out with the FFTW library [125]. All simulations in this work were performed on an Intel® Core™ i9-10900X CPU using 20 parallel threads. The implementation of the linear Drucker-Prager plasticity model from Sec. 2.1 in Abaqus user defined material subroutine (UMAT) format is taken from [126]. For convergence reasons, the (squared) characteristic length parameter within the non-damaging phases l^2_{nd} cannot be set to zero as in Eq. (2.44). $l^2_{\mathrm{nd}} = 0.02\, l^2_{\mathrm{d}}$ was used instead as an approximation in all simulations, which is sufficient to effectively constrain the non-local equivalent plastic strain field to the damaging phase, cf. [34]. Furthermore, numerical experiments revealed that choosing $l^2_0 = l^2_{\mathrm{d}} + l^2_{\mathrm{nd}}$ provided robust and fast convergence of Alg. 3.

The tolerances of the mechanical homogenization and the damage solver were set to $tol^{\mathrm{M}} = tol^{\mathrm{D}} = 10^{-4}$ in all simulations. This is a commonly accepted value for simulations with non-linear materials for tol^{M}. tol^{D} was determined by numerical experiments in order to ensure sufficiently accurate results. For a detailed discussion on various convergence criteria and the chosen tolerances for FFT-based homogenization, the reader is referred to [31].

3. Extension of the FFT-based homogenization to Cohesive Zone Modeling

3.1. Governing equations and scale transition relations

In contrast to the bulk case, the governing equations at the macroscale for cohesive zones with a finite thickness are not as widely used. Hence, this concept from [127, Chapter 4] is briefly summarized first before the governing homogenization equations at the microscale are derived. The concept generally allows for finite rigid body rotations and large deformations, which is why the kinematics is based on an undeformed reference configuration and a deformed current configuration. It should be noted that this has no implications for the small deformation theory used at the microscale since micro- and macroscale are decoupled by the scale separability, see Sec. 2.1.

A scheme of the cohesive zone with a finite thickness is presented in Fig. 9, where the capital, black variables correspond to the reference configuration and the small, blue ones to the current configuration. The subscript "M" marks that the variables live at the macroscale only. Moreover, the red area indicates the cohesive zone in the reference configuration. The blue area in the zoom on the left-hand side of Fig. 9 corresponds to the cohesive zone in the current, deformed configuration. Both configurations are related by the displacements from the reference to the current configuration $\vec{u}_{\mathrm{M}}^{+}\left(\vec{X}_{\mathrm{M}}^{+}, t\right)$ and $\vec{u}_{\mathrm{M}}^{-}\left(\vec{X}_{\mathrm{M}}^{-}, t\right)$. The superscripts + and − denote that they belong to the top interface with the surrounding bulk material, S_{coh}^{+}, and the bottom one S_{coh}^{-}, respectively. The displacements are dependent on the corresponding points in the reference configuration $\vec{X}_{\mathrm{M}}^{+}$ and $\vec{X}_{\mathrm{M}}^{-}$, and the time t.

These interfaces are depicted as black lines in the reference configuration. The blue lines are those in the current configuration, s_{coh}^{+} and s_{coh}^{-}, accordingly. The geometrical description of the cohesive zone is based on its middle surface, which is represented by the dashed lines. The position of a point on this middle surface is indicated by the vectors $\vec{X}_{\mathrm{M}}$ and $\vec{x}_{\mathrm{M}}\left(\vec{X}_{\mathrm{M}}, t\right)$ in the reference and current configuration, respectively. The global coordinate system is given by the axes x_{M}, y_{M}, z_{M} and X_{M}, Y_{M}, Z_{M} in the corresponding configurations.

The kinematic quantity of interest for the constitutive law of the cohesive zone is the separation $\vec{\delta}_{\mathrm{M}}$ between the interfaces s_{coh}^{+} and s_{coh}^{-} with respect to the initial thickness t_{coh} between S_{coh}^{+} and S_{coh}^{-}. It is defined in the local coordinates systems with axes $x_{\mathrm{M}}^{\mathrm{l}}$, $y_{\mathrm{M}}^{\mathrm{l}}$, $z_{\mathrm{M}}^{\mathrm{l}}$. In the reference configuration, the local coordinate system is given by the axes

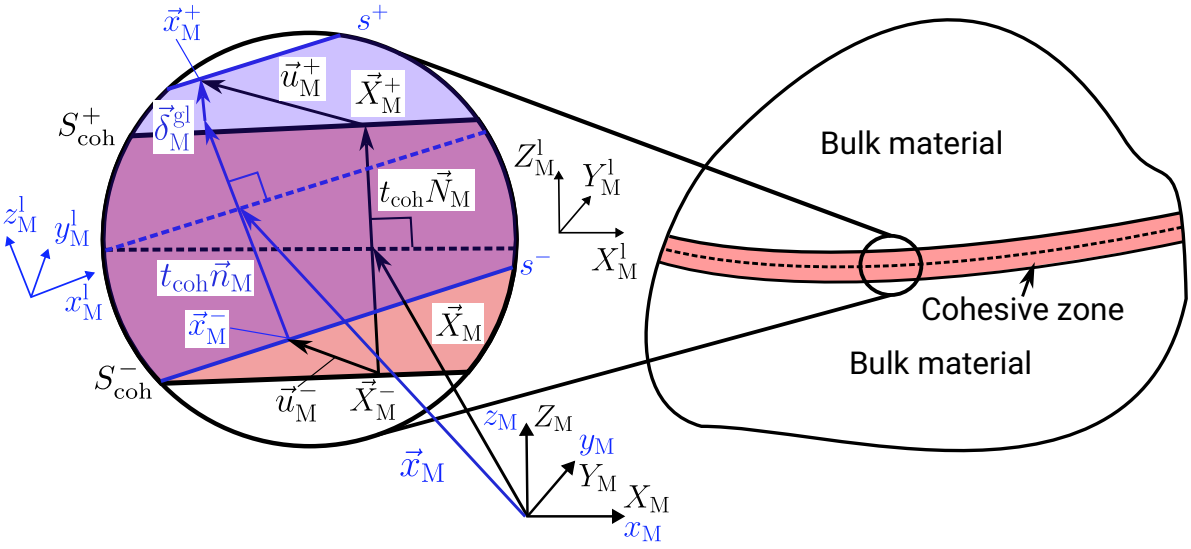

Figure 9: The concept of a cohesive zone with a finite thickness.

$X_{\mathrm{M}}^{\mathrm{l}}$, $Y_{\mathrm{M}}^{\mathrm{l}}$, $Z_{\mathrm{M}}^{\mathrm{l}}$.

For the derivation of $\vec{\delta}_{\mathrm{M}}$, it is started with the separation in global coordinates of the current configuration that can be computed as

$$\vec{\delta}_{\mathrm{M}}^{\mathrm{gl}} = \vec{x}_{\mathrm{M}}^{+} - \vec{x}_{\mathrm{M}}^{-} - t_{\mathrm{coh}}\,\vec{n}_{\mathrm{M}}, \tag{3.1}$$

as shown in Fig. 9. The superscript "gl" marks this global coordinates of the current configuration. $\vec{n}_{\mathrm{M}}$ denotes the normal on the middle surface of the cohesive zone and therefore indicates the direction in which peel mode I is usually defined. Furthermore, the position vectors at the interfaces $\vec{x}_{\mathrm{M}}^{+}\left(\vec{X}_{\mathrm{M}}^{+}, t\right)$ and $\vec{x}_{\mathrm{M}}^{-}\left(\vec{X}_{\mathrm{M}}^{-}, t\right)$ can be obtained from the corresponding positions in the reference configuration and the displacements according to

$$\vec{x}_{\mathrm{M}}^{+} = \vec{X}_{\mathrm{M}}^{+} + \vec{u}_{\mathrm{M}}^{+} \quad \text{and} \quad \vec{x}_{\mathrm{M}}^{-} = \vec{X}_{\mathrm{M}}^{-} + \vec{u}_{\mathrm{M}}^{-}, \tag{3.2}$$

respectively. Moreover, the position vectors at the interface can also be calculated based on the position on the middle surface, which yields

$$\vec{X}_{\mathrm{M}}^{+} = \vec{X}_{\mathrm{M}} + \frac{t_{\mathrm{coh}}}{2}\,\vec{N}_{\mathrm{M}} \quad \text{and} \quad \vec{X}_{\mathrm{M}}^{-} = \vec{X}_{\mathrm{M}} - \frac{t_{\mathrm{coh}}}{2}\,\vec{N}_{\mathrm{M}}. \tag{3.3}$$

$\vec{N}_{\mathrm{M}}$ denotes the normal to the middle surface in the reference configuration. The orientation vectors of the cohesive zone in both configurations are related by the rigid

body rotation $\underline{R}_{\mathrm{M}}^{\mathrm{rig}}$ according to

$$\vec{n}_{\mathrm{M}} = \underline{R}_{\mathrm{M}}^{\mathrm{rig}} \cdot \vec{N}_{\mathrm{M}}, \tag{3.4}$$

cf. [127, Eq. (4.27)]. Then, summarizing Eqs. (3.1)–(3.4) ultimately yields

$$\vec{\delta}_{\mathrm{M}}^{\mathrm{gl}} = \vec{u}_{\mathrm{M}}^{+} - \vec{u}_{\mathrm{M}}^{-} + t_{\mathrm{coh}}\Big(\underline{I} - \underline{R}_{\mathrm{M}}^{\mathrm{rig}}\Big) \cdot \vec{N}_{\mathrm{M}} \tag{3.5}$$

for the kinematics of the global separation vector. The first two terms in Eq. (3.5), the difference of the displacement of both interfaces, are the "displacement jump" in the context of infinitely thin cohesive zones, e.g., see [128, 129]. However, in the case of cohesive zones with a finite thickness, the difference of the displacements also contains a part that is caused by the rigid body rotations. This part needs to be subtracted in order to satisfy the principle of material objectivity for the constitutive law. This is done in the third term of Eq. (3.5), and one obtains the "displacement jump" for the cohesive zone with a finite thickness. Moreover, the global separation can be transformed into the (co-rotational) local coordinate system with axes $x_{\mathrm{M}}^{\mathrm{l}}$, $y_{\mathrm{M}}^{\mathrm{l}}$, $z_{\mathrm{M}}^{\mathrm{l}}$ by

$$\vec{\delta}_{\mathrm{M}} = \underline{R}_{\mathrm{M}}^{\mathrm{l}} \cdot \vec{\delta}_{\mathrm{M}}^{\mathrm{gl}}, \tag{3.6}$$

where $\underline{R}_{\mathrm{M}}^{\mathrm{l}}$ is the respective rotation matrix, see [127, Chapter 4] for details on its computation.

It is useful to choose the local coordinate system such that the axes and therefore also the components of $\vec{\delta}_{\mathrm{M}}$ are attributed to the fracture modes. The local separation vector then reads

$$\vec{\delta}_{\mathrm{M}} = (w \;\; v \;\; u)^{\mathrm{T}}. \tag{3.7}$$

Its entries w, v, and u correspond to the separations in out-of-plane shear mode III, in-plane shear mode II and peel mode I. Similar to the separation, the macroscopic traction vector is given by

$$\vec{t}_{\mathrm{M}} = (\tau_{\mathrm{III}} \;\; \tau_{\mathrm{II}} \;\; \sigma)^{\mathrm{T}}, \tag{3.8}$$

accordingly. σ, τ_{II}, and τ_{III} denote the peel stress in mode I and the shear stresses in mode II and III, respectively.

In the next step, the governing equations at the microscale are derived. Similar to the homogenization of bulk materials in Sec. 2.1, the principle of scale separation and homogenization of cohesive zones is depicted in Fig. 10. The zoom on the left-hand side

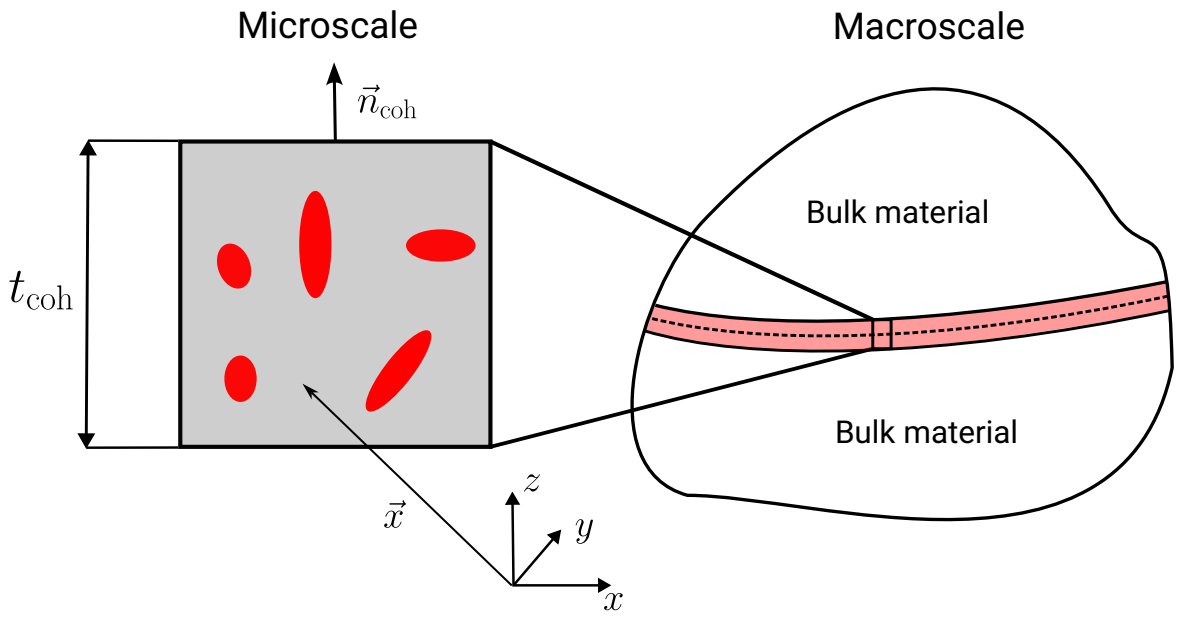

Figure 10: Principle of scale separation in the homogenization of cohesive zones.

shows the heterogeneous model for the microstructure, which has the full thickness of the cohesive zone now. $\vec{n}_{\mathrm{coh}}$ is the (local) orientation vector at the microscale, which is for convenience and without loss of generality chosen to be in the z-direction. This choice ensures that the fracture modes correspond to those in the local coordinate system at the macroscale.

In FFT-based homogenization, the volumetric average strain derived from kinematics at the macroscale must be prescribed in the microscale simulations for the macro-to-micro transition, as separations cannot be directly imposed. Following [42], this average strain in the cohesive zone can be approximated by

$$\underline{E} = (0 \;\; 0 \;\; u/t_{\mathrm{coh}} \;\; v/t_{\mathrm{coh}} \;\; w/t_{\mathrm{coh}} \;\; 0)^{\mathrm{T}}, \tag{3.9}$$

where Voigt notation is used. In-plane strains and stresses are typically neglected in CZM of material layers at the macroscale, which already represents a significant model simplification. Since the average in-plane strains at the microscale can correspondingly not be derived from macroscale kinematics, they are assumed to be zero. For most applications, this assumption is justified, since most points within the material layer are typically surrounded by material, which constrains deformation within the layer. Nevertheless, this assumption represents a further simplification and is particularly critical for material layers with at least one relatively small in-plane dimension. Owing to

the boundary effects, it would be more appropriate to set the respective average stresses instead of the strains to zero for these cases.

A constant displacement field at the interfaces of the cohesive zone is required to describe the displacement jump $\vec{\delta}_{\mathrm{M}}$ from the macroscale at the microscale. Therefore, the displacement fluctuations must vanish there, and one arrives at the homogenization problem for cohesive zones

$$\begin{cases} \underline{\sigma}\,(\vec{x}\,) \text{ computed from constitutive law} \\ \operatorname{div}\underline{\sigma}\,(\vec{x}\,) = \vec{0} \\ \underline{\varepsilon}\,(\vec{u}\,(\vec{x}\,)) = \underline{E} + \operatorname{grad}^{\mathrm{S}}\vec{u}^{\,*}\,(\vec{x}\,) \\ \vec{u}^{\,*} = \vec{0} \text{ at the cohesive zone interface} \\ \text{periodic boundary conditions elsewhere} \end{cases} \tag{3.10}$$

from the original bulk homogenization problem in Eq. (2.1). Again, the system of equations is composed of the computation of the stress field from the constitutive law, the balance of momentum and the strain compatibility. Furthermore, the periodic boundary conditions for the displacement fluctuation and the strain (fluctuation) fields are maintained except at the interface of the cohesive zone.

The FFT solver discussed in the previous section inherently imposes periodic boundary conditions on the displacement and strain fields owing to the FFTs themselves. Therefore, a method for approximating this Dirichlet-type boundary condition at the interface is required. This approximation can be achieved by adding marginal layers that have a significantly higher stiffness than the material in the virtual model of the microstructure. An infinite stiffness would lead to a perfect satisfaction of the boundary condition, but higher stiffness contrasts can also significantly increase the computational times. The practical determination of stiffness and thickness of these layers is further discussed in Sec. 3.3. Apart from the marginal layers, Dirichlet-type boundary conditions can also be directly implemented into FFT solvers, see [130–132], but the computational efficiency is also reduced.

As in Sec. 2.2 for the computational homogenization of bulk materials, the micro-to-macro transition is established based on the Hill-Mandel condition. The procedure to obtain these transitions is briefly summarized in the following. The energy rate balance between macro- and microscale is given by

$$\vec{t}_{\mathrm{M}} \cdot \dot{\vec{\delta}}_{\mathrm{M}} = t_{\mathrm{coh}} \left\langle \underline{\sigma} : \dot{\underline{\varepsilon}} \right\rangle_{\mathrm{V}}, \tag{3.11}$$

where spatial and time dependences are neglected for notational clarity. $\dot{\underline{\varepsilon}}$ can then be split into the homogeneous average part $\langle \dot{\underline{\varepsilon}} \rangle_{\mathrm{V}}$ and a fluctuating part $\dot{\underline{\varepsilon}}^*$, which yields

$$\vec{t}_{\mathrm{M}} \cdot \dot{\vec{\delta}}_{\mathrm{M}} = t_{\mathrm{coh}} \Big(\langle \underline{\sigma} \rangle_{\mathrm{V}} : \langle \dot{\underline{\varepsilon}} \rangle_{\mathrm{V}} + \langle \underline{\sigma} : \dot{\underline{\varepsilon}}^* \rangle_{\mathrm{V}} \Big). \tag{3.12}$$

Furthermore, the time derivative of the average strain from Eq. (3.9) can be inserted into Eq. (3.12) for $\langle \dot{\underline{\varepsilon}} \rangle_{\mathrm{V}}$ without loss of generality. Then, the rate of work on the right-hand side is replaced by its equivalent surface integral over the boundary S of the virtual model of the microstructure. For this purpose, the same steps as in the bulk case Eq. (2.13)-Eq. (2.16) are followed. Accordingly, one arrives at

$$\vec{t}_{\mathrm{M}} \cdot \dot{\vec{\delta}}_{\mathrm{M}} = \Big(\langle \underline{\sigma} \rangle_{\mathrm{V}} \cdot \vec{n}_{\mathrm{coh}} \Big) \cdot \dot{\vec{\delta}}_{\mathrm{M}} + \frac{1}{A_{\mathrm{coh}}} \int_S \vec{t} \cdot \dot{\vec{u}}^* \, \mathrm{d}S. \tag{3.13}$$

A_{coh} denotes the transverse area of the virtual model that is orthogonal to the axis in the through-thickness direction (or the orientation) of the cohesive zone, i.e., the xy-plane if the orientation of the cohesive zone is in z-direction.

The surface integral vanishes owing to the vanishing displacement fluctuations at the cohesive zone interface and the periodic boundary conditions elsewhere, for which this was already shown in Sec. 2.2 for the bulk homogenization. Consequently, the Hill-Mandel condition for the cohesive zone becomes

$$\vec{t}_{\mathrm{M}} \cdot \dot{\vec{\delta}}_{\mathrm{M}} = \Big(\langle \underline{\sigma} \rangle_{\mathrm{V}} \cdot \vec{n}_{\mathrm{coh}} \Big) \cdot \dot{\vec{\delta}}_{\mathrm{M}} \tag{3.14}$$

and is satisfied, if the macroscopic traction vector is computed as

$$\vec{t}_{\mathrm{M}} = \langle \underline{\sigma} \rangle_{\mathrm{V}} \cdot \vec{n}_{\mathrm{coh}} \tag{3.15}$$

from the stress field at the microscale. This result is also consistent with [42], where a modified Hill's Lemma was applied. Furthermore, a similar derivation can be found in [45].

3.2. Representativeness of the mechanical behavior compared with bulk homogenization

Referring to previous studies using classical FEM-based homogenization schemes, it is claimed in Sec. 1.3.2 that a representative mechanical behavior for softening materials can be obtained. This contrasts with the homogenization of bulk materials, as discussed

in this overview of the state of the art in the computational homogenization of cohesive zones.

In the current section, the existence of this representative mechanical behavior is investigated for the FFT-based homogenization scheme for cohesive zones and compared with the (FFT-based) standard bulk homogenization. For this purpose, a simple, deterministic material is studied as a numerical example. It consists of a periodic microstructure with infinite repetitions of a two-dimensional circular pore in a matrix, which is shown in Fig. 11c. In the case of the bulk homogenization, the material is periodic in y- and z-direction, whereas in the homogenization of cohesive zones a material layer with a periodicity in the y-direction only is considered. The single pore in the matrix represents the full thickness of the material layer in z-direction in the case of the cohesive zone. The cohesive zone is also oriented in z-direction.

The two-dimensional circular pore in a matrix from Fig. 11c is used as a basic virtual model for the microstructure and is sufficient to represent the geometry of the microstructure. The structure is discretized with 64 x 64 voxels and the pore has a radius of ten voxels. For simplicity, the voxel size was set to 1 mm. Furthermore, thin, stiff marginal layers with a thickness of five voxels each were added in through-thickness direction z to approximate the boundary conditions for a cohesive zone from Eq. (3.10), see Fig. 11a. To show a representative mechanical behavior, the stress-strain curve or TSL should remain unchanged as the model size increases. For this purpose, the basic virtual model is extended with copies of itself at the boundaries, such that a larger part of microstructure of the material is included in the model. In the case of bulk homogenization, four copies of the basic model in the yz–plane with an overall size of 128 x 128 voxels are used to compare the resulting mechanical behavior. For the cohesive zone, only one copy needs to be added in the y–direction, as the basic model already has the full thickness in the z–direction. With the marginal layers included, the models have sizes of 64 x 74 and 128 x 74 voxels for the basic model and the extended one, respectively.

Simulations in peel mode I and in-plane shear mode II were performed for the investigated models, where the mode I separation u and the mode II separation v were prescribed. Please also refer to Eq. (3.9) for the corresponding average strain in the FFT solver and Eq. (3.15) for the resulting traction vector in each load case. The material parameters used are summarized in Tab. 1, where E is the Young's modulus and ν is the Poisson's ratio. Setting $\eta = \bar{\eta} = 0$ and $\xi = \frac{1}{\sqrt{3}}$ recovers a standard von Mises plastic behavior here. The characteristic length parameter of 3.2 mm was purely selected by

numerical experiments. On the one hand, this choice ensures a sufficient distribution of the damage field for smooth convergence of the solution scheme and prevents the typical mesh dependence of local damage models. On the other hand, a localization of the crack in a sufficiently small zone is obtained.

Table 1: Material parameters used for the matrix and the marginal layers (ML).

	E (MPa)	ν (-)	d^0 (MPa)	H (MPa)	ξ (-)	η (-)	$\bar{\eta}$ (-)	p^0_{nl} (-)	$p^{\mathrm{f}}_{\mathrm{nl}}$ (-)
Matrix	2000	0.3	10	1	0.577	0	0	0.03	0.5
ML	30000	0.33	-	-	-	-	-	-	-

As shown in Fig. 12a, a perfect agreement was found between the resulting TSLs in mode I, which can also be observed for the mode II simulations in Fig. 13a. Therefore, the mechanical behavior of the basic model in Fig. 11a is representative of the entire material layer, even for the softening part of the TSLs. The simulations for the bulk homogenization were performed using the same load cases as for the cohesive zone and the resulting stress-strain curves are presented in Figs. 12b and 13b. Until softening sets in, the curves from both models show good agreement. However, a significant deviation occurs in the softening part of the stress-strain curves. Consequently, the basic model in Fig. 11c is no longer representative of the entire mechanical behavior.

These results can be understood by evaluating the damage fields in the simulations, which are shown in Figs. 12c –12f and 13c – 13f. Furthermore, the respective periodic copies are added to the basic models, so that the resulting damage fields can be better compared with those from the extended models. The basic model is marked with a black frame. A clear localization of damage is observed in all simulations, which also causes the nonexistence of a representative mechanical behavior in the case of the bulk homogenization.

If the basic model were representative of the mechanical behavior, the damage field in the extended model would be identical to the four periodic copies of the damage field in the smaller basic model. This is contradicted by the damage localization in the lower part of the extended model for the peel load case in Fig. 12f and in the left part of the extended model for the shear load case in Fig. 13f. Consequently, the extended model dissipates less volumetric energy through the fracture process compared with the basic model. This reduction is also observed in the stress-strain curves in Figs. 12b and 13b. The observed localization effect is also referred to as loss of statistical homogeneity by Gitman et al. [41], since the localized softening region of a material has mechanical properties which are different from those of the region where no softening

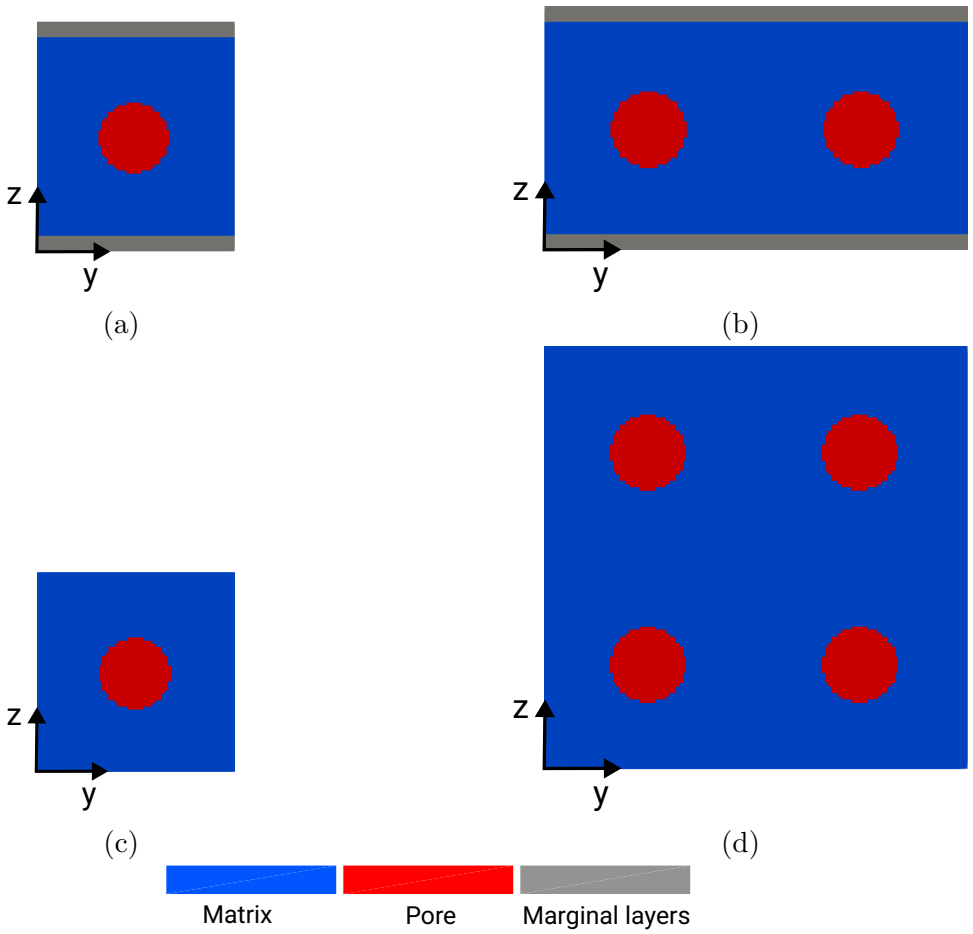

Figure 11: Two-dimensional matrix with a pore: Virtual model of the microstructure (a) and extended model (b) for cohesive zone approach and virtual model of the microstructure (c) and extended model (d) for bulk homogenization

occurs. However, as discussed in Sec. 2.1, statistical homogeneity is a key assumption in computational homogenization. Consequently, it is not applicable to materials with damage localization, which also means that no RVE or UC exist.

In contrast, the damage field in the extended model corresponds to the two copies of the damage field in the basic model for the cohesive zone, see Figs. 13c – 13f. This also results in the agreement between the TSLs in Figs. 12a and 13a, and of the energy dissipated per area of crack growth. Furthermore, the marginal layers ensure that the global crack propagates parallel to them. This effect can be observed in the shear load case, where the crack propagates vertically in bulk simulations but horizontally in cohesive zone simulations. Owing to the symmetry of the virtual microstructure model, vertical and horizontal crack propagation are physically equivalent. The actual propagation direction

is determined by slight numerical asymmetries. These numerical asymmetries can be caused by the discretization method used or asymmetries in the regular voxel mesh, see also Sec. 2.4.1.

For the cohesive zone, only the observed crack propagation direction parallel to the marginal layers is physically meaningful. Furthermore, the cohesive zone thickness in the z-direction acts as an intrinsic, characteristic length for the fracture process. This arises from the fact that the entire thickness of the cohesive zone is explicitly modeled. Changing the cohesive zone thickness therefore results in different TSLs as well.

Hence, it was demonstrated that the mechanical behavior in FFT-based homogenization for cohesive zones is indeed representative of the entire material layer. Consequently, the basic virtual model of the material layer in Fig. 11a serves as the corresponding UC. The consistency of the FFT-based method could be shown with this simple numerical example, accordingly. Furthermore, damage localization, as a physical explanation for the representative mechanical behavior in contrast to bulk homogenization, applies not only to the investigated deterministic material but also to random materials. This means that a mechanically representative model of the microstructure, an RVE, can also be found using the FFT-based homogenization method for cohesive zones, even for softening materials.

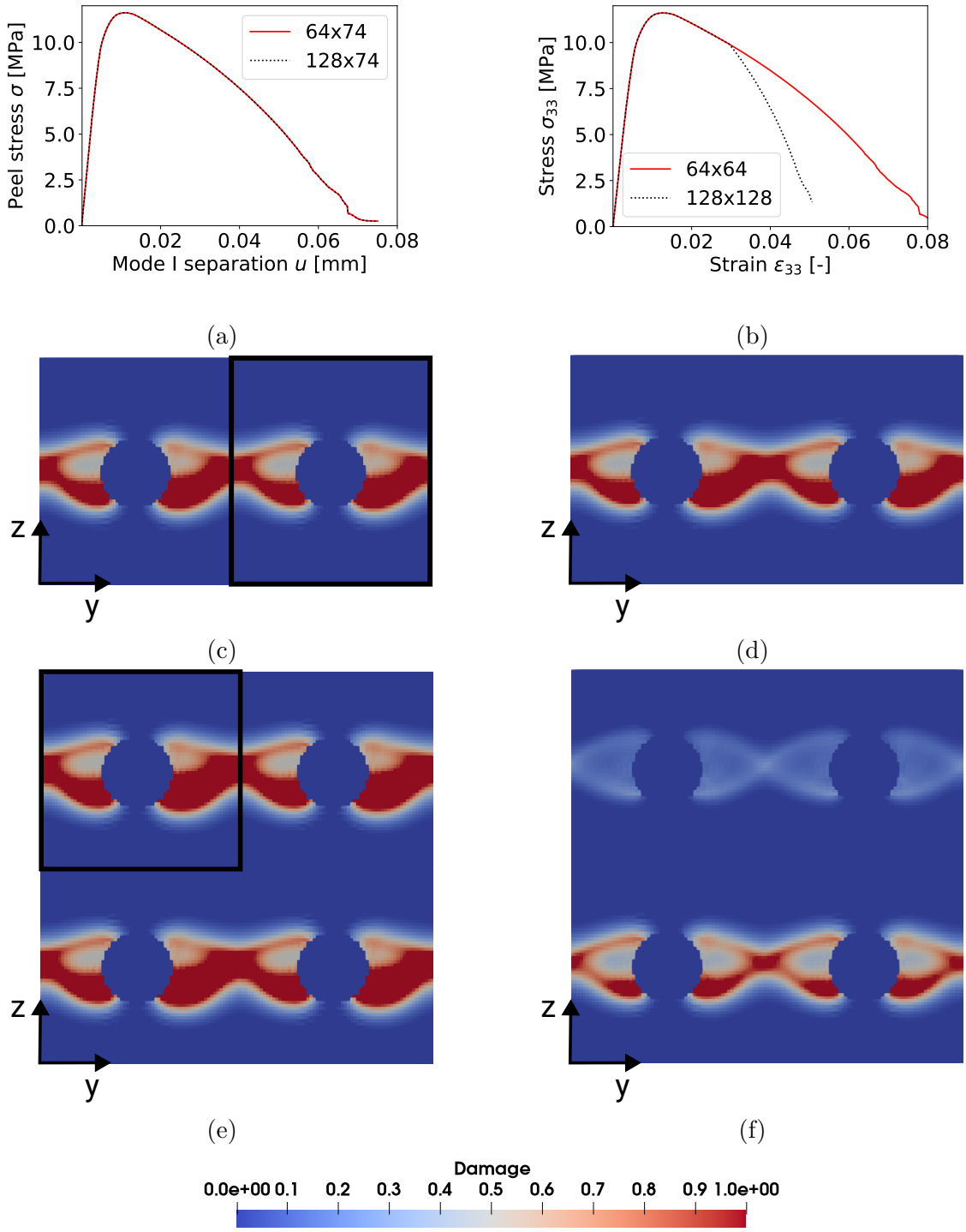

Figure 12: Peel mode I: TSLs of basic virtual model and extended model for cohesive zone approach (a) and stress-strain curves for bulk homogenization (b).; Final damage field of basic virtual model (c) and extended model (d) for cohesive zone approach and of basic virtual model (e) and extended model (f) for bulk homogenization. For comparison, periodic copies are added to the basic model in (c) and (e), where the original basic model is marked with a black frame.

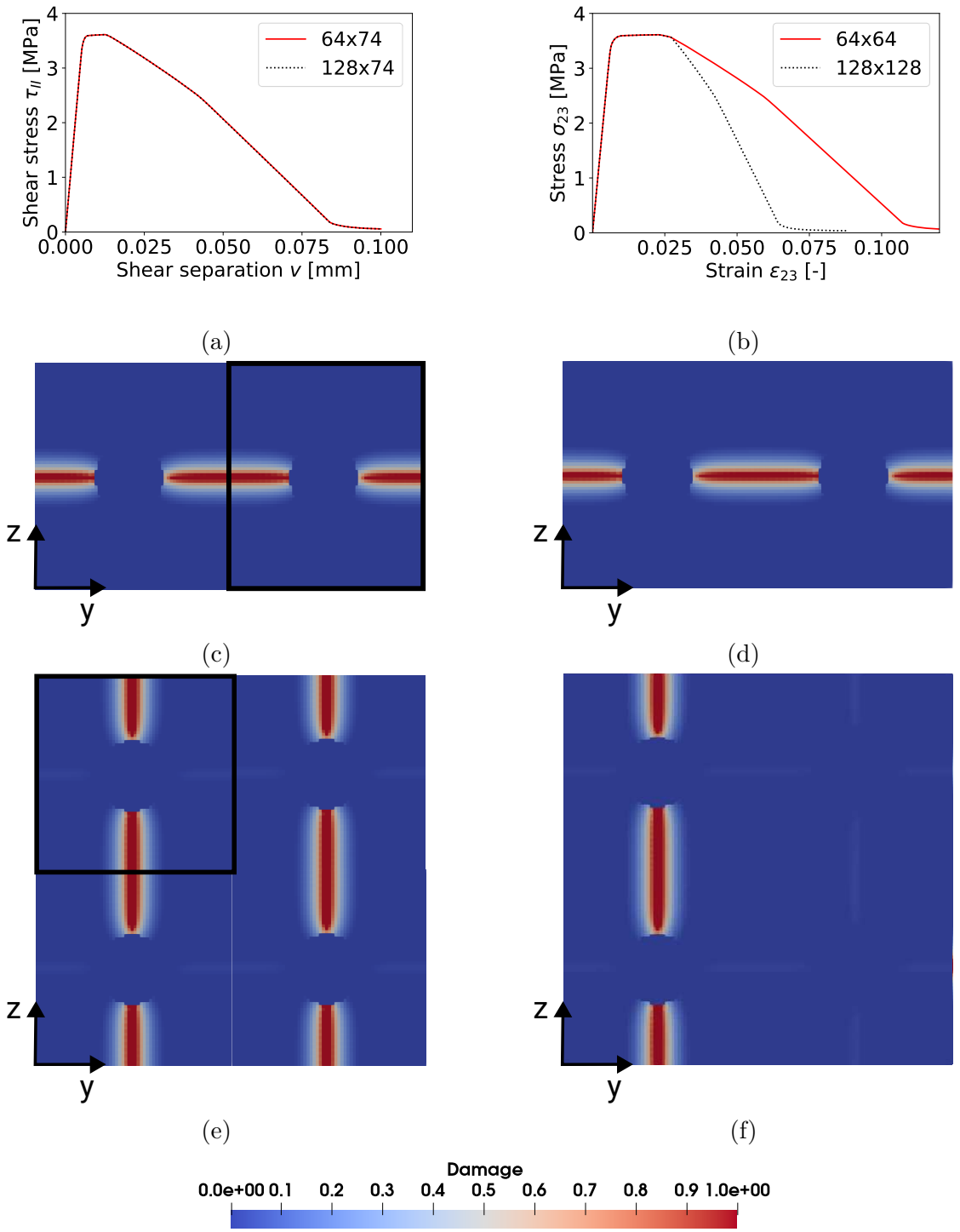

Figure 13: Shear mode II: TSLs of basic virtual model and extended model for cohesive zone approach (a) and stress-strain curves for bulk homogenization (b).; Final damage field of basic virtual model (c) and extended model (d) for cohesive zone approach and of basic virtual model (e) and extended model (f) for bulk homogenization. For comparison, periodic copies are added to the basic model in (c) and (e), where the original basic model is marked with a black frame.

3.3. Estimation of the required marginal layer properties using numerical experiments

3.3.1. Peel mode I

The choice of material parameters and thickness of the marginal layers is critical for an application of the FFT-based homogenization for cohesive zones in the industry. Stiff marginal layers were also used in [133] to eliminate the periodicity of the solution fields and obtain the local mechanical response of a non-periodic composite material. A marginal layer thickness of one voxel was chosen, and the marginal layer stiffness was increased until the mechanical response converged toward an (approximately) unique stress-strain curve. It was observed that the computational times also increased with increasing stiffness. On the one hand, the boundary condition at the cohesive zone interface should be approximated well enough to obtain valid results. On the other hand, the computational times should not increase significantly, and the required effort to identify the parameters of the marginal layers should also be reasonable.

In this section, the effect of the marginal layer thickness on the boundary conditions at the interface and the periodicity of the resulting displacement fields is investigated. The goal is to provide recommendations for applying the novel homogenization method in the industry. Additionally, the effect of the marginal layer stiffness is discussed. For this purpose, FFT-based homogenization for cohesive zones is applied to a representative adhesive layer in order to estimate appropriate parameters. This model is used because computational times for the FFT simulation with the sandwich core are currently too high for a parameter study, and adhesive layers are one of the most prominent applications of CZM.

The virtual RVE for the heterogeneous adhesive layer with typical constituents is shown in Fig. 14a. It consists of a polymer matrix with spherical glass beads as filler and pores that are often induced during the manufacturing process of an adhesive joint. Furthermore, the virtual RVE has a size of $80 \times 80 \times 40$ voxels (without the marginal layers) and is periodic in x- and y-direction. The voxel size is 5 µm and was determined from a mesh convergence study. The diameter of the solid glass beads is 35 µm and the volume fraction was set to 10%. Furthermore, the assumption of spherical pores with a diameter of 42 µm was made. The diameter and the volume fraction of 2.6% were taken from [134], where, among other things, the porosity of epoxy resin-based adhesives was analyzed using a µ-CT scan. As also shown in [134], it can also be assumed that the pores are concentrated at the center of the adhesive layer. Hence, a minimal distance of

60 µm from the layer boundary to the pore center was imposed.

The RVE was generated using an RSA algorithm, as was also discussed in Sec. 1.3.3. The representativeness of the generated RVE for the geometry of the microstructure is ensured by the RSA algorithm, since all assumptions about the characteristics of the microstructure, e.g., size, shape, and volume fractions of pores and glass spheres as well as their distribution within the microstructure, are input parameters. Moreover, the representativeness of the mechanical behavior was verified. For this purpose, virtual models of the microstructure with different sizes were generated, and the resulting TSLs were compared. The TSLs of the RVE and larger models showed a good agreement considering the typical scattering in experimentally determined TSLs. Similarly, a good agreement was also found for five different realizations of the same size, showing the representativeness of the mechanical behavior. This is a typical procedure to determine the size of an RVE, see [41].

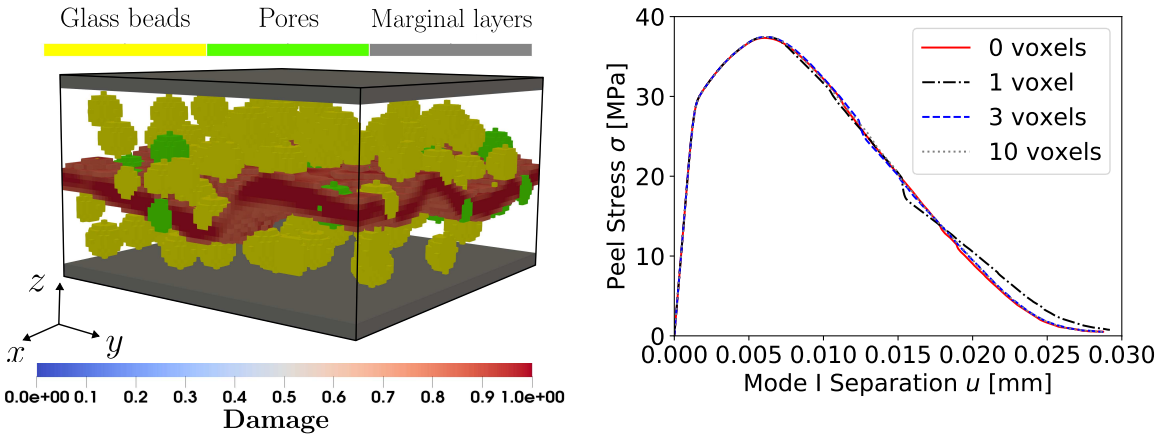

Figure 14: (a) Virtual RVE for the adhesive layer with crack pattern under mode I loading. The polymer matrix is displayed transparently for better clarity; (b) Mode I TSLs for different marginal layer thicknesses.

The linear Drucker-Prager model with non-local ductile damage from Sec. 2.1 was used to describe the mechanical behavior of the polymer matrix, whereas the glass beads were modeled as isotropic, linear elastic. The material parameters used in the simulations are summarized in Tab. 2. The characteristic length parameter was 40 µm, which was determined using numerical experiments, following the same process described for the two-dimensional model in Sec. 3.2. It should be remarked that especially the parameters of the polymer matrix are only assumptions for a typical behavior from laboratory

experience and do not correspond to any existing adhesive. There is also a wide range of adhesives with significantly different mechanical properties available in research and industry, which will not be further addressed.

Table 2: Material parameters used for the polymer matrix, the glass beads (GB), and the marginal layers (ML) in the adhesive.

	E (MPa)	ν (-)	d_0 (MPa)	H (MPa)	ξ (-)	η (-)	$\bar{\eta}$ (-)	p_{nl}^{0} (-)	$p_{\mathrm{nl}}^{\mathrm{f}}$ (-)
Matrix	2000	0.4	40	100	0.577	0.577	0	0.07	0.5
GB	68900	0.21	-	-	-	-	-	-	-
ML	70000	0.33	-	-	-	-	-	-	-

The computational homogenization was carried out for peel mode I considering four different thicknesses of the marginal layers: zero voxels, one voxel, three voxels, and ten voxels. The computational times of the FFT simulation were 5934 s, 6905 s, 7518 s, and 10719 s, respectively. Especially when compared with the typical scattering in experimental results, as, e.g., shown in [92, Figure 16], a good agreement between the resulting TSLs can be observed in Fig. 14b, even if no marginal layer is present. As shown in Fig. 14a, the crack is fully contained within the adhesive layer, which corresponds to a cohesive failure.

In order to further assess the effects of the marginal layer thickness, the displacement fields in z-direction (peel) at the interface of the cohesive zone are shown in Fig. 15, where a mode I separation of 0.023 mm was prescribed. These displacement fields and displacement fluctuations at the interface are the most critical throughout the entire load history. The displacements $\vec{u}$ were computed at each voxel center using the resulting displacement fluctuation field from simulations and the macroscopic (average) displacement gradient of the separation vector $\underline{H}$, which reads

$$\vec{u}\,(\vec{x}\,) = \underline{H} \cdot \vec{x} + \vec{u}^{*}\,(\vec{x}\,) \quad \text{with} \quad \underline{H} = \frac{1}{t_{\mathrm{coh}}} \begin{pmatrix} 0 & 0 & w \\ 0 & 0 & v \\ 0 & 0 & u \end{pmatrix}. \tag{3.16}$$

It can be observed in Fig. 15 that the marginal layer thickness influences the approximation accuracy of the desired Dirichlet-type boundary condition at the interfaces of marginal layers and cohesive zone. Increasing this thickness reduces deviations from the constant displacement field and thus improves the approximation accuracy. In the cases without marginal layer in Fig. 15a and with a thin marginal layer of one voxel thickness in Fig. 15b, the maximum deviations were both on the order of magnitude of about

10^{-4} mm. This value is roughly 100 times smaller than the separation. The effect of the one-voxel-thick marginal layer on the approximation accuracy of the boundary condition is therefore small, which shows that it is too thin.

These deviations for a three-voxel marginal layer thickness and a ten-voxel thickness, presented in Fig. 15c and 15d, were on the order of magnitude of about 10^{-5} mm and 10^{-6} mm, respectively. This is 10^{-3} times smaller than the prescribed separation for the three-voxel case and 10^{-4} times smaller for the ten-voxel case. Thus, a significant effect of the three-voxel-thick marginal layers on the approximation accuracy can already be observed, while the increase in computational time is not as large for the ten-voxel thickness. This indicates that the three-voxel thick layer provides a good compromise between approximation accuracy of the boundary conditions and computational times. Furthermore, it was verified that the difference between the displacements at the upper and the lower interfaces, the separation, generally coincides well with the prescribed separation. This also indicates a sufficiently good approximation of the prescribed separations using the volumetric average strains from Eq. (3.9) in the FFT solver.

Furthermore, the stiffness of the layers was increased by a factor of ten to 700,000 MPa, but the simulations failed to converge within 100,000 iterations. Nevertheless, Fig. 15 already offers information on the error, which is induced by the use of non-infinitely stiff marginal layers. As already mentioned in Sec. 3.1, marginal layers with an infinite stiffness perfectly satisfy the desired Dirichlet-type boundary condition. For an infinite stiffness, the thickness of the layers becomes irrelevant. The deviation of the displacement field at the interface from the prescribed constant separation in Fig. 15 represents the absolute error in the boundary condition and thus the induced error compared with infinitely stiff marginal layers. Accordingly, it is expected that increasing the stiffness reduces the error compared with more compliant layers of the same thickness. This would allow for a reduction in the thickness of the layers while maintaining the same level of accuracy.

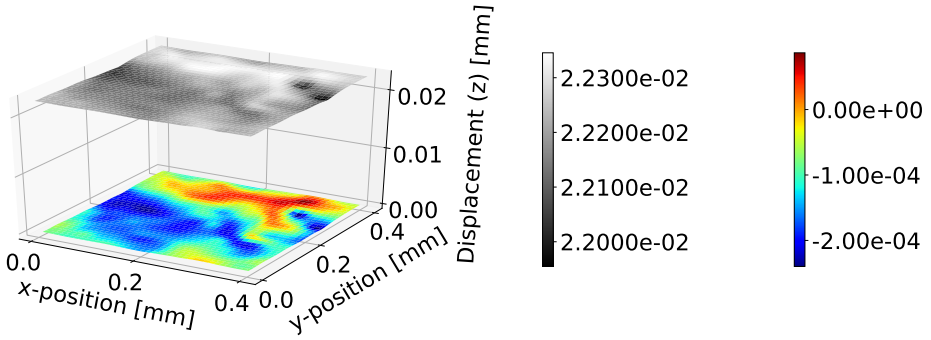

(a)

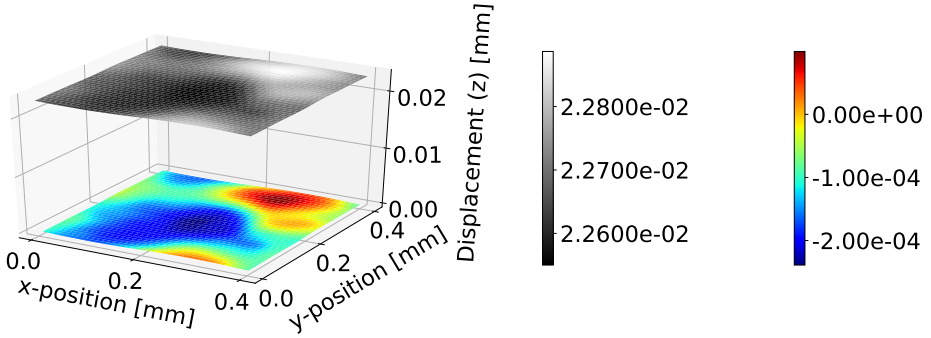

(b)

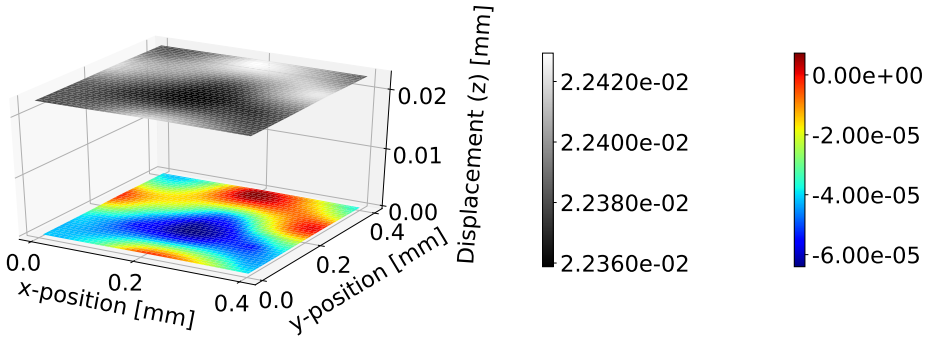

(c)

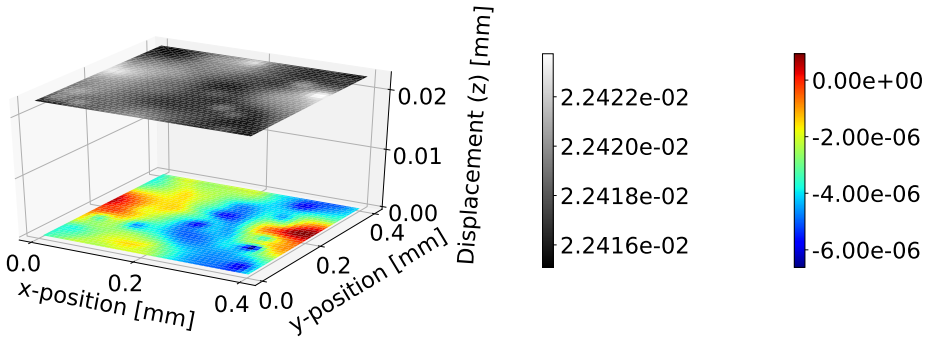

(d)

Figure 15: Displacement fields at the adhesive layer interface in peel mode I without marginal layers (a) and for a marginal layer thickness of (b) one voxel, (c) three voxels, and (d) ten voxels at a peel separation of 0.023 mm.

3.3.2. Shear modes II/III

Besides the study for peel mode I, investigations for the out-of-plane shear mode III were also carried out. However, it is not distinguished between mode II and III owing to the fact that the RVE is (approximately) isotropic in the xy–plane and therefore in shear.

The investigations in shear mode revealed a similarly good agreement between the TSLs in Fig. 16b as in mode I. Only the simulation results without a marginal layer and those with a marginal layer thickness of one voxel show a deviation from the other curves. However, this deviation is still very small when compared with the expected experimental scattering between different measurements using the same adhesive layer and test setup, see, e.g., [92, Figure 16]. Similar trends as in mode I could also be observed for the computational times, which were 11989 s, 5812 s 9797 s, and 13573 s for a marginal layer thickness of zero voxels, one voxel, three voxels, and ten voxels, respectively. Only the computational time for the model without marginal layers was relatively high, which could be caused by the crack location.

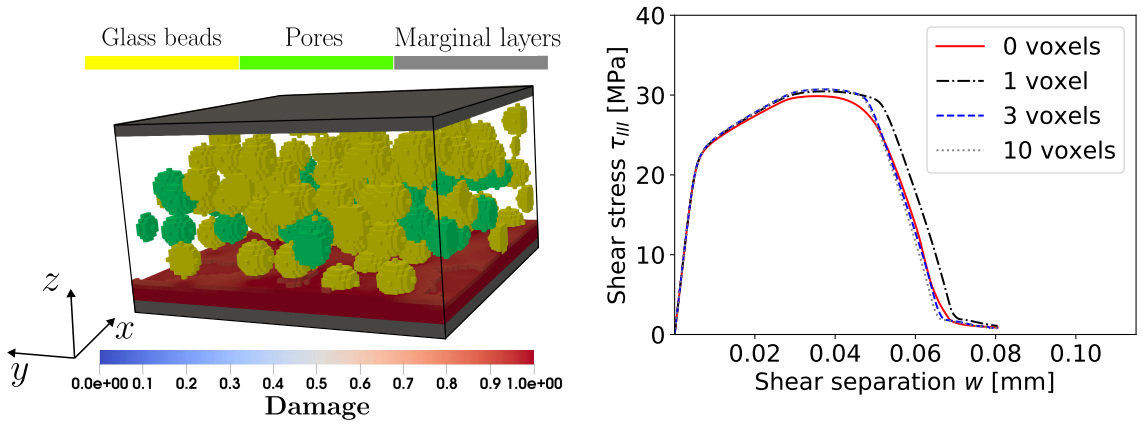

(a) (b)

Figure 16: (a) Virtual RVE for adhesive layer with crack pattern under shear (mode III) loading. The polymer matrix is displayed transparently for better clarity; (b) Shear mode TSLs with different marginal layer thicknesses.

As shown in Fig. 16a, the crack occurred close to the lower interface of the adhesive layer, which corresponds to adhesive failure between the marginal layer and the polymer. Without a marginal layer, the damage field can also propagate through the interface in the z-direction, which represents a completely different model. Hence, the fracture behavior and the computational times cannot be compared straightforwardly to the other cases. The failure at the interface between polymer and marginal layer is usually not

desired but also often observed in experiments in shear mode, even if there is perfectly cohesive fracture in mode I. However, the fracture behavior of an adhesive failure at an interface is usually completely different from the fracture behavior of the bulk. Such a particular fracture model for interface failure at the microscale was not implemented in the model. Hence, the validity of the model in shear mode is questionable from a physical standpoint, and the corresponding results should be interpreted with caution.

Nevertheless, the simulations are purely numerical experiments and are useful to support the observations for mode I. Accordingly, the relevant displacement fields, in this case those in the x-direction, were also investigated regarding the satisfaction of the desired boundary conditions for the cohesive zone. They were computed according to Eq. (3.16) and the results are presented in Figs. 17a, 17b, 17c, and 17d, for the marginal layer thicknesses of zero voxels, one voxel, three voxels, and ten voxels, respectively. The depicted displacement and displacement fluctuation fields at a separation of 0.063 mm were the most critical throughout the entire load history.

Without marginal layers, the typical deviation from the required constant displacement field was approximately one-tenth of the shear separation. This value was reduced to 10^{-2} for a marginal layer thickness of one voxel, which is the same as in mode I. Moreover, for thicknesses of three and ten voxels, it further decreased to 10^{-3}. However, for three voxels, the value is at the upper limit of this order of magnitude, while for ten voxels, it lies in the lower range. As in mode I, it can therefore be concluded that a marginal layer thickness of three voxels is already sufficient, as further increases do not significantly improve the accuracy.

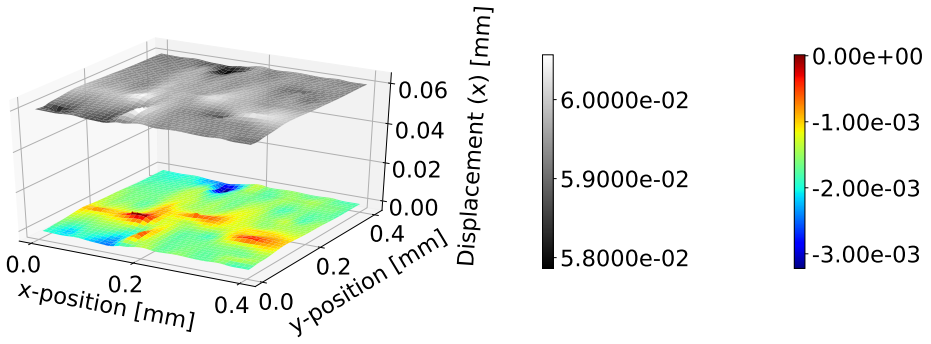

(a)

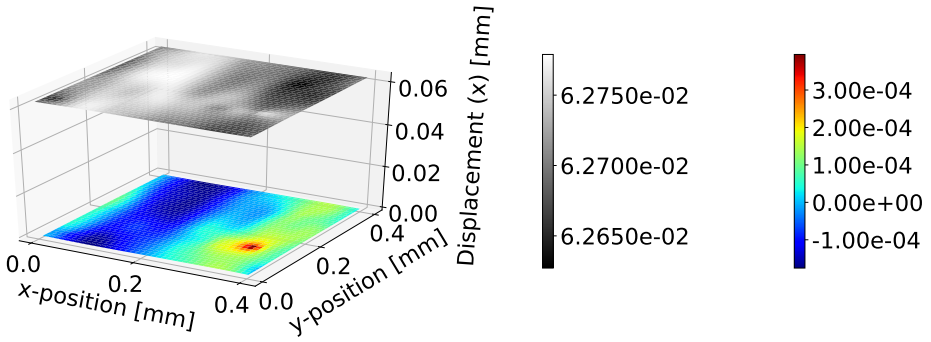

(b)

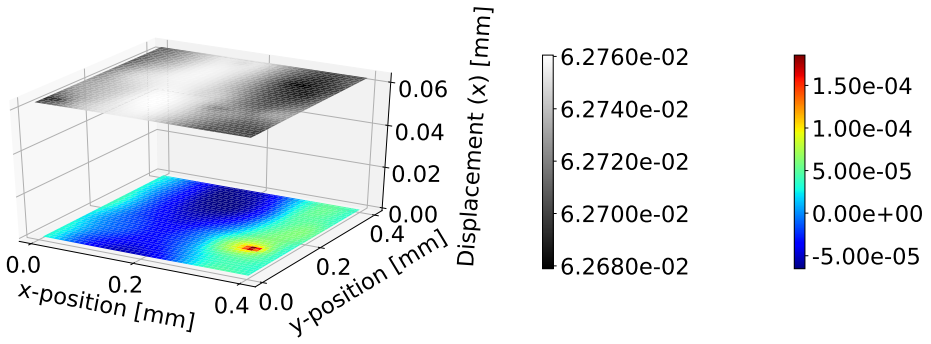

(c)

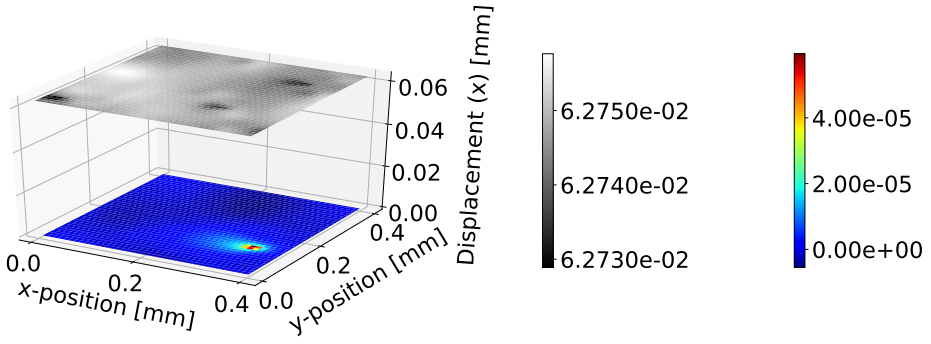

(d)

Figure 17: Displacement fields at the adhesive layer interface in shear mode (III) without marginal layers (a) and for a marginal layer thickness of (b) one voxel, (c) three voxels, and (d) ten voxels at a shear separation of 0.063 mm.

3.3.3. Discussion and recommendations for the parameter estimation

The observations from the previous simulations of the adhesive can now be used to derive recommendations for the estimation of appropriate parameters of the marginal layers.

First, one may argue that the marginal layers are not necessary based on the good agreement between all resulting TSLs in shear and peel. However, apart from approximating the desired Dirichlet-type boundary conditions from Eq. (3.10), they also ensure that the (global) direction of crack extension is parallel to them. This is required to be consistent with the macroscopic crack plane of the cohesive zone, as discussed in Sec. 3.2. The results also indicate that the thickness of three voxels or 15% of the material layer thickness is sufficient with the given linear elastic, isotropic material parameters, which are typical for aluminum. This is a commonly used material for adherends.

Based on these findings, it is recommended to use the elastic material parameters of the adherends, or the surrounding bulk in the case of other material layers that are not adhesives, as a starting point for an industrial application of the proposed method. First, the process of optimizing the parameters toward the best compromise between computational time and accuracy may be very time-consuming, depending on the computational times of the simulations. Second, the approach considers that even in real material layers, the displacement field at the interfaces of the cohesive zone and the surrounding bulk material is not exactly constant from a physical standpoint. Therefore, more realistic fields are obtained if these material parameters are selected for the marginal layers.

A marginal layer thickness of approximately 15% of the material layer thickness is suggested as an initial estimate, based on the findings for the adhesive. However, the results cannot generally be extended to other material layers. Thus, it should be checked if the Dirichlet-type boundary conditions are satisfied with sufficient accuracy by analyzing the corresponding displacement fields for each simulation as in Figs. 15 and 17. Then, the thickness and/or stiffness can be increased if the achieved accuracy with the initially estimated parameters is not sufficient. The simulations also showed that, if possible, an increase in thickness is preferable to an increase in stiffness, as a higher stiffness led to convergence problems.

Furthermore, it is also recommended to check if the Hill-Mandel condition holds with sufficient accuracy in each simulation. This condition is significantly influenced by modifying the boundary conditions of the material layer using the marginal layers, see Sec. 3.1. However, care must be taken in the interpretation of the results. Only investigating the Hill-Mandel condition without checking the displacement fields is not sufficient to

evaluate the accuracy of the boundary conditions, because the Hill-Mandel condition is also satisfied by the periodic boundary conditions without marginal layers. If the Hill-Mandel condition is not satisfied sufficiently by the initially estimated parameters, increasing the stiffness and/or thickness of the marginal layers nevertheless improves this accuracy. This improvement arises since the accuracy of the desired boundary conditions, for which it could be shown in Sec. 3.1 that the Hill-Mandel condition holds, is also increased. Note that the corresponding analysis was also carried out for the adhesive layers and the condition was satisfied in all simulations.

Moreover, care has to be taken if the stiffnesses of the material layer and the surrounding bulk material are on the same order of magnitude or if the latter is more compliant. Then, the boundary conditions cannot be approximated sufficiently. In addition, even the influence of the local fields at the microscale on the macroscopic fields in the vicinity of the material layer should be examined, which requires further research. Despite the fact that there may be some special exceptions, this case is expected to be rather unlikely in industrial applications. If it does occur, CZM would not be well-suited for most cases, as in-plane loads are neglected in CZM and are therefore expected to be small in the material layer compared with the surrounding bulk.

4. Virtual model of the microstructure of the sandwich core

4.1. Experimental characterization of the microstructure of the sandwich core

In this section, the generation of the virtual model of the microstructure for the Hybrix™ sandwich core is presented. As discussed in Sec. 1.3.3 on the state of the art in the generation of virtual models of a microstructure, these models are usually developed based on an experimental characterization of the microstructure. This characterization is typically performed using µ-CT scans and microscopy. Both methods were also applied to the sandwich core.

The configuration of the metal plates used in this study consists of aluminum face sheets with a thickness of 0.5 mm each and the core with a thickness of 1.5 mm, see also Sec. 1.1. For the experimental characterization of the microstructure, microscopy was used to determine the fiber diameter, the fiber length, the volume fraction of the fibers, and the fiber orientation. These parameters also serve as input to the model of the fiber

structure. Apart from the fiber orientation, which is linked to the other parameters in the next Sec. 4.2.1, they are all production parameters for the plates as well, see also Sec. 1.2.

The fiber length was determined to be 2 mm by extracting a fiber from the sandwich core and measuring it using an Olympus Stereomicroscope SZH 10 (Olympus Corporation, Hachioji, Tokyo, Japan). Furthermore, micrographs in the xy–plane at two different positions were taken for the determination of the other parameters. Position 1 is close to the face sheet, referred to as the "top face sheet", and position 2 is located near the "bottom face sheet", as shown in Fig. 18. This distinction between the face sheets is necessary because the microstructure is not homogeneous in the through-thickness direction z, which will become clear at the end of this section. The two positions are sufficient for the experimental characterization, since the idea behind the plates is that the fibers connect the face sheets. The binder should only bond the fibers to the face sheets and to one another in the vicinity of the face sheets.

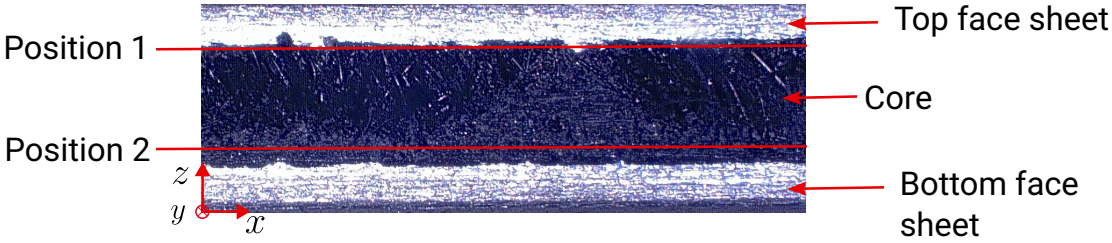

Figure 18: Cross section of a Hybrix^{TM} plate with a core thickness of 1.5 mm and 0.5 mm thick aluminum face sheets, including a schematic illustration of the positions of the micrographs taken.

In order to obtain the micrographs, a small specimen was cut and embedded into microscopy resin using a vacuum infusion technique. The vacuum infusion is needed owing to the high porosity of the sandwich core. The polishing process can cause defects in the free fiber segments, which are not fully embedded in binder. Starting from the top face sheet, the specimen was ground in (negative) through-thickness direction z until the intended position within the core was reached. The surface was then polished following standard procedures, see [135, pp.143-146]. Correspondingly, position 1 was at a distance of about 0.03 mm from the top face sheet and position 2 at a distance of about 0.15 mm from the bottom one. Both values were determined by measurements of the thickness of the sample with a standard caliper and the known face sheet thickness and core thickness.

Positions 1 and 2 were selected to ensure that all fibers at the face sheets were captured by the microscopy. Furthermore, position 2 was set to 0.15 mm from the face sheet

because specimens at this location were also used for microindentation experiments in the parameter identification of the material models, see Sec. 5. The use of micrographs ensures that the composition of the investigated surface is known, which prevents the inclusion of microscopy resin in the measurements.

The microindentations were carried out at position 2 owing to the fact that, unlike position 2, the surface at position 1 mainly consisted of microscopy resin and only a small amount of fibers and binder. Furthermore, the microscopy resin could not completely fill the core despite the application of vacuum infusion. In the microindentation, these pores could lead to an unstable substrate beyond the indentation and therefore to incorrect measurement results. Accordingly, the grinding process for position 2 was performed in the negative z-direction from the top to the bottom face sheet, such that only a small layer of the core remained. However, as discussed in detail in Sec. 5.1, the maximum indentation depth should be limited to a tenth of a characteristic length of the microstructure, which is 50 µm. The thickness of the remaining layer of the core should also be larger than this characteristic length, since the layer thickness would otherwise act as this characteristic length. Hence, the layer thickness was chosen as 0.15 mm in order to have some additional safety in the case of small variations of the core thickness and in the production of the specimens.

Each of the obtained micrographs has a size of 2048 × 1536 pixels or 2.38 × 1.78 mm at position 1 and 1.59 × 1.19 mm at position 2, respectively. Magnifications of 20x and 30x were used. The overall surface area investigated was 41.0 mm^2 for position 1 and 24.3 mm^2 for position 2. A typical micrograph is shown in Fig. 19a. The fibers were then separated from the rest of the image based on the gray values of the pixels according to standard image processing methods [54, pp.129-156] using the Python package OpenCV [136]. Smaller subsamples of varying sizes were extracted from all micrographs to ensure that a sufficient number of micrographs was investigated for statistical significance. The analysis of these subsamples confirmed that the number of observed fibers was adequate.

The identified fibers from the exemplary micrograph Fig. 19a are marked with red ellipses in Fig. 19b. The fitted ellipses were then used to determine the fiber diameter. For this purpose, the assumption of a circular fiber cross section was made, such that the minor axis of the ellipse corresponds to the fiber diameter. The length of the major axis of the ellipse is then determined by the fiber orientation with respect to the z-axis. The (mean) fiber diameter was found to be 50 µm.

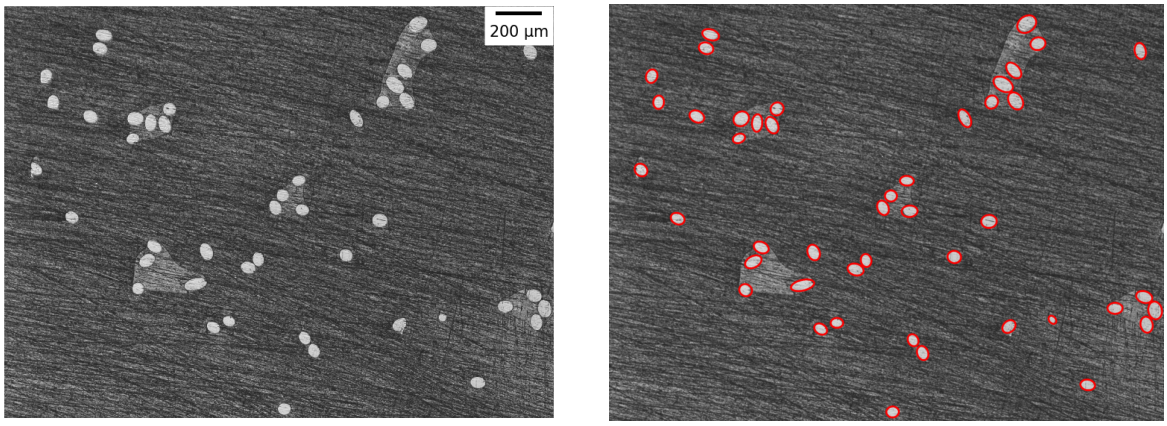

(a) (b)

Figure 19: (a) Typical micrograph of the Hybrix^{TM} core and (b) ellipses fitted to the identified fibers.

Furthermore, it was also found that the surface area of the observed ellipses in the micrographs is the smallest for those that have the highest aspect ratio. This aspect ratio is defined as the length of the minor axis divided by the length of the major axis. Here, the highest possible aspect ratio of one indicates a circular fiber cross section. The corresponding data is presented in Fig. 20. Note that lower aspect ratios, and consequently larger ellipse areas, occur at position 2. This is due to the greater orientation angles compared with position 1, as discussed in the following paragraphs. Since the surface area of a fiber in the micrograph is the smallest when aligned with the z-axis, the highest aspect ratio corresponds to fibers in this direction. Hence, a circular cross section can be attributed to fibers oriented along the z-axis. Accordingly, it can be concluded that the assumption of a circular cross section holds.

The confirmation of this assumption was then used to estimate the fiber volume fraction. For this purpose, the volume of a single fiber can be computed with the known radius of the circular cross section and the also known fiber length. This calculation results in a fiber volume fraction of 4% at position 1 and 13% at position 2. This difference can be explained by the fact that many fibers do not connect both face sheets and therefore are only present at the bottom face sheet at position 2. This observation demonstrates that the sandwich core is inhomogeneous in the through-thickness direction.

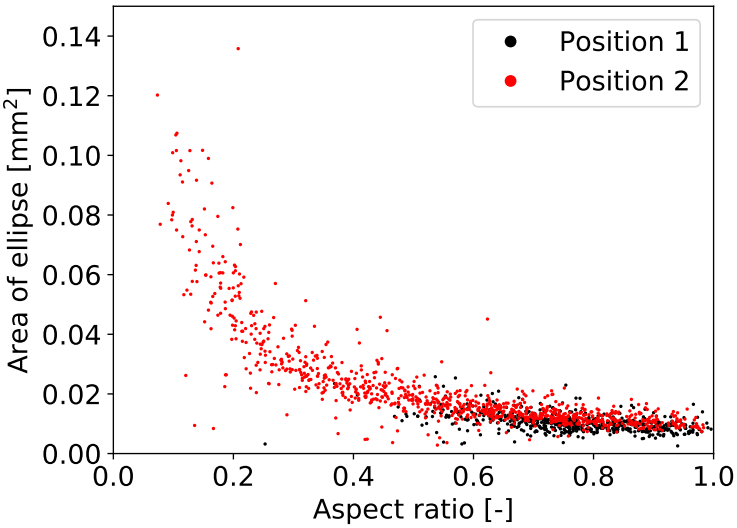

Figure 20: Area of the ellipses fitted to the observed fibers in the micrographs versus their aspect ratio.

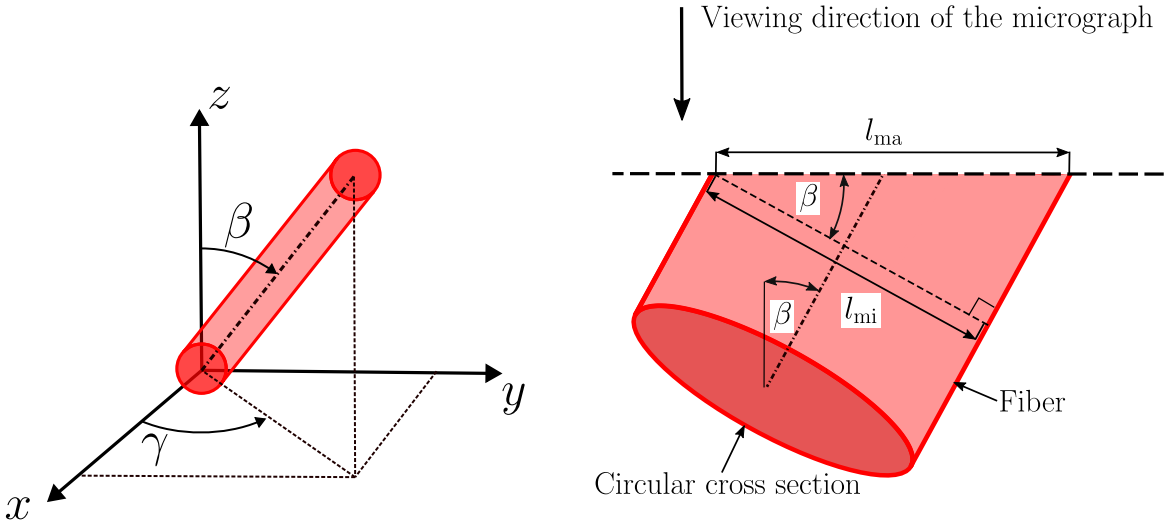

(a) (b)

Figure 21: (a) Scheme of the orientation of a fiber segment.; (b) Schematic illustration of the method of ellipses.

Following [54, pp.199-204], the method of ellipses for fibers with circular cross sections was used to obtain the fiber orientation in the next step. A scheme of the fiber orientation with the orientation angle γ between the fiber and the x-axis, and the orientation angle β between the fiber and the z-axis is shown in Fig. 21a. Moreover, Fig. 21b depicts a scheme of the method of ellipses. It is exploited that the intersection angle of a cylinder

with a cutting plane can be computed by means of the resulting ellipse. According to this model, β is obtained by

$$\cos\beta = \frac{l_{\mathrm{mi}}}{l_{\mathrm{ma}}}. \tag{4.1}$$

l_{mi} and l_{ma} represent the length of the minor and major axis of the corresponding ellipse in the micrograph, respectively. The resulting probability density function (PDF) and cumulative distribution function (CDF) of β are depicted in Figs. 22a and 22b. The curves for position 1 are relative to those for position 2. If all fibers with a length of l_{fib} had been straight and had connected both face sheets (or positions), they would have had an orientation angle of $\beta_{\mathrm{str}} = \cos^{-1}(t_{\mathrm{coh}}/l_{\mathrm{fib}}) = 41°$. At this value, the maximum of the PDF is also approximately located. Therefore, fibers with smaller orientation angles are expected to be curved, whereas fibers with larger orientation angles likely do not connect both face sheets. The latter have one end close to position 2 and the other one somewhere between position 1 and 2. Furthermore, the angle γ is not evaluated owing to the fact that no information was available on the orientation in the xy-plane during the production process of the plates.

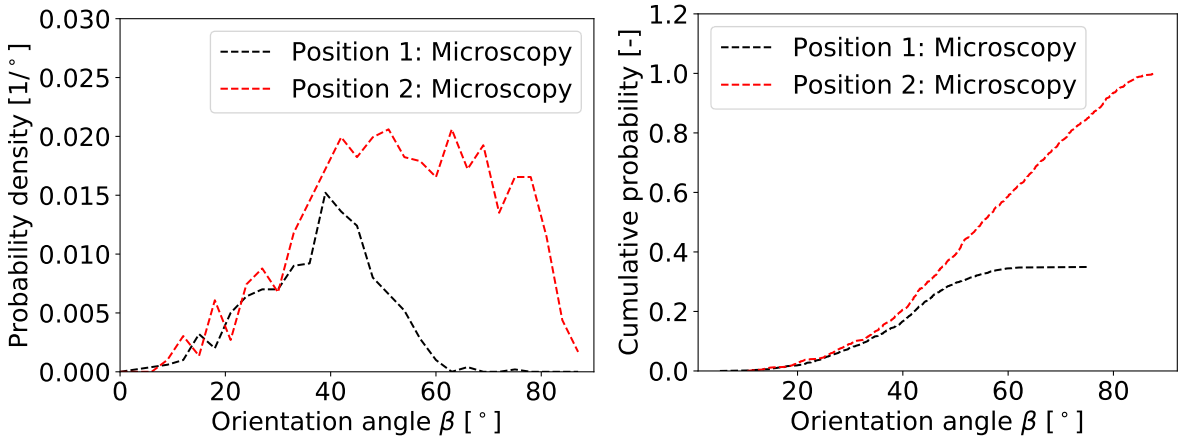

(a) (b)

Figure 22: PDF (a) and CDF (b) for the orientation angle β from microscopy at z-positions 1 and 2.

In addition to the microscopy, a µ-CT scan was performed with a small specimen of the plate using a TomoScope® XS (Werth Messtechnik GmbH, Gießen, Germany). The scan produces a three-dimensional gray value image of the specimen. Standard three-dimensional image processing methods [55, pp.79-148] were then used to segment the image into the constituents of the core. The gray value contrast between fibers and

binder was not significant enough for a successful segmentation. Nevertheless, it was possible to distinguish the porosity from fibers and binder.

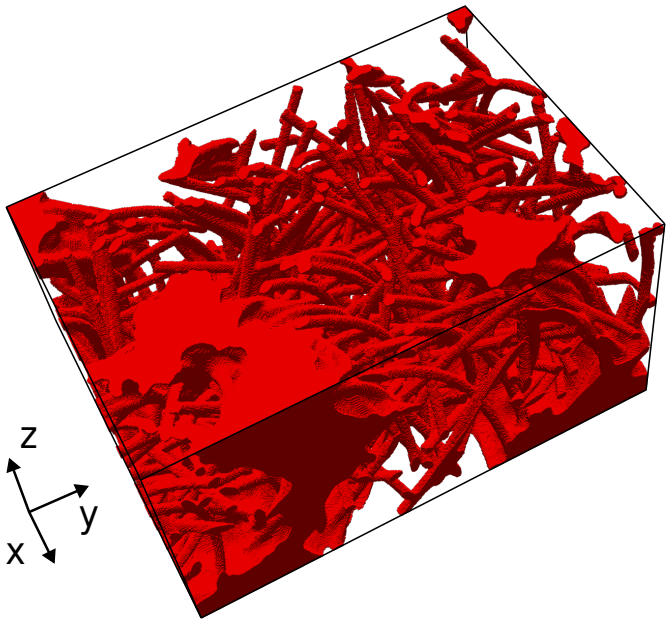

Figure 23: Fibers and binder (red) in the segmented µ-CT scan of the Hybrix^{TM} core.

The segmented scan is presented in Fig. 23, where fibers and binder are shown in red and the pore space is transparent. The free fiber segments reveal that the fibers are significantly curved, as it was also expected based on the analysis of the orientation angle β. Furthermore, a concentration of fibers and binder can be observed in the xy-plane at low z values, which corresponds to position 2. In contrast, only a small amount of fibers and binder is observed at high values of z, which corresponds to position 1. These observations also coincide qualitatively well with the observed inhomogeneity of the estimated fiber volume fractions from microscopy.

Moreover, the segmented scan was used to determine the binder volume fraction. The porosity was found to be at about 65%, which leaves a volume fraction of 35% for fibers and binder. With the known fiber volume fraction of 13%, the binder volume fraction was therefore estimated to be 22%. Furthermore, a thin layer of binder at the interface of the face sheet near position 1 is expected to connect the fibers to the face sheet, but it does not appear in the segmented scan. This can be explained by the fact that the interface between the top face sheet and the core was blurred in the gray value image and could not be segmented properly.

4.2. Generation of the virtual model of the microstructure

4.2.1. Generation of the fiber structure

Based on the experimental observations, an algorithm for the generation of virtual models of the microstructure was developed. It is also ensured that the generated virtual model of the microstructure is periodic within the cohesive zone to be in accordance with the corresponding periodic boundary conditions in Eq. (3.10).

Following the principal ideas of the literature discussed in the last paragraph of Sec. 1.3.3, the fiber structure is created using a CRA by minimizing an objective function, whose detailed construction is discussed below. Furthermore, four key requirements are considered with the purpose of getting a realistic model of the fiber structure:

- The fibers are curved.
- Fiber orientation and volume fraction should match the results from microscopy.
- The overlap between all fibers should be avoided or at least be as small as possible.
- The fibers should not exceed the domain boundaries of the cohesive zone in through-thickness direction.

The first and the second points arise from the observations of the previous Sec. 4.1. The third and fourth points emerge owing to the fact that large overlaps between the fibers and between fibers and the face sheets are unphysical.

The fibers are geometrically modeled as cylinders, where each fiber is divided into 20 segments with an equal length of $l_{\mathrm{seg}} = 0.1$ mm. Each of the cylindrical segments is mathematically described by its central line segment, also referred to as "axis of a cylinder". It connects the center points of the circular bases and is orthogonal to them. These center points of the circular bases are referred to as "segment end points" in the following.

Fig. 24 shows the geometric model of a fiber i, which only has three segments instead of 20 for the sake of clarity. In general, the relative angles between the segments j and $j+1$, β_{ij}^{r} and γ_{ij}^{r}, allow for the consideration of fiber curvature in the model, which is also demonstrated for segments 1 to 3 in the figure. β_{i1}^{r} is the orientation angle between segment 2 and the z_1-axis of the local coordinate system of segment 1. γ_{i1}^{r} is the orientation angle between segment 2 and the local x_1-axis. The relative orientations of segment 3 with respect to the local coordinate system of segment 2 are defined correspondingly. Apart from these relative angles and the given segment length,

the global angles of the bottom segment 1, β_i^{b} and γ_i^{b}, the position of the bottom end point $\vec{x}_i^{\mathrm{b}}$ as well as the fiber radius r_{fib} are assigned to each fiber i.

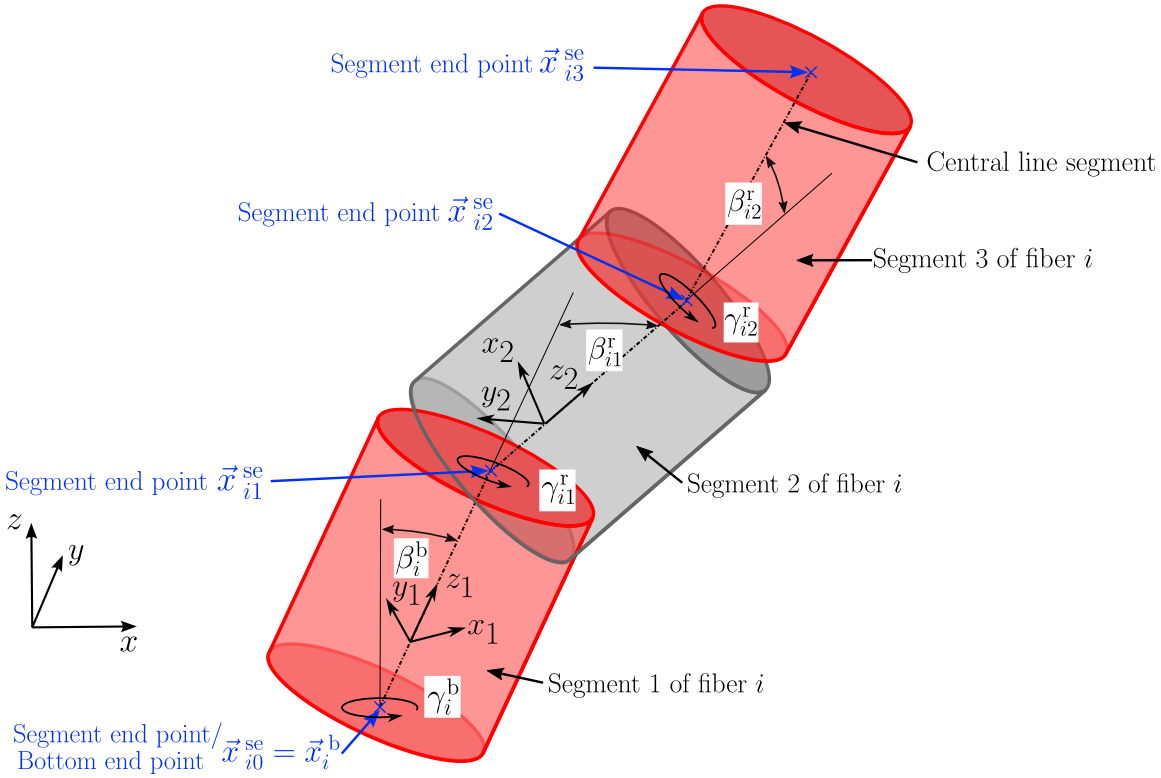

Figure 24: Scheme of the geometrical model of an exemplary fiber i with three segments.

The bottom end point of each fiber is used as the base point for its geometrical description, as it is usually the closest point to the bottom face sheet/position 2. Only at this position, the correct fiber volume fraction and, hence, the required number of fibers in the model are known. Following the same argument, the observed distribution of the fiber orientation angle β is also applied to the bottom segment of each fiber. Accordingly, the global angles β_i^{b} and γ_i^{b} are assigned to these segments. All points on the central line segments and also the global orientation angles of each fiber segment can be computed with the above parameters. Hence, the segment end points are sufficient for a full geometrical description of the fibers.

The segment end point of each segment j of fiber i on the central line segment can be

computed as

$$\vec{x}_{ij}^{\,\mathrm{se}} = \begin{cases} \vec{x}_i^{\,\mathrm{b}}, & \text{for } j = 0 \\ \vec{x}_i^{\,\mathrm{b}} + l_{\mathrm{seg}}\, \underline{R}_{\gamma_i^{\mathrm{b}}} \cdot \underline{R}_{\beta_i^{\mathrm{b}}} \cdot (0 \;\; 0 \;\; 1)^{\mathrm{T}}, & \text{for } j = 1 \\ \vec{x}_{i(j-1)}^{\,\mathrm{se}} + l_{\mathrm{seg}} \left(\underline{R}_{\gamma_i^{\mathrm{b}}} \cdot \underline{R}_{\beta_i^{\mathrm{b}}} \cdot \prod_{k=1}^{j-1} \left[\underline{R}_{\gamma_{ik}^{\mathrm{r}}} \cdot \underline{R}_{\beta_{ik}^{\mathrm{r}}} \right] \cdot \begin{pmatrix} 0 \\ 0 \\ 1 \end{pmatrix} \right), & \text{else} \end{cases} \tag{4.2}$$

in the global coordinate system. The parentheses around the entries in the index are used to clarify to which index the corresponding mathematical operations belong. Here, i represents the first index and $(j-1)$ the second one. The first line of Eq. (4.2) is the first segment end point of the bottom segment 1, and corresponds to the bottom end point of a fiber. Furthermore, the second segment end point is computed in the second line of Eq. (4.2). The segment, which is initially oriented in the z-direction, is first rotated around the global y-axis by β_i^{b}. Then, it is rotated around the global z-axis by γ_i^{b}. Here, $\underline{R}_{\beta_i^{\mathrm{b}}}$ and $\underline{R}_{\gamma_i^{\mathrm{b}}}$ represent the corresponding standard rotation matrices.

Similarly, all other segment end points are calculated, as described in the third line of Eq. (4.2). The cumulative product from $k = 1$ to $j - 1$ arises from the fact that the rotation angles β_{ik}^{r} and γ_{ik}^{r} are defined in the local coordinate system of the corresponding fiber segment. Therefore, the multiplication of $\underline{R}_{\beta_{i(j-1)}^{\mathrm{r}}}$ and $\underline{R}_{\gamma_{i(j-1)}^{\mathrm{r}}}$ with the initial orientation vector $(0 \;\; 0 \;\; 1)^{\mathrm{T}}$ yields the orientation vector of the segment j in the local coordinate system of segment $j - 1$. $\underline{R}_{\beta_{ik}^{\mathrm{r}}}$ and $\underline{R}_{\gamma_{ik}^{\mathrm{r}}}$ represent the standard rotation matrices around the local y-axis with angle β_{ik}^{r} and the local z-axis with angle γ_{ik}^{r}. The obtained orientation vector of the segment then needs to be transformed into the global coordinate system. This is achieved through multiplication by the relative transformation matrices of all previous segments k, $\underline{R}_{\gamma_{ik}^{\mathrm{r}}} \cdot \underline{R}_{\beta_{ik}^{\mathrm{r}}}$, and the global transformation matrices $\underline{R}_{\gamma_i^{\mathrm{b}}}$ and $\underline{R}_{\beta_i^{\mathrm{b}}}$. To obtain the desired segment end point, the global orientation vector from this computation is multiplied by the segment length and then added to the position vector of the previous segment end point.

Each point on the central line segment can be calculated from the segment end points by

$$\vec{x}_{ij}^{\,\mathrm{cs}}(s) = \vec{x}_{i(j-1)}^{\,\mathrm{se}} + s \left(\vec{x}_{ij}^{\,\mathrm{se}} - \vec{x}_{i(j-1)}^{\,\mathrm{se}} \right) \text{ with } s \in [0, 1], \tag{4.3}$$

since each central line segment is a straight line from a geometrical standpoint.

In the next part of this work, the construction of the objective function for the

optimization problem is discussed. Despite the fact that the fiber curvature is intended, from a physical point of view, the fibers are expected to be straight initially. Hence, elastic energy is needed to bend the fibers during the production process. A penalty for fiber curvature is added to the objective function, which is of a similar type to the overlap between two fibers. Following the trigonometric considerations presented in Fig. 25, this overlap between two neighboring fiber segments j and $j+1$ of fiber i is calculated according to

$$\delta_{ij}^{\mathrm{c}} = r_{\mathrm{fib}} \sin\left(\beta_{ij}^{\mathrm{r}}\right), \tag{4.4}$$

where r_{fib} is the radius of the fiber cross section.

Then, the corresponding part in the objective function is determined by forming the sum of these squared overlaps of all segments and fibers

$$f_{\mathrm{c}}\left(\beta^{\mathrm{r}}\right) = \frac{1}{2} \sum_{i=1}^{n_{\mathrm{fib}}} \sum_{j=1}^{n_{\mathrm{seg}}-1} \left(\delta_{ij}^{\mathrm{c}}\right)^2. \tag{4.5}$$

n_{fib} and n_{seg} denote the number of fibers and segments, respectively.

The square ensures that the function is continuously differentiable and could also potentially be used in gradient-based optimization methods. The factor $\frac{1}{2}$ then would yield a more compact form of the gradient by eliminating the factor two in the derivative. Similar formulations for the individual parts of the objective functions were also proposed by other authors in the literature for the same reasons, see e.g. [66–68]. Moreover, the dependent variables in the contribution to the objective function f_{c} are summarized as

$$\beta^{\mathrm{r}} = \left(\beta_{11}^{\mathrm{r}}, ..., \beta_{n_{\mathrm{fib}}1}^{\mathrm{r}}, ..., \beta_{n_{\mathrm{fib}}(n_{seg}-1)}^{\mathrm{r}}\right). \tag{4.6}$$

The n-tuple β^{r} includes all orientation angles β_{ij}^{r} for all fibers i and segments j.

Additionally, a model for the distribution of the orientation angle β and a consideration in the objective function of the optimization problem are needed to match the desired experimentally determined distribution. The PDF for β_i^{b} is modeled by a triangular distribution from its limits of 0° to $\beta_{\max} = 90°$ with the maximum at β_{str}. It is given by

$$PDF_{\mathrm{m}}(\beta) = \begin{cases} \dfrac{2\beta}{\beta_{\max}\,\beta_{\mathrm{str}}}, & \text{for } \beta \leq \beta_{\mathrm{str}} \\ \dfrac{2\,(\,\beta_{\max} - \beta\,)}{\beta_{\max}\,(\,\beta_{\max} - \beta_{\mathrm{str}}\,)}, & \text{for } \beta_{\mathrm{str}} < \beta < \beta_{\max}. \end{cases} \tag{4.7}$$

The corresponding model PDF is also shown in Fig. 26 in comparison with the experi-

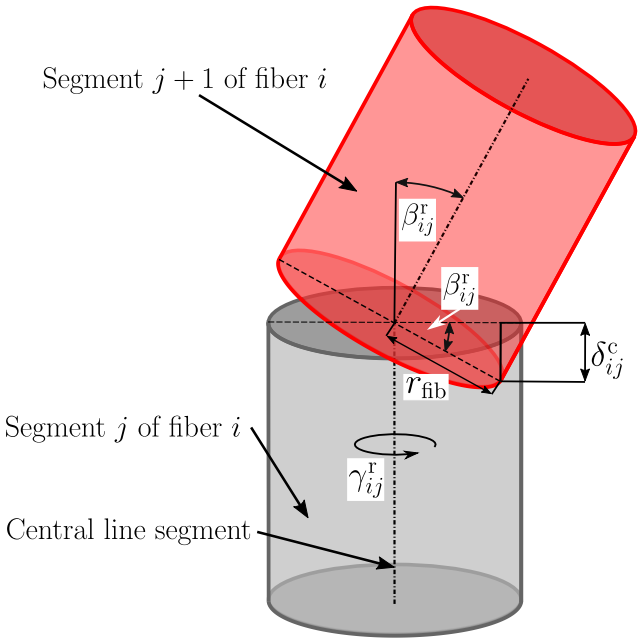

Figure 25: Overlap between two fiber segments through fiber curvature.

mental data from microscopy. The CDF of the triangular model then yields

$$CDF_{\mathrm{m}}(\beta) = \begin{cases} \dfrac{\beta^2}{\beta_{\max}\,\beta_{\mathrm{str}}}, & \text{for } \beta \leq \beta_{\mathrm{str}} \\ 1 - \dfrac{2\,(\beta_{\max} - \beta)^2}{\beta_{\max}\,(\beta_{\max} - \beta_{\mathrm{str}})}, & \text{for } \beta_{\mathrm{str}} < \beta < \beta_{\max}. \end{cases} \tag{4.8}$$

As it was already discussed above, $\beta_{\mathrm{str}} = \cos^{-1}(t_{\mathrm{coh}}/l_{\mathrm{fib}}) = 41°$ presents the orientation angle for a straight fiber connecting both face sheets. This is the preferred and most likely state of a fiber from an energetic standpoint.

Furthermore, an alternative model PDF with a different shape was tested. This function increases linearly from 0° to β_{str} and remains constant from β_{str} to 90°. However, the triangular model provided the best agreement with the experimental results.

At first glance, this result may seem counterintuitive, since the initially linear and then constant model appears to better match the experimentally determined distribution. However, the triangular distribution is prescribed at the bottom segment and, for some fibers, this segment can be located below position 2, where β is evaluated in the microscopy. Hence, the triangular model can deviate from the experimentally determined distribution of β and still lead to a good agreement between the microscopy and the virtual model of the microstructure, as demonstrated in Sec. 4.3.1.

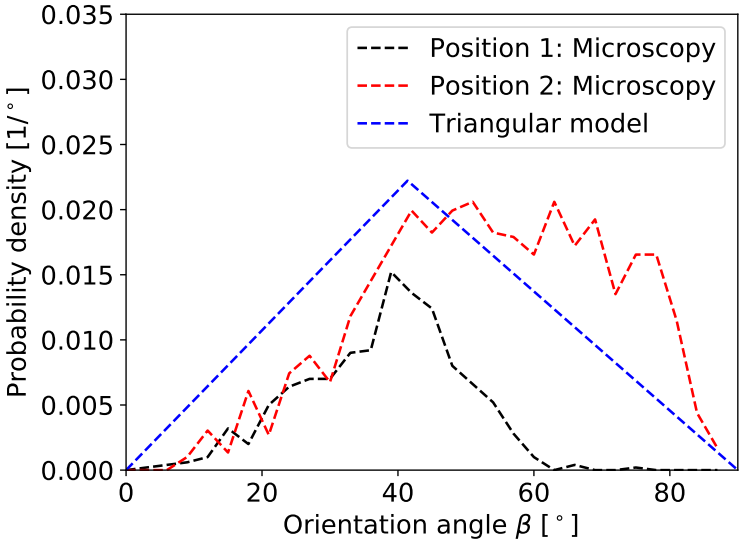

Figure 26: Triangular model distribution for the orientation angle β compared with the resulting PDFs from microscopy at z-positions 1 and 2.

Moreover, the empirical CDF of the fibers in the generated fiber structure can be computed as

$$CDF_{\mathrm{emp}}(\beta) = \frac{1}{n_{\mathrm{fib}}} \sum_{i=1}^{n_{\mathrm{fib}}} I\left(\beta_{\mathrm{i}}^{\mathrm{b}} \leq \beta\right). \tag{4.9}$$

$I(\bullet)$ denotes the indicator function, which is one if the statement in the argument of the function is true and zero otherwise.

In the objective function, the empirical CDF_{emp} is compared with the model one, CDF_{m}, using the mean squared error

$$MSE_{\beta} = \frac{1}{n_{\mathrm{fib}}} \sum_{i=1}^{n_{\mathrm{fib}}} \left[CDF_{\mathrm{emp}}\left(\beta_i^{\mathrm{b}}\right) - CDF_{\mathrm{m}}\left(\beta_i^{\mathrm{b}}\right)\right]^2. \tag{4.10}$$

Furthermore, the angle γ_i^{b} of each fiber i is assumed to be arbitrary in the model, since there was no information available on how to link the orientation in the xy-plane to the production process of the plates. Nonetheless, the microstructure can be regarded as isotropic in the xy-plane, considering a reasonable tolerance. This is demonstrated in detail in Sec. 4.3.5.

In the next step, the contribution of the overlap between the fibers to the objective function is described. In order to compute this overlap, the shortest distance between the central line segments is used. For the computation of this distance $\Delta_{ijkl}^{\mathrm{fib\_fib}}$ between the central line segments of segment j of fiber i and segment l of fiber k, the geometrical

method presented in [137, 138] is applied. The method is described in detail in Appendix A.

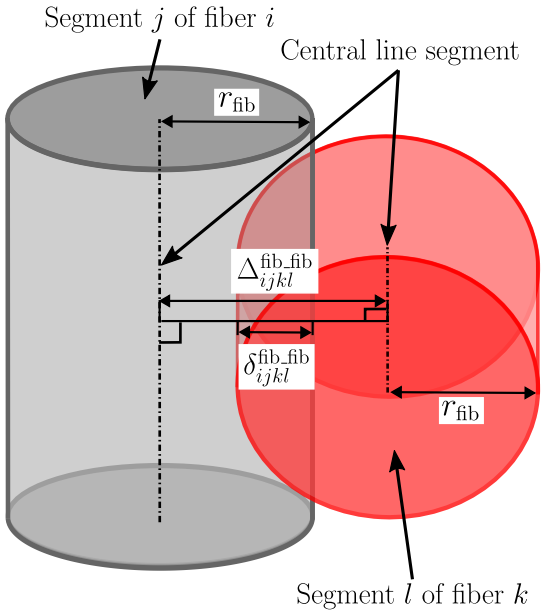

Figure 27: Overlap between two fiber segments of different fibers.

Then, the overlap can be calculated according to

$$\delta_{ijkl}^{\mathrm{fib\_fib}} = \max\left(0, -\Delta_{ijkl}^{\mathrm{fib\_fib}} + 2r_{\mathrm{fib}}\right) \quad \text{for} \quad i \neq k, \tag{4.11}$$

which is also schematically displayed in Fig. 27. No overlap occurs, if $\Delta_{ijkl}^{\mathrm{fib\_fib}}$ is larger than the sum of the fiber radii. Actually, the equation was developed for sphero-cylindrical fibers with spherical fiber ends. However, in the model, the fibers have flat ends. Therefore, Eq. 4.11 does not hold in the special case that the shortest distance of two fiber segments includes at least one of the flat fiber ends. Nevertheless, this simplification is accepted in this work, as it only leads to an increase of the distance between the fibers and still does not allow for overlap. Moreover, the simplification was also made by other authors, e.g., in [68, 137]. As for the fiber curvature, the corresponding objective function is computed as the sum of these squared overlaps between all segments of all fibers, which is given by

$$f_{\mathrm{f}}\left(\beta^{\mathrm{r}}, \beta^{\mathrm{b}}, \gamma^{\mathrm{r}}, \gamma^{\mathrm{b}}, \vec{x}^{\,\mathrm{b}}\right) = \frac{1}{2}\sum_{i=1}^{n_{\mathrm{fib}}}\sum_{j=1}^{n_{\mathrm{seg}}}\sum_{k=i+1}^{n_{\mathrm{fib}}}\sum_{l=1}^{n_{\mathrm{seg}}}\left(\delta_{ijkl}^{\mathrm{fib\_fib}}\right)^2. \tag{4.12}$$

The dependent variables are summarized as

$$\beta^{\mathrm{b}} = \left(\beta_1^{\mathrm{b}}, ..., \beta_{n_{\mathrm{fib}}}^{\mathrm{b}}\right),\ \gamma^{\mathrm{b}} = \left(\gamma_1^{\mathrm{b}}, ..., \gamma_{n_{\mathrm{fib}}}^{\mathrm{b}}\right),\ \gamma^{\mathrm{r}} = \left(\gamma_{11}^{\mathrm{r}}, ..., \gamma_{n_{\mathrm{fib}}1}^{\mathrm{r}}, ..., \gamma_{n_{\mathrm{fib}}(n_{\mathrm{seg}}-1)}^{\mathrm{r}}\right), \quad (4.13)$$
$$\text{and } \vec{x}^{\,\mathrm{b}} = \left(\vec{x}_1^{\,\mathrm{b}}, ..., \vec{x}_{n_{\mathrm{fib}}}^{\,\mathrm{b}}\right).$$

The n-tuples β^{b}, γ^{b}, and $\vec{x}^{\,\mathrm{b}}$ include all β_i^{b}, γ_i^{b}, and $\vec{x}_i^{\,\mathrm{b}}$ for all fibers i, whereas the entries of γ^{r} are all angles γ_{ij}^{r} for all fibers i and segments j.

Furthermore, the fibers should not exceed the domain boundaries of the cohesive zone in through-thickness direction z. A penalty for the corresponding overlap is added to the objective function for this purpose. The penetration of the fiber through the upper boundary, the top face sheet, at $z = t_{\mathrm{coh}}$ is given by

$$\delta_i^{\mathrm{ts}} = \max\left(0, \left[\vec{x}_i^{\,\mathrm{ts}}\right]_3 + r_{\mathrm{fib}} \sin\left(\beta_i^{\mathrm{ts}}\right) - t_{\mathrm{coh}}\right). \quad (4.14)$$

$[\vec{x}_i^{\,\mathrm{ts}}]_3$ corresponds to the z-component of the segment end point of fiber i with the largest value of z. It is defined according to

$$\left[\vec{x}_i^{\,\mathrm{ts}}\right]_3 = \max\left(\left[\vec{x}_{i1}^{\,\mathrm{se}}\right]_3, ..., \left[\vec{x}_{i(n_{\mathrm{segs}})}^{\,\mathrm{se}}\right]_3\right). \quad (4.15)$$

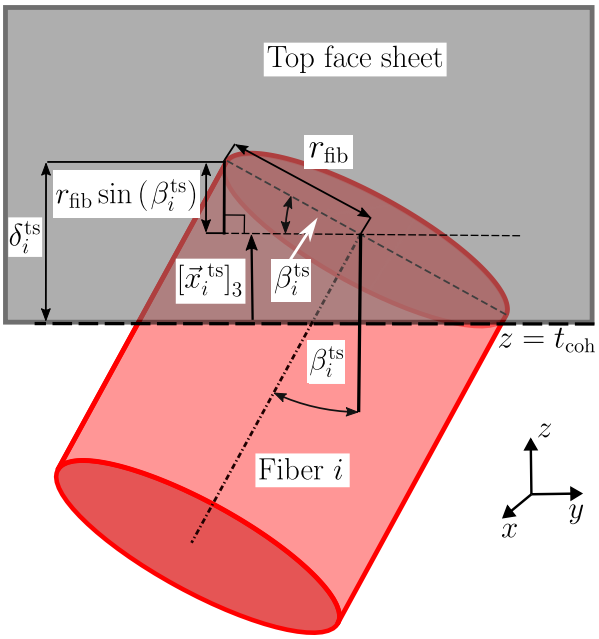

Figure 28: Overlap of a fiber with the top face sheet.

In addition, β_i^{ts} represents the orientation angle of the segment that belongs to $\vec{x}_i^{\mathrm{ts}}$ with respect to the z-axis. It can be computed from the analytical segment end points in Eq. (4.2). The expression for the overlap, Eq. (4.14), was derived from a geometrical consideration, which is schematically shown in Fig. 28. Besides the penetration depth of the highest segment end point into the top face sheet, $[\vec{x}_i^{\mathrm{ts}}]_3 - t_{\mathrm{coh}}$, the additional penetration of the flat fiber end is accounted for by the term $r_{\mathrm{fib}} \sin(\beta_i^{\mathrm{ts}})$. As before, the max condition ensures that δ_i^{ts} cannot become negative if no overlap occurs.

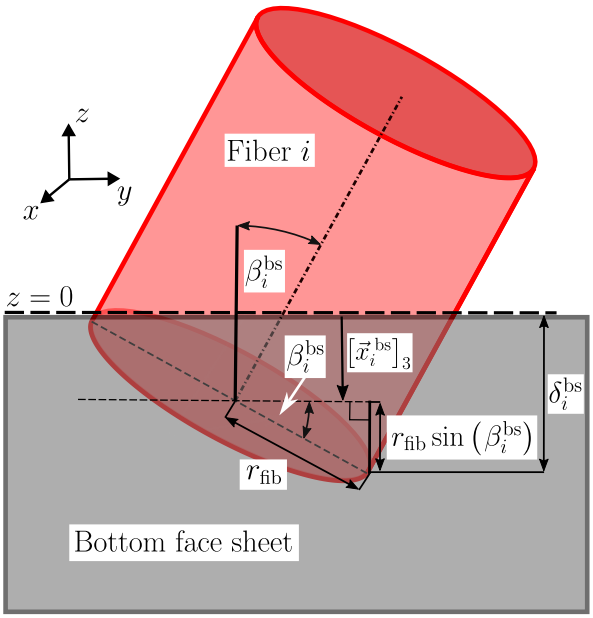

Figure 29: Overlap of a fiber with the bottom face sheet.

Similarly, the overlap of fiber i with the bottom face sheet at $z = 0$ is given by

$$\delta_i^{\mathrm{bs}} = \max\left(0, -\left[\vec{x}_i^{\mathrm{bs}}\right]_3 + r_{\mathrm{fib}} \sin\left(\beta_i^{\mathrm{bs}}\right)\right). \tag{4.16}$$

$\left[\vec{x}_i^{\mathrm{bs}}\right]_3$ denotes the z-component of the lowest segment end point of fiber i, which is negative if the segment end point contributes to the overlap. It is computed as

$$\left[\vec{x}_i^{\mathrm{bs}}\right]_3 = \min\left(\left[\vec{x}_{i1}^{\mathrm{se}}\right]_3, ..., \left[\vec{x}_{i(n_{\mathrm{segs}})}^{\mathrm{se}}\right]_3\right). \tag{4.17}$$

The same geometrical considerations as for the top face sheet were used for the derivation and the corresponding scheme is presented in Fig. 29. Moreover, β_i^{bs} denotes the orientation angle with respect to the z-axis belonging to the fiber segment of $\vec{x}_i^{\mathrm{bs}}$.

Similar to the other overlap types, the corresponding contribution to the objective

function is formulated as the sum of the squared overlaps of all fibers with the face sheets. It reads

$$f_{\mathrm{s}}\left(\beta^{\mathrm{r}}, \beta^{\mathrm{b}}, \gamma^{\mathrm{r}}, \gamma^{\mathrm{b}}, \vec{x}^{\,\mathrm{b}}\right) = \frac{1}{2}\sum_{i=1}^{n_{\mathrm{fib}}}\left[\left(\delta_i^{\mathrm{bs}}\right)^2 + \left(\delta_i^{\mathrm{ts}}\right)^2\right]. \tag{4.18}$$

In summary, the objective function for the optimization problem is given by

$$f\left(\beta^{\mathrm{r}}, \beta^{\mathrm{b}}, \gamma^{\mathrm{r}}, \gamma^{\mathrm{b}}, \vec{x}^{\,\mathrm{b}}\right) = f_{\mathrm{c}} + f_{\mathrm{f}} + f_{\mathrm{s}} + w_\beta\, MSE_\beta. \tag{4.19}$$

This (constrained) optimization problem then yields

$$\begin{aligned} &\underset{\substack{\beta^{\mathrm{r}},\,\beta^{\mathrm{b}},\,\gamma^{\mathrm{r}},\\ \gamma^{\mathrm{b}},\,\vec{x}^{\,\mathrm{b}}}}{\text{minimize}} && f\left(\beta^{\mathrm{r}}, \beta^{\mathrm{b}}, \gamma^{\mathrm{r}}, \gamma^{\mathrm{b}}, \vec{x}^{\,\mathrm{b}}\right) \\ &\text{subject to} && \beta_{ij}^{\mathrm{r}} \in [0°, 10°]\,,\ \beta_i^{\mathrm{b}} \in [0°, 90°]\,,\ \gamma_{ij}^{\mathrm{r}} \in [0°, 360°)\,, \\ & && \gamma_i^{\mathrm{b}} \in [0°, 360°)\,,\ \text{and}\ \vec{x}_i^{\,\mathrm{b}} \in [0, L_1] \times [0, L_2] \times [0, 2r_{\mathrm{fib}}] \end{aligned} \tag{4.20}$$

in the CRA for the generation of the fiber structure, where the dependent variables that minimize f are sought. Here, w_β is a weight factor, which is required because MSE_β and the other parts of f have completely different physical significance and orders of magnitude. It is chosen so that the order of magnitude of MSE_β matches that of the other contributions to f when the objective function is first evaluated in the optimization process. This choice prevents one part from being overweighted and the other one from being almost completely neglected during the optimization.

Furthermore, the upper bound for β_{ij}^{r} of 10° ensures that the curved fibers still appear smooth despite their geometrical description as straight line segments. The bounds of γ_{ij}^{r}, β_i^{b}, and γ_i^{b} ensure that any other desired fiber and segment orientations can be achieved. The bottom end point $\vec{x}_i^{\,\mathrm{b}}$ should be close to the bottom face sheet to account for the observed fiber concentration and apply the measured fiber orientation from Sec. 4.1. Consequently, the z-component of $\vec{x}_i^{\,\mathrm{b}}$ is bounded from 0 mm to $2\,r_{\mathrm{fib}}$. The upper bound provides some flexibility in the positioning of the fibers, which reduces overlap with other fibers, especially for those with a β_i^{b} close to 90°. The upper bounds of $\vec{x}_i^{\,\mathrm{b}}$ and β_{ij}^{r} were determined by numerical experiments. The x- and y-components of $\vec{x}_i^{\,\mathrm{b}}$ are constrained by the dimensions of the virtual model of the microstructure.

In this work, the minimization was performed using Particle Swarm Optimization (PSO) [139, 140], which is a global optimizer that tries to imitate the behavior of natural swarms. Furthermore, bounds on the search space can be applied. In this optimization process, "particles" are randomly distributed throughout the search space and the velocity

of each particle in step $n+1$ is assigned by

$$v_{n+1}^{\mathrm{PSO}} = \omega v_n^{\mathrm{PSO}} + c_1 r_1^n \left(x_{\mathrm{lm}}^{\mathrm{PSO}} - x_n^{\mathrm{PSO}} \right) + c_2 r_2^n \left(x_{\mathrm{gm}}^{\mathrm{PSO}} - x_n^{\mathrm{PSO}} \right). \tag{4.21}$$

The corresponding position in the search space is updated according to $x_{n+1}^{\mathrm{PSO}} = x_n^{\mathrm{PSO}} + v_{n+1}^{\mathrm{PSO}}$ with

$$x^{\mathrm{PSO}} = \left(\beta^{\mathrm{b}}, \gamma^{\mathrm{b}}, \beta^{\mathrm{r}}, \gamma^{\mathrm{r}}, x^{\mathrm{b3}} \right) \text{ and } x^{\mathrm{b3}} = \left(\left[\vec{x}_1^{\,\mathrm{b}} \right]_3, ..., \left[\vec{x}_{n_{\mathrm{fib}}}^{\,\mathrm{b}} \right]_3 \right). \tag{4.22}$$

x^{b3} contains the z-component of all $\vec{x}_i^{\,\mathrm{b}}$. $x_{\mathrm{lm}}^{\mathrm{PSO}}$ and $x_{\mathrm{gm}}^{\mathrm{PSO}}$ are the position of the individual particle with the minimum of the objective function during the optimization process and the position of the particle with the global minimum, respectively. The corresponding variables in the PSO are all n-tuples.

c_1 and c_2 are parameters that mimic the cognitive and social behavior of the swarm, whereas r_1^n and r_2^n are random variables that are generated for each particle in each step separately. ω is an inertia parameter. After a given number of iterations, the position of the particle that yields the lowest value of the objective function is kept as the best solution of the optimization problem.

In practice, the position in the xy-plane could not be included in the optimization. Otherwise, strong unphysical concentrations of fibers in the center of the virtual model of the fiber structure were observed in numerical experiments. In order to avoid this observed effect, the initially straight fibers, which are oriented in the z-direction, are placed randomly. During this placement, it is ensured that no overlap between fibers occurs. Note that this random positioning, together with the natural random choice of initial parameters in the first step of the PSO, also corresponds to an RSA. As discussed in Sec. 1.3.3 and according to [64], such an RSA is typically performed in the first step of a CRA.

The generation of the fiber structure is summarized in Alg. 4, where lines 2-5 describe this initial placement of the fibers in the xy-plane. The x- and y-components of the bottom end point $\vec{x}_i^{\,\mathrm{b}}$ of fiber i are selected randomly within the domain boundaries and all other geometrical descriptors are set to zero. Then, the contribution of the overlap between fibers, f_{f}, to the objective function is computed. If it equals zero, the next fiber, $i+1$, is placed. Otherwise, the process is repeated until a position without overlap is found. The algorithm for the initial fiber placement is stopped when the specified fiber volume fraction v_{ft} is reached within the tolerance tol. The current volume fraction of the fiber structure v_{f} is purely calculated from the cylindrical geometry of the fibers and known edge lengths of the cuboidal domain L_1, L_2, and $L_3 = t_{\mathrm{coh}}$.

Line 6 then corresponds to the minimization of the objective function f using the PSO, which provides all required geometrical information for the fiber structure. In the final step of the algorithm, line 7, the generated geometrical model of the fiber structure from the optimization process is meshed with a regular voxel mesh (grid). In addition, meshed spheres with the same radius as the fibers are added at the shared segment end points in order to obtain a smooth connection between the cylindrical segments. Similar to two-dimensional standard binary images, the discretized fiber structure on the voxel grid is stored as a three-dimensional array. Its indices are stored in set A_f.

The meshing at this stage of the generation of the virtual model is required for the addition of binder in the next step. Furthermore, it should also be noted that, besides PSO, other global optimizers were tested, e.g., simulated annealing [67, 141] and genetic algorithms [142]. Nevertheless, PSO provided the best results at reasonable computational times.

Algorithm 4 CRA for generating the virtual model of the Hybrix$^{\mathrm{TM}}$ fiber structure

1: **Function** Generate fiber structure (CDF_m, v_ft, r_fib, l_fib, L_j):
2: **Inititalize:** $i = 0$ and **iterate:** i **until** $|v_\mathrm{ft} - v_\mathrm{f}| < tol$:
3: **Set** $\left[\vec{x}_i^\mathrm{b}\right]_1$ and $\left[\vec{x}_i^\mathrm{b}\right]_2$ randomly and $\left[\vec{x}_i^\mathrm{b}\right]_3, \beta_i^\mathrm{b}, \gamma_i^\mathrm{b}, \beta_{i1}^\mathrm{r}, ..., \beta_{in_\mathrm{seg}}^\mathrm{r}, \gamma_{i1}^\mathrm{r}, ..., \gamma_{in_\mathrm{seg}}^\mathrm{r} = 0$
4: Compute f_f according to Eq. 4.12
5: **If** $f_\mathrm{f} = 0$ **then** $i = i + 1$
6: Solve optimization problem in Eq. 4.20 using the PSO in Eq. 4.21
7: Mesh and generate discretized fiber structure A_f
8: **Return:** A_f

4.2.2. Addition of binder

In the next step, the binder is added to the meshed fiber structure on the corresponding voxel grid. For this purpose, the morphological operation "(binary) closing", which is a combination of dilation and erosion from classical image processing, is used. This has also been applied similarly in the literature for the generation of virtual models for microstructures, see, e.g., [55, pp.82-93] and [143]. As already mentioned at the end of the previous Sec. 4.2.1, the meshed virtual model of the microstructure on the voxel grid is stored as a three-dimensional array in practice. Therefore, its indices can be interpreted as a subset of the integer lattice $\mathbb{Z}^3$, which was also used in Sec. 2.4.1 for the discretization of the Lippmann-Schwinger equation. This allows for a simple implementation of the

morphological operation similar to the implementation for standard binary pixel images that can also be defined on an integer lattice.

Following [144], the dilation of the three-dimensional image A with the structuring element B, which both are sets in $\mathbb{Z}^3$, is mathematically defined as

$$A \oplus B = \bigcup_{\vec{b} \in B} A_b \quad \text{with} \quad A_b = \left\{ \left(\vec{a} + \vec{b} \right) \in \mathbb{Z}^3 \middle| \vec{a} \in A \right\}. \tag{4.23}$$

The set A_b is created by a translation of all points $\vec{a}$ that belong to A with a point of the structuring element $\vec{b}$. The union of all A_b, which are computed for every point $\vec{b}$ of the structuring element B, yields the corresponding dilation of A with B. The dilation is schematically visualized in Fig. 30b for the two-dimensional object in Fig. 30a.

Similarly, the corresponding erosion is defined as

$$A \ominus B = \bigcap_{\vec{b} \in B} A_{-b} \quad \text{with} \quad A_{-b} = \left\{ \left(\vec{a} - \vec{b} \right) \in \mathbb{Z}^3 \middle| \vec{a} \in A \right\}, \tag{4.24}$$

where the set A_{-b} is formed by the transformation of A by $-\vec{b}$. Then, one obtains the intersection of all A_{-b} as the erosion of A with structuring element B. An exemplary scheme of the erosion applied to the dilation from Fig. 30b is presented in Fig. 30c. More details regarding the mathematical fundamentals of the morphological operations are given in [145][pp.63-137] and [144]. The closing operation can be performed in multiple iterations as

$$\left((A \oplus B)^n \ominus B \right)^n, \tag{4.25}$$

where n denotes this number of iterations. In this case, the image A always represents the fiber structure, including a padding with half the size of the structuring element to handle the boundary effects. In the x- and y-directions, the padding consists of periodic copies of the respective parts of the microstructure, such that the result of the closing remains periodic. The padding in the z-direction is completely assigned to the fiber structure, which ensures a physically realistic and smooth connection of fibers and face sheets by the binder.

The pseudocode for the addition of the binder to the fiber structure is presented in Alg. 5. In the first step after initializing the variables, lines 4-7, the iteration number of the closing operation n is increased until the binder volume fraction v_b exceeds the target value v_bt or the specified accuracy of *tol* is achieved. A spherical structuring element with radius r_se is used, which is always a positive integer, as the structuring element is

also defined on the integer lattice. The current binder model and, hence, volume fraction v_b is computed as the set difference between the combined fiber-binder set A_n^i and the initial fiber structure, set A, within domain of the model (line 6). Then, the model with the highest volume fraction that is still below the target value is stored as $A_0^{i+1} = A_{n-1}^i$ and the size of the structuring element is reduced by one (line 7). The process is repeated by iterating i (lines 2 and 3) until the specified accuracy of the volume fraction *tol* is achieved. The algorithm is stopped, and the resulting binder model is returned (line 8), or the size of the structuring element becomes zero (lines 2 and 7). If the algorithm is stopped because r_se becomes zero, the error can either be accepted or an improvement can be achieved by increasing the mesh resolution until the desired tolerance is reached.

Algorithm 5 Addition of binder to the virtual model of the Hybrix$^{\mathrm{TM}}$ fiber structure

1: **Function** Binder (A, v_bt): ▷ A is A_f including padding
2: **Initialize:** r_se, $A_0^1 = A$, $i = 0$ and **iterate:** $i = i + 1$ **until** $r_\mathrm{se} = 0$
3: **Initialize:** $n = 0$ and **iterate:** $n = n + 1$ **until** $v_\mathrm{b} > v_\mathrm{bt}$
4: $A_n^i = ((A_{n-1}^i \oplus B(r_\mathrm{se}))^n \ominus B(r_\mathrm{se}))^n$
5: Compute binder model and volume fraction v_b from A_n^i/A
6: **If** $|v_\mathrm{b} - v_\mathrm{bt}| < tol$ **then**
stop algorithm and **return** A_n^i/A ▷ return binder model
7: **Set** $r_\mathrm{se} = r_\mathrm{se} - 1$ and $A_0^{i+1} = A_{n-1}^i$
8: **Return** A_{n-1}^i/A ▷ return binder model if $r_\mathrm{se} = 0$

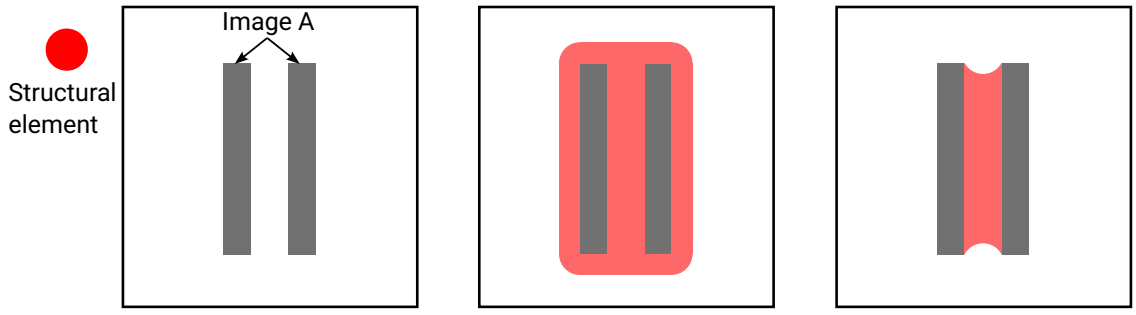

Figure 30: Morphological closing operation of image A by a circular structuring element: Base image (a), image after the dilation operation (b), and final image after dilation and erosion (closing) (c).

4.2.3. Marginal layers and final algorithm

The final algorithm is summarized in Alg. 6. First, recall that the production parameters for the core fiber length l_{fib}, fiber radius r_{fib}, (target) fiber volume fraction v_{ft}, (target) binder volume fraction v_{bt}, and core thickness $L_3 = t_{\mathrm{coh}}$ should serve as the only input parameters for the generation of virtual models, see also Sec. 1.2. The model CDF for the fiber distribution, CDF_{m}, also only depends on l_{fib} and t_{coh}, as defined in Eq. (4.8). Furthermore, the edge lengths L_1 and L_2 in the xy-plane are input parameters in Alg. 6, but they are not strictly input parameters for the generation itself. They typically need to be determined through numerical experiments to ensure that the generated model is an RVE. However, this was not feasible in this work owing to high computational times, see Sec. 4.3.6 for details. Nevertheless, it can be concluded that this generation process for the virtual model of the microstructure relies solely on the production parameters as input.

In the final step of the algorithm for generating virtual models of the microstructure, the marginal layers are added to the boundaries of the cohesive zone. These layers have a thickness of 0.1 mm each, a Young's modulus of 70 GPa, and a Poisson's ratio of 0.33. The parameters were selected following the recommendations from Sec. 3.3.3. Accordingly, the material parameters correspond to those of the bulk material surrounding the cohesive zone, the aluminum face sheets. The thickness of the marginal layers is 13.3% of the core thickness and thus similar to the 15% found for the adhesive. In Secs. 5.3 and 6.2, where the FFT simulations are presented, it is demonstrated that the desired Dirichlet-type boundary conditions at the interface from Eq. (3.10) and the Hill-Mandel condition from Sec. 3.1 are sufficiently satisfied for these marginal layer parameters.

The final virtual model of the microstructure including the marginal layers is depicted in Fig. 31c. The corresponding fiber structure and the fiber structure with the added binder are shown in Figs. 31a and 31b, respectively.

Algorithm 6 Generation of virtual models of the Hybrix$^{\mathrm{TM}}$ microstructure

1: **call** Generate fiber structure $(CDF_{\mathrm{m}}, v_{\mathrm{ft}}, r_{\mathrm{fib}}, l_{\mathrm{fib}}, L_j)$ ▷ obtain meshed fiber structure A_{f}
2: **call** Binder (A, v_{bt}) ▷ add the binder; A is A_{f} including padding
3: **Add marginal layers**

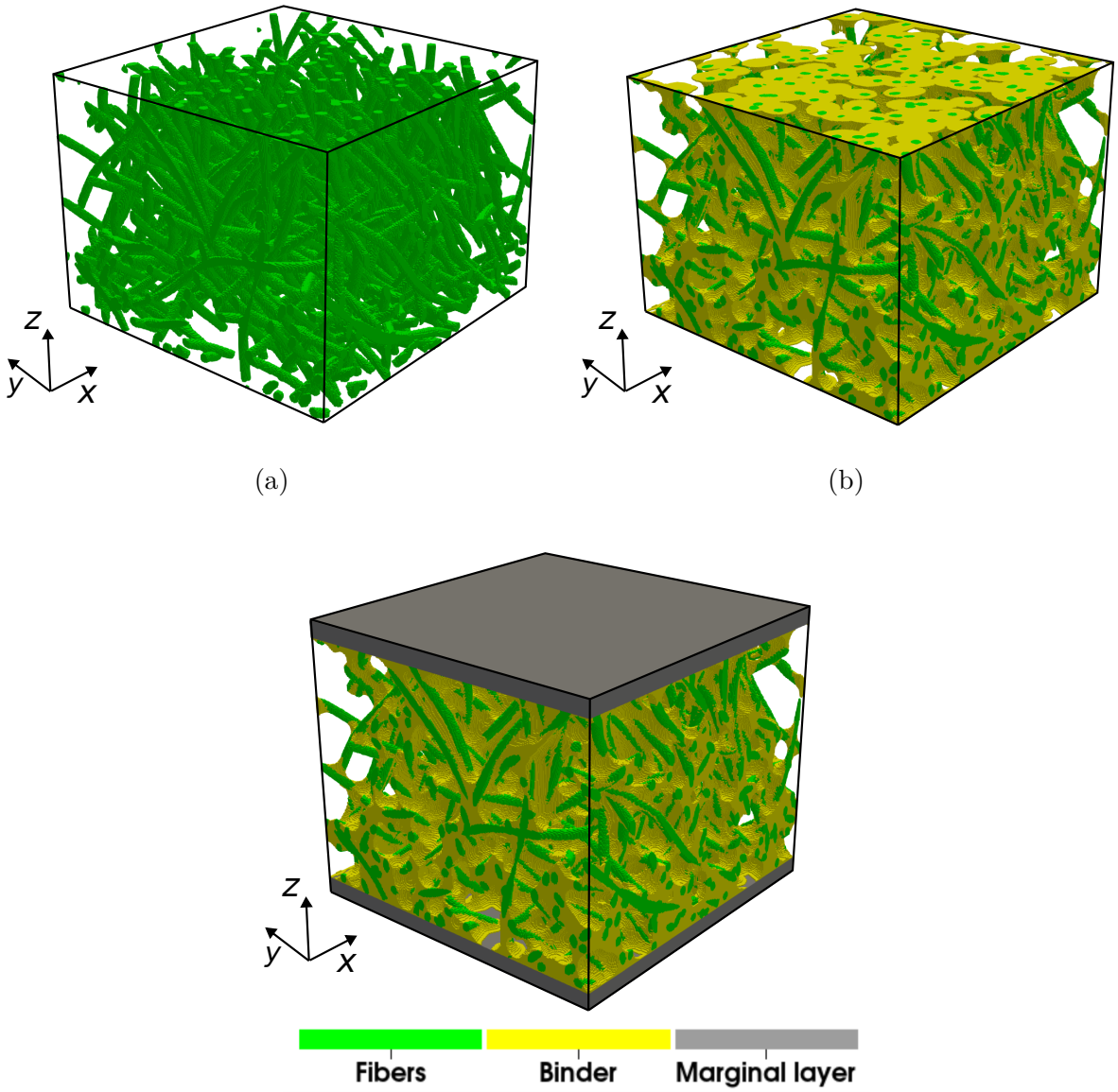

(a) (b)

(c)

Figure 31: Generation of the virtual model of the microstructure for the Hybrix^{TM} core material: Fiber structure (a), addition of the binder (b), final model including the marginal layers (c).

4.2.4. Implementation details

The algorithm was implemented in a mixture of Fortran and Python code. For the generation of the fiber structure, the objective function is calculated by the Fortran code and the PSO is performed in Python using the package PySwarms [139]. The parameters $c_1 = 0.1$, $c_2 = 0.1$, and $\omega = 0.9$ were used and the number of particles was 30. All

parameters were determined from numerical experiments, where they proved to be the best compromise between the quality of the final solution and numerical efficiency.

Furthermore, the morphological operations for the addition of the binder were also implemented as Fortran code. The corresponding tolerance with respect to the target binder volume fraction was set to $tol = 0.01$. The generation of the virtual model for the microstructure was performed on an Intel® Core™ i9-10900X CPU using 20 parallel threads and the OpenMP library [124] for parallelization. The process took about 20 minutes. The model has a size of 300 × 300 × 255 voxels with a voxel size of 6.7 µm, which was determined only from an elastic mesh convergence study owing to the high computational times for a full simulation.

4.3. Evaluation of the representativeness of the generated model for the geometry and mechanical behavior of the sandwich core

4.3.1. Orientation angle β

This section first discusses the representativeness of the virtual model for the microstructure geometry. For this purpose, a comparison of the generated virtual model with the experimental micrographs and the µ-CT scan was carried out using the statistical descriptors presented in Sec. 1.3.3. Subsequently, the representativeness of the model for the mechanical behavior of the sandwich core is assessed to determine if it can be considered an RVE, see also Sec. 1.3.1 for a discussion on the corresponding definition.

The distribution of the orientation angle β is the first statistical measure for the microstructure geometry that is analyzed in this work. A comparison of the experimentally determined PDFs and CDFs from the microscopy and the generated virtual model is shown in Figs. 32a and 32b. In addition, the prescribed triangular model distribution for β_b is depicted as the blue dotted line. The "virtual model of the microstructure" is referred to as "FFT model" for notational clarity in the figures. Furthermore, the curves for position 1 are relative to those for position 2 and indicate the number of fibers from position 2 that also reach position 1. The global orientation angles β in the virtual model were computed from the analytical segment end points according to Eq. (4.2) at positions 1 and 2.

The relative number of fibers at position 1 is overestimated by the virtual model, whereas the trends of the curves match well, especially in the PDF of β in Fig. 32a. Here, the position of the peak is one important characteristic of the microstructure of the sandwich core, as it indicates the orientation, where straight fibers from position 2

would reach position 1. This important characteristic is captured well by the model. Moreover, the approximately linear increase up to the peak value and the steep decline of the curve behind it appear both in the experimental data and in the virtual model. Only the peak value itself is higher owing to the overestimated relative number of fibers at that point. For the same reason, the corresponding CDF in Fig. 32b is higher as well. For position 2, the curves also match well except for a slight deviation in the beginning for small values of β, which can also be clearly observed in the CDFs in Fig. 32b.

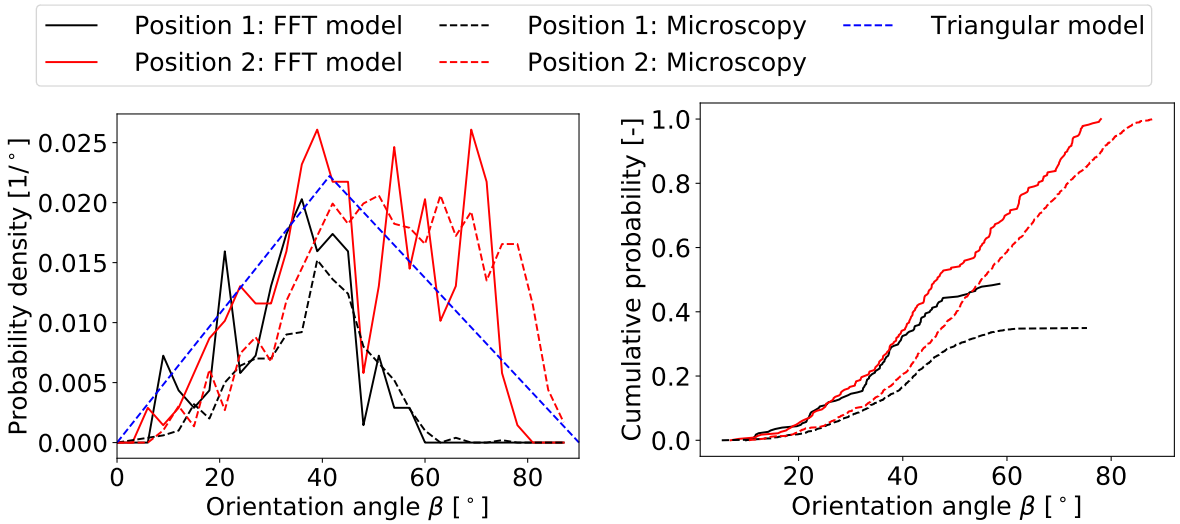

(a) (b)

Figure 32: Comparison of the PDF (a) and CDF (b) of the orientation angle β between the virtual model of the microstructure (FFT model), microscopy results at z-positions 1 and 2, and the triangular model in (a).

In summary, despite some minor deviations, the agreement between the virtual model and the microscopy results is sufficient for the purposes of this work. However, this relatively good agreement was expected, as the model distribution for β_b was chosen to match the experimental results. Hence, this comparison only serves as a verification that the generation in Alg. 6 works as expected but is not sufficient to evaluate the representativeness of the model itself. This highlights the importance of considering additional statistical descriptors for microstructures.

4.3.2. Fiber nearest neighbor distance

Besides the fiber orientation, statistical descriptors for the spatial distribution of the fibers also represent important characteristics of the microstructure. As already mentioned in

Sec. 1.3.3, the fiber nearest neighbor distance is such a statistical descriptor, which is very sensitive to fiber clustering in particular. It is computed as the PDF of the distance of each fiber to its nearest one, e.g., see [59, 60].

The corresponding fiber nearest neighbor distances from the microscopy and the virtual model of the microstructure are presented in Figs. 33a and 33b as PDF and CDF. Similar to the orientation angles in the previous Sec. 4.2.1, the distances of the fibers in the virtual model of the microstructure were calculated from the analytical segment end points in Eq. 4.2 at the corresponding z–positions. The curves for position 1 are again relative to those at position 2. The figures show a reasonable agreement between the trends of the curves. The peaks as well as the approximately linear decline until 120 µm behind the peaks in the PDFs are similar for microscopy and the model at both positions. This relatively good agreement between the slopes in the CDFs supports this observation further.

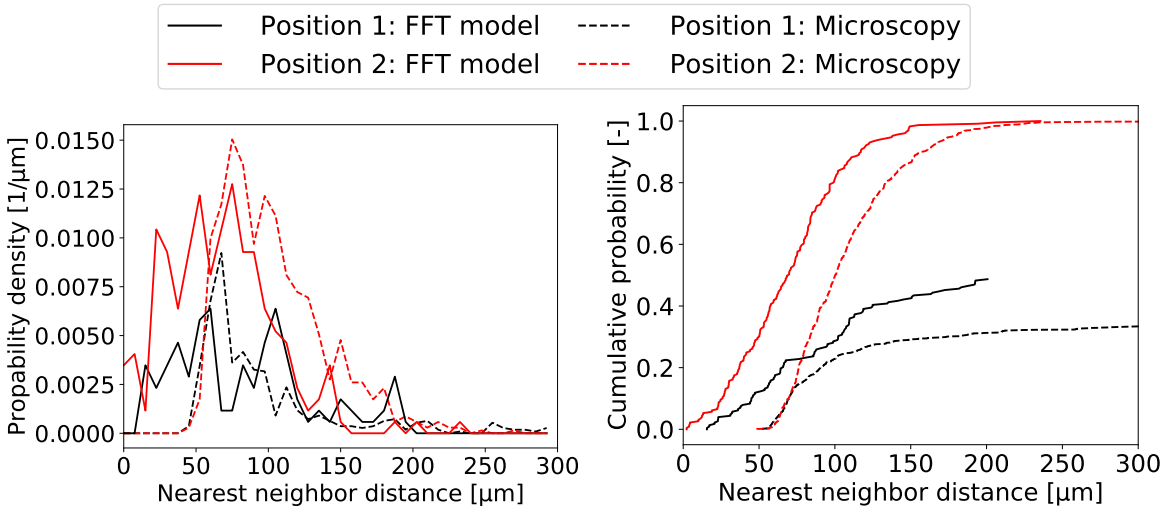

(a) (b)

Figure 33: Comparison of PDFs (a) and CDFs (b) of the fiber nearest neighbor distance between the virtual model of the microstructure (FFT model) and the results from microscopy at z-positions 1 and 2.

However, in contrast to the experimental results from microscopy, the minimum fiber distance in the virtual model is significantly lower than the fiber diameter of 50 µm at both positions 1 and 2. The curves also appear to be shifted by the 50 µm. This shows that the algorithm for the generation of the virtual model along with the PSO does not completely prevent overlap of the fibers. As in the previous case of the orientation angle β, the overestimation of the relative number of fibers leads to higher values at the final

plateau in the CDF of the virtual model at position 1.

4.3.3. Radial pair distribution function

Another widely used statistical descriptor for the spatial distribution of fibers in micrographs and generated virtual microstructures is the radial distribution function, see Sec. 1.3.3 and [59–63]. It represents the probability that a fiber is located within an annulus of an inner radius r and a width Δr around another, randomly selected fiber.

Following [62, 146], the radial pair distribution function can be calculated according to

$$G_{\mathrm{r}}(r) = \frac{1}{2\pi\,\rho_{\mathrm{fib}}\,r\,\Delta r\,n_{\mathrm{fib}}} \sum_i \sum_{j \neq i} I\left(r < d_{ij}^{\mathrm{f}} \leq r + \Delta r\right). \tag{4.26}$$

d_{ij}^{f} denotes the distance between the centers of fibers i and j, and ρ_{fib} the area density of fibers on the surface of the micrographs or at the corresponding z-position of the virtual model of the microstructure. Moreover, $I(\bullet)$ again represents the indicator function, which is one if the statement in the argument of the function is true and zero otherwise.

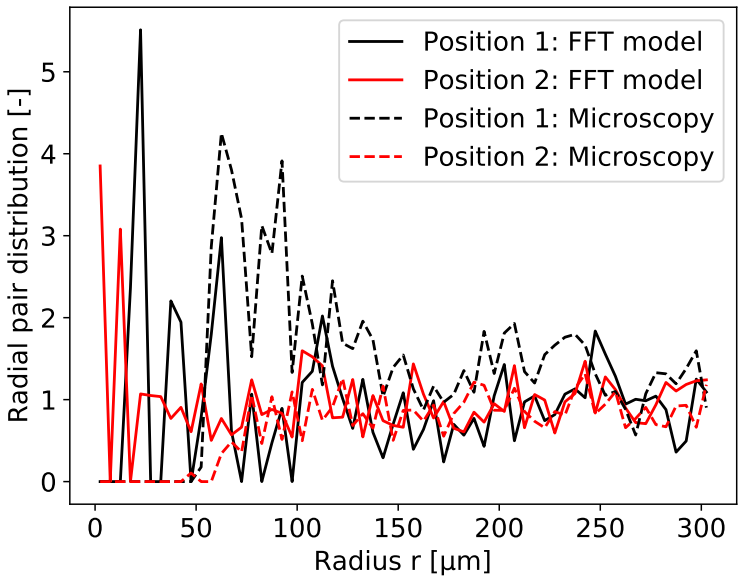

Figure 34: Comparison of the radial pair distribution function between the virtual model of the microstructure (FFT model) and the results from microscopy at z-positions 1 and 2.

The resulting radial pair distribution functions are depicted in Fig. 34, where an annulus width of $\Delta r = 5$ µm was selected. As already described in the previous Secs. 4.3.1 and 4.3.2, the curves for the virtual model of microstructure were computed

analytically from the corresponding segment end points at the given z-positions. The curves show satisfactory agreement overall, except in the initial range for radii below the fiber diameter. This discrepancy arises due to the overlap between fibers in the virtual model, which does not occur in the experimental data from microscopy, where the values are zero in this region. Then, all curves scatter around a value of one, which also indicates a random distribution of the fibers. Nevertheless, at position 1, the experimental results generally tend to have slightly higher values of G_r than those from the virtual model of the microstructure. Moreover, there are similar initial peaks, which are again shifted by the fiber diameter.

4.3.4. Ripley's K function

As discussed in the part of Sec. 1.3.3, which deals with the state of the art in the statistical description of microstructures, Ripley's K function serves as another important statistical descriptor for the spatial distribution of fibers. It can be interpreted as the ratio between the number of fibers that are expected to be located within a circle of radius r with another randomly selected fiber as the center point, and the number of fibers per unit area, see also Sec. 1.3.3 and [59, 60].

Ripley's K function can be estimated according to

$$K_r(r) = \frac{1}{\rho_\mathrm{fib} n_\mathrm{fib}} \sum_i \sum_{j \neq i} \frac{I\left(d_{ij}^\mathrm{f} \leq r\right)}{w_{ij}}, \tag{4.27}$$

where ρ_fib again denotes the area density of fibers of the micrograph or investigated virtual model of the microstructure and n_fib corresponds to the overall number of the fibers. w_{ij} represents a weight factor for the correction of edge effects if the circle with fiber i as the center point and through fiber j crosses the boundary of the investigated domain [147, 148]. w_{ij} is one if the circle lies entirely within the domain and corresponds to the proportion of the circumference of the circle within the domain otherwise. As previously, I denotes the indicator function and d_{ij}^f is the distance between the fiber centers i and j.

The resulting Ripley's K functions from the microscopy and the virtual model of the microstructure at the given z-positions are depicted in Fig. 35. Please note that the largest radii r for which K_r is calculated, differ between the curves for positions 1 and 2. This is caused by the different sizes of the micrographs and the fact that one-half of the length of the smallest side of the rectangular domain is usually taken as the largest radius

by convention. Similar to the previous Secs. 4.3.1, 4.3.2, and 4.3.3, a generally reasonable agreement between the corresponding curves can be observed. Only at position 1 are the experimental K_r values from microscopy higher than those from the virtual model, as it was similarly observed for the radial pair distribution function.

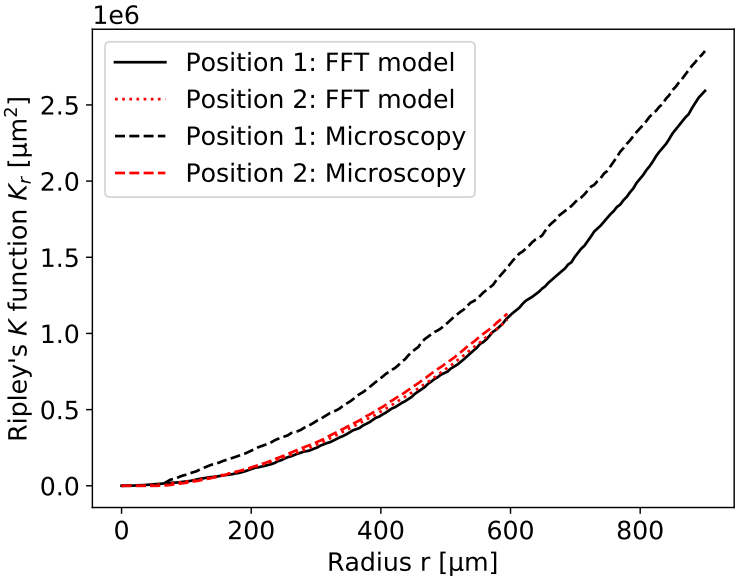

Figure 35: Comparison of the Ripley's K function between the virtual model of the microstructure (FFT model) and the results from microscopy at z-positions 1 and 2.

4.3.5. Two-point correlation and volume fractions

In the next step, the generated virtual model of the microstructure is statistically compared with the µ-CT scan presented in Sec. 4.1. Since fibers and binder could not be distinguished in the µ-CT scan, it contains both as a combined constituent. Accordingly, the scan is composed of only two constituents, the combined fiber-binder constituent and the porosity.

As discussed in Sec. 1.3.3, a relatively general statistical descriptor for such microstructures with two constituents is the two-point correlation function. For statistically homogeneous microstructures, it provides the probability of finding two points of the same constituent at the end of a line segment of given length and orientation, see also [57] for more details. This line segment is denoted as $\vec{r}$ in the following. However, the microstructure of the sandwich core is not statistically homogeneous in the through-thickness direction z, see Sec. 4.1, but the statistical homogeneity is expected in the xy-plane. Therefore, the µ-CT scan and the virtual model of the microstructure were

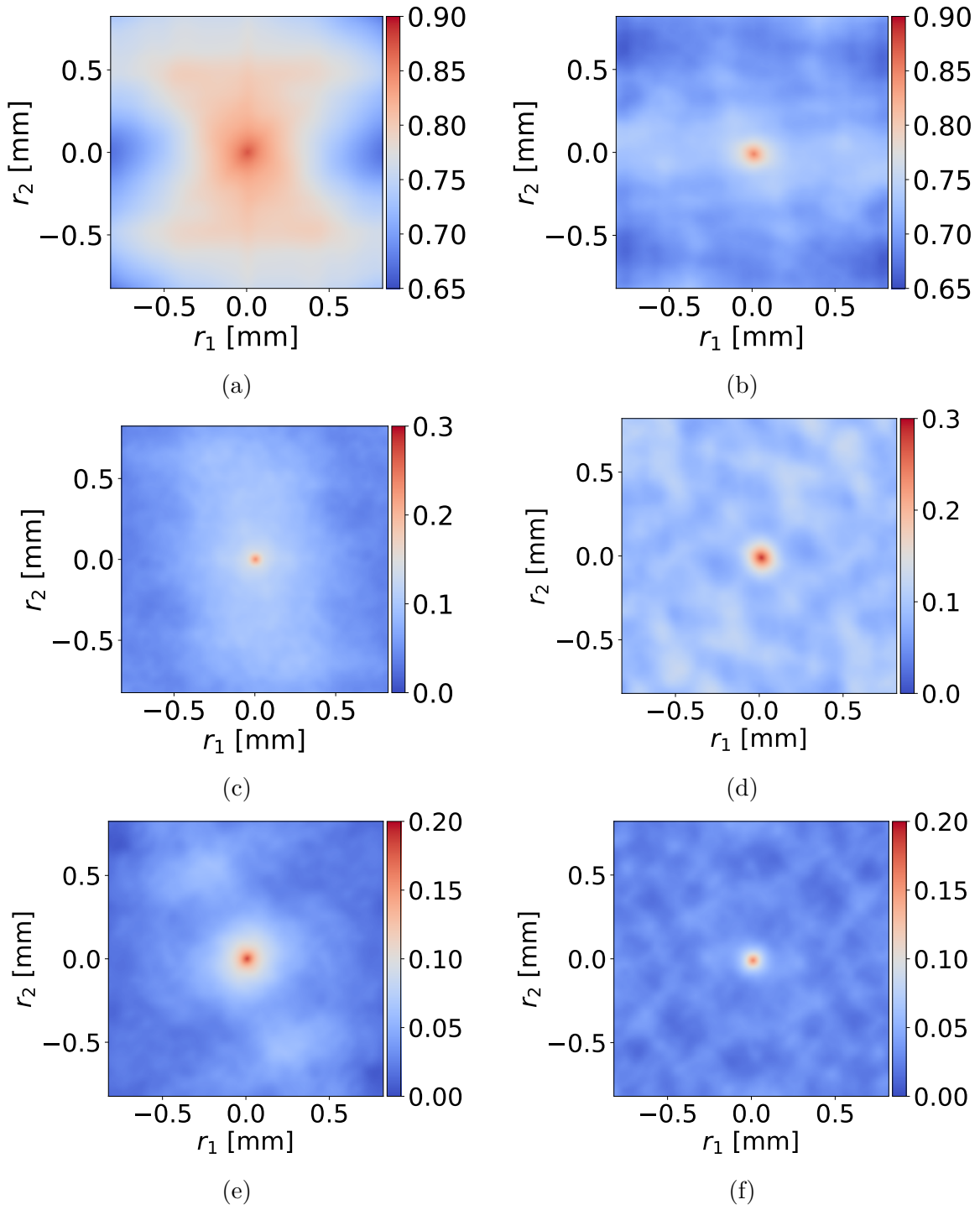

Figure 36: Comparison of the two-dimensional representation of the two-point correlation functions just above the bottom face sheet: Experiment (a) and virtual model (b); At the center: Experiment (c) and virtual model (d); just below the top face sheet: Experiment (e) and virtual model (f).

compared in the xy-plane at three representative z-positions: just above the bottom face sheet and just below the top face sheet, and at the center.

The two-point correlation function is calculated by

$$S_{\mathrm{TP}}\left(\vec{r}\right) = \frac{1}{S_{\mathrm{f}}} \sum m\left(\vec{x}\right) m\left(\vec{x}+\vec{r}\right) \tag{4.28}$$

according to [149], where S_{f} denotes the possible number of placements of the line segment $\vec{r}$. Furthermore, m is one, if the position vector in the argument of the function is within the combined fiber-binder constituent and zero otherwise. In this work, PyMKS implementation in Python [150] was used for the practical computation of the two-point correlation functions.

The resulting two-dimensional two-point correlation functions of the µ-CT scan and the virtual model of the microstructure at the given z-positions are shown in Fig. 36. Figs. 36a, 36c, and 36e correspond to the two-point correlation functions from the µ-CT scan at the locations just above the bottom face sheet, at the center, and just below the top face sheet. Figs. 36b, 36d, and 36f similarly represent the two-point correlation functions from the virtual model at the respective locations.

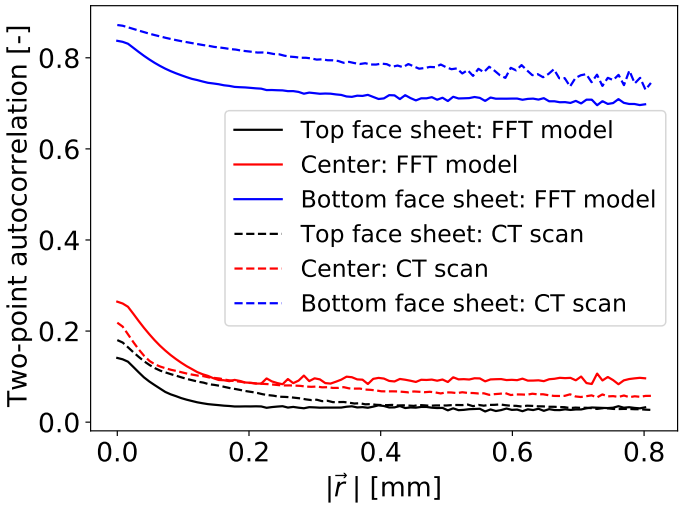

Figure 37: Comparison of the radial average of the two-point correlation functions.

However, as already mentioned in Sec. 4.1, the thickness of the µ-CT scan is smaller than expected and only 1.4 mm instead of 1.5 mm. Hence, care had to be taken when choosing the investigated z-positions. This is because the interface between the top face sheet and the core appeared blurred in the scan and could not be distinguished properly. Accordingly, it is assumed that the positions of the bottom face sheets in scan and virtual

model of the microstructure agree, whereas the top of the scan is 0.1 mm below the top face sheet. Therefore, the position "top face sheet" is at a z-position of 1.4 mm from the bottom face sheet.

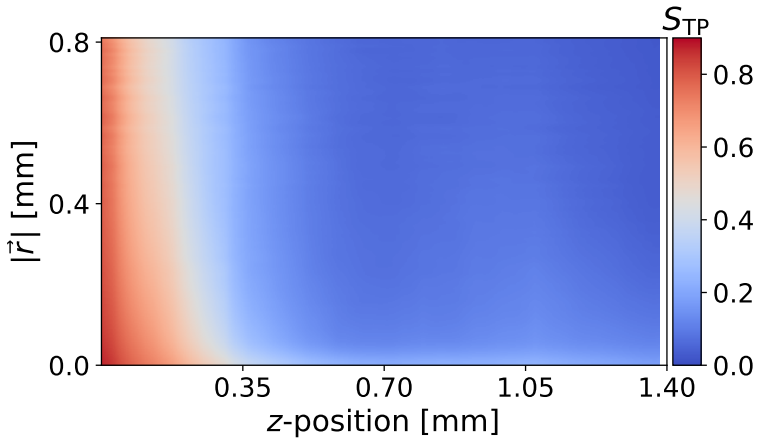

(a)

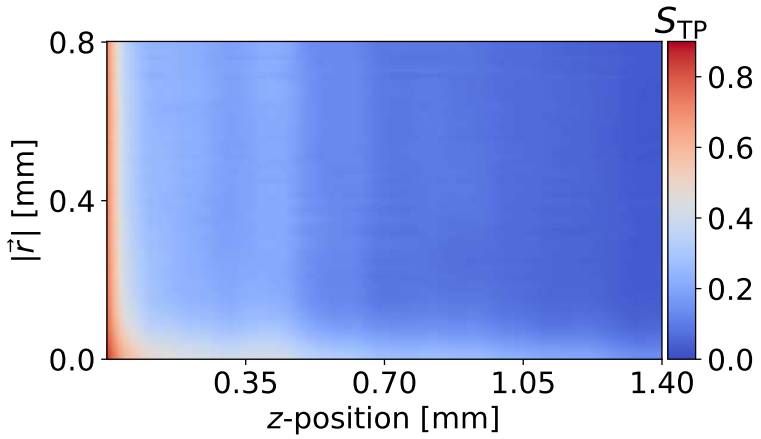

(b)

Figure 38: Comparison of the (radially) averaged two-point correlation functions: µ-CT scan (a) and virtual model of the microstructure (b).

Furthermore, r_1 and r_2 denote the x- and y-components of the line segment $\vec{r}$. Overall, a satisfactory agreement between the two-point correlation function fields is observed. It should also be noted that the scaling of the color map emphasizes already slight differences. Moreover, it can be observed that, considering a reasonable tolerance, the fields are isotropic around the origin, which indicates that the microstructure is also isotropic in the xy-plane. Consequently, the radial averages of the two-point correlation functions are also compared, as depicted in Fig. 37 with the length of the line segment

$|\vec{r}|$ on the abscissa. Again, the curves generally show satisfactory agreement. However, small local deviations occur in some regions and the curve from the µ-CT scan is higher for the z-position just above the bottom face sheet.

In this context, further insight can be gained by analyzing the distribution of the radial averages of the two-point correlation function along the through-thickness direction z. This distribution is presented in Fig. 38a for the µ-CT scan and in Fig. 38b for the virtual model, respectively. The length of the line segment $|\vec{r}|$ is represented on the ordinate, whereas the position along the through-thickness direction z is shown on the abscissa. In the figure, the position just above the bottom face sheet corresponds to a z-value of 0 mm. Furthermore, the color map depicts the radially averaged two-point correlation S_{TP}.

As also observed for the three specified z-positions in Fig. 37, a reasonable agreement between µ-CT scan and model is observed. However, differences occur in the z-direction between 0.05 mm and 0.3 mm. In this region, the two-point correlation function from the µ-CT scan remains almost constant over $|\vec{r}|$, which indicates a strong concentration of fibers and binder in a single connected region. In contrast, the virtual model exhibits smaller concentrations of fibers and binder, which are interrupted by pores. Again, the colormap highlights these differences, particularly in this critical region. The largest deviation occurs at approximately 0.2 mm, where the curve from the µ-CT scan is also about 0.2 mm higher than the one from the virtual model.

Furthermore, the values of the two-point correlation functions at $|\vec{r}| = 0$ correspond to the respective volume fraction of fibers and binder combined. Fig. 39 shows that the virtual model of the microstructure reasonably captures the respective experimental distribution along the through-thickness direction z from the µ-CT scan. As expected from the two-point correlation functions, the most significant deviations also occur between z values of 0.05 mm and 0.3 mm. Apart from the curves at $|\vec{r}| = 0$, those at other values of $|\vec{r}|$ were also analyzed, revealing a very similar trend, albeit with different absolute values.

The use of spherical structuring elements with partially small diameters in the morphological operations for the addition of binder leads to the formation of small pores in the model. This prevents large connected regions of fibers and binder, which is most likely the main reason for the observed deviations in the two-point correlation. Note that no specific distribution of the binder or fibers in the through-thickness direction was prescribed, nevertheless the results are matched relatively well.

The relatively good agreement also holds for the overall volume fractions of fibers

and binder, which are 13 % and 22 % in the virtual model of the microstructure and, therefore, the same as in the experiments.

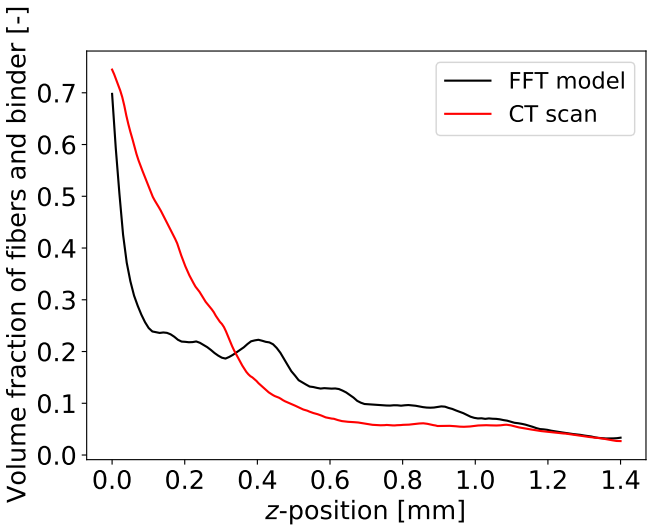

Figure 39: Distribution of the volume fraction of fibers and binder combined in through-thickness direction z in the µ-CT scan and the virtual model of the microstructure (FFT model).

4.3.6. Mechanical behavior and discussion

According to the literature, it can be verified if the virtual model is representative of the mechanical behavior by performing simulations with models of different sizes and different variants of the same size, see [41] and Sec. 1.3.1. However, this verification was not possible for this model owing to the high computational times of about 37 days for a mode I simulation and 31 days for mode III. Therefore, it is referred to as "virtual model of the microstructure" rather than "RVE" in this work. The length and width of 2×2 mm correspond to the smallest physically feasible size, as smaller models would not adequately represent theoretically possible, straight fibers oriented at 90° to the z-axis. Nevertheless, if the model were not representative of the mechanical behavior, significant deviations would have been expected in the validation of the FFT simulations with experiments in Sec. 6.

In summary, a satisfactory statistical agreement was found between the generated virtual model of the microstructure and the experimental results, especially considering the simplifications and assumptions made for the input parameters of the model generation. This indicates that the model is sufficiently representative of the geometry. Nonetheless,

the algorithm for generating virtual models could not completely avoid overlap between the fibers, and an improvement may be necessary for future work. Possible improvements could be achieved by employing alternative optimization algorithms, such as Sequential Addition and Migration [68], or by modifying the objective function itself, which requires further investigation. However, the overlap of the fibers can be neglected in this work owing to the simplification of modeling fibers and binder with the same material model, as discussed in Sec. 5. For the same reason, the two-point correlation function is the most relevant measure here, and the one obtained from the model is in satisfactory agreement with the one from the µ-CT scan.

5. Experimental parameter identification for the material models at the microscale

5.1. Elastic properties

Based on the discussion in Sec. 1.3.4 on the state of the art for experimentally identifying local material models at the micro- and nanoscale, microindentation was selected to determine the isotropic linear-elastic and plastic material parameters of fibers and binder. The experimental setup is simpler than atomic force microscopy and the microindentation also allows for measurements of properties at the microscale instead of the nanoscale, which is the scale of interest here. Moreover, the production of specimens for miniaturized classical test setups, such as a micro-tensile test, would require extracting homogeneous specimens of each constituent directly from the sandwich core. Compared with microindentation, where microscopy samples already available from Sec. 4.1 can be used, this production process is very cumbersome, especially since the properties of the constituents of the sandwich core are not known in advance.

As also already mentioned in Sec. 1.3.4, a grid indentation technique enables determining the properties of each constituent of a heterogeneous material through a single series of experiments. This series of indentation experiments is usually performed on a rectangular grid on the sample surface with an equal spacing between the measurement points. The corresponding properties of interest, the Young's modulus and the dissipated plastic work in this study, are then evaluated at each of the measurement points and an experimental distribution is obtained. Typically, a Gaussian distribution of the respective property for each individual constituent of the composite material is expected, see [83]. This yields a superposition of the Gaussian distributions in the overall experimental

results of the grid indentation.

These superimposed Gaussian distributions are then typically decomposed using statistical methods, such as those presented in [83, 84] for different types of composite materials and various statistical deconvolution methods. However, in order to ensure that the results are valid from a statistical point of view and that the individual indentations do not interfere with one another, several rules should be considered in the experiments. These rules were initially developed for the Berkovich tip geometry, which is a three-sided pyramid with a half angle of 65.3° between the central axis and the pyramid flats. These rules can be summarized as follows:

(i) The indentation depth h should not exceed a tenth of the characteristic length scale of the constituent, $h < 0.1\, l_{\mathrm{ch}}$, in order to measure the properties of the constituent only [83, 84].

(ii) The grid size should be significantly larger than the characteristic size of the constituents. This avoids statistical bias of the results toward one of the constituents owing to its spatial distribution on the sample surface [83, 84].

(iii) The minimum indent spacing should be ten times the indentation depth to prevent interference between individual indentation experiments [151].

The related test setup used for the microindentation experiments is depicted in Fig. 42. The experiments were performed under force control up to 50 mN at 25 mN/s (both: load and unload) with an LNP Nanotouch 3 (Ludwig Nano Präzision GmbH, Northeim, Germany). The indentation depth was measured by means of the (displacement) sensor. As discussed previously in this work in Sec. 4.1, the polished specimens from the microscopy at position 2 were used in the indentation tests. The grid indentation was performed at 121 points that were equally distributed within a square of 0.5 mm edge length on the specimen surface. Hence, there was a distance of 50 µm between each of the measurement points. The radius of the spherical indenter tip was 20 µm.

In the following, the fulfillment of the conditions (i)-(iii) to obtain valid results for the grid microindentation experiments is discussed. At this point, it should be noted again that a spherical indenter geometry instead of a Berkovich one was used, for which condition (i) was initially developed. However, it was developed based on analytical considerations of the projected contact area of the indenter surface, which was further supported by results from FE simulations in the literature, see [83, 152]. Hence, Sanchez-Camargo et al. [84] suggested applying this condition to spherical indentation as well by comparing the projected contact areas of Berkovich and spherical indenter geometries.

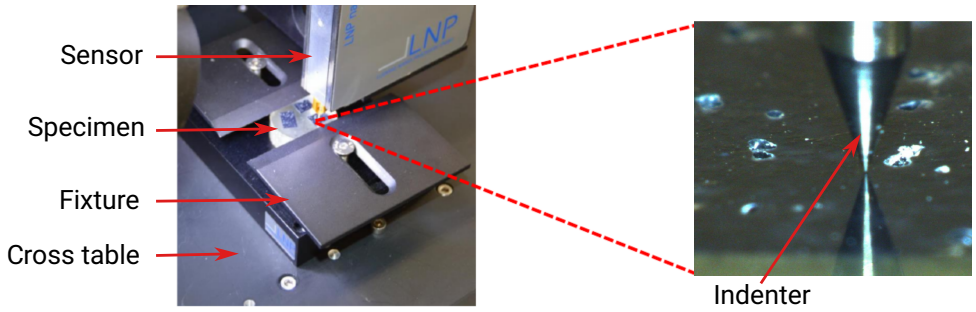

Figure 40: Test setup of the microindentation experiments.

For this purpose, they used the diameter of a projected contact area of the Berkovich indenter

$$d_{\mathrm{B}} = 2h \tan\left(\theta_{\mathrm{a}}\right), \tag{5.1}$$

which can be represented by a similar conical indenter with a half-apex angle $\theta_{\mathrm{a}} = 70.3°$ and the corresponding diameter for the spherical one

$$d_{\mathrm{S}} = 2\sqrt{2Rh - h^2}. \tag{5.2}$$

Furthermore, they chose the maximum indentation depth h, such that d_{B} and d_{S} were equal and condition (i) was also applicable to their experiments with a spherical indenter. Based on their arguments, the indentation depth at which $d_{\mathrm{B}} = d_{\mathrm{S}}$ holds is at about 4.5 µm in the experiments for this work.

Moreover, the characteristic size l_{ch} of the fibers is the fiber diameter of 50 µm. For the estimation of the characteristic size of the binder, the median nearest neighbor distance of the fibers, about 100 µm, can be determined from the experimental nearest neighbor distribution in Fig. 33. This value refers to the distance between the fiber centers and, therefore, the fiber diameter is subtracted. Then, one arrives at a median length of binder between two fibers of about 50 µm. Consequently, 50 µm is the critical characteristic length for the first condition (i), which is satisfied by the 4.5 µm indentation depth at which the projected contact areas of Berkovich and spherical indenter geometries coincide. The maximum indentation depth in all experiments with the spherical indenter remained well below this threshold. Thus, condition (i) can be considered satisfied in the experiments.

In order to satisfy condition (ii), the edge length of the grid was chosen to be ten times larger than the characteristic length of the microstructure. This value is expected to be sufficient to avoid a significant statistical bias of the measurement data. In [84], the

ratio between the grid size and the characteristic length was also on the same order of magnitude.

Condition (iii) was also derived only for the Berkovich indenter. However, in order to apply it to the spherical indenter, the same argument as for condition (i), that the projected contact areas of Berkovich and spherical indenters coincide at an indentation depth of about 4.5 µm, can be used. Therefore, the condition is also satisfied, as the spacing between the individual experiments is 50 µm, which is more than ten times the maximum indentation depth of less than 4.5 µm. As shown in Sec. 5.2, the plastic strain field from the FE simulations indicates that no interference occurred between the individual indentation measurements, which confirms that condition (iii) is satisfied.

The reduced modulus was evaluated according to the method of Oliver and Pharr [153] using the proprietary software of the test equipment. The resulting PDF of the measurement is shown in Fig. 41a. If the typical procedure from the literature had been followed, at this point, a statistical deconvolution method would have been applied to split the data into multiple Gaussian distributions and assign them to the corresponding constituent. The mean value of each Gaussian distribution would then have been considered as its reduced modulus. However, the results fall within a relatively narrow range, and the (mean) reduced moduli of fibers and binder are expected to be very close to one another. Based on this observation, the simplifying assumption is made to model the fibers and binder with the same (elastic) material parameters.

In the following, it is shown that the experimental data can also be attributed to a single Gaussian distribution from a statistical perspective. Note again that the results of a homogeneous material would correspond to a single Gaussian distribution and, hence, this would support the validity of the assumption. For this purpose, the data were tested for normality using several widely used methods.

One common graphical method to evaluate whether a dataset follows a certain statistical distribution is the Quantile-Quantile (QQ) plot. In this approach, the quantiles of the experimental data are plotted against the quantiles of the assumed model distribution. Fig. 41b depicts the QQ plot of the experimentally determined reduced modulus compared with the corresponding Gaussian distribution with a mean of 2770 MPa and a standard deviation of 680 MPa. The QQ plot and the confidence intervals were calculated following Fox [154, pp.37-41]. It can be observed that all experimental data points clearly fall within the 95% confidence bands, which indicates that the experimental data can indeed be attributed to a single Gaussian distribution.

In addition to the visual QQ plot, the experimental data were also investigated

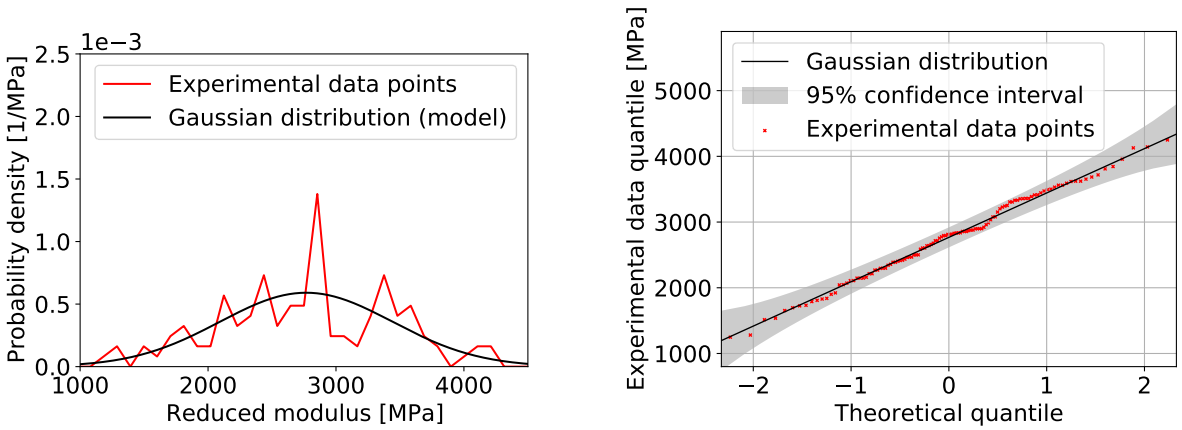

(a) (b)

Figure 41: Experimental PDF of the reduced modulus from microindentation experiments (a), and the corresponding QQ plot of the experimental data points and the Gaussian distribution model (b).

for normality using statistical tests. They provide a quantitative measure for the likelihood of the hypothesis of a normal distribution. For these normality tests, the SciPy implementations [155] of the Kolmogorov-Smirnov test, the D'Agostino-Pearson test [156], and the Shapiro-Wilk test [157] were used. In all of the tests, the probability (p)-value is computed. It is defined as a measure between 0 and 1 of the likelihood that the investigated data set occurs under the assumption that the null hypothesis (of normally distributed data) holds. The p-values obtained from the Kolmogorov-Smirnov, D'Agostino-Pearson, and Shapiro-Wilk tests were 0.79, 0.63, and 0.65, respectively. Usually, a p-value greater than 0.05 already indicates that the data can be considered Gaussian, see [158].

Hence, these results support the previous observations from the QQ plot that the experimental data can be attributed to a single Gaussian distribution. However, statistical normality tests are only indicators and cannot formally prove the null hypothesis of normally distributed data. They can only reject it with a given significance level if the resulting p-value falls below the specified threshold. Despite this limitation, both the statistical normality tests and the graphical QQ plot clearly support the simplifying assumption of modeling the fibers and binder with the same (elastic) material parameters.

In the next step, the Young's modulus E was determined from the reduced modulus

E_{red} using the Hertzian contact equation

$$\frac{1}{E_{\mathrm{red}}} = \frac{1-\nu^2}{E} + \frac{1-\nu_{\mathrm{ind}}^2}{E_{\mathrm{ind}}}. \tag{5.3}$$

The Poisson's ratio ν of 0.4 was estimated as a typical value for (epoxy resin-based) polymers. Young's modulus E_{ind} and Poisson's ratio ν_{ind} of the indenter material (tungsten carbide) are 630 GPa and 0.22, respectively. Consequently, the resulting Young's modulus of fibers and binder was determined to be 2330 ± 570 MPa.

5.2. Plastic properties

In the following, the identification of the parameters for the plastic material model with a linear Drucker-Prager yield condition, which is presented in Eqs. (2.2)–(2.6), is discussed. To reduce the number of parameters and ensure unique identification, the model was simplified to associative flow ($\bar{\eta} = \eta$) and perfect plasticity ($H = 0$). In the first step, it is investigated if the assumption to use the same elastic material parameters for fibers and binder can also be applied to the plasticity (and damage) model.

For this purpose, statistical investigations were conducted similar to the elastic case, where the dissipated work of the indentations

$$W_{\mathrm{diss}} = W_{\mathrm{t}} - W_{\mathrm{el}} \tag{5.4}$$

is used as a characteristic parameter for the plastic behavior. It is assumed that the dissipation is mainly caused by the plastic deformation and rate effects are neglected in the model for simplicity, see Sec. 2.1.

Besides rate effects, damage mechanisms can also dissipate energy during the indentation process. However, if damage mechanisms play a role in energy dissipation, this would further support the assumption of applying the same model parameters for fibers and binder in the damage model, as discussed in Sec. 5.3. In this case, the influence of damage mechanisms on dissipated work would be acceptable. Moreover, similar assumptions have been made in other studies, such as [159], where metals were investigated.

Here,

$$W_{\mathrm{t}} = \int_0^{h_{\max}} F_{\mathrm{load}}(h)\,\mathrm{d}h \tag{5.5}$$

corresponds to the total indentation work and

$$W_{\mathrm{el}} = \int_0^{h_{\max}} F_{\mathrm{unload}}(h)\,\mathrm{d}h \tag{5.6}$$

to the elastic work during the indentation, respectively. Furthermore, W_{diss}, W_{t} and W_{el} are also assumed to follow a Gaussian distribution for each constituent and, hence, also for a single homogeneous material. This assumption for W_{t} and W_{el} was successfully applied in [84] to identify the parameters of a plasticity model for different constituents of a heterogeneous material with a grid indentation technique, supporting its validity.

PDF and QQ plot for the dissipated work during indentation are presented in Figs. 42a and 42b, respectively. Both were calculated from the same experiments used for elasticity in the previous Sec. 5.1. Similar to the reduced modulus, all experimental data points clearly fall within the 95% confidence bands. This further supports the assumption that the experimental data correspond to a single homogeneous material. Moreover, p-values of 1.0, 0.24, and 0.64 were obtained in the Kolmogorov-Smirnov test, the D'Agostino-Pearson test, and the Shapiro-Wilk test, respectively. Consequently, both the statistical normality tests and the graphical QQ plot comparison support the simplifying assumption of modeling fibers and binder with the same plasticity model.

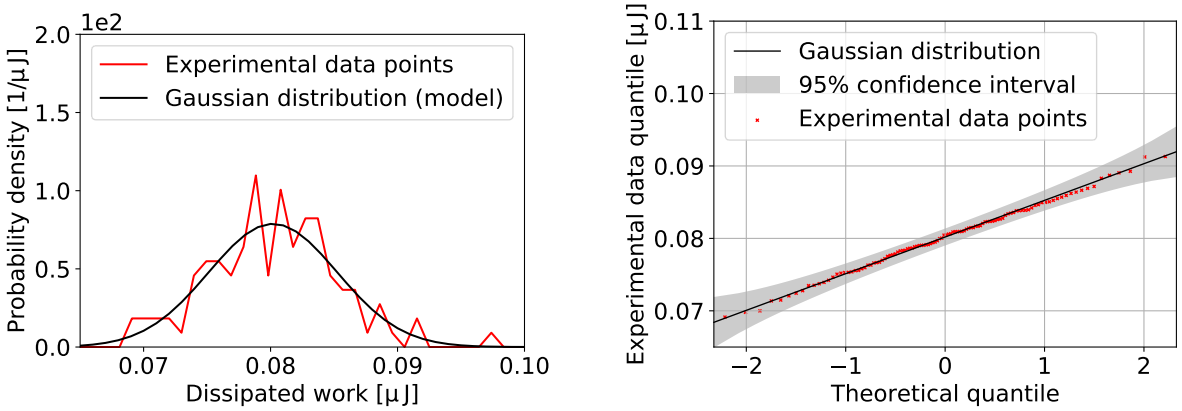

(a) (b)

Figure 42: Experimental PDF of the dissipated work from microindentation experiments (a), and the corresponding QQ plot of the experimental data points and the corresponding Gaussian distribution model (b).

In the next step, implicit FE simulations of the microindentation tests with the commercial software Abaqus (version 2018) [7] were used for the identification of parameters

η and d^0. Additional indentation experiments with a Berkovich indenter tip on the specimen surface were performed to determine a unique set of parameters for the linear Drucker-Prager model. This is not possible using spherical indentation experiments only, see [82].

As in the experiments with the spherical tip, the tests were force-controlled at 25 mN/s up to a maximum force of 50 mN. The distance between the individual indentations was at least 0.3 mm, which is significantly larger than ten times the indentation depth. This ensures that condition (iii) from Sec. 5.1 is satisfied and prevents interference between the individual indentations. Conditions (i) and (ii) can be neglected here because they are only relevant for a grid indentation on a heterogeneous surface and the same material model is assumed for fibers and binder.

The indentation tests with the Berkovich and the spherical tip were both modeled using an axisymmetric model in Abaqus, although the Berkovich indenter is a three-sided pyramid and hence not axisymmetric. However, as already mentioned in the previous Sec. 5.1, it is common to model a Berkovich shaped indenter as an equivalent (axisymmetric) conical indenter tip with a half-apex angle of 70.3°, such that the projected contact areas at each indentation depth agree [82, 160]. Owing to the fact that convergence was not achieved for all parameters under force control, all simulations were performed under displacement control with about 100 time increments.

The indenter materials tungsten and diamond are both much stiffer than the sandwich core and were modeled as rigid bodies in the FE model. The model was discretized with 7043 4-node "CAX4" and 3-node "CAX3" fully integrated elements. The edge length of the elements was at 0.25 µm directly beneath the indenter and up to 5 µm at the model boundaries. Model and mesh size of the FE model were determined by a convergence study. Owing to the relatively low computational time of about 7 hours for all simulations, a grid search was performed to identify the parameters of the plasticity model. The parameter η was varied from 0 to 0.9 in increments of 0.1, whereas d^0 was varied from 20 MPa to 200 MPa in increments of 10 MPa.

For each simulation, the overall absolute MSE

$$MSE_{\mathrm{a}} = \frac{1}{n_{\mathrm{s}}} \sum_{i=1}^{n_{\mathrm{s}}} \left[(F_{\mathrm{s}}^{\mathrm{exp}})_i - \left(F_{\mathrm{s}}^{\mathrm{sim}} \right)_i \right]^2 + \frac{1}{n_{\mathrm{b}}} \sum_{i=1}^{n_{\mathrm{b}}} \left[(F_{\mathrm{b}}^{\mathrm{exp}})_i - \left(F_{\mathrm{b}}^{\mathrm{sim}} \right)_i \right]^2 \tag{5.7}$$

was computed to evaluate the agreement between experiments and simulations. n_{s} and n_{b} correspond to the number of experimental data points of the spherical and Berkovich indentation measurements, respectively. For each indentation depth of all experimental

data points i, the corresponding measured forces $(F_{\mathrm{s}}^{\mathrm{exp}})_i$ and $(F_{\mathrm{b}}^{\mathrm{exp}})_i$ were compared with the respective forces from the FE simulation at the same indentation depth, $(F_{\mathrm{s}}^{\mathrm{sim}})_i$ and $(F_{\mathrm{b}}^{\mathrm{sim}})_i$. The simulated forces were interpolated among the simulated data points. Additionally, the subscript "s" refers to the spherical indenter tip and "b" to the Berkovich indenter tip.

The results of the grid search are shown in Fig. 43a, where the relative MSE

$$MSE = MSE_{\mathrm{a}}/\max\left(MSE_{\mathrm{a}}\right) \tag{5.8}$$

is presented. It can be observed that the optimal parameters are 0 for η and 90 MPa for d^0. These parameters actually correspond to a von Mises (J_2) plasticity model with a yield stress of 90 MPa. A comparison between the experimental and simulated curves that are computed with these parameters are shown in Figs. 43c and 43e. In both cases, the simulation results clearly lie within the experimental curves, and therefore, the resulting plasticity model leads to a sufficiently good agreement with the experiments.

Furthermore, the resulting equivalent plastic strain fields with values above 0.1% are shown in Figs. 43b and 43d. Compared with the indenter size in the model, these plastic strain fields are significantly smaller than the spacing between individual indents for both indenter tip types. This further confirms that the indentations do not interfere with one another. It should only be noted that the plastic strain fields differ slightly between the real Berkovich geometry and the axisymmetric simplification as a conical tip, see [161]. However, even if the plastic strain field is slightly larger in the real geometry, it remains an order of magnitude smaller than the 0.3 mm spacing between two indents.

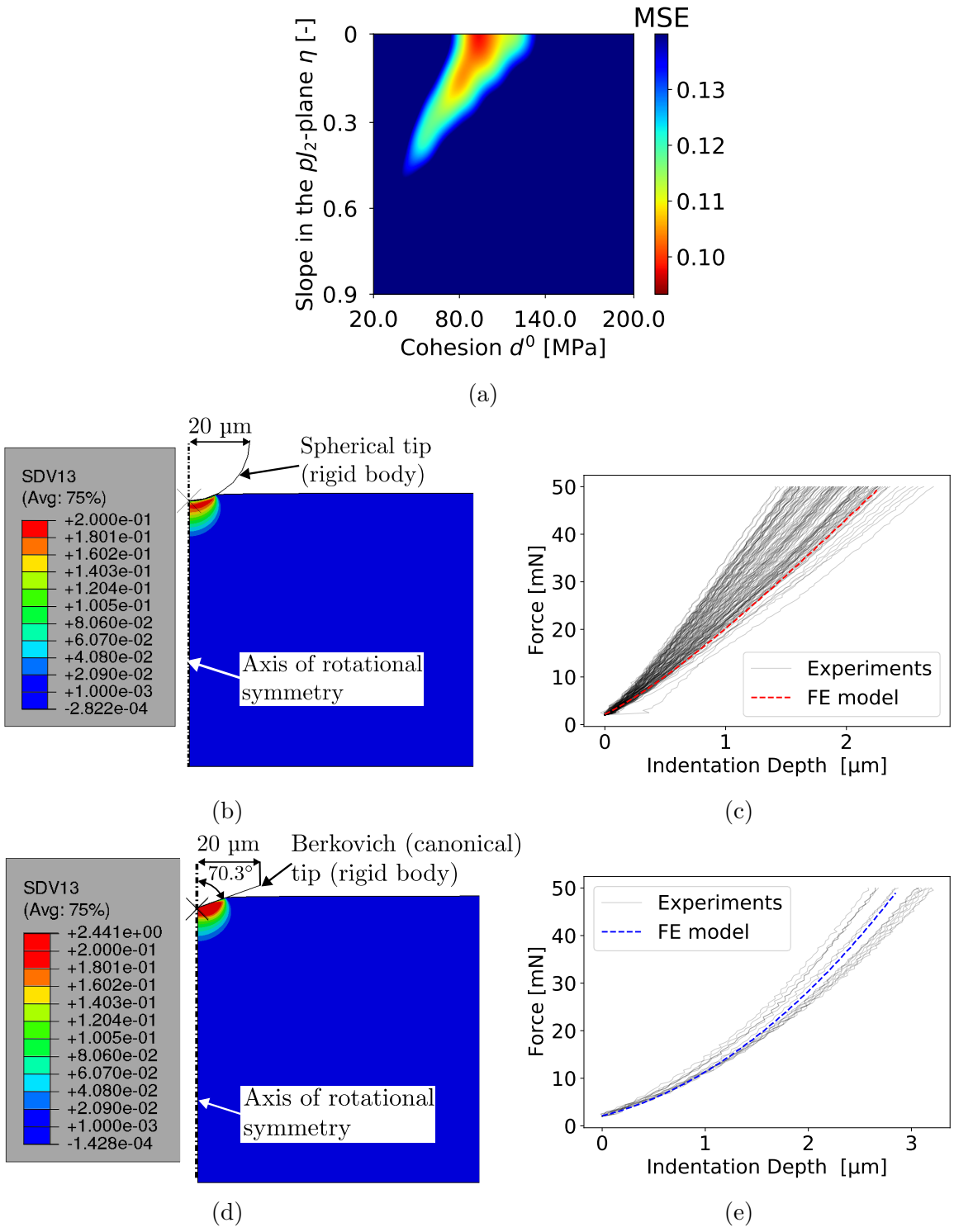

Figure 43: Relative MSE between the spherical and Berkovich microindentation experiments and the corresponding FE simulations for different parameters of the Drucker-Prager model (a).; FE model with equivalent plastic strain of the spherical (b) and Berkovich (d) indentation.; Comparison of experimental and simulated force-indentation depth curves for spherical (c) and Berkovich (e) indentation using the identified model parameters.

5.3. Damage properties

In the final step of the parameter identification, the parameters for the non-local damage model presented in Sec. 2.1 were determined. However, to the best of my knowledge, there is no commonly accepted method for identifying parameters for a non-local damage model using solely indentation experiments, where also high compressive stresses occur underneath the indenter tip. These compression loads are often less critical for the fracture of many materials compared with tensile loads, see e.g. [162, 163].

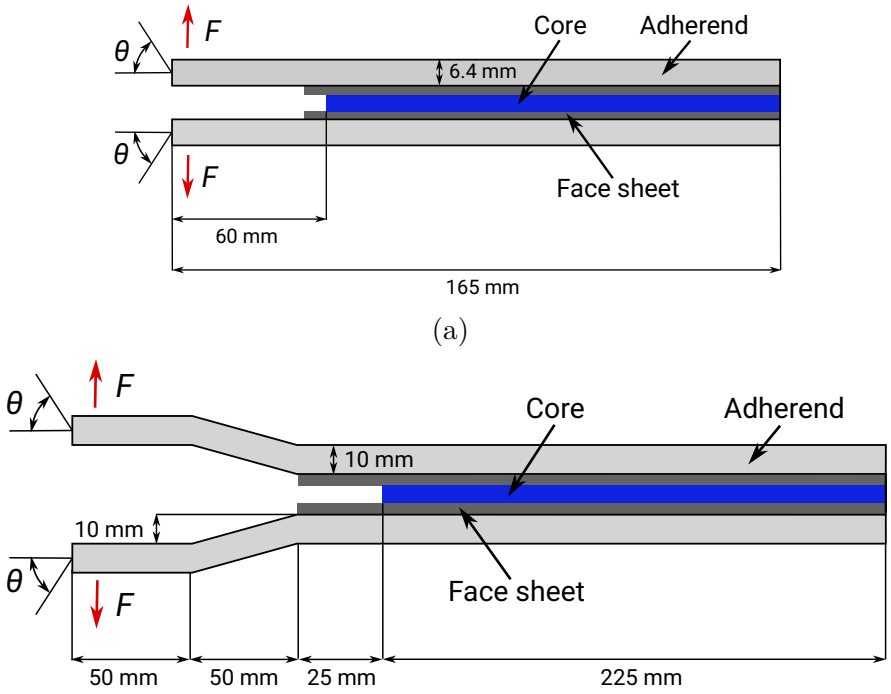

Figure 44: Scheme of the mode I DCB test and specimen geometry at Lab A (a) and Lab B (b).

A reinforced DCB test, which is shown schematically in Fig. 44, was used along with mode I FFT simulations for this purpose instead. As discussed in Sec. 1.3.5 on the state of the art in the experimental determination of TSLs, DCB tests combined with J-integral-based evaluation methods are a relatively well-established approach for determining the Energy Release Rate (ERR) and TSLs of adhesives in peel mode I. They can also be applied to any other material layer that can be modeled as a cohesive zone, see also Sec. 1.1.

In this work, a reinforced variant of the DCB test was developed for the sandwich plates, where the adherends are bonded to the specimen using a thin, stiff adhesive layer. This

layer has a negligible influence on the overall mechanical response of the joint, see also [164] for the analysis of a similar setup. In contrast to the microindentation experiments, the macroscopic DCB test provides only a homogenized TSL at the macroscale, without experimental data for the individual constituents at the microscale. Hence, the same assumption of a unified model for fibers and binder, previously applied to elasticity in Sec. 5.1 and plasticity in Sec. 5.2, is also adopted for the damage behavior.

Owing to the lack of experimental data for the individual constituents, statistical methods for testing the validity of the assumption cannot be applied here. Nonetheless, from a physical standpoint, it can be argued that the assumption is reasonable, since a ductile damage model is used. This model is driven by the (non-local) equivalent plastic strain and the validity of the assumption has already been statistically demonstrated for both the plastic and elastic behavior.

The reinforced DCB tests with the plates were conducted using two different test setups in separate laboratories: At Karlstad University, which is referred to as "Lab A" in the following, and at Technische Hochschule Mittelhessen, which is referred to as "Lab B". The corresponding schemes of the test and the specimen geometries for Lab A and B are depicted in Figs. 44a and 44b, respectively. At Lab A steel adherends with an out-of-plane width b of 5 mm were used, whereas the aluminum adherends at Lab B had a width of 15 mm. All surfaces were either ground or sandblasted and cleaned with acetone before the plates were bonded to the adherends.

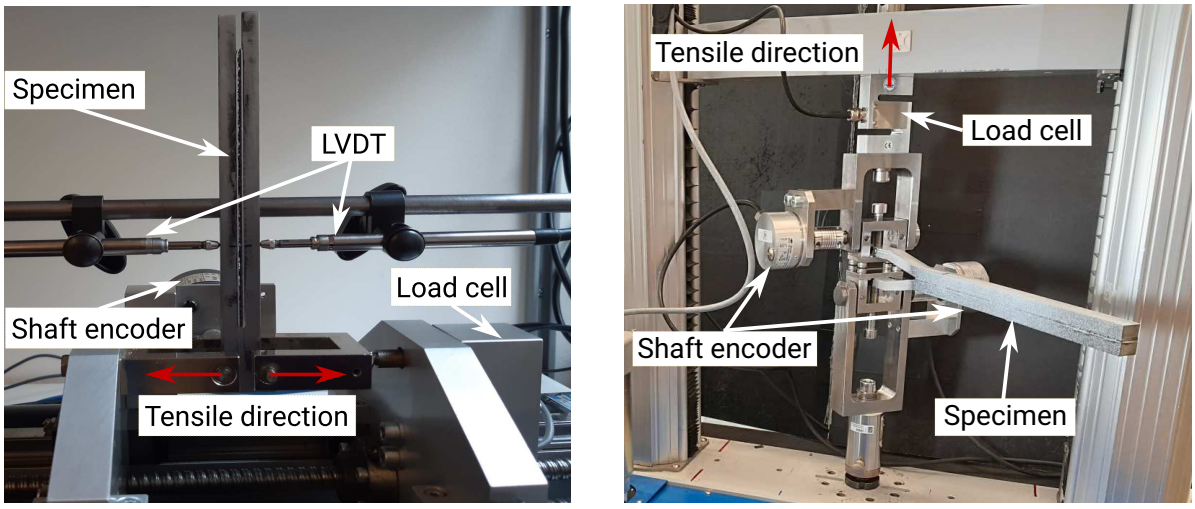

(a) (b)

Figure 45: Realized test setup of the mode I DCB test at Lab A (a) and Lab B (b).

Furthermore, the J-integral can be computed from the external load F, the beam

rotation angle of the adherends at the load introduction points θ, and the specimen width b as

$$J = \frac{2F\theta}{b} \tag{5.9}$$

[85]. Then, the mode I component of the traction vector, peel stress σ, is obtained by

$$\sigma(u) = \frac{\mathrm{d}J}{\mathrm{d}u}. \tag{5.10}$$

u is the mode I CTOD, which is measured as the separation between the two adherends at the initial crack tip.

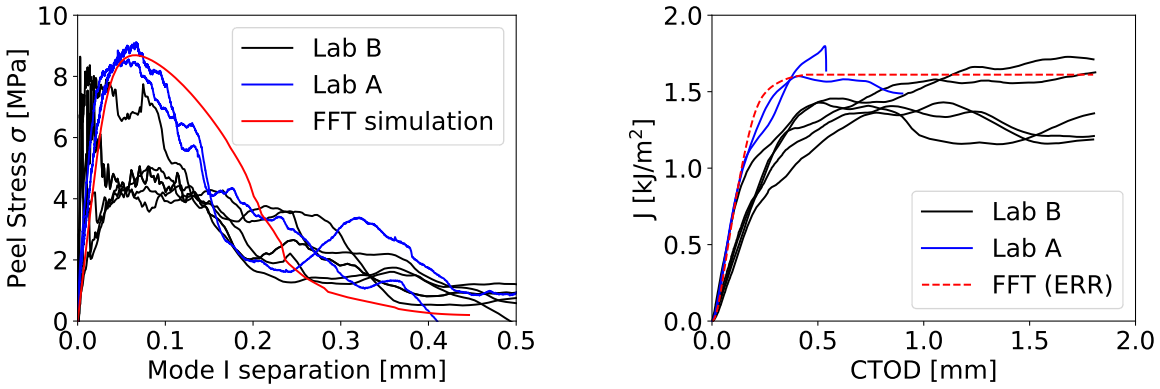

(a) (b)

Figure 46: Comparison of experimental and simulated TSLs with the identified model parameters of the non-local damage model (a) and the corresponding J-CTOD curves (b).

The test setup at Lab A is shown in Fig. 45a, where θ was measured using shaft encoders and the CTOD was measured u using Linear Variable Differential Transformers (LVDT). At Lab B, a three-dimensional camera system combined with Digital Image Correlation (DIC) was used for CTOD measurement. For clarity, the camera system is not shown in Fig. 45b, which presents the test setup at Lab B. As at Lab A, the beam rotation θ was also measured using shaft encoders. Moreover, all tests were performed under displacement control at a rate of 30 µm/s at the load introduction points.

The resulting TSLs for both test setups of the reinforced DCB test are shown in Fig. 46a and the J-CTOD curves are presented in Fig. 46b. The TSLs from Lab A generally tend to have a higher maximum stress (strength) than the curves from Lab B and some of TSLs measured at Lab B seem to be stiffer than their counterparts in the initial,

linear-elastic regime. In contrast to this, the measured critical ERRs, which are typically considered the plateau values of the J-CTOD curves in the DCB tests, are very similar in both test setups. Nevertheless, the J-CTOD curves from Lab A are slightly above the curves from Lab B, especially in the initial part, and the J plateaus are much shorter. The latter can be very likely explained by the different specimen geometries and the different adherend materials used. For the shorter and stiffer steel adherends at Lab A, a lower crack length is needed for a complete failure of the specimen than in the case of the longer, less stiff adherends at Lab B. Hence, the measured separation at the initial crack tip, the CTOD, is also smaller, when the specimen fails completely. Additionally, the differences in the measured TSLs could be attributed to the different measurement equipment and sensors as well as different production batches of the plates used in the experiments.

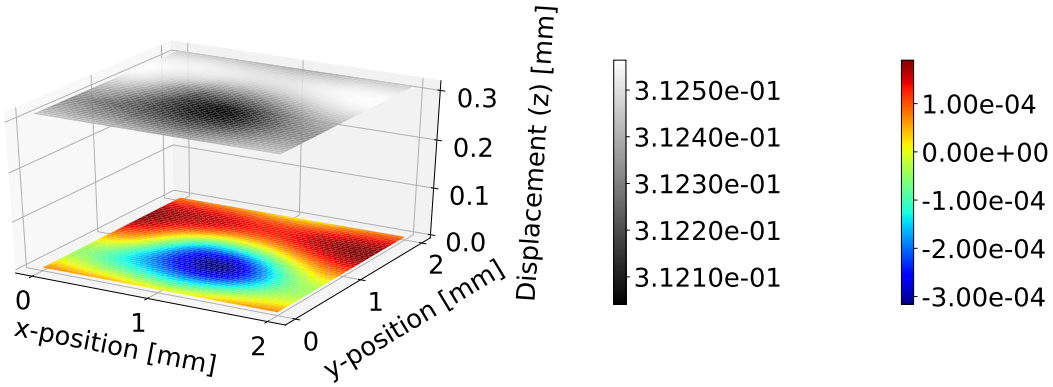

Figure 47: z-component of the displacement field at the boundary of the sandwich core in mode I for a separation of 0.3124 mm.

The results were then used to adjust the parameters of the linear damage evolution law, p_{nl}^{0} and $p_{\mathrm{nl}}^{\mathrm{f}}$, until the resulting TSL from a mode I FFT simulation matched the experimental TSLs. Following the FFT-based homogenization scheme for cohesive zones from Sec. 3, a mode I separation u was prescribed according to Eq. (3.9) in the FFT solver, and the resulting peel stress was obtained by Eq. (3.15). The virtual model of the microstructure from Sec. 4 and the parameters for the elastic-plastic model of fibers and binder, which were determined with the microindentation experiments, were used in the simulations. The characteristic length parameter was set to 40 µm based purely on numerical experiments to ensure both a realistic localization zone for crack propagation and a smooth convergence of the solution scheme.

As discussed in Sec. 3, the marginal layers were used to approximate the Dirichlet-

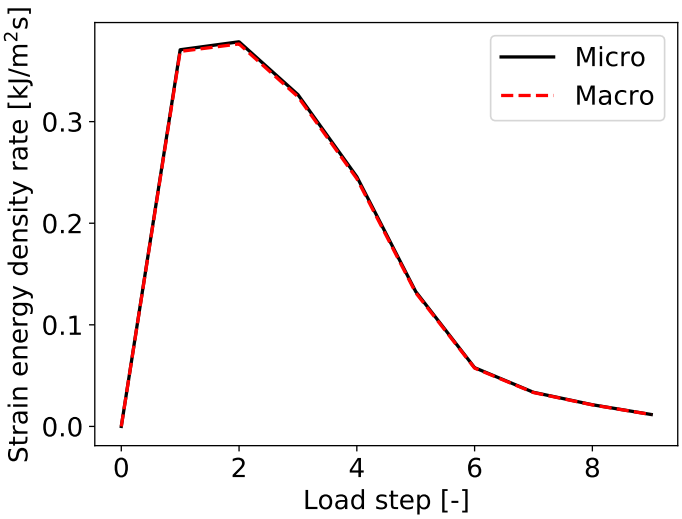

Figure 48: Comparison of energy rate density (Hill-Mandel condition) at the macro- and microscale for the sandwich core in peel mode I.

type boundary conditions at the interface between the cohesive zone, the core, and the surrounding bulk, the face sheets in this case. The parameters of the marginal layers are presented in Sec. 4.2.3. Following the recommendations for the parameter estimation from Sec. 3.3.3, the accuracy of the desired boundary conditions can be evaluated in Fig. 47. It shows the z-component of the displacement field at the interfaces of interest for a separation of 0.3124 mm, which was computed using Eq. (3.16). The observed deviations are on the order of 10^{-3} relative to the applied separation and were the most critical throughout the entire load history. This value was also found to be a sufficient approximation of the boundary conditions in Sec. 3.3 for the adhesive layer. Hence, it can be considered adequate in this case as well.

To assess whether the Hill-Mandel condition is satisfied with a sufficient accuracy, the energy density rates of the macro- and microscale from the left- and right-hand sides in Eq. (3.11) are compared in Fig. 48. The strain rates were calculated using a forward finite difference between the load steps, for which the full strain fields were stored in the simulation. Since the FFT simulations are not time-dependent, it should be noted that the selection of the time steps and therefore exact values of the energy density rates is arbitrary. The good agreement between both curves confirms that the Hill-Mandel condition is well satisfied.

Owing to the relatively high computational time of 37 days for the full FFT simulation, no mathematical optimization technique could be applied directly. Therefore, the sought

parameters p_{nl}^{0} and $p_{\mathrm{nl}}^{\mathrm{f}}$ were adjusted manually until the agreement between the simulated TSL with the experimental TSLs was sufficient. The final simulated TSLs are shown in Fig. 46a, and the identified model parameters for fibers and binder are presented in Tab. 3.

Moreover, the ERR can be computed by integrating the TSL over the CTOD. The ERR from the FFT simulation is also depicted in the J-CTOD curves of the experiments in Fig. 46b. A good agreement is observed with the data from Lab A, whereas the agreement with the data from Lab B is less accurate. The plateau value corresponds to the critical ERR and matches well with all experimental data.

Table 3: Identified material parameters for the FFT-based homogenization of the sandwich core.

	E (MPa)	ν (-)	d^0 (MPa)	η (-)	p_{nl}^{0} (-)	$p_{\mathrm{nl}}^{\mathrm{f}}$ (-)	l_{d} (µm)
Fibers and binder	2330	0.4	90	0	0.07	1.5	40
Marginal layers	70000	0.33	-	-	-	-	-

6. Model validation using mode III Split Cantilever Beam tests

6.1. Experimental procedure

This section describes the experimental validation procedure for the novel modeling approach of the sandwich core in Hybrix$^{\mathrm{TM}}$ plates. For this purpose, macroscopic fracture mechanics experiments in out-of-plane shear mode III were compared with corresponding FFT and FE simulations at the macroscale. The tests were evaluated using a J-integral approach and OFS measurements of the bending strain, which are also discussed in Sec. 1.3.5 on the corresponding state of the art. Mode III represents a load case that had not been previously used for the identification of the material model parameters and is therefore appropriate for a validation.

Reinforced Split Cantilever Beam (SCB) tests [3] were carried out as the mode III tests in this work. Similar to the mode I DCB tests from the previous Sec. 5.3, a plate was bonded to the adherends with a thin layer of adhesive. The aluminum adherends have a C-shaped cross section to position the shear center outside the adherends within the plate. This reduces the mode I load components that occur owing to the typical beam

torsion for other cross section shapes. More details regarding the theoretical background and design of the test can be found in [3, 4].

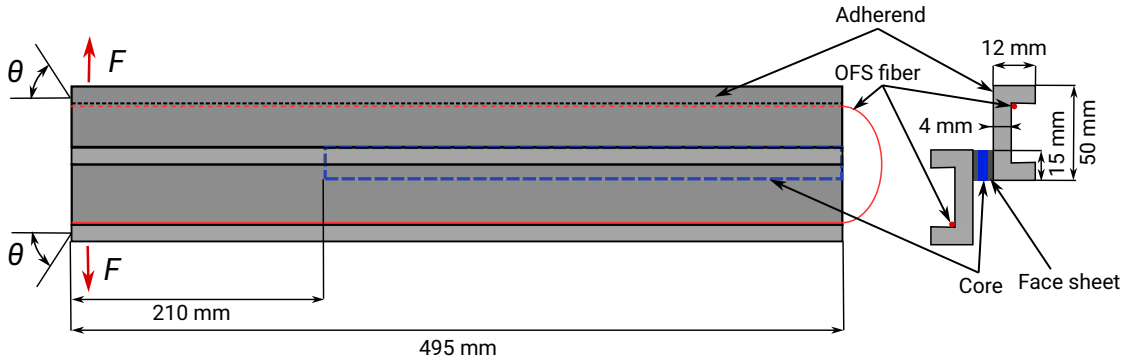

Figure 49: Scheme of the mode III SCB test and specimen geometry.

The specimen geometry and a scheme of the SCB test are shown in Fig. 49. Similar to the DCB tests, a displacement rate of 30 µm/s was applied at the load introduction points. During the SCB tests, force, beam rotation, and CTOD were recorded. The external J-integral was then computed using Eq. (5.9), and the mode III component of the traction vector, shear stress τ_{III}, was calculated as

$$\tau_{\mathrm{III}}(w) = \frac{\mathrm{d}J}{\mathrm{d}w}, \tag{6.1}$$

where w denotes the mode III CTOD.

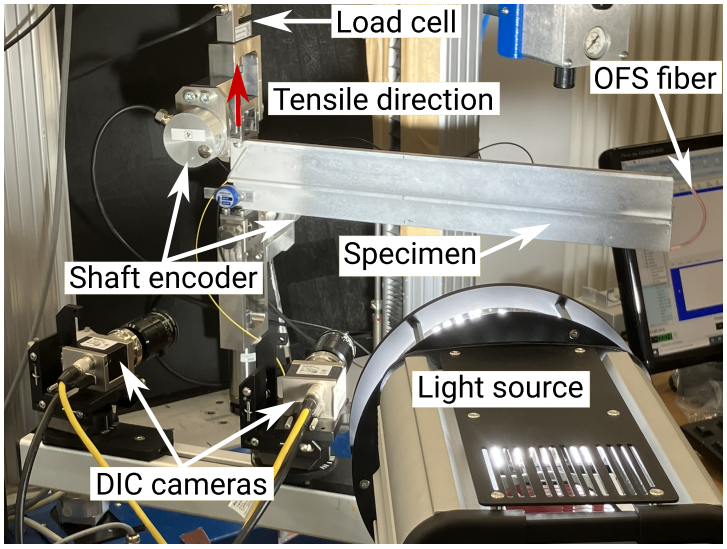

Figure 50: Realized test setup of the mode III Split Cantilever Beam test.

Moreover, the ODiSI 6101 (Luna Inc., Blacksburg, Virginia, USA) OFS measurement system was used to record the bending strain in the adherends during three of the tests. The OFS fiber was bonded to the inner edge of the C-shaped cross section on both adherends, as shown in Fig. 49, such that the compressive part of the bending strain was measured. With this system, a measurement point can be obtained every 0.65 mm along the fiber. Using the proprietary software of the OFS system, markers were set along the fiber to correlate each spatial measurement point with its corresponding position on the adherend.

The realized SCB test setup is presented in Fig. 50. Similar to the DCB test setup at Lab B in Fig. 45b, the load cell, shaft encoders, and DIC system were used to measure force F, beam rotation θ, and the mode III CTOD w during the tests. The OFS fiber itself is barely visible in the figure owing to its small diameter. However, the "free" segment of the OFS fiber, which is not bonded to the adherends, is protected with an additional heat shrink tubing and can therefore be seen in Fig. 50.

6.2. Numerical modeling

In order to validate the proposed modeling approach, a mode III FFT simulation was performed using the virtual model of the microstructure from Sec. 4 and the material model from Sec. 2.1 with the parameters from Tab. 3. The FFT-based homogenization scheme presented in Sec. 3 was applied. A mode III separation w was prescribed according to Eq. (3.9), and the resulting shear stress was computed from the results of the FFT simulation by Eq. (3.15). The full simulation required approximately 31 days.

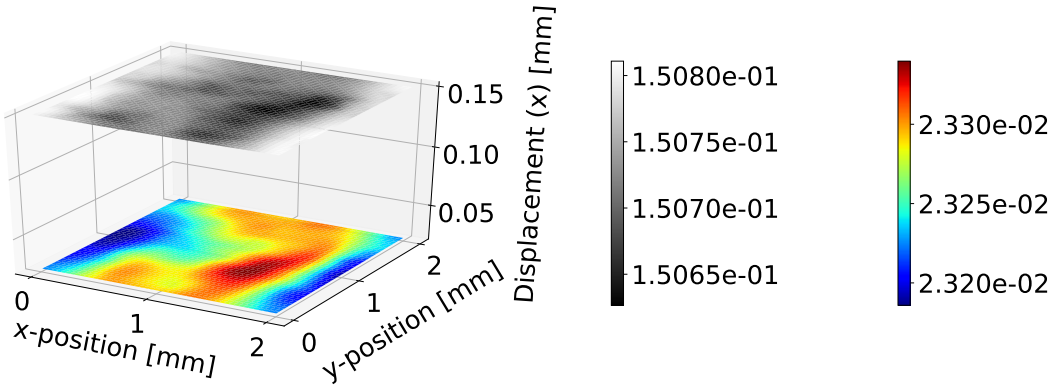

Figure 51: x-component of the displacement field at the boundary of the sandwich core in mode I for a separation of 0.1275 mm.

The Dirichlet-type boundary conditions, which are required in the FFT homogenization

for cohesive zones according to the results from Sec. 3.1, were approximated using marginal layers with the parameters from Sec. 4.2.3. Following the recommendations from Sec. 3.3.3, the accuracy of the approximation was evaluated as in Sec. 5.3 for mode I. For this purpose, the displacement fields at the corresponding interfaces, computed from Eq. (3.16), are presented in Fig. 51 for a separation of 0.1275 mm. At this separation, the largest deviations from the desired boundary conditions were observed throughout the load history. The maximum deviations are on the order of 10^{-3} relative to the applied separation. This is the same order of magnitude that was found to be sufficient in Sec. 3.3.2 for the adhesive layer, and can therefore be considered a reasonably accurate approximation for the homogenization. Furthermore, the close agreement between the energy density rates at the macro- and microscale in Fig. 52 confirms that the Hill-Mandel condition from Eq. (3.11) is well satisfied.

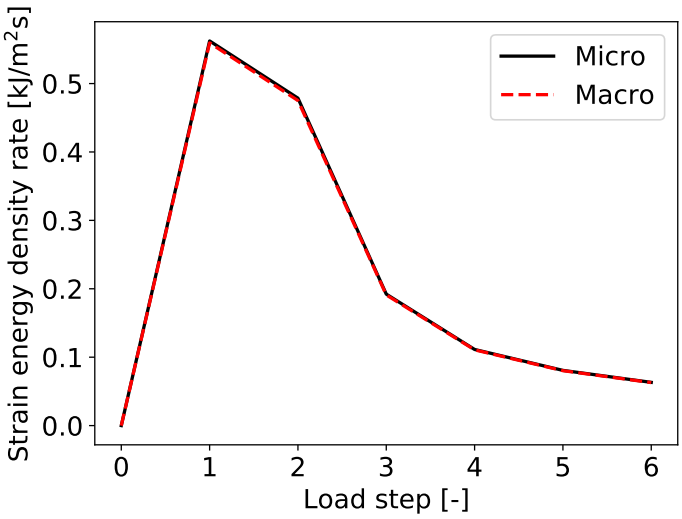

Figure 52: Comparison of energy rate density (Hill-Mandel condition) at the macro- and microscale for the sandwich core in mode III.

In the next step, an implicit FE model of the SCB test was created in Abaqus (version 2018) [7]. The TSLs from the single mode FFT simulations were implemented as the constitutive law of the CZM for the Hybrix^{TM} sandwich core using a tabular damage evolution and the cohesive stiffness. In this tabular damage evolution, the estimated scalar damage variable, the corresponding separation since damage initiation, and the energy-based mode mixity, 0 for peel mode I and 1 for shear, were specified. In addition, isotropy of the damage evolution in both shear modes II and III was assumed.

For each separation, the damage variable was estimated as one minus the ratio of the

stress from the FFT simulations and the undamaged stress computed as the product of the cohesive stiffness with the respective separation. It should be noted that this implementation does not account for plastic behavior and attributes all non-linearities in the TSL solely to damage. However, this simplification can be made, as only monotonic loading without unloading is considered. The respective mixed-mode behavior is then inherently interpolated by Abaqus, such that even the small mixed-mode contributions that occur during the test are taken into account. The corresponding energy-based mixed-mode variable was always above 0.98 throughout the entire cohesive zone, and thus very close to a pure shear mode loading.

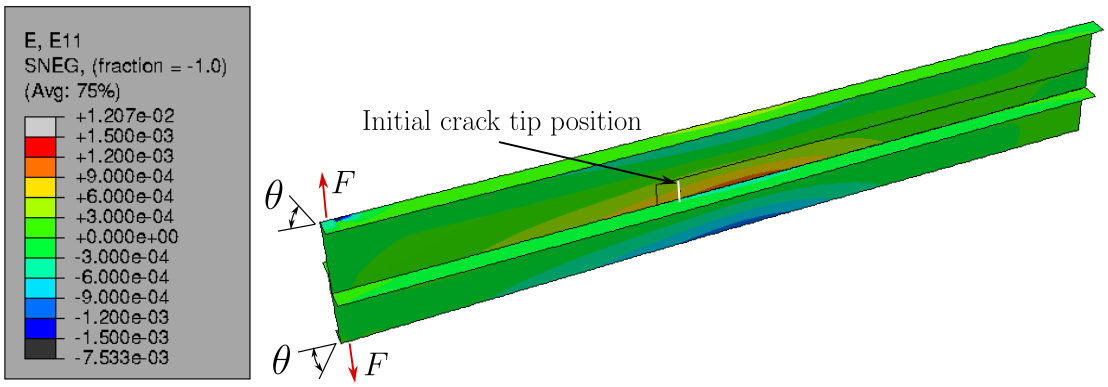

Figure 53: Bending strain in the FE model of the mode III SCB test.

In the FE model, cohesive zone elements of the type "COH3D8" were used, while the face sheets were meshed with "SC8R" type continuum shell elements. The adherends were discretized using fully integrated shell elements of type "S4". An edge length of 3 mm was used for all element types. The meshes of adherends and face sheets were then connected by surface-to-surface tie constraints. Additionally, Multi-Point Constraints (MPC) were used to connect the load introduction points to the adherends. At these points, force F and beam rotation θ were evaluated in the simulations. The boundary conditions were also applied at the load introduction points in the FE model. In accordance with the test setup, all rotations and displacements were constrained, except for the tensile direction and beam rotation, as shown in Fig. 53. Default settings were used for all simulation parameters not explicitly mentioned in this paragraph. The FE simulation was not stopped until it failed to converge.

6.3. Results

The resulting F-θ and J-CTOD curves from the FE simulation and the experiments are shown in Figs. 54a and 54b. Fig. 54c presents the TSLs from the FFT simulation and experiments. Moreover, the bending strain curves, which were obtained with the OFS system and the FE simulation, are depicted in Figs. 55b, 55c, and 55d. They were determined at a CTOD of 0.1 mm, 0.5 mm, and 1 mm, respectively. The corresponding CTOD values are marked with dashed blue lines in the F-CTOD curves in Fig. 55a.

The F-θ curves in Fig. 54a show that the initial slope of the simulated curve is steeper than that of the experimental results. In contrast to the deviation of the initial slope, the predicted overall joint strength, the maximum force, is in good agreement with the experiments. This agreement also applies to the shape of the force plateau and the slope of the final unloading phase.

A deviation between the simulation and the experiments can be found in the initial part of the J-CTOD curves in Fig. 54b, while the other parts of the curves agree satisfactorily. In particular, the experimental critical ERR, which is considered to be the maximum value of the J-integral, is captured well by the simulations. Furthermore, the J-CTOD curves reveal that, unlike the mode I DCB tests in the previous section, no plateau value for J was reached in the final phase of the experiment. An explanation is that the traction field behind the crack tip reached the end of the specimen before a J plateau could form. This is critical for the computation of the TSLs based on the J-integral, as it is required that no load is present at the end of the specimen. However, the maximum CTOD, which is shown in Fig. 54c, is at 1 mm only. A significant effect on the TSL can therefore be neglected, since Fig. 55d indicates that the specimen end remains free of bending strain and is thus not subjected to any significant load at this CTOD value.

Given the challenges encountered in this work, an overall satisfactory agreement between the TSLs in Fig. 54c is observed, which indicates the plausibility of the novel modeling approach and the corresponding models. Nonetheless, the shear strength of the sandwich core is overestimated by the FFT simulations and the predicted shear stress in the final segment of the TSL is lower than in the experiments. This overestimation of strength can explain the deviation in the initial part of the simulated J-CTOD curves, as it results in higher values of the J-integral. Up to a shear CTOD of about 0.35 mm, the predicted shear stress in the TSL gradually converges toward the experimental values and falls below them for larger CTODs. Consequently, the global J values in the simulations also approach the experimental ones, which leads to an agreement of the curves in the middle and final parts.

Similar observations as for the J-CTOD curves can be made for the F-CTOD curves in 55a: A deviation between the simulation and the experiments occurs in the initial part below a CTOD of 0.35 mm. Above this value, the simulated curves approach the experimental ones, so that the middle and final parts as well as the maximum force, the joint strength, match very well. As for the J-CTOD curves, this observation can be attributed to the overestimated strength in the simulated TSL.

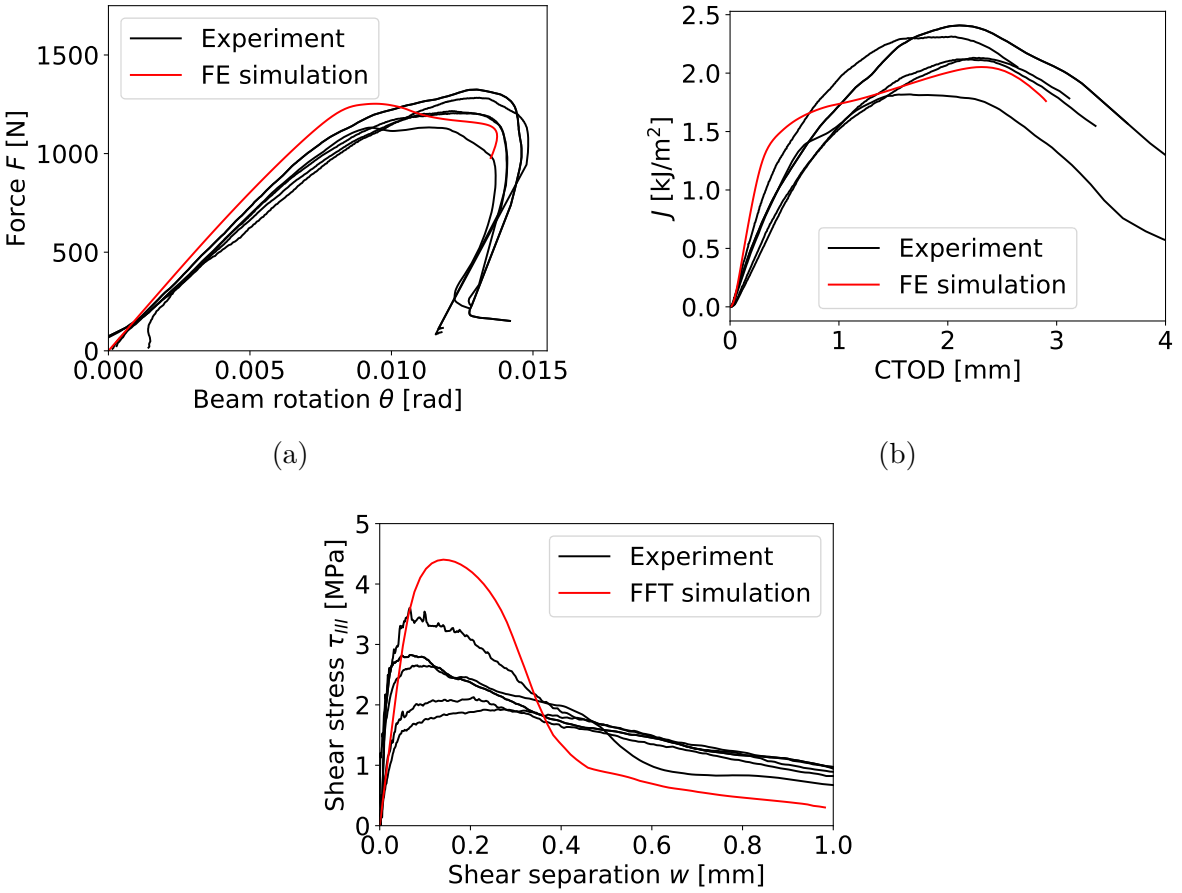

(a) (b)

(c)

Figure 54: Comparison of F-θ curves (a), J-CTOD curves (b), and TSLs (c) from the experiments and simulations.

Furthermore, the investigation of the bending strain distribution along the adherends provides valuable information on the accuracy of the simulated traction field in the sandwich core behind the crack tip. As discussed in Sec. 1.3.5, the bending strain is directly linked to the traction field through Euler–Bernoulli beam theory. In order to

determine this relationship, the bending moment is first computed from the bending strain, the area moment of inertia, and the Young's modulus of the adherends. Differentiating twice along the adherend then yields the line load, which is caused by the tractions in the cohesive zone. Dividing this line load by the specimen width provides the corresponding traction field, see [99].

However, bending strain measurements can be quite noisy, and numerically computing the second derivative of a noisy signal requires substantial filtering, which introduces additional uncertainty in the interpretation of results. Since the goal is only to compare the traction fields behind the crack tip to evaluate the modeling approach, it is more straightforward to directly compare the bending strain distributions. These measurements already implicitly contain the necessary information about the traction field, which eliminates the need for further computations.

The simulated bending strain distribution along the adherends was taken from the integration points that are the closest to the path of the OFS fiber on the specimen in the experiments. The results are presented in Figs. 55b, 55c, and 55d for CTOD values of 0.1 mm, 0.5 mm, and 1 mm, respectively, alongside the corresponding experimental results. In contrast to the experimental curves, which depict results from both adherends, only one curve is shown for the simulation, as the results are identical for both adherends. In addition, the bending strain field in the FE model is shown in Fig. 53 for a CTOD value of about 0.5 mm.

In the next step, the physical plausibility of the curves is examined before interpreting the results in the context of the validation of the novel modeling approach. First, the extreme value of the bending strain distribution, in this case the minimum, serves as a reliable criterion for determining the crack tip position, see [165]. In Fig. 55b, the initial crack tip position observed in the experiments and the simulation is approximately 210 mm from the loaded end of the specimen. This distance corresponds to the expected initial crack tip position from specimen production, see Fig. 49.

The physical plausibility of the curves can be further evaluated by investigating the region ahead of the crack tip, which corresponds to the free lever arm of the specimen. According to beam theory, the bending strain in this region should be a straight line, which passes through the abscissa at the load introduction point. This expectation is also at least approximately confirmed in the corresponding curves from experiments and simulation, except for the simulated one in Fig. 55b at the CTOD value of 0.1 mm. Here, the simulated bending strain distribution at the free lever arm is not completely linear, which may be caused by a slight torsion of the C-shaped adherends in the beginning

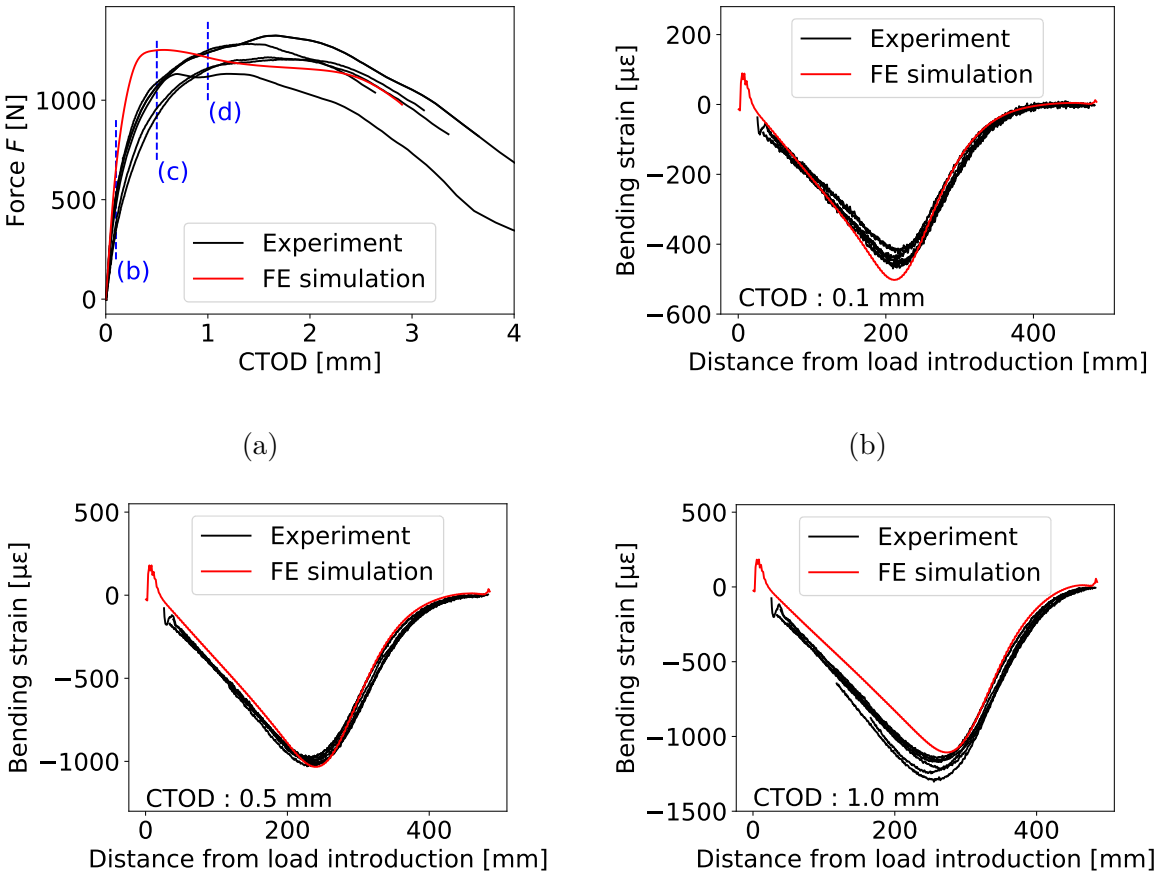

Figure 55: Comparison of FE simulation and experiments: (a) F-CTOD curve with markers indicating the corresponding CTODs of the OFS measurements (dashed blue), (b) OFS measurement at a CTOD of 0.1 mm, (c) 0.5 mm, and (d) 1 mm.

of the test. However, it becomes approximately linear in both other figures at higher CTOD values, which indicates that the bending strain distribution in the simulation is also plausible from a physical standpoint.

Apart from the plausibility of the results themselves, a satisfactory agreement was found between the bending strain distribution from the FE simulation and the OFS measurements in the experiments. At CTODs of 0.5 mm and 1 mm, the crack tip position was overestimated by the simulation. In the experiments, the crack propagates by 17–21 mm between CTODs of 0.1 mm and 0.5 mm, whereas in the simulations, the crack growth is 30 mm over the same interval. The corresponding crack propagation between CTODs of 0.1 mm and 1.0 mm is 39–52 mm in the experiments and 65 mm in

the simulation, respectively.

6.4. Comparison of experimental fracture surfaces with simulated crack patterns

In order to further evaluate the novel modeling approach for the Hybrix^{TM} sandwich core, a qualitative comparison was carried out between the experimental fracture surfaces and the simulated crack pattern from the FFT simulation. The typical experimental fracture surfaces from a SCB test are shown in Fig. 56a, where the fibers appear black, and the binder is transparent with a shiny surface.

Furthermore, the aluminum face sheet is visible through the transparent binder at the lower fracture surface in the figure. Here, a few remaining fiber fragments and a thin layer of binder, which covers the face sheet, can also be observed. This face sheet corresponds to the top face sheet from Fig. 18. Most of the remaining fibers and binder are located at the opposite fracture surface, the upper one in Fig. 56a. This shows that the global crack occurred close to the top face sheet. Nevertheless, the fracture still occurred within fibers and binder, and was therefore a cohesive fracture within the core. Moreover, the bright spots on the upper fracture surface represent microcracks. They are interconnected through the pore space, which both together form the global crack.

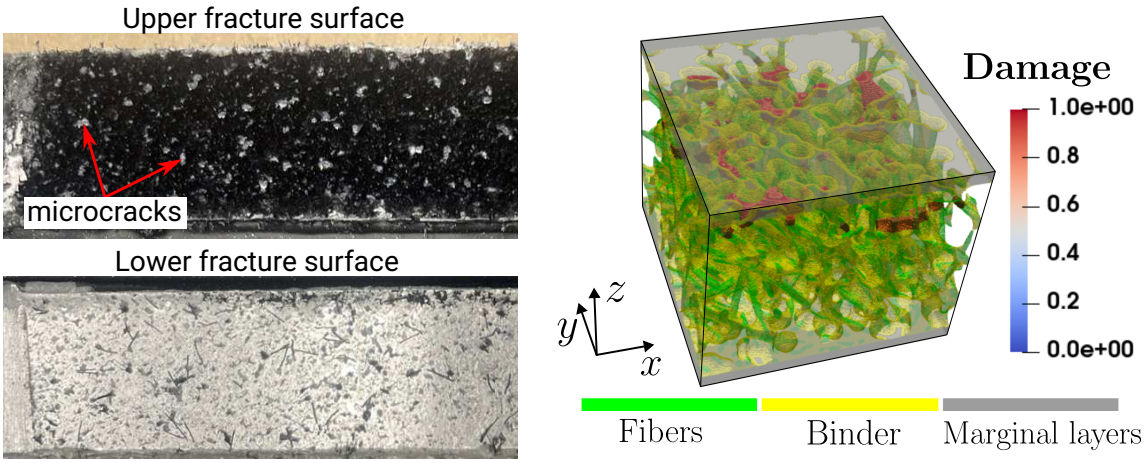

(a) (b)

Figure 56: Typical fracture surface from a SCB test (a) and crack pattern from the mode III FFT simulation (b).

The resulting crack pattern from the FFT simulation is shown in Fig. 56b, where microcracks are identified as regions where the scalar damage variable D exceeds 0.9. The

microcracks are concentrated in specific areas of the virtual model of the microstructure and are not directly connected. Similar to the analysis of the experimental fracture surface, this suggests that the global crack consists of both microcracks and pore space. The figure also reveals that the microcracks, and consequently the global crack, are located near the top face sheet, which is represented by the upper marginal layer in the simulation. Furthermore, the fracture occurred within the fibers and binder. Both of these findings are consistent with the experimental observations. Therefore, it can be concluded that the crack pattern in the FFT simulation and the experimental fracture surface from the SCB tests are generally in reasonable qualitative agreement.

Furthermore, high-resolution images of the typical fracture surfaces in a DCB test from Lab A were taken and compared with the crack pattern from the corresponding mode I FFT simulation, see also Sec. 5.3 for details on test setup and simulation. The experimental fracture surfaces are shown in Figs. 57a and 57b, where the former corresponds to the bottom face sheet and the latter to the top face sheet. Both the fracture surfaces and the simulated crack pattern in Fig. 57c are very similar to those observed in mode III. They also show a reasonable qualitative agreement with one another.

Nevertheless, these high-resolution images allow for a more detailed investigation of the microcracks than the mode III fracture surfaces. In the zooms on the right-hand side of both fracture surfaces, even individual fibers can be identified within the microcracks, and broken fibers and binder appear on both sides of the crack. Hence, the crack propagates through both constituents, as also observed in the simulation. This finding further supports the reasonable qualitative agreement between the experimental and simulated fracture behavior of the core.

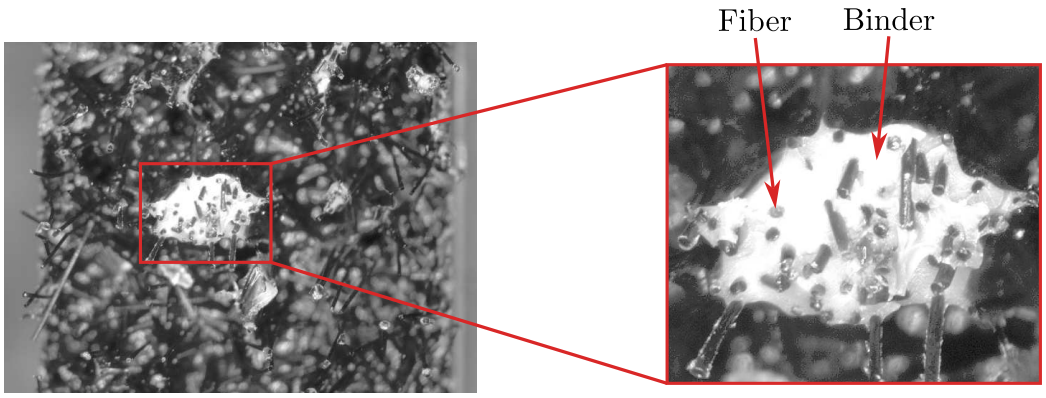

(a)

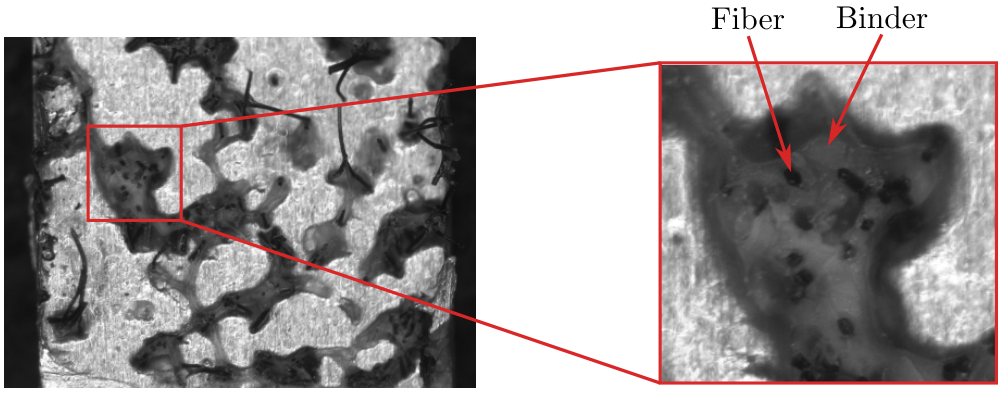

(b)

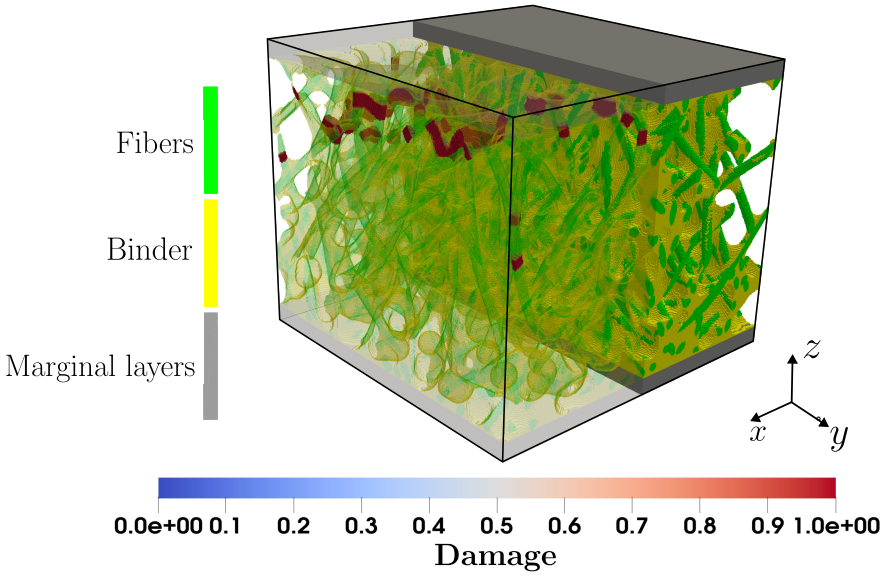

(c)

Figure 57: Typical fracture surface in DCB test from Lab A (a) and (b); and crack pattern in mode I FFT simulation (c).

6.5. Discussion

In summary, the simulations matched the experimental results from the mode III SCB test sufficiently. Particularly, the joint strength and the ERR, which are both important global parameters in fracture mechanics, were predicted well by the FFT simulations. Nevertheless, deviations in the predicted strength in the TSL, the initial parts of the J-CTOD and F-CTOD curves, and an overestimation of the simulated crack length occurred. Since many simplifications and assumptions had to be made throughout this work, it can still be concluded that the modeling approach, along with the developed FFT-based homogenization scheme for cohesive zones, can be deemed validated.

The observed deviations may be attributed to model simplifications and the identification process for the material model parameters of fibers and binder. The simulated strength in the DCB test for the identification of the damage parameters was also already at the upper limit of the experimental results, similar to the SCB tests. During the identification of the damage parameters, it was found that these parameters have only a minor influence on the strength within the relevant range and that the strength is mainly determined by the elasticity and plasticity model.

Accordingly, the source of these deviations is likely related to the microindentation experiments for the identification of the plastic and elastic material parameters. These experiments represent a fundamentally different load case compared with the DCB and SCB tests, where a high hydrostatic pressure occurs beneath the indenter. Some polymers exhibit an increased yield strength under this high hydrostatic pressure compared with shear or tensile load cases. Moreover, hardening is not considered in the perfectly plastic model, and possible rate effects are neglected, which could also influence the simulation results.

7. Conclusions

First, a novel FFT-based homogenization scheme for cohesive zones was developed in this work. It is based on the existing FFT-based homogenization method for bulk materials and incorporates a non-local, implicit gradient ductile damage model. The novel scheme takes advantage of the reduced computational times expected from FFT-based homogenization methods compared with classical FEM-based methods, as observed for many materials and discussed in Sec. 1.3.1.

For this purpose, the Lippmann-Schwinger-type equations for both the homogenization and damage regularization problems were derived and discretized using the staggered grid

and Moulinec-Suquet discretization methods, respectively. A novel displacement-based FFT solver, which uses the Barzilai-Borwein solution method, and a fixed-point iteration method for damage regularization were then implemented in Fortran as fully parallelized high-performance code. The coupled, multi-physics regularization and homogenization problem is solved in a staggered manner within the solver.

Moreover, it was demonstrated that, unlike standard bulk homogenization, the proposed method can accurately capture the mechanical behavior of softening materials, even in the presence of a localized damage field. In order to demonstrate this, a simple, deterministic, and periodic two-dimensional model of a circular pore in a matrix was studied.

Owing to the intrinsic periodicity of the FFT-based homogenization, additional stiff marginal layers are required to approximate the Dirichlet-type boundary conditions at the interface of the cohesive zone. The choice of thickness and stiffness of the marginal layers is crucial for the applicability of the proposed method in the industry, as it affects the approximation accuracy of the boundary conditions, the computational times, and the modeling effort. A model of an adhesive layer with glass bead filler and pores with typical material parameters and volume fractions was then used to estimate the parameters for the marginal layers. Based on these simulations, recommendations were derived for determining the corresponding parameters for other material layers. The recommended process consists of the following steps:

1. Set the elastic material parameters of the marginal layer to those of the surrounding bulk material and set its thickness to about 15% of the cohesive zone thickness. This choice provided a good compromise between computational time and accuracy of the boundary conditions for the adhesive layer, whereas a thickness of 13.3% was sufficient for the sandwich core.

2. After conducting the FFT simulations, it should be verified whether the boundary conditions are approximated with the desired accuracy and whether the Hill-Mandel condition is satisfied. Deviations of the displacement fields from the desired boundary conditions, which are at least on the order of magnitude 10^{-3} times smaller than the separation in peel mode I and in the shear modes, were found to be acceptable in this work.

3. If either the boundary conditions are not approximated with sufficient accuracy or the Hill-Mandel condition is not satisfied, the thickness and/or stiffness of the marginal layers should be increased. However, when the stiffness was increased

tenfold, the simulations of the adhesive layer failed to converge within an adequate number of iterations. Accordingly, it is recommended to prioritize increasing the thickness when possible.

Based on the developed FFT-based homogenization scheme for cohesive zones, a novel modeling approach for the sandwich core of Hybrix^{TM} metal sandwich plates was introduced. The approach incorporates a novel method for generating virtual models for the microstructure of the core. In this process, the production parameters core thickness, fiber length and diameter, fiber volume fraction, and binder volume fraction serve as the only input parameters.

In the first step of the method, the fiber structure is created by solving the minimization problem for an objective function. This objective function accounts for fiber curvature, overlap between the fibers, the deviation from the triangular target PDF of the fibers, and overlap of fibers with the domain boundary of the cohesive zone. In the next step, the binder is added to the fiber structure using an algorithm based on morphological operations. Finally, the marginal layers with parameters determined by the above process are added.

A statistical comparison between the experimental data from microscopy and a µ-CT scan, and the generated model revealed a reasonable overall agreement. The following statistical measures were investigated:

- fiber orientation
- fiber nearest neighbor distance
- Ripley's K function
- radial pair distribution function
- volume fractions of fibers and binder
- and the two-point correlation function

Nevertheless, small deviations were observed in the statistical comparison owing to the fact that the minimization using the PSO could not entirely eliminate the overlap of the fibers. Moreover, deviations in the radially averaged two-point correlation function and the volume fraction of fibers and binder combined were found between z-values of 0.05 mm and 0.3 mm.

Despite the observed deviations, and considering the purposes of this work, it could be concluded that the model is representative of the geometry of the microstructure.

However, the representativeness of the virtual model for the mechanical behavior could not be verified owing to the high computational times of the FFT simulations, which were 37 days in mode I and 31 days in mode III. Therefore, the term "virtual model of the microstructure" is used instead of "Representative Volume Element" in this work.

Apart from the virtual model of the microstructure, the material models for fibers and binder at the microscale are required for the modeling approach. The parameters of the linear, isotropic elasticity model and the perfectly plastic, linear Drucker-Prager plasticity model, were identified using grid microindentation experiments. Based on these results, the simplification was made that fibers and binder can both be modeled using the same material model and parameters.

A statistical analysis using QQ plots and several statistical tests confirmed that this simplification is reasonable. Moreover, peel mode I TSLs from fracture mechanics DCB tests were used to identify the parameters for the non-local ductile damage model. For this purpose, the parameters were adjusted in mode I FFT simulations until a sufficient agreement between the simulated and experimental TSLs was achieved.

In the final step of this work, the modeling approach, along with the homogenization scheme, was experimentally validated. Considering the necessary assumptions and simplifications made in this work, the approach is deemed successfully validated through mode III SCB tests. The SCB test represents a completely different load case compared with the mode I DCB test and typically yields significantly different TSLs.

A mode III FFT simulation was performed, and the resulting TSL was implemented in a macroscopic FE model of the SCB test. This allowed for a comparison of local TSLs and global measured quantities to validate the model. Furthermore, an OFS measurement system was used to determine the bending strain distribution along the adherends, which is characteristic of the traction field behind the crack tip. Its extreme value can also be interpreted as the crack tip position.

A generally reasonable agreement between experiments and the simulation was found, particularly in the prediction of the critical ERR and the joint strength. Both were predicted well by the modeling approach. The resulting TSLs also showed satisfactory agreement. However, the FFT simulation overestimated the strength. The effect of this deviation becomes apparent in the initial part of the (global) J-CTOD and F-CTOD curves. The results of the OFS measurements also aligned satisfactorily with the simulations, as demonstrated by three representative curves at CTOD values of 0.1 mm, 0.5 mm, and 1 mm. Nevertheless, the crack tip position was overestimated at CTOD values of 0.5 mm and 1 mm.

Furthermore, a qualitatively reasonable agreement was observed between the experimental fracture surface and the crack pattern in both the mode III and mode I FFT simulations. It is emphasized that this work represents the first experimental validation of the FFT-based homogenization scheme for cohesive zones and, to the best of my knowledge, also the first experimental validation of computational homogenization for cohesive zones in general.

In summary, the successful development and validation of the novel modeling approach for the investigated composite material layer demonstrate that it is generally well-suited to reducing the number of extensive experiments. Accordingly, it could also accelerate the design process for novel configurations of metal sandwich plates. It is worth noting here that if the modeling approach is applied in the industry for designing novel configurations of Hybrix$^{\mathrm{TM}}$ plates, the constituents of the microstructure are typically known. Thus, the experimental effort required to identify the material models is significantly reduced compared with this study.

To conclude, both the desired novel micromechanical modeling approach for the sandwich core and the FFT-based homogenization scheme for cohesive zones were successfully developed, so that the objectives of this work, presented in Sec. 1.2, were achieved.

8. Outlook

Nevertheless, some challenges remain that can be addressed in future work to enhance the applicability of the modeling approach in the industry. Among other aspects, this includes reducing the remaining overlaps in the generation of virtual models of the microstructure by improving the optimization algorithm, as well as refining the formulation of the objective function itself. An improved model for the fiber structure may also help reduce the observed deviations in the radially averaged two-point correlation function and the volume fraction of fibers and binder combined between z-values of 0.05 mm and 0.3 mm. Furthermore, an extension to account for rate effects and hardening in the plasticity model may be necessary to address the simplifications made in this work.

Further improvements to the FFT solver itself, or the use of a computer cluster instead of a standard workstation could help reduce the currently high computational times for the simulation of the sandwich core. The likely reason for these high computational times and the corresponding slow convergence for damage localization and softening is the absence of a condensed, incremental strain energy density that acts as a convex

potential for the stress with respect to the strain. One possible approach to addressing this challenge is the use of reconvexification techniques for such condensed potentials that include damage-softening, as discussed in Sec. 2.5.1.

However, the computational times of a few hours per simulation were reasonable for the adhesive layer, which also makes them directly applicable for the development of new adhesives in the industry. The strong difference in the computational times between the sandwich core and the adhesive layer can be attributed, on the one hand, to the difference in model sizes. On the other hand, a single global crack is almost entirely formed by the damage field in the adhesive layer, whereas in the sandwich core, small microcracks occur and are connected by the large pore space.

The formation of these microcracks can lead to numerical instabilities, because if one region of the sandwich core fails during the numerical solution procedure, the loading in the other regions changes drastically. Hence, the solution field deviates significantly from a convergent solution once again. In contrast, the coherent damage field in the adhesive layer grows steadily, which prevents abrupt changes in the solution fields during the numerical solution procedure. Consequently, the solution fields remain closer to convergence, and the solver requires fewer iterations and less time to find a convergent solution.

This observation can also serve as a starting point for reducing the computational times. A significantly softer material with a much lower fracture energy than fibers and binder could be used to replace the pore space. This approach enables the formation of a coherent damage field for the crack, similar to the adhesive layer, but also introduces inaccuracies in the simulation results depending on the exact material parameters. A similar approximation strategy is commonly used for porous elastic microstructures (without fracture) [14].

Another option for reducing the computational times is the use of composite voxels, which consist of different materials at the subvoxel scale and are homogenized to obtain a representative mechanical behavior using analytical methods. This approach can significantly reduce the model size and, consequently, the computational times without significantly decreasing the accuracy of the solution [166]. Furthermore, Chen et al. [133] introduced a damage stabilization technique for FFT solvers that may also be applicable here.

However, all of these options for reducing the computational times introduce inaccuracies in the simulation results. Therefore, further research is required in order to determine suitable parameters for sufficient stabilization on the one hand, while main-

taining adequate accuracy of the results on the other hand. Moreover, it should be noted that FFT simulations of the sandwich core using only elasticity and plasticity, and thus without the damage model, required only about seven hours on the standard workstation used for all simulations in this work. With these simulations, the homogenized strength of the sandwich core can already be determined, which is sufficient for many industrial applications. Therefore, this reduced modeling approach could enable the development and optimization of novel configurations of Hybrix$^{\text{TM}}$ for such applications.

Owing to the significant dependence on the material of the constituents and the geometry of the microstructure, it is not possible to provide a reliable estimate of how the FFT-based method performs compared with the classical FEM-based approach at this stage. A comparison of FEM-based and FFT-based homogenization for cohesive zones in terms of the computational times for various materials is also beyond the scope of the current work, but requires future research in order to provide recommendations on the most suitable method for different applications.

Furthermore, uncertainties remain regarding the physical plausibility of the FFT-based homogenization scheme for cohesive zones itself, as discussed in Sec. 1.3.2. In particular, the unphysical periodic crack and the gradient loads in the vicinity of the crack tip are not considered in the homogenization scheme. Despite this, the computational homogenization scheme for cohesive zones could be successfully validated in this work, which, along with the numerical study from [48], supports the plausibility of these underlying assumptions.

However, further investigations are needed to assess how the method performs for different materials and to identify its limitations. Additionally, the predictive capabilities for complex load cases and different microstructures should be evaluated in future work. Extending the validation procedure to the mixed-mode behavior and other configurations of Hybrix$^{\text{TM}}$ plates would be particularly valuable here. In this context, a machine-learning-based surrogate model was already developed in [167] that enables a seamless integration into FE simulations at the macroscale. This model can also be extended to mixed-mode behavior straightforwardly, when sufficient FFT simulations are available.

Moreover, it should be emphasized that only the small deformation theory was applied, which, as discussed at the beginning of Sec. 2.1, is often used in FFT-based homogenization. Nevertheless, relatively large macroscopic deformations occurred in the simulations of the sandwich core and it is also possible to extend the FFT-based homogenization to large deformations [21]. Therefore, it would be valuable for future research to investigate the effect of this simplification. Furthermore, interfacial fracture

between the constituents at the microscale was not considered in the models, even though it has been shown to significantly influence macroscopic fracture behavior [46]. Such models can be incorporated into the FFT-based homogenization, see [106, 168–170], but it may be challenging to obtain the required experimental data for all constituents of the microstructure.

Appendices

A. Distance between the central line segments of two fiber segments

To compute the distance between the central line segments of segment j of fiber i and segment l of fiber k, the method proposed in [137, 138] is applied. The vector from one central line segment to the other is given by

$$\vec{w}_{ijkl}(s_1, s_2) = \vec{x}_{ij}^{\,\mathrm{cs}}(s_1) - \vec{x}_{kl}^{\,\mathrm{cs}}(s_2) \quad \text{for} \quad i \neq k, \tag{A.1}$$

cf. Eq. (4.3). At the closest point between the fiber segments $\vec{w}_{ijkl}(s_1^{\mathrm{c}}, s_2^{\mathrm{c}})$ is usually orthogonal to the vectors

$$\vec{d}_{ij} = \vec{x}_{ij}^{\,\mathrm{se}} - \vec{x}_{i(j-1)}^{\,\mathrm{se}} \qquad \text{and} \qquad \vec{d}_{kl} = \vec{x}_{kl}^{\,\mathrm{se}} - \vec{x}_{k(l-1)}^{\,\mathrm{se}}. \tag{A.2}$$

These are the vectors that connect the two segment end points of the corresponding fiber segments from Eq. (4.2), such that

$$\vec{d}_{ij} \cdot \vec{w}_{ijkl}(s_1^{\mathrm{c}}, s_2^{\mathrm{c}}) = 0 \qquad \text{and} \qquad \vec{d}_{kl} \cdot \vec{w}_{ijkl}(s_1^{\mathrm{c}}, s_2^{\mathrm{c}}) = 0. \tag{A.3}$$

Solving Eq. A.3 yields

$$s_1^{\mathrm{c}} = \frac{a_2 a_5 - a_3 a_4}{a_1 a_3 - a_2^2} \qquad \text{and} \qquad s_2^{\mathrm{c}} = \frac{a_1 a_5 - a_2 a_4}{a_1 a_3 - a_2^2} \tag{A.4}$$

with

$$a_1 = \vec{d}_{ij} \cdot \vec{d}_{ij}, \quad a_2 = \vec{d}_{ij} \cdot \vec{d}_{kl}, \quad a_3 = \vec{d}_{kl} \cdot \vec{d}_{kl}, \quad a_4 = \vec{d}_{ij} \cdot \left(\vec{x}_{i(j-1)}^{\,\mathrm{se}} - \vec{x}_{k(l-1)}^{\,\mathrm{se}} \right), \tag{A.5}$$
$$\text{and} \quad a_5 = \vec{d}_{kl} \cdot \left(\vec{x}_{i(j-1)}^{\,\mathrm{se}} - \vec{x}_{k(l-1)}^{\,\mathrm{se}} \right).$$

Other candidates for the closest points are the segment end points

$$(s_1^{\mathrm{c}} = 0,\ s_2^{\mathrm{c}} = 0), \quad (s_1^{\mathrm{c}} = 0,\ s_2^{\mathrm{c}} = 1), \quad (s_1^{\mathrm{c}} = 1,\ s_2^{\mathrm{c}} = 0), \tag{A.6}$$
$$\text{and} \quad (s_1^{\mathrm{c}} = 1,\ s_2^{\mathrm{c}} = 1)$$

themselves, or one end point and a point on the central line segment of the other fiber segment, which are

$$\begin{gathered}(s_1^{\mathrm{c}} = -a_4/a_1,\ s_2^{\mathrm{c}} = 0)\,, \quad (s_1^{\mathrm{c}} = a_2 - a_4/a_1,\ s_2^{\mathrm{c}} = 1)\,, \quad (s_1^{\mathrm{c}} = 0,\ s_2^{\mathrm{c}} = a_5/a_3) \\ \text{and} \quad (s_1^{\mathrm{c}} = 1,\ s_2^{\mathrm{c}} = (a_2 + a_5)/a_3)\,.\end{gathered} \tag{A.7}$$

The distance is then computed as

$$\Delta_{ijkl}^{\mathrm{fib\_fib}} = |\vec{w}_{ijkl}(s_1^{\mathrm{c}}, s_2^{\mathrm{c}})| \tag{A.8}$$

using the magnitude $|\vec{\bullet}|$. The minimum distance among all candidate points is ultimately retained as the distance between the corresponding central line segments for computing the overlap.

B. Operator norm of the tangent stiffness

In order to compute the operator norm from Eq. (2.158), the optimization problem

$$\begin{aligned} &\sup_{\overline{\Delta\varepsilon}_i^{*1,2}} && \sum_{i=1}^{6}\left(\lambda_i^{\mathrm{eig}}\ \overline{\Delta\varepsilon}_i^{*1,2}\right)^2 \\ &\text{subject to} && \sum_{i=1}^{6}\left(\overline{\Delta\varepsilon}_i^{*1,2}\right)^2 - \left\|\underline{\Delta\varepsilon}^{*1,2}\right\|_{\mathrm{F}}^2 = 0 \end{aligned} \tag{B.1}$$

is considered, where the numerator is maximized under the constraint that the denominator remains constant, $\left\|\underline{\Delta\varepsilon}^{*1,2}\right\|_{\mathrm{F}} = const.$. The squared operator norm is maximized to simplify the equations without affecting the result.

This problem can be solved using the method of Lagrange multipliers, where the Lagrange function is given by

$$\mathcal{L} = \sum_{i=1}^{6}\left(\lambda_i^{\mathrm{eig}}\ \overline{\Delta\varepsilon}_i^{*1,2}\right)^2 + \kappa\left(\sum_{i=1}^{6}\left(\overline{\Delta\varepsilon}_i^{*1,2}\right)^2 - \left\|\underline{\Delta\varepsilon}^{*1,2}\right\|_{\mathrm{F}}^2\right) \tag{B.2}$$

with Lagrangian multiplier κ. Accordingly, the equations for the stationary points

$$\begin{cases} \dfrac{\partial\mathcal{L}}{\partial\,\overline{\Delta\varepsilon}_i^{*1,2}} = 2\,\widetilde{\Delta\varepsilon}_i^{*1,2}\left[\left(\lambda_i^{\mathrm{eig}}\right)^2 + \kappa\right] = 0, & \forall i \in \{1,2,...,6\} \\ \dfrac{\partial\mathcal{L}}{\partial\kappa} = \sum_{i=1}^{6}\left(\widetilde{\Delta\varepsilon}_i^{*1,2}\right)^2 - \left\|\underline{\Delta\varepsilon}^{*1,2}\right\|_{\mathrm{F}}^2 = 0 \end{cases} \tag{B.3}$$

are obtained, where $\widetilde{\Delta\varepsilon}_i^{*1,2}$ replaces $\overline{\Delta\varepsilon}_i^{*1,2}$ and denotes the specific values of $\overline{\Delta\varepsilon}_i^{*1,2}$ that solve the optimization problem. The first line contains the six equations for all i.

In general, exactly one of the equations from the first line of Eq. (B.3) can be solved for κ, which yields

$$2\,\widetilde{\Delta\varepsilon}_i^{*1,2}\left[\left(\lambda_i^{\mathrm{eig}}\right)^2+\kappa\right]=0 \quad\Longrightarrow\quad \kappa=-\left(\lambda_j^{\mathrm{eig}}\right)^2=:-\left(\tilde{\lambda}^{\mathrm{eig}}\right)^2, \qquad \exists! j\in\{1,2,...,6\} \tag{B.4}$$

in the non-trivial case. The second line emphasizes this uniqueness by explicitly stating that a single index j exists, which represents the equation that is solved for κ. For notational clarity, the corresponding eigenvalue of index j is denoted as $\tilde{\lambda}^{\mathrm{eig}}$.

Inserting the solution into the remaining equations from the first line of Eq. (B.3), for cases where $\lambda_i^{\mathrm{eig}}\neq\tilde{\lambda}^{\mathrm{eig}}$, gives

$$2\,\widetilde{\Delta\varepsilon}_i^{*1,2}\left[\left(\lambda_i^{\mathrm{eig}}\right)^2-\left(\tilde{\lambda}^{\mathrm{eig}}\right)^2\right]=0 \quad\Longrightarrow\quad \widetilde{\Delta\varepsilon}_i^{*1,2}=0, \qquad \forall i\in\{1,2,...,6\}\mid\lambda_i^{\mathrm{eig}}\neq\tilde{\lambda}^{\mathrm{eig}}. \tag{B.5}$$

Please note that this result would usually hold for all i except j. However, depending on the symmetry of the tangent stiffness tensor, some eigenvalues can be identical. Therefore, the equation must hold for all $\lambda_i^{\mathrm{eig}}\neq\tilde{\lambda}^{\mathrm{eig}}$. Hence, all $\widetilde{\Delta\varepsilon}_i^{*1,2}$ vanish except for those that belong to $\lambda_i^{\mathrm{eig}}=\tilde{\lambda}^{\mathrm{eig}}$.

Consequently, the solution of the second line of Eq. (B.3) becomes

$$\sum_i\left(\widetilde{\Delta\varepsilon}_i^{*1,2}\right)^2-\left\|\underline{\Delta\varepsilon}^{*1,2}\right\|_{\mathrm{F}}^2=0 \quad\Longrightarrow\quad \sum_i\left(\widetilde{\Delta\varepsilon}_i^{*1,2}\right)^2=\left\|\underline{\Delta\varepsilon}^{*1,2}\right\|_{\mathrm{F}}^2, \qquad \forall i\in\{1,2,...,6\}\mid\lambda_i^{\mathrm{eig}}=\tilde{\lambda}^{\mathrm{eig}}, \tag{B.6}$$

where only the non-zero $\widetilde{\Delta\varepsilon}_i^{*1,2}$ belonging to $\lambda_i^{\mathrm{eig}}=\tilde{\lambda}^{\mathrm{eig}}$ occur.

Using this result, the objective function of the optimization problem in Eq. (B.1) simplifies to

$$\sum_i\left(\tilde{\lambda}^{\mathrm{eig}}\,\widetilde{\Delta\varepsilon}_i^{*1,2}\right)^2=\left(\tilde{\lambda}^{\mathrm{eig}}\right)^2\sum_i\left(\widetilde{\Delta\varepsilon}_i^{*1,2}\right)^2=\left(\tilde{\lambda}^{\mathrm{eig}}\right)^2\left\|\underline{\Delta\varepsilon}^{*1,2}\right\|_{\mathrm{F}}^2, \qquad \forall i\in\{1,2,...,6\}\mid\lambda_i^{\mathrm{eig}}=\tilde{\lambda}^{\mathrm{eig}}. \tag{B.7}$$

$\tilde{\lambda}^{\mathrm{eig}}$ is constant over the sum and can thus be factored out.

This procedure provides candidate solutions for the optimization problem. The value

of the objective function depends only on $\tilde{\lambda}^{\mathrm{eig}}$ and thus which of the equations in the first line of Eq. (B.3) is solved for κ. Consequently, the objective function is maximized for

$$\tilde{\lambda}^{\mathrm{eig}} = \lambda_1^{\mathrm{eig}}, \tag{B.8}$$

which represents the largest eigenvalue, provided the tangent stiffness is positive semi-definite.

Using the numerator from Eq. (2.158), the denominator from Eq. (2.150), and the results from this optimization problem, the squared operator norm reads

$$||\underline{\underline{C}}^{\mathrm{t}}||_{\mathrm{op}}^2 = \sup \frac{\sum_{i=1}^{6} \left(\lambda_i^{\mathrm{eig}} \overline{\Delta\varepsilon}_i^{*1,2}\right)^2}{||\underline{\underline{\Delta\varepsilon}}^{*1,2}||_{\mathrm{F}}^2} = \left(\lambda_1^{\mathrm{eig}}\right)^2. \tag{B.9}$$

Thus, the final result for the operator norm is

$$||\underline{\underline{C}}^{\mathrm{t}}||_{\mathrm{op}} = \lambda_1^{\mathrm{eig}}. \tag{B.10}$$

References

[1] R. Campilho, M. Banea, J. Neto, and L. da Silva, "Modelling adhesive joints with cohesive zone models: effect of the cohesive law shape of the adhesive layer," *International Journal of Adhesion and Adhesives*, vol. 44, pp. 48–56, 2013, doi:10.1016/j.ijadhadh.2013.02.006.

[2] F. Bödeker and S. Marzi, "Applicability of the mixed-mode controlled double cantilever beam test and related evaluation methods," *Engineering Fracture Mechanics*, vol. 235, p. 107149, 2020, doi:10.1016/j.engfracmech.2020.107149.

[3] U. Stigh, A. Biel, and D. Svensson, "Cohesive zone modelling and the fracture process of structural tape," *Procedia Structural Integrity*, vol. 2, pp. 235–244, 2016, 21st European Conference on Fracture, ECF21, 20-24 June 2016, Catania, Italy. doi:10.1016/j.prostr.2016.06.031.

[4] A. Biel, J. Tryding, M. Ristinmaa, M. Johansson-Näslund, O. Tuvesson, and U. Stigh, "Experimental evaluation of normal and shear delamination in cellulose-based materials using a cohesive zone model," *International Journal of Solids and Structures*, vol. 252, p. 111755, 2022, doi:10.1016/j.ijsolstr.2022.111755.

[5] M. Geers, V. Kouznetsova, K. Matouš, and J. Yvonnet, "Homogenization Methods and Multiscale Modeling: Nonlinear Problems," in *Encyclopedia of Computational Mechanics*, 2nd ed. Chichester, UK: John Wiley & Sons, pp. 1–34.

[6] J. Fish, *Practical Multiscaling*. Chichester, UK: John Wiley & Sons, 2013.

[7] *ABAQUS/Standard 2018 User's Manual*, Dassault Systèmes Simulia Corp, Vélizy-Villacoublay, Frankreich, 2018.

[8] H. Moulinec and P. Suquet, "A fast numerical method for computing the linear and nonlinear mechanical properties of composites," *Comptes Rendus de l'Acadèmie des Sciences. Sèrie II*, vol. 318, no. 11, pp. 1417–1423, 1994.

[9] H. Moulinec and P. Suquet, "A numerical method for computing the overall response of nonlinear composites with complex microstructure," *Computer Methods in Applied Mechanics and Engineering*, vol. 157, no. 1, pp. 69–94, 1998, doi:10.1016/S0045-7825(97)00218-1.

[10] S. Li and E. Sitnikova, *Representative Volume Elements and Unit Cells: Concepts, Theory, Applications and Implementation*, ser. Woodhead Publishing series in composites science and engineering. Duxford, UK: Woodhead Publishing, 2020.

[11] F. Willot, "Fourier-based schemes for computing the mechanical response of composites with accurate local fields," *Comptes Rendus Mècanique*, vol. 343, no. 3, pp. 232–245, 2015, doi:10.1016/j.crme.2014.12.005.

[12] M. Schneider, D. Merkert, and M. Kabel, "FFT-based homogenization for microstructures discretized by linear hexahedral elements," *International Journal for Numerical Methods in Engineering*, vol. 109, no. 10, pp. 1461–1489, 2017, doi:10.1002/nme.5336.

[13] M. Schneider, "Voxel-based finite elements with hourglass control in fast Fourier transform-based computational homogenization," *International Journal for Numerical Methods in Engineering*, vol. 123, no. 24, pp. 6286–6313, 2022, doi:10.1002/nme.7114.

[14] M. Schneider, F. Ospald, and M. Kabel, "Computational homogenization of elasticity on a staggered grid," *International Journal for Numerical Methods in Engineering*, vol. 105, no. 9, pp. 693–720, 2016, doi:10.1002/nme.5008.

[15] J. Vondřejc, J. Zeman, and I. Marek, "Guaranteed upper–lower bounds on homogenized properties by FFT-based Galerkin method," *Computer Methods in Applied Mechanics and Engineering*, vol. 297, pp. 258–291, 2015, doi:10.1016/j.cma.2015.09.003.

[16] J. Vondřejc, "Improved guaranteed computable bounds on homogenized properties of periodic media by the Fourier–Galerkin method with exact integration," *International Journal for Numerical Methods in Engineering*, vol. 107, no. 13, pp. 1106–1135, 2016, doi:10.1002/nme.5199.

[17] S. Brisard and L. Dormieux, "FFT-based methods for the mechanics of composites: A general variational framework," *Computational Materials Science*, vol. 49, no. 3, pp. 663–671, 2010, doi:10.1016/j.commatsci.2010.06.009.

[18] S. Brisard and L. Dormieux, "Combining Galerkin approximation techniques with the principle of Hashin and Shtrikman to derive a new FFT-based numerical method for the homogenization of composites," *Computer Methods in Applied Mechanics and Engineering*, vol. 217-220, pp. 197–212, 2012, doi:10.1016/j.cma.2012.01.003.

[19] W. H. Müller, "Fourier Transforms and Their Application to the Formation of Textures and Changes of Morphology in Solids INPRO," in *IUTAM Symposium on Transformation Problems in Composite and Active Materials*, Y. A. Bahei-El-Din and G. J. Dvorak, Eds. Dordrecht: Springer Netherlands, 1998, pp. 61–72, doi:10.1007/0-306-46935-9_5.

[20] J. Zeman, J. Vondrejc, J. Novák, and I. Marek, "Accelerating a FFT-based solver for numerical homogenization of periodic media by conjugate gradients," *Journal of Computational Physics*, vol. 229, no. 21, pp. 8065–8071, 2010, doi:10.1016/j.jcp.2010.07.010.

[21] M. Kabel, T. Böhlke, and M. Schneider, "Efficient fixed point and Newton-Krylov solvers for FFT-based homogenization of elasticity at large deformations," *Computational Mechanics*, vol. 54, no. 6, pp. 1497–1514, 2014, doi:10.1007/s00466-014-1071-8.

[22] M. Schneider, "A dynamical view of nonlinear conjugate gradient methods with applications to FFT–based computational micromechanics," *Comput. Mech.*, vol. 66, no. 1, pp. 239–257, 2020, doi:10.1007/s00466-020-01849-7.

[23] M. Schneider, "On the Barzilai-Borwein basic scheme in FFT-based computational homogenization," *International Journal for Numerical Methods in Engineering*, vol. 118, no. 8, pp. 482–494, 2019, doi:10.1002/nme.6023.

[24] D. Wicht, M. Schneider, and T. Böhlke, "On Quasi-Newton methods in fast Fourier transform-based micromechanics," *International Journal for Numerical Methods in Engineering*, vol. 121, no. 8, pp. 1665–1694, 2020, doi:10.1002/nme.6283.

[25] Y. Chen, L. Gélébart, C. Chateau, M. Bornert, C. Sauder, and A. King, "Analysis of the damage initiation in a SiC/SiC composite tube from a direct comparison between large-scale numerical simulation and synchrotron X-ray micro-computed tomography," *International Journal of Solids and Structures*, vol. 161, pp. 111–126, 2019, doi:10.1016/j.ijsolstr.2018.11.009.

[26] M. Schneider, "An FFT-based fast gradient method for elastic and inelastic unit cell homogenization problems," *Computer Methods in Applied Mechanics and Engineering*, vol. 315, pp. 846–866, 2017, doi:10.1016/j.cma.2016.11.004.

[27] J. Michel, H. Moulinec, and P. Suquet, "A computational scheme for linear and non-linear composites with arbitrary phase contrast," *International Journal for Numerical Methods in Engineering*, vol. 52, no. 1-2, pp. 139–160, 2001, doi:10.1002/nme.275.

[28] D. Wicht, M. Schneider, and T. Böhlk, "Anderson-accelerated polarization schemes for fast Fourier transform-based computational homogenization," *International Journal for Numerical Methods in Engineering*, vol. 122, no. 9, pp. 2287–2311, 2021, doi:10.1002/nme.6622.

[29] M. Schneider, "On non-stationary polarization methods in fft-based computational micromechanics," *International Journal for Numerical Methods in Engineering*, vol. 122, no. 22, pp. 6800–6821, 2021, doi:10.1002/nme.6812.

[30] Lucarini, Sergio and Upadhyay, Manas and Segurado, Javier, "FFT based approaches in micromechanics: Fundamentals, methods and applications," *Modelling and Simulation in Materials Science and Engineering*, vol. 30, Oct. 2021, doi:10.1016/10.1088/1361-651X/ac34e1.

[31] M. Schneider, "A review of nonlinear FFT-based computational homogenization methods," *Acta Mechanica*, 2021, doi:10.1007/s00707-021-02962-1.

[32] S. Lucarini and J. Segurado, "On the accuracy of spectral solvers for micromechanics based fatigue modeling," *Computational Mechanics*, vol. 63, no. 2, pp. 365–382, 2019, doi:10.1007/s00466-018-1598-1.

[33] S. Lucarini, L. Cobian, A. Voitus, and J. Segurado, "Adaptation and validation of FFT methods for homogenization of lattice based materials," *Computer Methods in Applied Mechanics and Engineering*, vol. 388, p. 114223, 2022, doi:10.1016/j.cma.2021.114223.

[34] M. Magri, S. Lucarini, G. Lemoine, L. Adam, and J. Segurado, "An FFT framework for simulating non-local ductile failure in heterogeneous materials," *Computer Methods in Applied Mechanics and Engineering*, vol. 380, p. 113759, 2021, doi:10.1016/j.cma.2021.113759.

[35] F. Ernesti, M. Schneider, and T. Böhlke, "Fast implicit solvers for phase-field fracture problems on heterogeneous microstructures," *Computer Methods in Applied Mechanics and Engineering*, vol. 363, p. 112793, 2020, doi:10.1016/j.cma.2019.112793.

[36] Y. Chen, D. Vasiukov, L. Gélébart, and C. H. Park, "A FFT solver for variational phase-field modeling of brittle fracture," *Computer Methods in Applied Mechanics and Engineering*, vol. 349, pp. 167–190, 2019, doi:10.1016/j.cma.2019.02.017.

[37] R. Ma and W. C. Sun, "FFT-based solver for higher-order and multi-phase-field fracture models applied to strongly anisotropic brittle materials," *Computer Methods in Applied Mechanics and Engineering*, vol. 362, p. 112781, 2020, doi:10.1016/j.cma.2019.112781.

[38] J. Köbler, N. Magino, H. Andrä, F. Welschinger, R. Müller, and M. Schneider, "A computational multi-scale model for the stiffness degradation of short-fiber reinforced plastics subjected to fatigue loading," *Computer Methods in Applied Mechanics and Engineering*, vol. 373, p. 113522, 2021, doi:10.1016/j.cma.2020.113522.

[39] N. Magino, J. Köbler, H. Andrä, F. Welschinger, R. Müller, and M. Schneider, "A space-time upscaling technique for modeling high-cycle fatigue-damage of short-fiber reinforced composites," *Composites Science and Technology*, vol. 222, p. 109340, 2022, doi:10.1016/j.compscitech.2022.109340.

[40] N. Magino, J. Köbler, H. Andrä, F. Welschinger, R. Müller, and M. Schneider, "Accounting for viscoelastic effects in a multiscale fatigue model for the degradation of the dynamic stiffness of short-fiber reinforced thermoplastics," *Computational Mechanics*, vol. 71, no. 2, pp. 493–515, 2023, doi:10.1016/10.1007/s00466-022-02246-y.

[41] I. Gitman, H. Askes, and L. Sluys, "Representative volume: Existence and size determination," *Engineering Fracture Mechanics*, vol. 74, no. 16, pp. 2518–2534, 2007, doi:10.1016/j.engfracmech.2006.12.021.

[42] K. Matouš, M. Kulkarni, and P. Geubelle, "Multiscale cohesive failure modeling of heterogeneous adhesives," *Journal of the Mechanics and Physics of Solids*, vol. 56, no. 4, pp. 1511–1533, 2008, doi:10.1016/j.jmps.2007.08.005.

[43] R. Larsson and Y. Zhang, "Homogenization of microsystem interconnects based on micropolar theory and discontinuous kinematics," *Journal of the Mechanics and Physics of Solids*, vol. 55, no. 4, pp. 819–841, 2007, doi:10.1016/j.jmps.2006.09.010.

[44] M. Mosby and K. Matouš, "Hierarchically parallel coupled finite strain multiscale solver for modeling heterogeneous layers," *International Journal for Numerical Methods in Engineering*, vol. 102, no. 3-4, pp. 748–765, 2015, doi:10.1002/nme.4755.

[45] C. Hirschberger, S. Ricker, P. Steinmann, and N. Sukumar, "Computational multi-scale modelling of heterogeneous material layers," *Engineering Fracture Mechanics*, vol. 76, no. 6, pp. 793–812, 2009, doi:10.1016/j.engfracmech.2008.10.018.

[46] M. Kulkarni, P. Geubelle, and K. Matouš, "Multi-scale modeling of heterogeneous adhesives: Effect of particle decohesion," *Mechanics of Materials*, vol. 41, no. 5, pp. 573–583, 2009, doi:10.1016/j.mechmat.2008.10.012.

[47] S. Soghrati and B. Liang, "Automated analysis of microstructural effects on the failure response of heterogeneous adhesives," *International Journal of Solids and Structures*, vol. 81, pp. 250–261, 2016, doi:10.1016/j.ijsolstr.2015.12.002.

[48] M. Kulkarni, K. Matouš, and P. Geubelle, "Coupled multi-scale cohesive modeling of failure in heterogeneous adhesives," *International Journal for Numerical Methods in Engineering*, vol. 84, no. 8, pp. 916–946, 2010, doi:10.1002/nme.2923.

[49] N. D. Sharp, J. E. Goodsell, and A. J. Favaloro, "Measuring Fiber Orientation of Elliptical Fibers from Optical Microscopy," *Journal of Composites Science*, vol. 3, no. 1, 2019, doi:10.3390/jcs3010023.

[50] G. M. Vèlèz-García, P. Wapperom, D. G. Baird, A. O. Aning, and V. Kunc, "Unambiguous orientation in short fiber composites over small sampling area in a center-gated disk," *Composites Part A: Applied Science and Manufacturing*, vol. 43, no. 1, pp. 104–113, 2012, doi:10.1016/j.compositesa.2011.09.024.

[51] B. R. Denos, D. E. Sommer, A. J. Favaloro, R. B. Pipes, and W. B. Avery, "Fiber orientation measurement from mesoscale CT scans of prepreg platelet molded composites," *Composites Part A: Applied Science and Manufacturing*, vol. 114, pp. 241–249, 2018, doi:10.1016/j.compositesa.2018.08.024.

[52] J. M. Sietins, J. C. Sun, and D. B. K. Jr, "Fiber orientation quantification utilizing x-ray micro-computed tomography," *Journal of Composite Materials*, vol. 55, no. 8, pp. 1109–1118, 2021, doi:10.1177/0021998320962555.

[53] L. Vásárhelyi, Z. Kónya, A. Kukovecz, and R. Vajtai, "Microcomputed tomography–based characterization of advanced materials: a review," *Materials Today Advances*, vol. 8, p. 100084, 2020, doi:10.1016/j.mtadv.2020.100084.

[54] A. Clarke and C. Eberhardt, *Microscopy techniques for materials science*. Boca Raton, FL, USA: CRC Press (Inc.), 2002.

[55] J. Ohser and K. Schladitz, *3D Images of Materials Structures: Processing and Analysis*. Weinheim, Germany: Wiley-VCH, 2009.

[56] H. Xu, D. Dikin, C. Burkhart, and W. Chen, "Descriptor-based methodology for statistical characterization and 3D reconstruction of microstructural materials," *Computational Materials Science*, vol. 85, pp. 206–216, 2014, doi:10.1016/j.commatsci.2013.12.046.

[57] S. Torquato, "Statistical Description of Microstructures," *Annual Review of Materials Research*, vol. 32, no. 1, pp. 77–111, 2002, doi:10.1146/annurev.matsci.32.110101.155324.

[58] D. Chen, X. He, Q. Teng, Z. Xu, and Z. Li, "Reconstruction of multiphase microstructure based on statistical descriptors," *Physica A: Statistical Mechanics and its Applications*, vol. 415, pp. 240–250, 2014, doi:10.1016/j.physa.2014.07.066.

[59] A. Melro, P. Camanho, and S. Pinho, "Generation of random distribution of fibres in long-fibre reinforced composites," *Composites Science and Technology*, vol. 68, no. 9, pp. 2092–2102, 2008, doi:10.1016/j.compscitech.2008.03.013.

[60] V. Romanov, S. V. Lomov, Y. Swolfs, S. Orlova, L. Gorbatikh, and I. Verpoest, "Statistical analysis of real and simulated fibre arrangements in unidirectional composites," *Composites Science and Technology*, vol. 87, pp. 126–134, 2013, doi:10.1016/j.compscitech.2013.07.030.

[61] W. Wang, Y. Dai, C. Zhang, X. Gao, and M. Zhao, "Micromechanical Modeling of Fiber-Reinforced Composites with Statistically Equivalent Random Fiber Distribution," *Materials*, vol. 9, 2016, doi:10.3390/ma9080624.

[62] T. Matsuda, N. Ohno, H. Tanaka, and T. Shimizu, "Effects of fiber distribution on elastic-viscoplastic behavior of long fiber-reinforced laminates," *International Journal of Mechanical Sciences*, vol. 45, no. 10, pp. 1583–1598, 2003, 6th Asia-Pacific Symposium on Advances in Engineering Plasticity and its Applications. doi:10.1016/j.ijmecsci.2003.09.021.

[63] R. Pyrz, "Correlation of microstructure variability and local stress field in two-phase materials," *Materials Science and Engineering: A*, vol. 177, no. 1, pp. 253–259, 1994, doi:10.1016/0921-5093(94)90497-9.

[64] S. Bargmann, B. Klusemann, J. Markmann, J. Schnabel, K. Schneider, C. Soyarslan, and J. Wilmers, "Generation of 3D representative volume elements for heterogeneous materials: A review," *Progress in Materials Science*, vol. 96, pp. 322–384, 2018, doi:10.1016/j.pmatsci.2018.02.003.

[65] B. Widom, "Random Sequential Addition of Hard Spheres to a Volume," *The Journal of Chemical Physics*, vol. 44, no. 10, pp. 3888–3894, 1966, doi:10.1063/1.1726548.

[66] D. Balzani, L. Scheunemann, D. Brands, and J. Schröder, "Construction of two- and three-dimensional statistically similar RVEs for coupled micro-macro simulations," *Comput. Mech.*, vol. 54, no. 5, pp. 1269–1284, 2014, doi:10.1007/s00466-014-1057-6.

[67] R. Nakka, D. Harursampath, M. Pathan, and S. A. Ponnusami, "A computationally efficient approach for generating RVEs of various inclusion/fibre shapes," *Composite Structures*, vol. 291, p. 115560, 2022, doi:10.1016/j.compstruct.2022.115560.

[68] M. Schneider, "The sequential addition and migration method to generate representative volume elements for the homogenization of short fiber reinforced plastics," *Computational Mechanics*, vol. 59, Feb. 2017, doi:10.1007/s00466-016-1350-7.

[69] C. Lauff, M. Schneider, J. Montesano, and T. Böhlke, "Generating microstructures of long fiber reinforced composites by the fused sequential addition and migration method," *International Journal for Numerical Methods in Engineering*, vol. 125, no. 22, p. e7573, 2024, doi:doi.org/10.1002/nme.7573.

[70] C. Lauff, M. Schneider, and T. Böhlke, "Microstructure generation of long fiber reinforced hybrid composites using the fused sequential addition and migration method," *Journal of Thermoplastic Composite Materials*, p. 08927057251314425, 2025, doi:10.1177/08927057251314425.

[71] G. Dehm, B. Jaya, R. Raghavan, and C. Kirchlechner, "Overview on micro- and nanomechanical testing: New insights in interface plasticity and fracture at small length scales," *Acta Materialia*, vol. 142, pp. 248–282, 2018, doi:10.1016/j.actamat.2017.06.019.

[72] P. Arnaud, E. Heripre, F. Douit, V. Aubin, S. Fouvry, R. Guiheux, V. Branger, and G. Michel, "Micromechanical tensile test investigation to identify elastic and toughness properties of thin nitride compound layers," *Surface and Coatings Technology*, vol. 421, p. 127303, 2021, doi:10.1016/j.surfcoat.2021.127303.

[73] K. Kumar, A. Pooleery, K. Madhusoodanan, R. Singh, J. Chakravartty, B. Dutta, and R. Sinha, "Use of Miniature Tensile Specimen for Measurement of Mechanical Properties," *Procedia Engineering*, vol. 86, pp. 899–909, 2014, structural Integrity. doi:10.1016/j.proeng.2014.11.112.

[74] J. Vogel, H.-J. Feige, J. Saupe, K. Rudolph, J. Grimm, and R. Herold, "Microtensile Test of HARMNST-Polymers–Downscaled in Dimension," *Materials Today: Proceedings*, vol. 3, no. 4, pp. 1205–1210, 2016, 32nd DANUBIA ADRIA SYMPOSIUM on Advanced in Experimental Mechanics. doi:10.1016/j.matpr.2016.03.005.

[75] G. Y. Choong, A. Canciani, and D. S. De Focatiis, "An adaptable flexural test fixture for miniaturised polymer specimens," *Polymer Testing*, vol. 85, p. 106430, 2020, doi:10.1016/j.polymertesting.2020.106430.

[76] K. Kutukova, S. Niese, J. Gelb, R. Dauskardt, and E. Zschech, "A novel micro-double cantilever beam (micro-DCB) test in an X-ray microscope to study crack propagation in materials and structures," *Materials Today Communications*, vol. 16, pp. 293–299, 2018, doi:10.1016/j.mtcomm.2018.07.006.

[77] D. Tranchida and S. Piccarolo, *Local Mechanical Properties by Atomic Force Microscopy Nanoindentations*. Berlin, Heidelberg, Germany: Springer, 2009, pp. 165–198.

[78] M. Brogly, H. Awada, and O. Noel, *Contact Atomic Force Microscopy: A Powerful Tool in Adhesion Science*. Berlin, Heidelberg, Germany: Springer, 2009, pp. 73–95.

[79] A. C. Fischer-Cripps, *Nanoindentation*. New York, NY, USA: Springer, 2011.

[80] M. Griepentrog, G. Krämer, and B. Cappella, "Comparison of nanoindentation and AFM methods for the determination of mechanical properties of polymers," *Polymer Testing*, vol. 32, no. 3, pp. 455–460, 2013, doi:10.1016/j.polymertesting.2013.01.011.

[81] S. Pathak and S. R. Kalidindi, "Spherical nanoindentation stress–strain curves," *Materials Science and Engineering: R: Reports*, vol. 91, pp. 1–36, 2015, doi:10.1016/j.mser.2015.02.001.

[82] R. Seltzer, A. Cisilino, P. Frontini, and Y. Mai, "Determination of the Drucker–Prager parameters of polymers exhibiting pressure-sensitive plastic behaviour by depth-sensing indentation," *International Journal of Mechanical Sciences*, vol. 53, no. 6, pp. 471–478, 2011, doi:10.1016/j.ijmecsci.2011.04.002.

[83] G. Constantinides, K. Ravi Chandran, F.-J. Ulm, and K. Van Vliet, "Grid indentation analysis of composite microstructure and mechanics: Principles and validation," *Materials Science and Engineering: A*, vol. 430, no. 1, pp. 189–202, 2006, doi:10.1016/j.msea.2006.05.125.

[84] C.-M. Sanchez-Camargo, A. Hor, M. Salem, and C. Mabru, "A robust method for mechanical characterization of heterogeneous materials by nanoindentation grid analysis," *Materials & Design*, vol. 194, p. 108908, 2020, doi:10.1016/j.matdes.2020.108908.

[85] S. Marzi, "16 - Innovations in fracture testing of structural adhesive bonds," in *Advances in Structural Adhesive Bonding*, 2nd ed., ser. Woodhead Publishing in Materials, D. A. Dillard, Ed. Cambridge, MA, USA: Woodhead Publishing, 2023, pp. 525–578.

[86] J. R. Rice, "A Path Independent Integral and the Approximate Analysis of Strain Concentration by Notches and Cracks," *Journal of Applied Mechanics*, vol. 35, no. 2, pp. 379–386, Jun. 1968, doi:10.1115/1.3601206.

[87] G. Cherepanov, "Crack propagation in continuous media: PMM vol. 31, no. 3, 1967, pp. 476–488," *Journal of Applied Mathematics and Mechanics*, vol. 31, no. 3, pp. 503–512, 1967, doi:10.1016/0021-8928(67)90034-2.

[88] M. de Moura, J. Gonçalves, and A. Magalhães, "A straightforward method to obtain the cohesive laws of bonded joints under mode I loading," *International Journal of Adhesion and Adhesives*, vol. 39, pp. 54–59, 2012, doi:10.1016/j.ijadhadh.2012.07.008.

[89] F. Sun and B. Blackman, "A DIC method to determine the Mode I energy release rate G, the J-integral and the traction-separation law simultaneously for adhesive joints," *Engineering Fracture Mechanics*, vol. 234, p. 107097, Jun. 2020, doi:10.1016/j.engfracmech.2020.107097.

[90] A. Biel, S. Alfredsson, and T. Carlberger, "Adhesive Tapes; Cohesive Laws for a Soft Layer," *Procedia Materials Science*, vol. 3, pp. 1389–1393, Dec. 2014, doi:10.1016/j.mspro.2014.06.224.

[91] L. Loh and S. Marzi, "An Out-of-plane Loaded Double Cantilever Beam (ODCB) test to measure the critical energy release rate in mode III of adhesive joints," *International Journal of Adhesion and Adhesives*, vol. 83, pp. 24–30, 2018, special issue on joint design. doi:10.1016/j.ijadhadh.2018.02.021.

[92] P. Schrader and S. Marzi, "Novel mode III DCB test setups and related evaluation methods to investigate the fracture behaviour of adhesive joints," *Theoretical and Applied Fracture Mechanics*, vol. 123, p. 103699, 2023, doi:10.1016/j.tafmec.2022.103699.

[93] A. Biel and U. Stigh, "Comparison of J-integral methods to experimentally determine cohesive laws in shear for adhesives," *International Journal of Adhesion and Adhesives*, vol. 94, May 2019, doi:10.1016/j.ijadhadh.2019.04.014.

[94] A. Arrese, F. Mujika, J. Renart, and C. Sarrado, "Analysis of displacement path dependence in mixed mode cohesive law," *Engineering Fracture Mechanics*, vol. 276, p. 108879, 2022, doi:10.1016/j.engfracmech.2022.108879.

[95] S. Marzi, "Experimental determination of coupled cohesive laws with an unsymmetrical stiffness matrix for structural adhesive joints loaded in mixed-mode I+III," *Engineering Fracture Mechanics*, vol. 283, p. 109215, 2023, doi:10.1016/j.engfracmech.2023.109215.

[96] J. Scheel, A. Schlosser, and A. Ricoeur, "The J-integral for mixed-mode loaded cracks with cohesive zones," *International Journal of Fracture*, vol. 227, pp. 79–94, 2021, doi:10.1007/s10704-020-00496-6.

[97] A. Bernasconi, R. A. A. Lima, S. Cardamone, R. B. Campbell, A. H. Slocum, and M. Giglio, "Effect of temperature on cohesive modelling of 3M Scotch-Weld™ 7260 B/A epoxy adhesive," *The Journal of Adhesion*, vol. 96, no. 1–4, pp. 437–460, 2019, doi:10.1080/00218464.2019.1665519.

[98] S. Cardamone, A. Bernasconi, and M. Giglio, "Characterization of the 3M Scotch-Weld™ 7260 B/A epoxy adhesive by cohesive damage models and application to a full-scale bonded sub-structure," *The Journal of Adhesion*, vol. 96, no. 14, pp. 1270–1301, 2019, doi:10.1080/00218464.2019.1591278.

[99] P. Schrader, D. Domladovac, and S. Marzi, "Influence of Loading Rate on the Cohesive Traction for Soft, Rubber-Like Adhesive Layers Loaded in Modes I and III," *Processes*, vol. 11, no. 2, 2023, doi:10.3390/pr11020356.

[100] M. Ameen, R. Peerlings, and M. Geers, "A quantitative assessment of the scale separation limits of classical and higher-order asymptotic homogenization," *European Journal of Mechanics - A/Solids*, vol. 71, pp. 89–100, 2018, doi:10.1016/j.euromechsol.2018.02.011.

[101] O. Zienkiewicz and R. Taylor, *The Finite Element Method*, 5th ed. Oxford, UK: Butterworth-Heinemann, 2000, vol. 2.

[102] E. de Souza Neto, D. Peric, and D. Owen, *Computational methods for plasticity: theory and applications*. Chichester, UK: John Wiley & Sons, 2008.

[103] K. Matouš, M. G. Geers, V. G. Kouznetsova, and A. Gillman, "A Review of Predictive Nonlinear Theories for Multiscale Modeling of Heterogeneous Materials," *J. Comput. Phys.*, vol. 330, no. C, pp. 192–220, Feb. 2017, doi:10.1016/j.jcp.2016.10.070.

[104] R. Hill, "Elastic properties of reinforced solids: Some theoretical principles," *Journal of the Mechanics and Physics of Solids*, vol. 11, no. 5, pp. 357–372, 1963, doi:10.1016/0022-5096(63)90036-X.

[105] A. Javili, S. Saeb, and P. Steinmann, "Aspects of implementing constant traction boundary conditions in computational homogenization via semi-Dirichlet boundary conditions," *Comput. Mech.*, vol. 59, no. 1, pp. 21–35, Jan. 2017, doi:10.1007/s00466-016-1333-8.

[106] L. Sharma, R. Peerlings, P. Shanthraj, F. Roters, and M. Geer, "FFT-based interface decohesion modelling by a nonlocal interphase," *Advanced Modeling and Simulation in Engineering Sciences*, vol. 5, no. 7, pp. 2213–7467, 2018, doi:10.1186/s40323-018-0100-0.

[107] M. Schneider, "Lippmann-schwinger solvers for the computational homogenization of materials with pores," *International Journal for Numerical Methods in Engineering*, vol. 121, no. 22, pp. 5017–5041, 2020, doi:10.1002/nme.6508.

[108] J. Barzilai and J. M. Borwein, "Two-Point Step Size Gradient Methods," *IMA Journal of Numerical Analysis*, vol. 8, no. 1, pp. 141–148, Jan. 1988, doi:10.1093/imanum/8.1.141.

[109] Y. Nesterov, *Introductury Lectures on Convex Optimization: A Basic Course*. New York, NY, USA: Springer, 2004.

[110] M. G. Larson and F. Bengzon, *Abstract Finite Element Analysis*. Berlin, Heidelberg, Germany: Springer, 2013, pp. 177–201.

[111] C. Heil, *Metrics, Norms, Inner Products, and Operator Theory BUCH*, ser. Applied and Numerical Harmonic Analysis. Cham, Switzerland: Birkhäuser, 2018.

[112] M. Itskov, "On the theory of fourth-order tensors and their applications in computational mechanics," *Computer Methods in Applied Mechanics and Engineering*, vol. 189, no. 2, pp. 419–438, 2000, doi:10.1016/S0045-7825(99)00472-7.

[113] M. M. Mehrabadi and S. C. Cowin, "Eigentensors of linear anisotropic elastic materials," *The Quarterly Journal of Mechanics and Applied Mathematics*, vol. 43, no. 1, pp. 15–41, Feb. 1990, doi:10.1093/qjmam/43.1.15.

[114] P. Dłużewski and P. Rodzik, "Elastic eigenstates in finite element modelling of large anisotropic elasticity," *Computer Methods in Applied Mechanics and Engineering*, vol. 160, no. 3, pp. 325–335, 1998, doi:10.1016/S0045-7825(97)00295-8.

[115] M. Kabel, S. Fliegener, and M. Schneider, "Mixed boundary conditions for FFT-based homogenization at finite strains," *Computational Mechanics*, vol. 57, Feb. 2016, doi:10.1007/s00466-015-1227-1.

[116] N. Lahellec and P. Suquet, "On the effective behavior of nonlinear inelastic composites: I. Incremental variational principles," *Journal of the Mechanics and Physics of Solids*, vol. 55, no. 9, pp. 1932–1963, 2007, doi:10.1016/j.jmps.2007.02.003.

[117] C. Miehe, "Strain-driven homogenization of inelastic microstructures and composites based on an incremental variational formulation," *International Journal for Numerical Methods in Engineering*, vol. 55, no. 11, pp. 1285–1322, 2002, doi:10.1002/nme.515.

[118] B. Halphen and Q. Nguyen, "Sur les Matériaux Standard Généralisés," *Journal de Mécanique*, vol. 14, pp. 39–63, Jan. 1975.

[119] P. Germain, Q. Nguyen, and P. Suquet, "Continuum thermodynamics ASME," *Journal of Applied Mechanics*, vol. 105, pp. 1011–1020, Dec. 1983, doi:10.1115/1.3167184.

[120] J. Görthofer, M. Schneider, A. Hrymak, and T. Böhlke, "A convex anisotropic damage model based on the compliance tensor," *International Journal of Damage Mechanics*, vol. 31, no. 1, pp. 43–86, 2022, doi:10.1177/10567895211019065.

[121] N. Magino, J. Köbler, H. Andrä, F. Welschinger, R. Müller, and M. Schneider, "A multiscale high-cycle fatigue-damage model for the stiffness degradation of fiber-reinforced materials based on a mixed variational framework," *Computer Methods in Applied Mechanics and Engineering*, vol. 388, p. 114198, 2022, doi:10.1016/j.cma.2021.114198.

[122] M. Köhler and D. Balzani, "Evolving microstructures in relaxed continuum damage mechanics for the modeling of strain softening," *Journal of the Mechanics and Physics of Solids*, vol. 173, p. 105199, 2023, doi:10.1016/j.jmps.2023.105199.

[123] D. Wicht, "Efficient fast fourier transform-based solvers for computing the thermomechanical behavior of applied materials," Ph.D. dissertation, Karlsruher Institut für Technologie (KIT), 2022, doi:10.5445/KSP/1000148765.

[124] L. Dagum and R. Menon, "OpenMP: An Industry-Standard API for Shared-Memory Programming," *Computing in Science & Engineering*, vol. 1, pp. 46–55, 1998, doi:10.1109/99.660313.

[125] M. Frigo and S. Johnson, "The Design and implementation of FFTW3," *Proceedings of the IEEE*, vol. 93, pp. 216 – 231, Mar. 2005, doi:10.1109/JPROC.2004.840301.

[126] K. Lee, K. Marimuthu, and H. Lee, "UMAT/VUMAT for linear, bilinear and piecewise Drucker-Prager models," *Mendeley Data, Version 7*, 2019, doi:10.17632/5ccwt5fv7y.7.

[127] F. Burbulla, "Kontinuumsmechanische und bruchmechanische modelle für werkstoffverbunde," PhD thesis, Kassel, Universität Kassel, Fachbereich Maschinenbau, 2015.

[128] P. Camanho and C. Dàvila, "Mixed-mode decohesion finite elements for the simulation of delamination in composite materials," NASA, Tech. Rep., 2002.

[129] N. Valoroso and S. de Barros, "Adhesive joint computations using cohesive zones," *Applied Adhesion Science*, vol. 1, Dec. 2013, doi:10.1186/2196-4351-1-8.

[130] L. Gélébart, "A modified FFT-based solver for the mechanical simulation of heterogeneous materials with Dirichlet boundary conditions," *Comptes Rendus. Mécanique*, vol. 348, no. 8-9, pp. 693–704, 2020, doi:10.1016/10.5802/crmeca.54.

[131] L. Risthaus and M. Schneider, "Imposing Dirichlet boundary conditions directly for FFT-based computational micromechanics," *Computational Mechanics*, Jun. 2024, doi:10.1016/10.1007/s00466-024-02469-1.

[132] L. Risthaus and M. Schneider, "FFT-based computational micromechanics with Dirichlet boundary conditions on the rotated staggered grid," *International Journal for Numerical Methods in Engineering*, p. e7569, Jul. 2024, doi:10.1016/10.1002/nme.7569.

[133] Y. Chen, D. Vasiukov, L. Gélébart, and C. Park, "Fast Fourier transform solver for damage modeling of composite materials," *JMST Advances*, vol. 1, pp. 49–55, 2019, doi:10.1007/s42791-019-0004-2.

[134] V. Dumont, C. Badulescu, G. Stamoulis, J. Adrien, E. Maire, A. Lefèvre, and D. Thévenet, "On the effect of the curing cycle on the creation of pores in structural adhesive joints by means of X-ray microtomography," *The Journal of Adhesion*, pp. 1–34, 2020, doi:10.1080/00218464.2020.1728257.

[135] L. C. Sawyer, D. T. Grubb, and G. F. Meyers, *Polymer Microscopy*, 3rd ed. New York, NY, USA: Springer, 2008.

[136] G. Bradski, "The OpenCV Library," *Dr. Dobb's Journal of Software Tools*, 2000.

[137] M. Bailakanavar, Y. Liu, J. Fish, and Y. Zheng, "Automated modeling of random inclusion composites," *Engineering with Computers*, vol. 30, pp. 609–625, 2014, doi:10.1007/s00366-012-0310-x.

[138] D. H. Eberly, "Robust Computation of Distance Between Line Segments," 2018.

[139] L. J. Miranda, "PySwarms: a research toolkit for Particle Swarm Optimization in Python," *Journal of Open Source Software*, vol. 3, no. 21, p. 433, 2018, doi:10.21105/joss.00433.

[140] J. Kennedy and R. Eberhart, "Particle swarm optimization," in *Proceedings of ICNN'95 - International Conference on Neural Networks INPRO*, vol. 4, 1995, pp. 1942–1948 vol.4, doi:10.1109/ICNN.1995.488968.

[141] S. Kirkpatrick, C. D. Gelatt, and M. P. Vecchi, "Optimization by Simulated Annealing," *Science*, vol. 220, no. 4598, pp. 671–680, 1983, doi:10.1126/science.220.4598.671.

[142] S. Sivanandam and S. N. Deepa, *Introduction to Genetic Algorithms*. Heidelberg, Berlin, Germany: Springer, 2008.

[143] S. Simaafrookhteh, R. Taherian, and M. Shakeri, "Stochastic Microstructure Reconstruction of a Binder/Carbon Fiber/Expanded Graphite Carbon Fiber Paper for PEMFCs Applications: Mass Transport and Conductivity Properties," *Journal of The Electrochemical Society*, vol. 166, pp. 3287–3299, May 2019, doi:10.1149/2.0331907jes.

[144] R. Haralick, S. Sternberg, and X. Zhuang, "Image Analysis Using Mathematical Morphology," *Pattern Analysis and Machine Intelligence, IEEE Transactions on*, vol. PAMI-9, pp. 532 – 550, Aug. 1987, doi:10.1109/TPAMI.1987.4767941.

[145] P. Soille, *Morphological Image Analysis*, 2nd ed. Berlin, Heidelber, Germany: Springer-Verlag, 2004.

[146] R. Pyrz, "Quantitative description of the microstructure of composites. Part I: Morphology of unidirectional composite systems," *Composites Science and Technology*, vol. 50, no. 2, pp. 197–208, 1994, doi:10.1016/0266-3538(94)90141-4.

[147] P. Dixon, "Ripley's K function," in *Encyclopedia of Environmetrics*, W. El-Shaarawi and H. Abdel, Eds. John Wiley & Sons, 2002, vol. 3, pp. 1796–1803, doi:10.1002/9781118445112.stat07751.

[148] B. D. Ripley, "Modelling Spatial Patterns," *Journal of the Royal Statistical Society: Series B (Methodological)*, vol. 39, no. 2, pp. 172–192, 1977, doi:10.1111/j.2517-6161.1977.tb01615.x.

[149] B. Yucel, S. Yucel, A. Ray, L. Duprez, and S. Kalidindi, "Mining the Correlations Between Optical Micrographs and Mechanical Properties of Cold-Rolled HSLA Steels Using Machine Learning Approaches," *Integrating Materials and Manufacturing Innovation*, vol. 9, pp. 1–17, Sept. 2020, doi:10.1007/s40192-020-00183-3.

[150] D. Brough, D. Wheeler, and S. Kalidindi, "Materials Knowledge Systems in Python - A Data Science Framework for Accelerated Development of Hierarchical Materials," *Integrating Materials and Manufacturing Innovation*, vol. 6, pp. 1–18, Oct. 2016, doi:10.1007/s40192-017-0089-0.

[151] P. Sudharshan Phani and W. Oliver, "A critical assessment of the effect of indentation spacing on the measurement of hardness and modulus using instrumented indentation testing," *Materials & Design*, vol. 164, p. 107563, 2019, doi:10.1016/j.matdes.2018.107563.

[152] K. Durst, M. Göken, and H. Vehoff, "Finite Element Study for Nanoindentation Measurements on Two-Phase Materials," *Journal of Materials Research*, vol. 19, pp. 85–93, Jan. 2004, doi:10.1557/jmr.2004.19.1.85.

[153] W. C. Oliver and G. M. Pharr, "An improved technique for determining hardness and elastic modulus using load and displacement sensing indentation experiments," *Journal of Materials Research*, vol. 7, pp. 1564 – 1583, 1992, doi:10.1557/JMR.1992.1564.

[154] J. Fox, *Applied Regression Analysis and Generalized Linear Models*, 3rd ed. Thousand Oaks, CA, USA: Sage Publications, 2015.

[155] P. Virtanen, R. Gommers, T. E. Oliphant, M. Haberland, T. Reddy, D. Cournapeau, E. Burovski, P. Peterson, W. Weckesser, J. Bright, S. J. van der Walt, M. Brett, J. Wilson, K. J. Millman, N. Mayorov, A. R. J. Nelson, E. Jones, R. Kern, E. Larson, C. J. Carey, İ. Polat, Y. Feng, E. W. Moore, J. VanderPlas, D. Laxalde, J. Perktold, R. Cimrman, I. Henriksen, E. A. Quintero, C. R. Harris, A. M. Archibald, A. H. Ribeiro, F. Pedregosa, P. van Mulbregt, and SciPy 1.0 Contributors, "SciPy 1.0: Fundamental Algorithms for Scientific Computing in Python," *Nature Methods*, vol. 17, pp. 261–272, 2020, doi:10.1038/s41592-019-0686-2.

[156] R. B. D'Agostino and E. S. Pearson, "Tests for departure from normality. Empirical results for the distributions of b2 and b1," *Biometrika*, vol. 60, pp. 613–622, 1973, doi:10.2307/2335012.

[157] S. S. Shapiro and M. B. Wilk, "An Analysis of Variance Test for Normality (Complete Samples)," *Biometrika*, vol. 52, pp. 591–611, 1965, doi:10.2307/2333709.

[158] A. Ghasemi and S. Zahediasl, "Normality Tests for Statistical Analysis: A Guide for Non-Statisticians," *International journal of endocrinology and metabolism*, vol. 10, pp. 486–489, Dec. 2012, doi:10.5812/ijem.3505.

[159] A. Recco, C. Viáfara, A. Sinatora, and A. Tschiptschin, "Energy dissipation in depth-sensing indentation as a characteristic of the nanoscratch behavior of coatings," *Wear*, vol. 267, no. 5, pp. 1146–1152, 2009, 17th International Conference on Wear of Materials. doi:10.1016/j.wear.2009.01.043.

[160] M. Dao, N. Chollacoop, K. Van Vliet, T. Venkatesh, and S. Suresh, "Computational modeling of the forward and reverse problems in instrumented sharp indentation," *Acta Materialia*, vol. 49, no. 19, pp. 3899–3918, 2001, doi:10.1016/S1359-6454(01)00295-6.

[161] N. Sakharova, J. Fernandes, J. Antunes, and M. Oliveira, "Comparison between Berkovich, Vickers and conical indentation tests: A three-dimensional numerical simulation study," *International Journal of Solids and Structures*, vol. 46, no. 5, pp. 1095–1104, 2009, doi:10.1016/j.ijsolstr.2008.10.032.

[162] J. Gosse and S. Christensen, "Strain Invariant Failure Criteria for Polymers in Composite Materials," in *Collection of Technical Papers - AIAA/ASME/ASCE/AHS/ASC Structures, Structural Dynamics and Materials Conference*, vol. 1, Jun. 2001, doi:10.2514/6.2001-1184.

[163] L. Asp, L. Berglund, and R. Talreja, "A criterion for crack initiation in glassy polymers subjected to a composite-like stress state," *Composites Science and Technology*, vol. 56, no. 11, pp. 1291–1301, 1996, doi:10.1016/S0266-3538(96)00090-5.

[164] V. Saseendran, C. Berggreen, and L. A. Carlsson, "Fracture Mechanics Analysis of Reinforced DCB Sandwich Debond Specimen Loaded by Moments," *AIAA Journal*, vol. 56, no. 1, pp. 413–422, 2018, doi:10.2514/1.J056039.

[165] I. Kididane, N. Ladwig, and S. Marzi, "Dual-actuator mixed-mode bending tests on structural adhesive joints," *Engineering Fracture Mechanics*, vol. 301, p. 110017, 2024, doi:10.1016/j.engfracmech.2024.110017.

[166] M. Kabel, D. Merkert, and M. Schneider, "Use of composite voxels in FFT-based homogenization," *Computer Methods in Applied Mechanics and Engineering*, vol. 294, pp. 168–188, 2015, doi:10.1016/j.cma.2015.06.003.

[167] P. Herr, F. Bödeker, and S. Marzi, "Numerical investigation on the effect of fillers on the fracture behavior of adhesives," *Procedia Structural Integrity*, vol. 42, pp. 498–505, 2022, 23 European Conference on Fracture. doi:10.1016/j.prostr.2022.12.063.

[168] L. Sharma, R. Peerlings, P. Shanthraj, F. Roters, and M. Geers, "An FFT-based spectral solver for interface decohesion modelling using a gradient damage approach," *Computational Mechanics*, vol. 65, no. 4, pp. 925–939, 2020, doi:10.1007/s00466-019-01801-4.

[169] L. Sharma, R. Peerlings, M. Geers, and F. Roters, "Integral nonlocal approach to model interface decohesion in FFT solvers," *Engineering Fracture Mechanics*, vol. 243, p. 107516, 2021, doi:10.1016/j.engfracmech.2020.107516.

[170] Y. Chen, L. Gélébart, A. Marano, and J. Marrow, "FFT phase-field model combined with cohesive composite voxels for fracture of composite materials with interfaces," *Computational Mechanics*, vol. 68, no. 2, pp. 433–457, 2021, doi:10.1007/s00466-021-02041-1.